POLITECNICO DI MILANO
DEPARTMENT OF ENERGY
DOCTORAL PROGRAMME IN ENERGY AND NUCLEAR SCIENCE AND TECHNOLOGY

NUMERICAL AND EXPERIMENTAL INVESTIGATION OF LASER-DRIVEN RADIATION SOURCES FOR MATERIALS CHARACTERIZATION

Doctoral Dissertation of:
Francesco Mirani

Supervisor:
Prof. Matteo Passoni

Tutor:
Prof. Carlo S. Casari

The Chair of the Doctoral Program:
Prof. Vincenzo Dossena

Year 2021 – Cycle XXXIII

Abstract

The atomic and nuclear analytical methods are a broad family of techniques exploited for the elemental characterization of materials. Particle and photon beams interact with the samples under study, inducing the emission of characteristic secondary radiation. The analysis of the emitted radiation allows retrieving the composition of a large variety of materials, avoiding visible damage or changes in the chemical composition. Many of these techniques have relied on massive and expensive radiation sources (e.g. particle accelerators) for several decades. As a result, their large-scale diffusion has been prevented until today.

In the last years, the advent of a new generation of ultra-short and super-intense lasers (intensity exceeding $\sim 10^{19}\ \mathrm{W/cm^2}$) paved the way for the exploration of new laser-plasma interaction scenarios. Among the others, laser-driven particle acceleration, consisting in the production of high-energy electrons and ions ($\sim 1 - 10\ \mathrm{MeV/u}$) when the laser pulse is focused onto a thin (i.e. less than 100 μm) solid target, is attracting increasing attention in the scientific community. Indeed, the compact size and multi-particle nature of laser-based accelerators make them attractive for applications in several fields, from astrophysics to medical science.

Certainly, atomic and nuclear analytical methods could greatly benefit from the adoption of a flexible, cost-effective and multi-radiation platform. However, the applicability of laser-driven radiation sources to the elemental analysis of materials remains substantially unexplored. Therefore, the goal of this thesis work is to address the possibility to exploit laser-driven particle acceleration for materials characterization, considering three specific analytical techniques: the Particle Induced X-ray Emission (PIXE), Energy Dispersive X-ray (EDX) spectroscopy and Photon Activation Analysis (PAA).

To this aim, both theoretical and experimental approaches are adopted. First, to make laser-driven radiation sources suitable for the mentioned applications, their shot-to-shot stability must be enhanced through optimization and full control of the target properties. This point is addressed via target production with an appropriate materials deposition technique (i.e. the Magnetron Sputtering). Next, feasibility studies of laser-driven PIXE, EDX and PAA are performed with Particle-In-Cell and Monte Carlo simulations. Lastly, the results of a proof-of-principle laser-driven PIXE and EDX experiment realized in an international laser facility are presented. The outcomes of this PhD work confirm that materials characterization can be performed in existing laser facilities hosting $10 - 100$ TW class lasers.

Sommario

I metodi analitici atomici e nucleari sono un'ampia famiglia di tecniche usate per la caratterizzazione elementale di materiali. Fasci di particelle e di fotoni interagiscono con i campioni oggetto di studio inducendo l'emissione di radiazione secondaria caratteristica. L'analisi della radiazione emessa consente di ricavare la composizione di una grande varietà di materiali evitando danni visibili o cambiamenti nella composizione chimica. Molte di queste tecniche hanno fatto affidamento su sorgenti di radiazioni grandi e costose (ad es. acceleratori di particelle) per diversi decenni. Di conseguenza, la loro diffusione su larga scala non è stata possibile fino a oggi.

Negli ultimi anni, l'avvento di una nuova generazione di laser ultra-brevi e super-intensi (intensità maggiori di $\sim 10^{19}\ \mathrm{W/cm^2}$) ha aperto la strada all'esplorazione di nuovi scenari d'interazione laser-plasma. Tra gli altri, l'accelerazione di particelle da laser, consistente nella produzione di elettroni e ioni ad alta energia ($\sim 1-10\ \mathrm{MeV/u}$) quando l'impulso laser è focalizzato su un bersaglio solido sottile (spessore inferiore a 100 μm), sta attirando sempre più attenzione nella comunità scientifica. Infatti, le dimensioni compatte e la possibilità di accelerare più tipi di particelle rendono gli acceleratori da laser interessanti per applicazioni in diversi campi, dall'astrofisica alla scienza medica.

Certamente, anche i metodi analitici atomici e nucleari potrebbero trarre ampio beneficio nel dotarsi di una piattaforma flessibile, economica e multiradiazione. Tuttavia, l'uso di sorgenti di radiazione da laser per l'analisi elementale di materiali rimane un'applicazione sostanzialmente inesplorata. Pertanto, l'obiettivo di questo lavoro di tesi è d'investigare la possibilità di sfruttare le sorgenti di radiazioni da laser per la caratterizzazione dei materiali, considerando tre tecniche analitiche specifiche: la Particle Induced X-ray Emission (PIXE), l'Energy Dispersive X-ray (EDX) spectroscopy e la Photon Activation Analysis (PAA).

A tale scopo, è stato adottato un approccio sia sperimentale che teorico. In primo luogo, per renderle adatte alle applicazioni citate, la stabilità delle sorgenti di radiazione da laser deve essere migliorata attraverso l'ottimizzazione e il pieno controllo delle proprietà del bersaglio. Questo punto viene affrontato tramite la produzione di bersagli con una tecnica di deposizione di materiali appropriata (ovvero il Magnetron Sputtering). Successivamente, tramite simulazioni Particle-In-Cell e Monte Carlo, viene fatto uno studio di fattibilità di PIXE, EDX e PAA svolte con sorgenti laser. Infine, vengono presentati i risultati di un esperimento PIXE ed EDX con sorgente di particelle da laser svolto in un centro di ricerca internazionale. I risultati di questo lavoro di dottorato confermano che la caratterizzazione dei materiali può essere eseguita nei centri di ricerca che ospitano laser di classe $10 - 100$ TW.

Contents

I State of the art and thesis goals **7**

1 Atomic and nuclear analytical methods for materials characterization **9**
- 1.1 Atomic and nuclear analytical methods, an overview . . . 9
- 1.2 Energy Dispersive X-ray (EDX) spectroscopy and Scanning Electron Microscope (SEM) . . . 12
- 1.3 Particle Induced X-ray Emission (PIXE) analysis . . . 14
  - 1.3.1 Experimental apparatus . . . 14
  - 1.3.2 Theoretical description and sample composition reconstruction . 16
  - 1.3.3 PIXE advantages and limitations . . . 19
- 1.4 Photon Activation Analysis (PAA) . . . 20
  - 1.4.1 Experimental apparatus . . . 20
  - 1.4.2 Photonuclear reactions and radioactive decay . . . 21
  - 1.4.3 Sample irradiation and composition reconstruction . . . 23
  - 1.4.4 PAA advantages and limitations . . . 24
- 1.5 Particle accelerators for the elemental analysis techniques . . . 24

2 Laser-driven particle acceleration and applications **27**
- 2.1 Ultra-short and super-intense laser technology . . . 27
- 2.2 Super-intense laser-matter interaction . . . 29
- 2.3 Ion acceleration via Target Normal Sheath Acceleration (TNSA) . . . 31
  - 2.3.1 Solid targets for TNSA . . . 33
  - 2.3.2 Enhanced TNSA with Near-critical Double Layer Targets (DLT) 34
  - 2.3.3 Theoretical description of the laser-DLT interaction . . . 36
- 2.4 Laser-driven electron acceleration . . . 38
  - 2.4.1 Laser wakefield acceleration (lwfa) . . . 39
- 2.5 Applications of laser-driven particle sources . . . 40

3 Thesis goals and methods **43**
- 3.1 Thesis motivations, objectives and personal contribution . . . 43
- 3.2 Magnetron Sputtering deposition techniques . . . 46
  - 3.2.1 The sputtering process . . . 46

3.2.2 Direct Current Magnetron Sputtering (DCMS) 48
3.2.3 High Power Impulse Magnetron Sputtering (HiPIMS) 50
3.2.4 Phase tailoring in titanium films with PVD techniques 53
3.3 Particle-In-Cell (PIC) method 55
3.4 Monte Carlo method 57
3.4.1 Geant4 57
3.4.2 Fluka 60

II Production of solid targets for TNSA via Magnetron Sputtering 63

4 DCMS and HiPIMS deposition of titanium (Ti) films and characterization 65
4.1 Experimental configuration and plasma characterization 66
4.1.1 Optical Emission Spectroscopy analysis 68
4.2 Ti films characterization 70
4.2.1 Morphological characterization 70
4.2.2 Phase composition and crystallographic orientation 72
4.2.3 Stress state evaluation 75
4.3 Phase tailoring and stress behaviour in Ti films 76
4.3.1 Low ion energy regime 77
4.3.2 High ion energy regime 79

5 Production of Ti substrates on perforated target holders 81
5.1 Strategy for the free-standing films deposition 81
5.1.1 Holder preparation prior deposition 83
5.2 Magnetron Sputtering deposition of Ti substrates. 86
5.2.1 Multilayer structures of DCMS and HiPIMS depositions 87
5.2.2 DCMS and HiPIMS depositions with bias application 92

III Investigation on laser-driven sources for materials characterization 95

6 Theoretical study on laser-driven PIXE 97
6.1 Laser-driven PIXE modeling 97
6.1.1 Iterative code for laser-driven PIXE quantitative analysis 99
6.2 Simulations of laser-driven PIXE experiments 100
6.2.1 Monte Carlo simulation of laser-driven in-air PIXE 102
6.2.2 Particle-In-Cell simulations of laser-driven proton acceleration . 103
6.3 Laser-driven PIXE quantitative analysis results 105
6.3.1 Elemental concentrations in a homogeneous sample 105
6.3.2 Differential PIXE analysis of non-homogeneous samples 106
6.4 Electron influence on laser-driven PIXE and laser-driven EDX 109

7 Experimental investigation on laser-driven PIXE and laser-driven EDX 113
7.1 Laser-driven EDX and PIXE experimental apparatus 113
7.1.1 Sample production via DCMS 115
7.1.2 Proton energy spectra characterization 116
7.1.3 X-ray spectra reconstruction and CCD energy calibration 117

7.2 Laser-driven EDX and PIXE experimental results 118
  7.2.1 Elemental analysis 118
  7.2.2 Stratigraphic analysis 120
7.3 Evaluation of the electron influence on laser-driven PIXE 123
  7.3.1 Finite Element Analysis of the magnetic field configuration . . . 123
  7.3.2 Monte Carlo simulations of the experimental setups 124
  7.3.3 Post hoc evaluation of the electron temperature 127

8 Theoretical study on Laser-driven PAA **131**
8.1 Theoretical description for the conventional and laser-driven PAA . . . 131
  8.1.1 Model for conventional PAA 133
  8.1.2 Model for laser-driven PAA 135
8.2 Comparison between conventional PAA and laser-driven PAA performances 137
8.3 Monte Carlo simulation of PAA experiments 139
  8.3.1 Simulation setup 139
  8.3.2 Assessment of the comparison 141
8.4 Combined PIC-Monte Carlo simulation of a laser-driven PAA experiment 142
  8.4.1 Particle-In-Cell simulations of laser-driven electron acceleration 143
  8.4.2 Monte Carlo simulation and sample composition reconstruction . 145

IV Conclusions and future perspectives **149**

Bibliography **169**

Introduction

Materials characterization is of exceptional importance in many industrial and scientific branches. Among the various analytical techniques, atomic and nuclear methods play a fundamental role. Indeed, they have unparalleled detection capabilities and, with only a few exceptions (e.g. accelerator-based carbon dating and mass spectroscopy), non-destructive nature. They rely on the irradiation of samples, having an unknown elemental composition, with photon, electron, ion and neutron beams and the detection of the emitted secondary radiation. Since the energy of the emitted secondary particles is characteristic of the irradiated element or isotope, they can be exploited to recover the sample composition. This broad family of techniques (among which we find X-ray Fluorescence Spectroscopy, Ion Beam Analysis and Energy Dispersive X-ray Spectroscopy) is applied in an impressive number of fields with a significant impact on our everyday life. For instance, they are routinely exploited in medicine, cultural heritage preservation, environmental monitoring, semiconductor industry, forensic analysis and nuclear fusion research.

As far as energetic ions as primary particles are concerned, Particle Induced X-ray Emission (PIXE) is probably the most widespread technique. It exploits MeV energy ions, usually protons provided by an electrostatic accelerator, to ionize the sample atoms. As a result, the atoms emit characteristic X-rays, which can be detected and collected in spectra. The spectra analysis allows recognizing the elements and retrieving their absolute concentrations in gaseous, liquid, and solid materials. Besides, if the material is irradiated with proton beams having different energies, the *differential PIXE* variant is applied to reconstruct the distribution of the elements as a function of the sample thickness down to several micrometres depth in solids. Usually, PIXE is carried in vacuum conditions, but it can also be performed in-air for the analysis of large objects.

Another analytical technique is the Energy Dispersive X-ray (EDX) Spectroscopy. The primary radiation is a keV energy electron beam, while the emitted radiation is represented again by characteristic X-rays. EDX is carried out in Scanning Electron Microscope (SEM) systems equipped with an electron gun. Contrary to PIXE, the in-vacuum condition is mandatory. Therefore, EDX allows quickly probing the composition only of solid samples and within a thickness range of just a few micrometres. Besides, merely the elemental concentrations of homogeneous materials are achievable. On the other hand, complex stratigraphic analyses of non-homogeneous materials are forbidden.

Lastly, for the aims of this work, the Photon Activation Analysis (PAA) technique is worthy of consideration. The probed samples are irradiated with a $\sim 10 - 30$ MeV photon beam. These photons interact with the material nuclei via photonuclear reactions. Following an interval of time, the activated nuclei decay with the emission of characteristic γ-rays. Usually, the sample composition is retrieved exploiting the co-irradiation of the sample and comparative material. The primary photons are generated via the interaction of high-energy electrons with high-Z materials and bremsstrahlung emission. The electrons are provided by LINAC machines. PAA stands for its capability of detecting elements down to several cm in thick samples because of the high penetration depth of MeV energy photons in solid matter.

Despite the outstanding capabilities of PIXE, EDX and PAA, these techniques are performed in a rather limited number of laboratories, where particle accelerators or SEM instrumentations are available. Indeed, the required radiation sources are affected by significant limitations, preventing the large-scale diffusion of the techniques. For instance, particle accelerators are large and expensive. Moreover, they can provide only one kind of particle and, in the case of particle accelerators, their energy is not always easily tunable. Thus, the mentioned analytical techniques could greatly benefit from the adoption of a more compact, cost-effective and multi-particle radiation source.

In this respect, laser-driven radiation sources are an appealing alternative to conventional accelerators. They rely on the interaction between ultrashort ($10 - 100$ fs) super-intense ($I > 10^{18}\ \mathrm{W/cm^2}$) laser pulses and target materials. Among the various target configurations (e.g. gas, liquid, cryogenic), micrometric solid foils allow accelerating electrons and ions to energies ranging from few MeV up to several 10s of MeV. Particles are accelerated almost simultaneously in an ultra-fast dynamic, and their energy spectra are broad.

A promising strategy, investigated within the framework of the ERC-ENSURE project, is to cover the solid foil (i.e. the substrate) with a low-density material (e.g. a carbon foam). The result is a Double-Layer Target (DLT) where the presence of the low-density layer enhances the laser absorption, with a consequent increment of the number and energy of the accelerated particles. Compared to conventional bare targets, DLTs represent a viable route to accelerate particles with reduced laser requirements in terms of costs and dimensions. Exploiting table-top 10s TW class lasers, they could provide ions and electrons with the energies and average fluxes required by the mentioned materials characterization techniques. Those lasers can also work at relatively high repetition rates (i.e. $1 - 10$ Hz). Lastly, the energy of the accelerated particles can be easily tuned by changing the laser intensity or the DLT properties (e.g. the near-critical layer and substrate thicknesses and densities).

A flexible and compact acceleration system able to provide different kinds of particles would represent a unique tool for several materials science applications. Despite the high potential interest, a feasibility study of laser-driven particle sources for materials characterization is still absent in existing literature, with only a few exceptions. Therefore, an investigation aimed at studying the applicability of laser-driven sources for PIXE, EDX and PAA studies requires addressing several unexplored aspects. For instance, the compatibility between the delivered particle properties and the selected techniques must be addressed theoretically and experimentally. Moreover, since the applications require excellent stability of the particle beam, absolute control of the target parameters is mandatory to guarantee the shot-to-shot stability.

Motivations and goals of the thesis

This thesis work aims at providing a theoretical and experimental investigation of the feasibility of laser-driven radiation sources for materials science applications. Besides, the study and production of substrates for DLTs with controlled properties, thus suitable for the applications, is performed.

As previously mentioned, the analytical techniques demand particle beams with high stability during operation. Different issues of laser-driven sources must be investigated to meet this requirement. Indeed, super-intense laser pulses can be characterized by shot-to-shot fluctuations. Moreover, plasma instabilities (e.g. current-filamentation instabilities) can be present, which worsen the particle beam spacial quality. Last, sub-micrometric bare targets or DLT substrates are affected by non-negligible local thickness uncertainty, with detrimental consequences on the shot-to-shot stability. Although significant efforts must be put to improve all the mentioned aspects, this PhD thesis will focus on the target. Therefore, the first fundamental goal of this work consists of the production and characterization of sub-micrometric targets or DLT substrates with enhanced planarity. To this aim, the new Magnetron Sputtering deposition system installed at the *Micro- and Nanostructured Materials Laboratory* (NanoLab) in Politecnico di Milano is exploited.

Laser-driven particle sources are intrinsically different from the conventional radiation sources exploited for materials characterization. Therefore, another goal is to preliminary investigate the compatibility between laser-driven particle sources and the PIXE and EDX techniques with theoretical and numerical tools. Specifically, 3D Particle-In-Cell (PIC) and Monte Carlo simulations are used to realistically describe the laser-driven particle acceleration and propagation through matter, respectively. Then, in light of the results obtained with the numerical studies, the first laser-driven EDX and quantitative PIXE analysis experiment is carried out in an international laser facility.

As far as PAA is concerned, the goal is to study near-critical targets, coupled with a converter material, for the generation of high-energy photons suitable for the considered activation technique. To this aim, a theoretical description of PAA performed either with LINACs and laser-driven electron sources is required. The model must be applied to design the optimal target, taking into account the laser operating parameters. Then, considering the target parameters retrieved from the model, realistic laser-driven PAA simulations must be carried out with the PIC and Monte Carlo tools.

This thesis was funded by the European Research Council (ERC) project ENSURE (*Exploring the New Science and engineering unveiled by Ultraintense ultrashort Radiation interaction with mattEr*, `https://www.ensure.polimi.it/`).

Structure of the thesis

The PhD thesis is organized as follows:

Part I: The first Part of the thesis is divided into three Chapters. **Chapter 1** provides an introduction to the main atomic and nuclear analytical methods, with particular emphasis on the PIXE, EDX and PAA techniques. **Chapter 2** gives an overview of the fundamental aspects of laser-driven particle acceleration, starting from the basic concepts of laser-plasma interaction. The Target Normal Sheath Acceleration (TNSA) mechanism is described, considering both micrometric solid foils and advanced DLTs. Lastly, the main applications of laser-driven radiation sources under investigation are reported. In **Chapter 3**, the motivations and goals of the thesis work are described in detail, along with the exploited numerical and experimental methods. In particular, a general description of the Monte Carlo tool, Particle-In-Cell method and Magnetron Sputtering deposition technique are provided.

Part II: The second Part of the work, divided into two Chapters, is devoted to the production and characterization of titanium (Ti) films and submicrometric targets via Magnetron Sputtering. In **Chapter 4**, an extensive production and characterization campaign of Ti films exploiting the Direct Current Magnetron Sputtering (DCMS) and High Power Impulse Magnetron Sputtering (HiPIMS) deposition regimes is shown. This activity is of crucial importance to understand the behaviour of the machine and to cover the lack of knowledge in literature about Ti deposition with DCMS and HiPIMS. Next, in light of the obtained results, a suitable strategy for Ti targets deposition on perforated holders is developed and presented in **Chapter 5**.

Part III: This Part is dedicated to the numerical and experimental investigation of PIXE, EDX and PAA performed with laser-driven radiation sources. Specifically, **Chapter 6** focuses on laser-driven PIXE exploiting a theoretical and numerical approach. Firstly, the theoretical model available for the PIXE description is extended to include the presence of a non-monoenergetic proton source. Next, a numerical code is developed to retrieve the sample elemental composition from a laser-driven PIXE measurement. Lastly, realistic laser-driven PIXE experiments are simulated using the PIC and Monte Carlo methods. In light of the results obtained from the simulations, the first quantitative laser-driven PIXE and EDX experiment is performed. The results of the campaign, conducted at the Centro de Láseres Pulsados (CLPU) in Salamanca, are shown and discussed in **Chapter 7**. Lastly, exploiting theoretical models, Monte Carlo and PIC simulations, the feasibility of laser-driven PAA is assessed in **Chapter 8**. The optimal target parameters for the laser-driven bremsstrahlung photon generation and subsequent sample activation are retrieved. Then, an extensive simulation campaign of conventional and laser-driven PAA experiments is carried out. The aim is to compare the performances of PAA achievable with conventional and laser-driven sources.

Part IV: The last part of this PhD thesis summarizes the conclusions of the work and the perspectives for future research.

Publications and research activity

The contents of this PhD thesis are published in the following peer-reviewed articles:

- Passoni, M., Fedeli, L. and **Mirani, F.** *Superintense laser-driven ion beam analysis.* Scientific reports 9.1 (2019): 1-11. Personal contribution: development of the theoretical model, writing the iterative code, development of the Monte Carlo simulations, contribution to the manuscript writing and figures production.

- Passoni, M., Arioli, F., Cialfi, L., Dellasega, D., Fedeli, L., Formenti, A., Giovannelli, A., Maffini, A., **Mirani, F.**, Pazzaglia, A., Tentori, A., Vavassori, D., Zavelani-Rossi, M. and Russo, V. *Advanced laser-driven ion sources and their applications in materials and nuclear science.* Plasma Physics and Controlled Fusion 62.1 (2019): 014022. Personal contribution: development of the activities and results presented in the 'Solid films production for advanced DLTs' and 'Laser-driven PIXE' sections, contribution to writing and production of the figures.
- **Mirani, F.**, Maffini, A., Casamichiela, F., Pazzaglia, A., Formenti, A., Dellasega, D., Russo, V., Vavassori, D., Bortot, D., Huault, M., Zeraouli, G., Ospina, V., Malko, S., Apiñaniz, J. I., Pérez-Hernández, J. A., De Luis, D., Gatti, G., Volpe, L., Pola, A. and Passoni, M. *Integrated quantitative PIXE analysis and EDX spectroscopy using a laser-driven particle source.* Science advances 7.3 eabc8660 (2021). Personal contribution: design of the experiment, participation in the experimental campaign, analysis of the data, preparation of the manuscript.
- Dellasega, D., **Mirani, F.**, Vavassori, D., Conti, C. and Passoni, M. *Role of energetic ions in the growth of fcc and ω crystalline phases in Ti films deposited by HiPIMS*. Applied Surface Science 556 (2021): 149678. Personal contribution: contribution to the Ti films deposition, characterization, analysis of the data, preparation of the manuscript and figures.
- **Mirani, F.**, Calzolari, D., Formenti, A. and Passoni, M. *Superintense laser-driven Photon Activation Analysis*. Accepted for publication at Communications Physics (2021), arXiv preprint arXiv:2104.07513. Personal contribution: development of the theoretical model for the comparison between conventional and laser-driven PAA, development of the Monte Carlo simulations, contribution to the PIC simulation and preparation of the manuscript and figures.

And in the following conference proceeding:

- Fedeli, L., **Mirani, F.**, Maffini, A., Formenti, A., Pazzaglia., A., Tentori, A., Dellasega, D., Russo, V. and Passoni, M. *Laser-plasma based hadron sources for materials science applications.* 45th EPS Conference on Plasma Physics, EPS 2018. Vol. 42. European Physical Society (EPS), 2018. Personal contribution: development of the theoretical model, writing the iterative code, development of the PIXE Monte Carlo simulations.

During my PhD, I attended these conferences and workshops with the following personal contributions:

- **Oral contribution** at the 'Laser plasma acceleration: project-driven modeling and codes development workshop', February 2018, Frascati, Italy.
- **Participation** to the 'Training workshop on Ion Beam Analysis Techniques', April 2018, Zagreb, Croatia.

- **Poster contribution** at the 'Nuclear Photonics 2018', June 2018, Brasov, Romania.
- **Poster contribution** at the 'SPIE Optics + Optoelectronics 2019', April 2019, Prague, Czech Republic.
- **Oral contribution** at the '4th Targetry for High Repetition Rate Laser-Driven Sources Workshop', June 2019, Milan, Italy.
- **Participation** to the 'VI CLPU Users Meeting', 1st - 2nd October 2020, on-line.

And to the following experimental campaigns:

- One-week experimental campaign at the Centro de Láseres Pulsados (CLPU), February 2018. Salamanca, Spain.
- Three-weeks experimental campaign at the Centro de Láseres Pulsados (CLPU), May 2019. Salamanca, Spain.

During my PhD, I have been co-supervision of two Master thesis students (Mr. Davide Vavassori and Mr. Daniele Calzolari) in Nuclear Engineering at Politecnico di Milano. In collaboration with other two ENSURE team members and one external collaborator, I submitted the project SCOPUM (*Sviluppo di un sistema Compatto per una sOrgente di Particelle da laser commerciale per nUove applicaziono industriali e Medicali*) to the Switch2Product innovation challenge organized by the Technology Transfer Office of PoliMi and PoliHub. The project aimed at designing a commercial laser-driven particle accelerator module. I performed a pitch presentation to a jury composed of experts from PoliMi and potential industrial investors. Lastly, I have been the P.I. of the IscraC 50000 CPU hours project 'IRONMAN' and 35000 CPU hours project 'THANOS' at CINECA supercomputer (Italy).

Part I

State of the art and thesis goals

CHAPTER 1

Atomic and nuclear analytical methods for materials characterization

The present Chapter provides an overview of the principal atomic and nuclear analytical methods for the elemental analysis of materials. Particular attention is devoted to the Energy Dispersive X-ray (EDX) spectroscopy, Particle Induced X-ray Emission (PIXE) and Photon Activation Analysis (PAA) techniques.

The Chapter is organized as follows. Section 1.1 reviews the most relevant existing elemental characterization techniques and their general classification. Then, EDX, PIXE and PAA are described in detail in Sections 1.2, 1.3 and 1.4, respectively. Lastly, the most relevant particle accelerator schemes exploited for elemental analysis purposes are presented in Section 1.5.

1.1 Atomic and nuclear analytical methods, an overview

Atomic and nuclear analytical methods for the elemental analysis of materials [1] are well-established techniques for the identification and quantification of the elements present in a large variety of samples. They rely on the irradiation of materials with exciting radiation and the detection of the emitted secondary particles. Since the energy of the secondary particles is characteristic of the emitting element or isotope, it is exploited to identify the sample constituents. Besides, the intensity of the emitted secondary radiation is used to retrieve quantitative information.

If the sample is homogeneous (i.e. the content of the element is constant as a function of the thickness), the analytical techniques usually provide the concentrations of the elements. On the other hand, if the sample is non-homogeneous (e.g. a multilayer structure), the goal is to retrieve the elemental concentration profiles as a function of the thickness or the local composition at a specific depth. In general, since the exploited primary radiation is not intense enough to cause any visible damage to the sample, these methods are considered non-destructive.

The analytical techniques can be classified accordingly to several aspects like the type of impinging and emitted particles (i.e. photons, electrons or ions) or the kind of interaction in place (i.e. atomic or nuclear). For this reason, the same elemental analysis method can belong to more than one of the categories shown below.

Analytical techniques of X-ray emission spectroscopy

The analytical techniques of X-ray emission spectroscopy exploit different primary radiations to ionize the sample. After ionization, an atomic transition occurs with the emission of a characteristic X-ray. These processes are represented in figure 1.1. The element is recognized accordingly to the wavelength (or the energy) of the X-ray (i.e. qualitative analysis), while its concentration is retrieved from the X-ray line intensity (i.e. quantitative analysis).

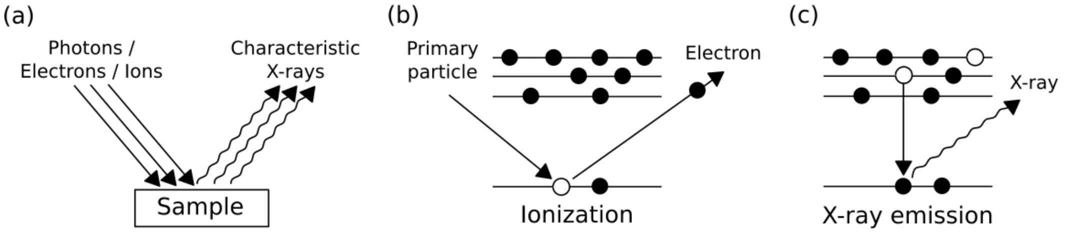

Figure 1.1: *Schematic representation of (**a**) X-ray emission spectroscopy, (**b**) creation of the vacancy in the inner shell and (**c**) atomic relaxation with X-ray emission.*

A well-known technique belonging to this family is X-ray Ray Fluorescence (XRF) [2] spectroscopy. It relies on a primary X-ray source, generally an X-ray tube, to induce the secondary emission of characteristic X-rays. XRF is a method for the multi-elemental analysis of homogeneous samples down to 10s μm depth in solids. Since it requires a relatively simple and inexpensive experimental apparatus, XRF is probably the most widespread analytical technique of X-ray emission spectroscopy. It also allows analyzing large samples in-air without the need to place them in a vacuum chamber.

Another widespread technique is Energy Dispersive X-ray (EDX) spectroscopy [3]. In this case, the primary particles are $1 - 20$ keV energy electrons. EDX is performed inside Scanning Electron Microscope (SEM) systems equipped with an electron gun. Therefore, no in-air sample irradiation can be carried out. Moreover, only the composition of small and solid samples is analyzed down to a few μm below the surface. Further details about EDX are provided in Section 1.2.

Lastly, the Particle Induced X-ray Emission (PIXE) [4] technique is worthy of consideration. PIXE exploits MeV energy ions (mainly protons), provided by an electrostatic accelerator, to ionize the sample atoms. Similar to XRF, the primary radiation can propagate in-air before reaching the sample. Therefore, PIXE can carry out the surface analysis of large objects down to several μm depth. Unlike XRF and EDX, PIXE is suitable for the analysis of non-homogeneous samples. As will be shown in Section 1.3, a specific variant of the technique called *differential PIXE* [5] enables retrieving the concentration profiles of the elements as a function of the thickness.

Lastly, XRF, EDX and PIXE are widely exploited in several fields of industrial, social and scientific interest like semiconductor industry [6–8], environment monitoring [9–11], cultural heritage preservation [12–14] and nuclear fusion research [15, 16].

Ion Beam Analysis techniques

The Ion Beam Analysis (IBA) techniques [1] share the use of monoenergetic MeV energy ions as primary radiation. An example is represented by PIXE, which is both an X-ray emission spectroscopy and an IBA technique. Besides PIXE, the Rutherford Backscattering Spectroscopy (RBS), Elastic Recoil Detection Analysis (ERDA), and Particle Induced Gamma-ray Emission (PIGE) techniques are part of the IBA category. RBS allows determining the depth distribution of impurities in surface layers ($\sim$10 μm) through the detection of particles elastically backscattered from the sample. The projectiles are few MeV protons, deuterons and α particles. The ratio between the energy before and after the collision is just a function of the projectile mass, the target mass and the scattering angle. The initial projectile energy and mass are known, while the scattering angle is fixed by the detector position. Therefore, by measuring the energy of the recoiled ion, the mass of the target atom is retrieved. The process is schematically shown in figure 1.2.a. Since the probability of backscattering increases with the atomic number of the target atom, RBS is particularly suitable for heavy elements identification in light matrices.
On the other hand, ERDA is based on the detection of the recoiled target nuclei elastically scattered in the forward direction (see the scheme in figure 1.2.b). To this aim, heavy particles (i.e. form $\mathrm{Z} = 6$ to 79) with energies $\sim$ $1\ \mathrm{MeV/u}$ are used. Similarly to RBS, the mass of the recoiled ion can be determined from the measure of its energy. Starting from hydrogen, ERDA is used to detect elements lighter than the projectiles with an accessible depth of the order of 1 μm.

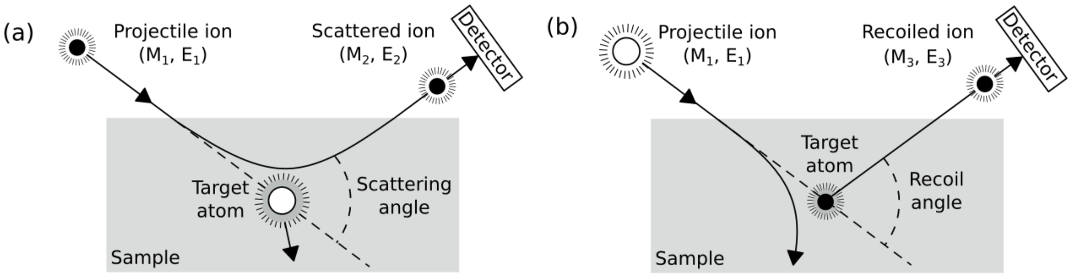

Figure 1.2: *Schematic representation of (**a**) Rutherford Backscattering Spectroscopy and (**b**) Elastic Recoil Detection Analysis.*

The fourth analytical technique considered part of the IBA family is PIGE. PIGE relies on the emission of γ-rays following excitation due to the interaction between the sample nuclei and MeV energy protons. The considered reactions are the (p, γ), $(p, p\gamma)$ and $(p, \alpha\gamma)$ ones. These reactions are not allowed for all the elements. For instance, elements with $Z > 15$ cannot be detected with primary protons of energy $\sim$ 3 MeV. Thus, PIGE is considered suitable for the identification of light elements. Like X-ray emission spectroscopy, the IBA techniques find uses for an impressive number of applications of industrial [17] and societal [18] relevance.

Activation and Nuclear Reaction Analysis techniques

When the detected radiation is emitted following a nuclear reaction, the technique is classified as Nuclear Reaction Analysis (NRA) [1]. In this case, the detected particles are γ-rays, protons, α-particles and neutrons. Since PIGE exploits a restricted class of nuclear reactions, it is considered an NRA as well. Unlike the other elemental characterization techniques, these methods allow distinguishing between different isotopes. They are comparative techniques because the concentration of the elements is obtained by comparing the activity induced in the sample and reference material. Among the NRA techniques, Neutron Activation Analysis (NAA) [19] and Photon Activation Analysis (PAA) [20] are the most relevant.

NAA exploits the irradiation of the sample with neutrons (generally at thermal energy) and the consequent conversion of the stable atoms in γ-emitting radioisotopes. As in the case of PIGE, the γ-rays are characteristic of the emitter. Therefore, from the knowledge of the γ-ray energy and the reaction in place, the parent element is identified. The most common neutron sources for NAA studies are nuclear reactors, Cf-252 radioactive sources and fusion-type neutron generators based on (D, D) and (D, T) reactions. Since the light elements (e.g. H, C, O, N) do not produce radioisotopes under thermal neutron irradiation, NAA is suitable for trace heavy elements detection in light matrices.

In PAA, samples are irradiated with high-energy (i.e. $10 - 30$ MeV) photons. The primary photons are obtained through the interaction of high-energy electrons, provided by high-power linear accelerators, microtrons or betatrons, with high Z materials and bremsstrahlung emission. Interactions between photons and sample nuclei occur as photonuclear reactions with the delayed emission of characteristic γ-rays. Further details about PAA will be provided in Section 1.4.

Unlike X-ray emission spectroscopy and IBA techniques, NAA and PAA allow detecting elements down to several centimetres inside samples thanks to the high penetration depth of neutrons and γ-rays in the matter. This peculiar feature makes NAA and PAA suitable for the elemental analysis of both small and large volumes of materials [21,22].

1.2 Energy Dispersive X-ray (EDX) spectroscopy and Scanning Electron Microscope (SEM)

EDX [3] is an analytical technique used in combination with SEM. It is exploited to identify near-surface elements in solid samples and to determine their amount at different points on their surface.

As already mentioned, the material under analysis is irradiated with an electron beam, its energy can range from a few up to $\sim 10-20$ keV. Electrons are emitted by a tungsten filament lamp via the thermionic effect. They are accelerated by a potential difference, deflected and collimated on the sample surface. The whole system is placed in-vacuum at $\sim 10^{-5}$ mbar to maximize the mean free path of the electrons.

As shown in figure 1.3.a, the primary electrons interact with the sample promoting the emission of secondary electrons, characteristic x-rays and back-scattered electrons (BSE). By collecting the secondary electrons scattered from the sample atoms, a high-resolution image of the surface is produced with a resolution of $1 - 5$ nm. This SEM

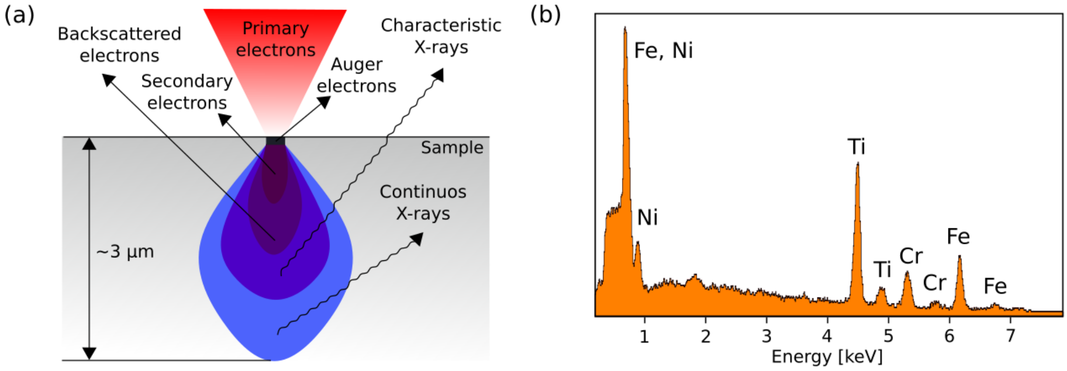

Figure 1.3: *(**a**) Conceptual scheme of EDX spectroscopy and (**b**) an example of EDX spectrum obtained from a stainless steel sample coated with a 1.0 µm thick Ti layer. The accelerating voltage was set equal to 8 kV.*

technique is called Secondary Electron Imaging. Heavy elements backscatter electrons with a larger probability than light elements. Therefore, when BSE are exploited, the contrast in the resulting image provides also an indication of the local chemical composition.

On the other hand, EDX analysis is performed by collecting the characteristic X-rays. An example of a spectrum is shown in figure 1.3.b. The elements are recognized from the energies of the X-ray peaks, while their concentrations are obtained by comparing the peak relative intensities with the data obtained from standard materials. Moreover, moving the electron beam over the sample surface, an image of the distribution of the elements is retrieved. However, the elemental map generation can take several hours since an X-ray spectrum must be produced and processed at each point of the scanned area. The elemental map can also be associated with image data generated by the electron microscope. The detection limit of EDX analysis is in the $0.1-0.5$ wt$\%$ range, and the actual value depends on the sample composition.

Despite its high versatility, EDX is subject to some limitations. Firstly, only solid and conductive samples can be analyzed. Moreover, since the analysis must be performed in vacuum conditions, the dimensions of the chamber often limit the size of the samples. Besides, like the other analytical methods presented in Section 1.1, EDX analysis allows recognizing only the elements and no further information about the chemical composition is provided (e.g. chemical compounds or molecules). Lastly, elements with atomic numbers smaller than 11 (Na) are hardly detected. That is due to the limited detection efficiency at low X-ray energies of the exploited Si-Li detectors protected by Be windows.

The X-ray detector

Usually, the detectors used for EDX analysis are Si(Li) or solid-state devices. They are energy-dispersive detectors because the X-rays are sorted accordingly to their energies. Indeed, when a photon interacts with the active volume, a number of electron-hole pairs are created. Their number is proportional to the incident photon energy. The corresponding charge is integrated into a current pulse, converted into a voltage pulse, amplified and send to a multichannel analyzer.

The parameters that characterize the performances of these devices are the energy resolution and counting efficiency. They are both functions of the incident photon energy. For instance, the energy resolution of Si(Li) detectors is expressed in terms of full width at the half maximum (FWHM) of the peaks. Usually, the resolution is equal to 110 eV at 5 keV X-ray energy.
The intrinsic detection efficiency is maximum (up to $\sim 100\%$) between a few keV and 20 keV energies [23]. At low energies, it is affected by the presence of the protective Be window in front of the active volume. It rapidly drops to zero around 1.0 keV. At energies higher than $20 - 30$ keV, the X-rays are rarely absorbed inside the active volume. That causes a progressive decrease of efficiency.

1.3 Particle Induced X-ray Emission (PIXE) analysis

PIXE [1] exploits MeV energy ions, usually protons, to ionize the sample atoms. After ionization, a de-excitation process takes place following two possible channels: the emission of an Auger electron or the emission of an X-ray. As with EDX, PIXE spectroscopy relies on the detection of X-rays leaving the sample and interacting with a detector. The analysis of the recorded X-ray spectra (a typical example is shown in figure 1.4) allows reconstructing the sample composition. As already mentioned in Section 1.1, PIXE allows analyzing both homogeneous and non-homogeneous samples. Moreover, the quantitative analysis does not require the use of comparative materials.

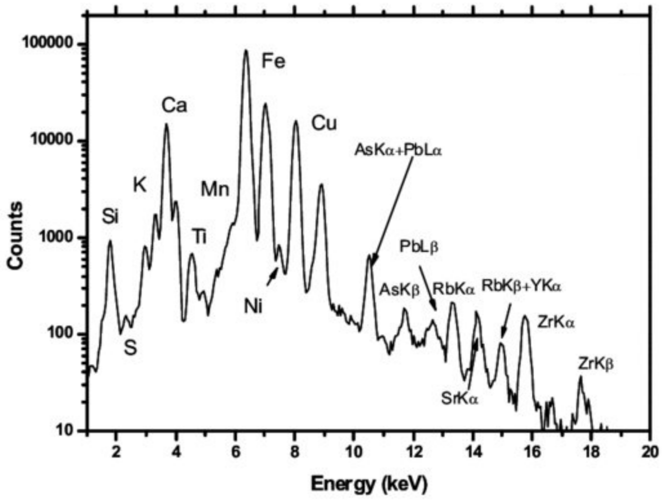

Figure 1.4: *Example of a typical PIXE spectrum from [24]. The elements and the atomic transitions are reported in correspondence with the peaks.*

1.3.1 Experimental apparatus

The basic experimental apparatus required for PIXE analysis includes a proton source and an interaction chamber where the sample is placed. Protons are provided by an electrostatic accelerator (i.e. Van de Graaff or TANDEM machines). A detailed description of the principal accelerator configurations can be found in Section 1.5. The ion beam is transported to the chamber by a beam handling system. The system includes several magnetic components like switching magnets and beam steerers.

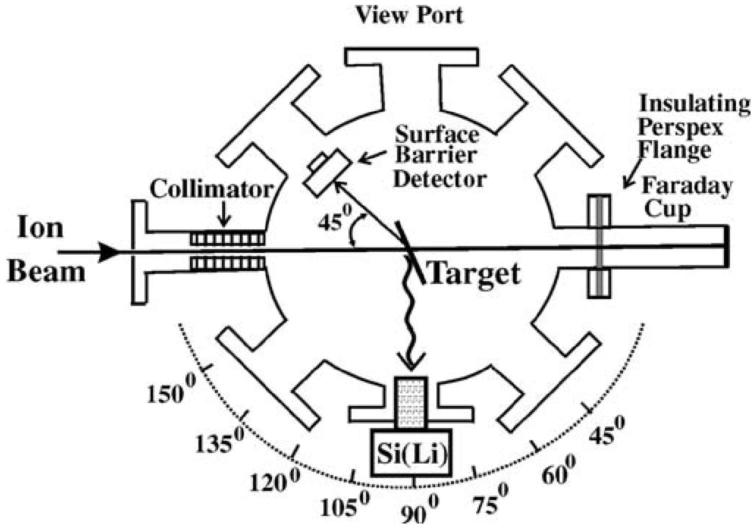

Figure 1.5: *Scheme of the vacuum chamber for PIXE analysis. From [1].*

The beam current on the sample is of the order of $1-100$ nA. Lower currents con be required under specific circumstances to avoid sample damage due to excessive heating. The scattering chamber where the ion beam strikes the sample is evacuated at a pressure lower than 10^{-6} mbar. As shown in figure 1.5, it is equipped with several ports and connected to the beamline with a gate valve. The valve allows maintaining the vacuum in the beamline and the scattering chamber separated. The sample is usually placed at $45°$ to the beam incidence direction. The sample holder can be translated to adjust the interaction point on the surface.

Surface barrier detectors are placed inside the chamber both in front and behind the sample to monitor the scattered charged particles. The X-ray detectors are Si(Li) or solid-state devices (see Section 1.2). The Si(Li) device is located at $90°$ to the beam incidence direction. To correctly positioning the detectors, angular positions are provided at the base of the chamber.

To avoid breaking the vacuum after each irradiation, the movable target holder can host many samples. They are self-supporting or sputtered on thin foils containing no detectable elements of interest. The widest variety of samples are analyzed in their original state. The irradiated volume must be representative of the whole sample composition. Therefore, if the material is not homogeneous, even for thicknesses larger than the adopted proton range, it must be crumbled to a fine powder and pressed into a pellet.

Gaseous samples, paintings and bulky archaeological finds cannot be placed into the vacuum chamber. Therefore, an external beam system is exploited to analyze volatile materials and large objects. The proton beam is brought into the atmosphere, and it interacts with the sample. A micrometric foil separates the vacuum inside the particle accelerator and the air. This configuration allows an effective heat dissipation from the surface of valuable samples (e.g. paintings and ancient objects), thus performing a safer analysis. On the other hand, the air causes the beam to be no longer exactly monoenergetic when it strikes the sample surface because of the energy straggling. Another drawback is the appearance in the spectrum of X-ray signals not related to the sample elements (e.g. the Ar peak at 2.96 keV).

1.3.2 Theoretical description and sample composition reconstruction

Several commercial codes [25, 26] are available to perform quantitative PIXE analysis without the need for standard materials. They are exploited in all IBA laboratories where PIXE is carried out. The codes rely on an analytical description of the involved physical phenomena. These tools allow correlating the X-ray line intensities with the material composition. This Section describes the underlying analytical PIXE model, considering the main physical processes and two possible types of sample structures: the homogeneous and the non-homogeneous composition.

Physical phenomena

Several physical phenomena must be considered to provide a theoretical description of PIXE. They are the proton slowdown inside the sample, ionization, X-ray emission and the photon attenuation before leaving the surface.

The first process to be taken into account is the proton slowdown. It is well-described by the stopping power $S(E)$, defined as the energy lost by a particle travelling inside matter per unit path length. This energy-dependent function can be evaluated analytically using the Bethe-Bloch formula or via numerical tools (e.g. the Stopping and Range of Ions in Matter (SRIM) code [27]). The stopping power in the sample is retrieved from those of the single elements $S_i(E)$ as:

$$S(E) = \sum_{i=1}^{I} W_i \times S_i(E) \tag{1.1}$$

where I is the total number of elements, and W_i are the elemental mass concentrations. The probabilities of ionization and subsequent X-ray emission are provided in terms of ionization cross section and fluorescence yield, respectively.

The ionization cross section $\sigma(E)$ is a function of the energy, the atomic number (Z) and the involved atomic shell. Its magnitude decreases with Z both in the case of K and L atomic shells. The proton ionization cross section is well-described by the Energy-Loss Coulomb-Repulsion Perturbed-Stationary-State Relativistic (ECPSSR) theory [28, 29]. Its behaviour is shown in figures 1.6.a and 1.6.b. Remarkably, the cross section can

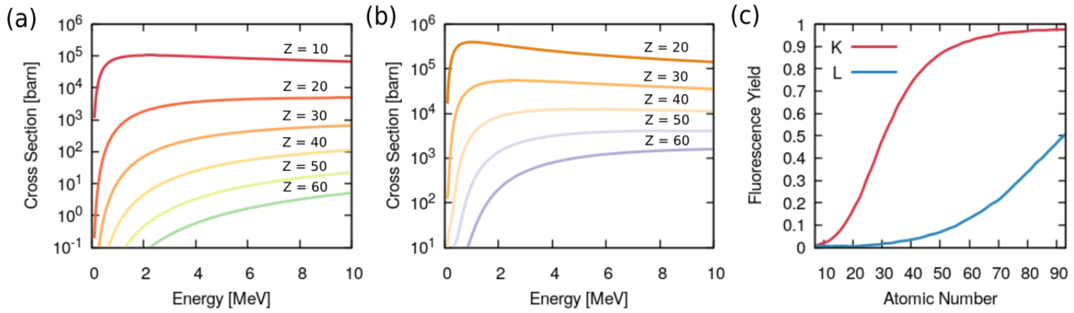

Figure 1.6: *Examples of (**a**) K-shell and (**b**) L1-shell ionization cross sections for different values of atomic number Z. (**c**) Behaviour of the fluorescence yields for the K and L shells.*

reach values up to 10^4 barns, leading to a significant amount of emitted characteristic X-rays. Indeed, compared to the cross sections of nuclear reactions exploited for NRA, ionization cross sections are several orders of magnitude higher. That leads to a detected signal more intense for PIXE analysis than for other IBA techniques.

The second parameter having a significant effect on the intensity of the recorded X-ray signal is the fluorescence yield ω [30]. Since also Auger electrons can be emitted after ionization, the fluorescence yield accounts for the probability of de-excitation following the X-ray emission channel. The K shell is a single shell and has no sub-shell. Therefore, the K shell fluorescence yield of an atom is:

$$\omega_K = \frac{Y_K}{N_K} \tag{1.2}$$

where Y_K is the total number of K X-rays emitted from a sample, and N_K is the total number of K shell vacancies. As shown in figure 1.6.c, the fluorescence yield increases with Z.

The X-ray attenuation is described by the mass attenuation coefficient (μ/ρ), which depends on the photon energy, material composition and density. The $(\mu/\rho)_i$ values of the elements can be retrieved from the online interface of the XCOM code [31]. The mass attenuation coefficient in a compound, evaluated for specific X-ray energy, is obtained from:

$$(\mu/\rho) = \sum_{i=1}^{I} W_i \times (\frac{\mu}{\rho})_i \tag{1.3}$$

For completeness, the secondary X-ray emission [32] has to be mentioned. It occurs when elements with a very close value of Z are present in the sample. Indeed, the characteristic X-rays emitted by the higher Z element induce fluorescence in the lower Z element. The secondary emission has a significant effect on the total X-ray yield only when the concentration of the exciter element is much higher than that of the secondary emitter one. Since this is a considerably rare condition, its contribution will be neglected in the description.

Lastly, the X-ray peaks in the PIXE spectra are always superimposed to a continuous background. It is caused by phenomena like the Compton scattering of γ-rays in the detector volume. These high-energy photons are produced by nuclear states excited in the sample during the irradiation. Another source of background is the bremsstrahlung associated with the projectiles and secondary electrons. Furthermore, an incomplete charge collection in the detector sensitive volume can occur because of the early recombination of the electrons and holes.

Homogeneous samples

Consider a thick homogeneous sample composed of I elements of atomic weights M_i and mass concentrations W_i, irradiated with a monoenergetic proton beam of energy E_p and a total number of protons N_p. Figure 1.7.a shows the geometry of the sample irradiation. The number of X-rays Y_i, associated to one characteristic line for the *i*-th element, is [1]:

$$Y_i = N_p \frac{\Delta\Omega}{4\pi} \varepsilon_i \frac{N_{av}}{M_i} W_i \int_{E_p}^{E_f} \sigma_i(E) \omega_i e^{-\mu_i \int_{E_p}^{E'} \frac{dE'}{S(E')} \frac{\cos\theta}{\cos\phi}} \frac{dE}{S(E)} \tag{1.4}$$

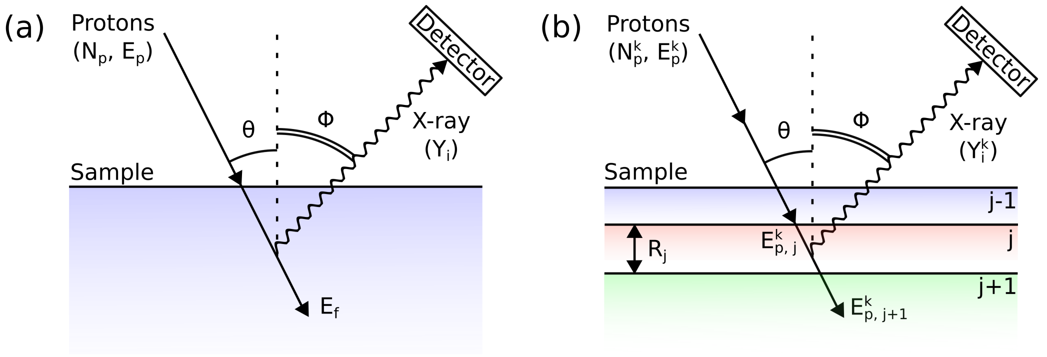

Figure 1.7: *Conceptual schemes for the (**a**) homogeneous and (**b**) non-homogeneous sample irradiation geometry.*

where $\Delta\Omega$ and ε_i are the subtended solid angle and the efficiency of the detector, N_{av} is the Avogadro's number, E_f is the final proton energy after the slowdown in the matter ($E_f = 0$ if the sample is thick enough to stop the protons), μ_i are the X-ray attenuation coefficients, θ is the proton impact angle, and ϕ is the X-ray emission angle. The integral takes into account the production of X-rays along the proton range and their attenuation inside the material. It is computed over the projectile energy.
Here, the goal of the quantitative PIXE analysis is to retrieve the mass concentrations W_i of the elements from the measured X-ray yields Y_i^* in the PIXE spectrum after the background subtraction. It can be performed by solving a system of I equations like equation 1.4. The system is non-linear because both the X-ray attenuation coefficients μ_i and the proton stopping power $S(E)$ depend on the sample composition. Accordingly, the solution can be found by minimizing a parameter like:

$$\chi^2 = \sum_i \left[\frac{(Y_i - Y_i^*)}{\sqrt{Y_i^*}} \right]^2 \tag{1.5}$$

making use of an iterative procedure.

Non-homogeneous and multilayer samples

If the sample is non-homogeneous, the elemental concentrations are not constant as a function of the sample thickness. Considering a complete lack of knowledge of the sample composition (i.e. no information about its structure are available), the *differential PIXE* analysis can be applied to retrieve the concentration profiles of the elements along the thickness. As shown in figure 1.7.b, the sample is ideally split in a finite number J of fictitious layers having mass thickness $\rho_j R_j$ and homogeneous composition $W_{i,j}$. Assuming to perform K measurements at different proton energies E_p^k, the following system of equations can be written [5, 33]:

$$\begin{aligned} Y_i^k = N_p^k \frac{\Delta\Omega}{4\pi} \varepsilon_i \frac{N_{av}}{M_i} \sum_{j=1}^{J-1} W_{i,j} e^{-\sum_{l=1}^{j-1} (\frac{\mu}{\rho})_{i,l} \frac{\rho_l R_l - \rho_l R_{l-1}}{\cos\phi}} \times \\ \times \int_{E^k_{p,j+1}}^{E^k_{p,j}} \sigma_i(E) \omega_i e^{-\mu_{i,j} \int_{E_p}^{E'} \frac{dE'}{S_j(E')} \frac{\cos\theta}{\cos\phi}} \frac{dE}{S_j(E)} \end{aligned} \tag{1.6}$$

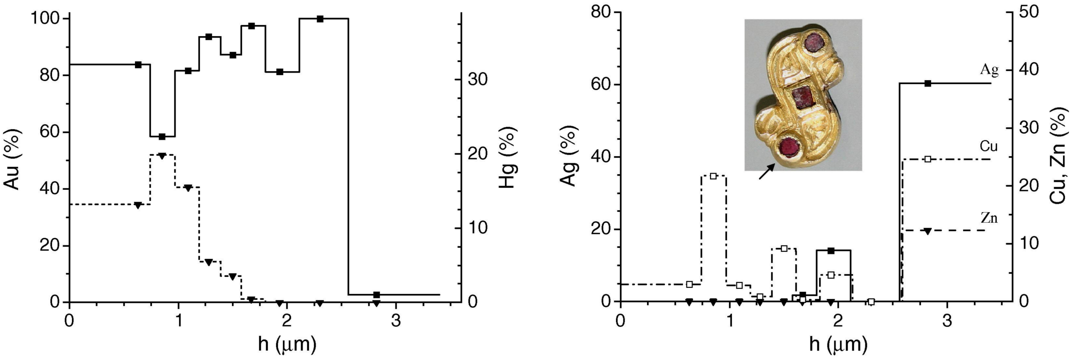

Figure 1.8: *Example of differential PIXE analysis result from [5]. The concentration profiles of the elements in an Early Medieval brooch are shown. The object under investigation is reported as an inset image in the right panel.*

where N_p^k is the number of protons with energy E_p^k, $(\frac{\mu}{\rho})_{i,j}$ and $S_j(E)$ are the X-ray attenuation coefficients and proton stopping powers associated to the j-th layer, $E_{p,j}^k$, and $E_{p,j+1}^k$ are the proton energies at the boundaries of the j-th layer. The system of $I \times K$ equations 1.6 can be solved if $K \geq J$ (i.e. if a number of measurements greater than or equal to the number of fictitious layers are performed) by a χ^2 minimization procedure. The solution is the set of discrete values of $W_{i,j}$ and mass thicknesses $\rho_j R_j$ that best fit the experimental X-ray yields Y_i^{k*}. An example of differential PIXE analysis result is shown in figure 1.8.

A very common example of a non-homogeneous sample is the multilayer one. Indeed, the sample is composed of a finite number of layers, each one having homogeneous composition. For instance, this is the case of paintings [12, 34]. In this condition, some sample properties are known a priori as the number of layers, their thicknesses or composition. The relation describing the X-ray emission is equation 1.6. However, the unknowns are specific properties of the structure like the mass thicknesses of actual layers $\rho_j R_j$ or their elemental composition $W_{i,j}$. They are retrieved by applying the χ^2 minimization procedure.

1.3.3 PIXE advantages and limitations

Because of its exceptional detection capability (sensitivities down to 0.1 ppm have been obtained) and non-destructive nature, PIXE is a powerful technique for the ultra-trace analysis of solid materials. It has been successfully applied in biological science [35], criminology [1], mineralogy [36], and for the study of archaeological [37] samples. Moreover, PIXE is extensively used for the quantification of polluting elements [38] in aerosol samples. It can discriminate between more than 20 different elements with a single measurement.

On the other hand, PIXE does not allow detecting elements with Z ≤ 13 because of the low counting efficiency of the Si(Li) detectors. In addition, PIXE can not distinguish between different chemical compounds. Other significant limits of PIXE are associated with the drawbacks of the particle accelerators. Indeed, the high costs and dimensions of these machines prevent its wide diffusion. Moreover, the oldest acceleration technology (see Section 1.5) is often exploited with detrimental limitations in terms of the flexibility of the particle beams. For instance, with electrostatic accelerators, the primary particle energy is not easily tunable. These machines are also subject to radiation protection issues [39] because of the progressive activation of the components.

1.4 Photon Activation Analysis (PAA)

PAA [20] is a non-destructive materials characterization technique that exploits high-energy photons to retrieve the elemental composition of a large variety of samples. The irradiation geometry is schematically shown in figure 1.9. Photons are generated through the interaction of a high-energy electron beam with a converter material (e.g. tungsten) via bremsstrahlung emission. They have an exponential energy spectrum (see the inset in figure 1.9), with maximum energy equal to the energy of the incident monoenergetic electron beam.

The primary photons interact with the sample under study and a comparative material inducing nuclear reactions. When the excited nuclei decay, the emission of characteristic γ-rays takes place. Photons emitted from both the sample and calibration material are measured with a spectrometer and exploited to retrieve the sample composition.

1.4.1 Experimental apparatus

As already mentioned, in addition to the sample and standard material, the experimental apparatus required to perform PAA includes an electron accelerator, an mm-thick converter, and a γ-ray detector. Here, these components are briefly described.

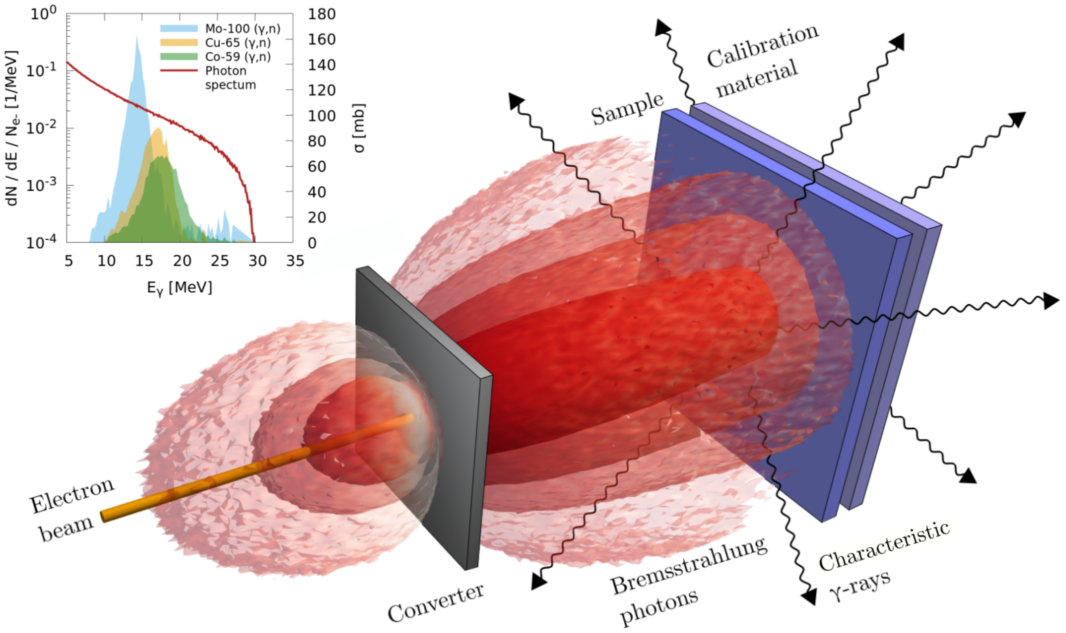

10^0
10^-1
10^-2
10^-3
10^-4
dN / dE / N_e- [1/MeV]
5
10
15
20
25
30
35
E_γ [MeV]
180
160
140
120
100
80
60
40
20
0
σ [mb]
Mo-100 (γ,n)
Cu-65 (γ,n)
Co-59 (γ,n)
Photon spectum
Sample
Calibration material
Electron beam
Converter
Bremsstrahlung photons
Characteristic γ-rays

Figure 1.9: *Typical PAA irradiation geometry. The inset plot shows the bremsstrahlung photon energy spectrum (red line) obtained from the irradiation of a 3 mm tungsten converter with 30 MeV energy electrons and three photonuclear reaction cross sections (from the EXFOR database [40]).*

The photon source

The monoenergetic electron beams used to perform PAA are characterized by energies and currents equal to $10-30$ MeV and ~ 10 μA, respectively. They are delivered by Van de Graaff generators, LINACs, betatrons, and microtrons (see Section 1.5 for details). However, LINACs are the electron sources exploited in the majority of PAA applications [20].

The high-energy electrons interact with a converter. The choice of converter material and thickness is intended to maximize the bremsstrahlung emission of radiation. Since the bremsstrahlung cross section scale with the square of the atomic number [41], high-Z materials like tungsten are usually exploited. The thickness is selected according to the same criterion and, for $\sim$ 30 MeV electron energy, it is of the order of some mm. The resulting photon beam is inhomogeneous both laterally and along the beam axis. For instance, the photon flux density obtained with a 30 MeV electron beam spans several orders of magnitude on a 10×10 cm plane located at a 10 cm distance from the converter. A greater uniformity can be achieved by increasing the distance from the converter but at the expense of flux density.

The sample is located at the centre of the bremsstrahlung cone. If the converter is not thick enough to stop all the electrons, particles can cause the overheating of the sample. In this case, an aluminum filter must be placed between the converter and sample to stop the surviving electrons.

γ-ray detectors

Two possible detector configurations are exploited in PAA, namely the scintillators and semiconductor crystals [23]. In both cases, the γ-rays are converted into electric pulses. The pulse intensities are quasi-proportional to the energy of the photons in the MeV energy range.

In scintillation detectors (NaI and BGO), γ-rays are converted into light flashes (i.e. radioluminescence) via secondary emission of electrons due to photoelectric effect, Compton scattering, and pair production. Then, the light is converted into an electric charge exploiting a photomultiplier tube. NaI detectors are characterized by very high detection efficiency. They are inexpensive and easy to use. However, the poor energy resolution ($5-10\%$ at 660 keV) makes them unsuitable for spectroscopy of complex matrices with many radioactive isotopes.

In semiconductor detectors (HPGe and Ge(Li)), the radiation interacts with an isolated single crystal producing a large amount of electron-hole pairs in cascade. Two ends of the active volume are used as electrodes and the charge is collected through an applied voltage. In the case of total absorption within the crystal, the amount of charge is proportional to the γ-ray energy. These devices are characterized by exceptional energy resolution ($0.1-1\%$ at 660 keV) compared to scintillators, but with lower detection efficiency. Another disadvantage is the requirement to cool them down to approximately -200 $^{\circ}$C during operation.

1.4.2 Photonuclear reactions and radioactive decay

The photonuclear reactions play a crucial role in PAA. They are characterized by the so-called *giant resonant* cross section because the probability of these events is higher than

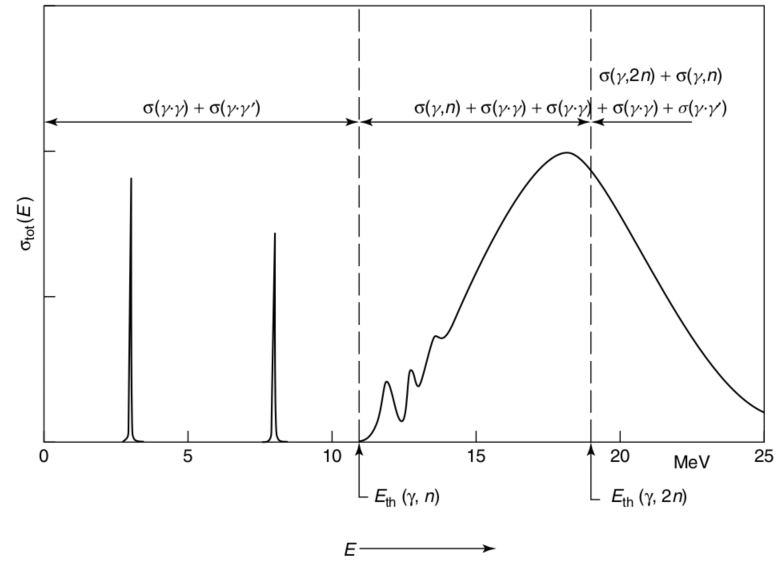

Figure 1.10: *Representation of the total photon absorption cross section. Energy regions associated with the different* (γ, γ') *and* (γ, xn) *reactions are highlighted. From [20].*

that of other nuclear interactions. Indeed, for photon energies ranging approximately from 10 to 25 MeV, the wavelength of the photons is comparable to the nucleus diameter. As a result, the electric dipole resonance mechanism takes place with a high degree of probability. The total photonuclear cross section, which is schematically shown in figure 1.10, is the result of several contributions like (γ, γ'), (γ, p), (γ, n) and $(\gamma, 2n)$ reactions. Experimentally evaluated nuclear reaction cross sections for many isotopes are available in the EXFOR: Experimental Nuclear Reaction Data database [40].
After the absorption of the primary photon and the emission of the secondary particle, the nucleus is left in an excited state with a very short lifetime. The energy in excess is released as prompt characteristic γ-ray emission. Then, if the ground state of the product nucleus is unstable, a radionuclide is produced that will decay with further production of a characteristic γ-ray. If the isomeric state of the reaction product has a lifetime sufficiently long, the delayed emission of characteristic radiation is detected for PAA purposes. Some examples of nuclear reactions exploited in PAA are listed in

Table 1.1: *Examples of nuclear reactions exploited in PAA.*

Element	Reaction	Half-life	γ-ray Energy [keV]
Ni	$^{58}\mathrm{Ni}(\gamma, \mathrm{n})^{57}\mathrm{Ni}$	36 hr	1379
Zr	$^{90}\mathrm{Zr}(\gamma, \mathrm{n})^{89}\mathrm{Zr}$	78.4 hr	909
Na	$^{23}\mathrm{Na}(\gamma, \mathrm{n})^{22}\mathrm{Na}$	2.6 yr	1275
As	$^{75}\mathrm{As}(\gamma, \mathrm{n})^{74}\mathrm{As}$	17.77 d	596
I	$^{127}\mathrm{I}(\gamma, \mathrm{n})^{126}\mathrm{I}$	12.8 d	388
Pb	$^{204}\mathrm{Pb}(\gamma, \mathrm{n})^{203}\mathrm{Pb}$	52.1 hr	279
Cd	$^{116}\mathrm{Cd}(\gamma, \mathrm{n})^{115}\mathrm{Cd}$	53.38 hr	336

table 1.1.

1.4.3 Sample irradiation and composition reconstruction

Samples are irradiated from minutes up to several hours (irradiation period t_i), depending on the expected half-lives of the products. Immediately after the irradiation, a large number of short-living radionuclides are present in the sample. If the characteristic γ-ray detection starts promptly after the irradiation, they will lead to a complex spectrum with many peaks and superposition of different signals. Therefore, a cooling period t_d, from several hours up to days, is waited before starting the measurement of the characteristic γ-rays. The counting period t_c can last from 10 minutes up to hours. Sometimes, two or three measures are performed separated by increasing cooling periods to exclude spectrum interference between nuclides. An example of the resulting spectrum is shown in figure 1.11. The elements are identified accordingly to the energies of the emitted γ-ray lines and the corresponding nuclear reaction. On the other hand, the number of counts Y_γ associated with each peak is related with the sample composition by the following equation:

$$Y_\gamma = I\frac{\Delta\Omega}{4\pi}\varepsilon\rho W\frac{N_{av}h}{Ar}\int_{E_{min}}^{E_{max}} f(E)\sigma(E)dE \cdot (1-e^{-\lambda t_i}) \cdot e^{-\lambda t_d} \cdot \frac{(1-e^{-\lambda t_c})}{\lambda} \tag{1.7}$$

where I is the primary photon fluence, $\Delta\Omega$ and ε are the solid angle and efficiency of the detector, ρ is the sample density, W is the mass concentration of the element, N_{av} is the Avogadro's number, h is the isotopic fraction, Ar is the relative atomic mass, E_{max} and E_{min} are the maximum and minimum primary photon energies of the continuum spectrum, f is the function describing the photon spectrum, σ is the photonuclear cross section and λ is the decay constant of the metastable nuclide.

In principle, equation 1.7 can be used to obtain the mass concentration of the elements, as in the case of PIXE quantitative analysis. However, several quantities are subject to a non-negligible degree of uncertainty (e.g. the cross section and the photon flux distribution). Therefore, the quantification is performed exploiting calibration materials

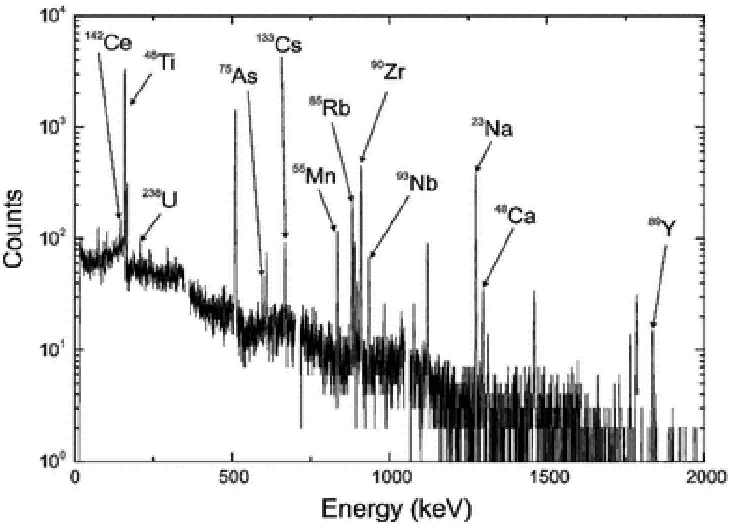

Figure 1.11: *Example of PAA spectrum. From [22].*

of known composition and co-irradiate with the samples. In this case, the formula for the evaluation of the concentrations is:

$$W^{sm} = \frac{W^{std} Y_{\gamma}^{sm} Ar^{sm}}{Y_{\gamma}^{std} Ar^{std}} \cdot \frac{e^{-\lambda(t_d^{std} - t_d^{sm})} \cdot e^{-\lambda(t_d^{std} - t_d^{sm} + t_c^{std})}}{1 - e^{-\lambda t_c^{sm}}} \tag{1.8}$$

where the apex sm and std stand for sample and standard, respectively.

It is worth mentioning that equation 1.8 is correct only if the flux is the same in each point of the sample and standard material. If this condition is not satisfied, a correction can be introduced by adding an internal or external flux monitor. External monitors are metal foils of known composition located upstream and downstream of the sample. On the other hand, the internal monitor is an element added to both the sample and standard with the same concentration. From the characteristic γ-rays emitted from the monitor, photon fluxes associated with the sample and standard are evaluated, and the effect of the discrepancies on the retrieved concentrations is taken into account.

1.4.4 PAA advantages and limitations

PAA is exploited for the analysis, both in-air and vacuum conditions, of environmental [42], geological [43], biological [44], industrial [45], and archaeological [46] samples. Unlike the IBA and X-ray spectroscopy techniques, it is suitable for the in-depth analysis of solid samples down to centimeters in depth. It is non-destructive since the samples generally do not require chemical pretreatment. The detection limit strongly depends on the elements, and it ranges from 100 to a few ppm. PAA is also a multi-elemental technique because up to $10 - 20$ elements can be identified with a single measurement.

As in PIXE, the main limitation of PAA relies on the high cost (about several million dollars) of the particle accelerators. Indeed, PAA is performed in dedicated laboratories hosting the LINAC machines. Another drawback of this technique is the relatively long time required to complete the measurement. For instance, the cooling period between the irradiation and the detection of the characteristic γ-rays can last several days.

1.5 Particle accelerators for the elemental analysis techniques

The design of the first proton accelerator dates back to 1929, and it is attributed to Robert J. Van de Graaff [47]. The prototype was able to accelerate protons up to 5 MeV energy. Subsequently, the TANDEM configuration was developed to double the delivered proton energies [48]. In the 1930s, Lawrence proposed the scheme of a circular machine (i.e. cyclotron) for the acceleration of ions [49] up to 16 MeV energy. On the other hand, the first linear particle accelerator, also called LINAC, for electron acceleration was constructed in 1927 [50]. Then, a renewed boost in particle acceleration technology was provided by the invention of the synchrotron in the 1940s.

During the second half of the 20th century, continuous growth in terms of delivered particle energy was achieved. Nowadays, particle accelerators are employed worldwide for several applications of high scientific and societal relevance [51] like nuclear physics research, nuclear medicine, sterilization, and materials processing. In the present Section, the principal accelerator concepts exploited for the elemental analysis of materials are briefly presented.

Single-ended Van de Graaff and Tandem accelerators

The simplest configuration for ion acceleration exploits an electrostatic potential formed between two terminals. One terminal is grounded and the other is positively charged. Positive ions are injected in correspondence with the charged terminal, and they accelerate toward the grounded terminal. The potential difference, which usually reaches values up to several millions of Volts, determines the energy gain of the particles. This configuration is adopted in Van de Graaff accelerators, and it is reported in figure 1.12.a. An insulating belt moves over two pulleys, one placed in the ground terminal and the other at the high-voltage terminal. At the ground terminal, a high voltage (e.g. several kV) causes a corona breakdown from a row of spray points. The moving belt collects the positive charges on its surface and takes them to the high voltage terminal. Then, the positive ions are removed from the belt by a second corona breakdown. In this way, an accelerating voltage equal to 10 MV can be reached between the two terminals. The particle source (e.g. a gaseous discharge produced by electron impact in a region of relatively high gas pressure) is placed in correspondence with the high-voltage terminal.
A two-steps acceleration is performed in TANDEM machines [52] to double the energy of the accelerated particles. Positive ions are produced by the source, and they are accelerated at few tens of keV through a gas. About 1% of them become negative ions by the pickup of two electrons. Negative ions are injected before the positively charged terminal, and they undergo the first acceleration. When they reach the positively charged terminal, a carbon foil strips the electrons and converts negative ions into positive ions. Then, the ions are further accelerated toward the grounded terminal. In this way, the final energy of the particles is doubled compared to that obtained with the single-stage configuration.
Van de Graaff and Tandem accelerators are used widely for PIXE and other IBA techniques. The maximum energy of the accelerated particles is of the order of 10 MeV. However, the presence of such strong, and therefore difficult to control, electric fields

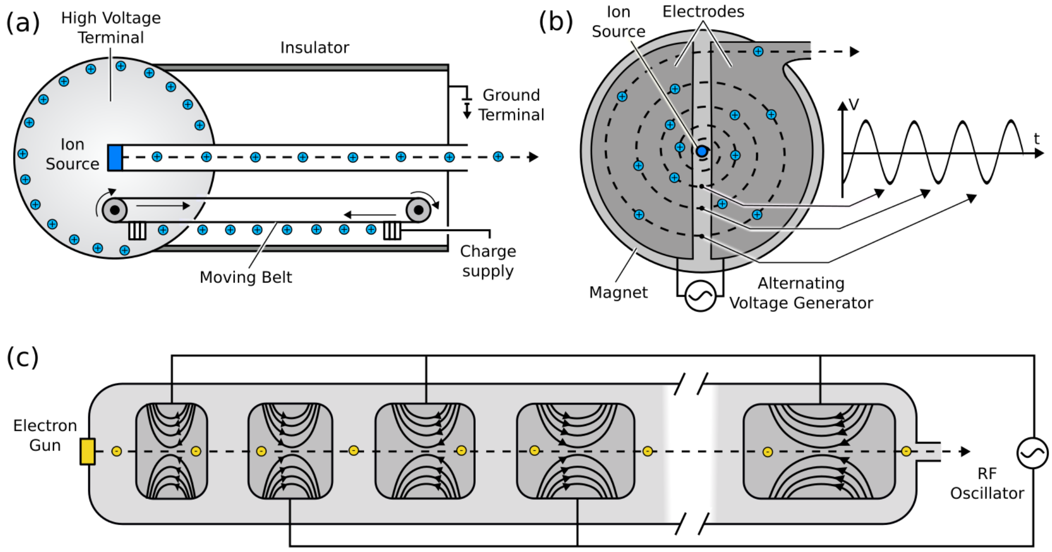

Figure 1.12: *Conceptual schemes of (**a**) the single-ended Van de Graaff, (**b**) cyclotron and (**c**) LINAC accelerators.*

limits the flexibility of these machines. For instance, the energy of the particles cannot be changed instantaneously, but it requires a time-consuming procedure. These machines are also subject to radiation protection issues [39] because of the progressive activation of the components.

Cyclotrons

Cyclotrons [53] are a possible alternative to electrostatic machines. The ions move along a spiral trajectory starting from the centre of a flat cylindrical vacuum chamber while accelerated by a radiofrequency electric field (see figure 1.12.b). In the non-relativistic regime, the frequency of circulation is independent of particle energy. Ions are produced at the centre of the magnet. The acceleration takes place when they pass through the gap between the electrodes. The field is in resonance with the cyclotron frequency. At each cycle, the positive charges, accelerated to a negative potential, receive a renewed boost by the inversion of the potential. Besides, the particles are held to the spiral trajectory by the static magnetic field. When the ions reach the periphery of the magnet, they enter a deflection channel where a constant electric field is present and forces them out of the magnetic field.
Cyclotrons can provide protons with an energy of several MeV. The maximum energy is limited by the relativistic increase in mass while the velocity rises. This effect causes a reduction in the orbital frequency and leads to an asynchronism between the particle motion and the voltage oscillation.

LINAC machines

The LINAC [53] is a linear machine constituted by a straight hollow pipe. It is schematically represented in figure 1.12.c. Along the cavity, a series of cylindrical electrodes are placed. The motion of the particles inside the channel is in phase with the oscillating radiofrequency voltage. When the ions move across the gap between two electrodes and the voltage between them is maximum, if the length of the second electrode is such that the particles move across the next gap after a one-half period, they will be accelerated. Since the velocity increases, the following electrode must be longer than the former so that the ions will remain a new half-period between the gaps.
Considering electron LINACs, the same principle is applied exploiting a standing or traveling wave. The electric field is reflected by the metallic ends of the loaded cavities and the resulting field distribution is obtained by the superposition of the reflected waves. The synchronism between the resonant mode and the particle motion is set by changing the length of the drift tubes. However, modern LINACs exploit traveling waves in loaded waveguides to accelerate electrons. They are constituted by a disc-loaded structure, where a single mode propagates. Electrons ride on the crest of the wave along the drift tube, being continuously accelerated. Depending on the required energy of the accelerated particles, the length of a LINAC can vary from several meters (for few MeV electrons) up to kilometers (for GeV electrons).

CHAPTER 2

Laser-driven particle acceleration and applications

This chapter offers an overview of the laser-driven ion and electron acceleration topic. Section 2.1 summarizes the steps that led to the development of the laser technology currently exploited for particle acceleration. Then, in Section 2.2, the main aspects related to laser-plasma interaction are presented. Section 2.3 describes the Target Normal Sheath Acceleration (TNSA) mechanism and the use of advanced Double Layer Targets (DLTs) to enhance its performances. In this framework, both some of the most relevant experimental results and theoretical descriptions are presented. Section 2.4 deals specifically with electron acceleration via both near-critical targets and the laser wakefield mechanism. Finally, the main foreseen applications of laser-driven particle sources are summarized in Section 2.5.

2.1 Ultra-short and super-intense laser technology

Among all existing light sources, lasers are characterized by exceptional spatial and temporal coherence and monochromaticity. Since the development of the first device in 1960 [54], this technology has led to unthinkable improvements in several scientific fields. The laser intensities progressively increased in the following years, thanks to the advent of the Q-switch [55] first and Mode-Locking [56] later. Exploiting these technologies, lasers were able to generate pulses with fs-time duration and intensities up to $10^{10}\ \mathrm{W/cm^2}$. As a consequence, the birth of new branches of physics became possible. For instance, the experimental study of non-linear optics started to be a very active field because the achievable intensities were comparable to that of the atomic electric field (i.e. $10^8\ \mathrm{W/cm^2}$).
However, in the $70'$, a significant increment of the achievable laser intensities was not realized. Indeed, the amplification through multiple stages was limited by the damage of the pumped gain medium exploited to increase the energy of the pulse. Then, in

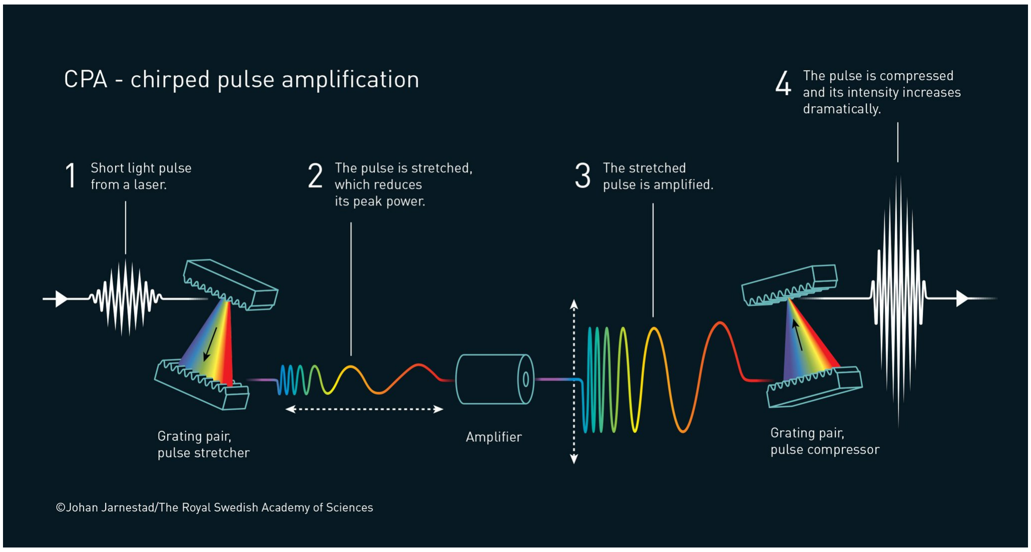
CPA - chirped pulse amplification
1 Short light pulse from a laser.
2 The pulse is stretched, which reduces its peak power.
3 The stretched pulse is amplified.
4 The pulse is compressed and its intensity increases dramatically.
Grating pair, pulse stretcher
Amplifier
Grating pair, pulse compressor
©Johan Jarnestad/The Royal Swedish Academy of Sciences

Figure 2.1: *Schematic representation of the Chirped Pulse Amplification working principle.*

the $80'$, Donna Strickland and Gérard Mourou developed the Chirped Pulse Amplification (CPA) [57], for which they were awarded with the Nobel prize in Physics in 2018. Briefly, with CPA, an ultra-short ($\leq$ ps) laser pulse is stretched to nanoseconds exploiting a grating. As a consequence, the laser frequencies are dispersed, and the maximum intensity is significantly reduced. The chirped pulse is sent through a sequence of amplification stages where the beam energy is enhanced. The stretching performed before the amplification prevents the damaging of the active media. Lastly, the pulse is compressed with a second grating. A scheme of the CPA working principle is shown in figure 2.1.

The invention of CPA paved the way for the development of a new generation of superintense lasers. Nowadays, they can reach intensities up to 10^{22} $\mathrm{W/cm^2}$ [58–60] and peak powers above the petawatts. During the last decades, many super-intense laser facilities were realized in the world. Among them, less than 20 are PW-class lasers. In particular, the European Extreme Light Infrastructure (ELI) project [61] is worthy of consideration. It consists of the implementation of four 10 PW laser facilities in Europe. The complete operation capabilities will be reached in the next few years, with foreseen highest intensities of the order of $10^{23} - 10^{24}$ $\mathrm{W/cm^2}$ never achieved before.

High-intensity lasers ($I > 10^{19}$ $\mathrm{W/cm^2}$) can be divided into two categories. The first group exploits Ti:Sapphire oscillators and CPA stages. They provide pulses with $10 - 100$ fs time duration and few Joules of energy. These lasers are characterized by high repetition rates (up to 1 kHz). The second category collects lasers that generate pulses with an Nd:YAG-based active medium. In this case, the pulses have longer time durations (i.e. $\sim$ ps) and higher energies (i.e. $\geq 10^2$ J). However, the repetition rate is significantly lower, ranging from 0.1 Hz to one shot per day.

As far as the first category is concerned, the number of lasers capable of delivering powers in the $10 - 100$ TW range is increasing. Their usages span from the development of novel ultrafast light and X-ray sources to high-energy density science and laboratory astrophysics. In particular, particle acceleration driven by superintense laser pulses is emerging as one of the most attractive topics.

2.2 Super-intense laser-matter interaction

To suitably describe the laser-driven particle acceleration phenomena, some basic concepts of super-intense laser-matter interaction must be introduced. When a super-intense laser pulse interacts with matter, it induces the transition to the plasma state via *Tunnel Ionization* and *Multi-Photon Ionization*. The first phenomenon is the distortion of the atomic field by the laser electric field. The second one is the direct overcoming of the binding energy of the electrons by multiple photons. Therefore, the matter is ionized within a single laser cycle, and the subsequent interaction is ruled by the electromagnetic effects in the plasma. The dispersion relation describing the interaction between electromagnetic radiation and cold plasmas is:

$$\omega^2 = \omega_p^2 + k^2c^2 \tag{2.1}$$

where $\omega_p = \sqrt{4\pi e^2 n_e/m_e}$ is the electron plasma frequency, n_e is the electron density, and m_e is the electron mass. Accordingly, an electromagnetic wave can propagate inside a plasma only if its frequency is greater than the electron plasma frequency. By fixing the laser wavelength, the threshold can be expressed in terms of the so-called critical density n_c:

$$n_c = \frac{m_e\omega^2}{4\pi e^2} \tag{2.2}$$

When the condition $n_e < n_c$ is satisfied, the plasma is called under-dense, and the laser pulse can propagate through it (i.e. the electromagnetic wave is transmitted). For lasers with a wavelength of the order of 1 μm, this condition is valid for gasses at atmospheric pressure. When $n_e > n_c$, the plasma is over-dense, and the laser pulse is reflected. That is the condition in the solid-state matter, having $n_e \approx 100n_c$. Lastly, if $n_e \approx n_c$, the plasma is called near-critical, and the interaction is characterized by strong laser-plasma coupling with complex non-linear phenomena in place.

In the ultra-high intensity regime, not only the non-linear effects occur, but also the relativistic ones can play an important role. The reason is that the velocity of the electrons can rapidly approach the speed of light. The importance of the relativistic effects can be estimated using the normalized vector potential $\mathbf{a}$:

$$\mathbf{a} = \frac{e\mathbf{A}}{m_e c^2} = \frac{\mathbf{p}_\perp}{m_e c} \tag{2.3}$$

where $\mathbf{A}$ is the laser vector potential and $\mathbf{p}_\perp$ is the transversal oscillating momentum of the electrons. Thus, assuming the transversal momentum equal to the total one, the Lorentz factor is evaluated as $\gamma = \sqrt{1 + \mathbf{A}^2}$. The pulse peak intensity can be expressed in terms of the normalized peak amplitude as:

$$a_0 = \sqrt{\frac{I[\mathrm{W/cm^2}] \cdot \lambda^2[\mu\mathrm{m}^2]}{1.37 \cdot 10^{18}}} \tag{2.4}$$

and the condition to have non-negligible relativistic effects becomes $a_0 > 1$. In this case, the dispersion relation is $\omega^2 = \omega_p^2/\gamma + k^2c^2$ and the relativist critical density n_c^{rel} takes this form:

$$n_c^{rel} = \gamma\frac{m_e\omega^2}{4\pi e^2} \tag{2.5}$$

From equation 2.5, it is clear that n_c^{rel} can be significantly higher compared to the non-relativistic value n_c. Therefore, an over-dense plasma in the non-relativistic regime could become under-dense in the relativistic one (i.e. when ultra-high intensity lasers are used).

The ponderomotive force

An important non-linear mechanism is the *ponderomotive force*. When an oscillating non-homogeneous electromagnetic field is present, particles move towards the region of weaker field strength. The ponderomotive force $\mathbf{f_p}$ acts as the result of the radiation pressure, and the average effect over the oscillations is described by the following relation:

$$\mathbf{f_p} = -\nabla \left(\frac{q^2}{4m\omega^2} \mid \mathbf{E_0} \mid^2 \right) = -\nabla U_p \tag{2.6}$$

in the non-relativistic approximation. $\mathbf{E_0}$ is the laser electric field, and $U_p = mc^2(\gamma - 1)$ is the ponderomotive potential directly related to the energy density of the electromagnetic field. Therefore, the particles move from regions of high-energy density to regions of a lower one. Remarkable, $\mathbf{f_p}$ is inversely proportional to the mass of the charged particles. As a consequence, its effect is much more intense on the electrons than on the ions. Moreover, the ponderomotive potential monotonically increases as a function of the normalized laser amplitude a_0.

The electron heating

When an ultra-intense laser pulse interacts with a steep solid material, the *electron heating* mechanism takes place. In the case of high plasma density, the laser pulse is almost reflected, and a short evanescent wave is formed at the surface. The superficial electrons are ejected from the surface under the action of the Lorentz force perpendicular to the interface. Then, the electrons are re-injected into the plasma with high energy. They are characterized by relativistic energies and broad momentum distribution. Depending on which part of the Lorentz force is considered (i.e. the electric or the magnetic component), two different processes responsible for the electron heating can be distinguished. They are depicted in figure 2.2.

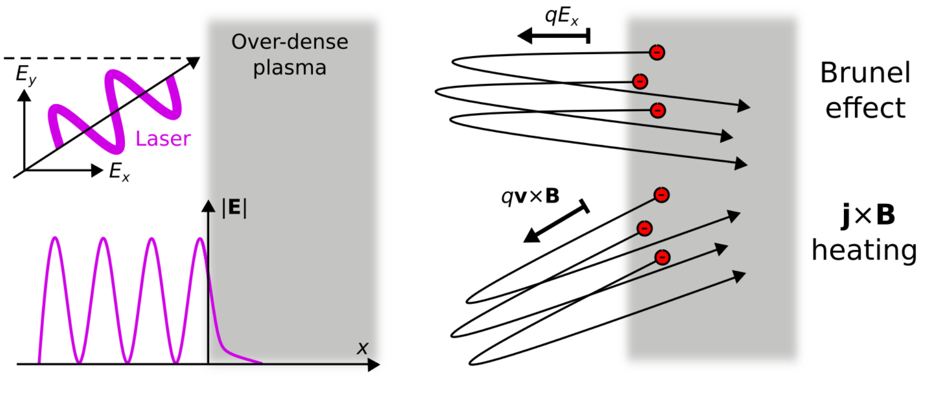

Figure 2.2: *Scheme of the electron heating processes in the interaction of an ultra-intense laser pulse with an over-dense plasma. Adapted from [62].*

The process associated with the electric field component is the *Brunel effect* (or *vacuum heating*). When the laser pulse interacts with the surface at an incident angle different from zero and with linear polarization in the plane of reflection (i.e. P-polarization), the electric field has a non-zero component perpendicular to the interface. Therefore, the electric field extracts electrons from the surface and, at the end of the wave cycle, it accelerates them into the plasma. Since the field rapidly vanishes over the skin depth, it cannot slow down the electrons that move toward the bulk. The Brunel effect fades in the case of normal laser incidence.

The $\mathbf{j} \times \mathbf{B}$ heating is driven by the magnetic component of the Lorentz force. The electrons are accelerated by the electric field and then pushed by the magnetic force along the laser propagation direction. The effect is more important as much as the electrons are relativistic. Unlike the Brunel effect, $\mathbf{j} \times \mathbf{B}$ heating is efficient with S-polarization or at normal incidence. On the other hand, in the case of C-polarization, the magnetic oscillating component of the Lorentz force tends to zero, and the $\mathbf{j} \times \mathbf{B}$ effect is negligible.

Lastly, the following semi-empirical formula [63] allows evaluating the hot electrons temperature T_h:

$$\begin{aligned} T_h = C_1(a_0, \wp) m_e c^2 \left[\sqrt{1 + \frac{a_0^2}{2}} - 1\right] + \\ + C_1(a_0, \wp) m_e c^2 \left[\sqrt{1 + f^2 \frac{a_0^2}{2} \sin^2\theta} - 1\right] \tan\theta \end{aligned} \tag{2.7}$$

where the first and second terms account for the $\mathbf{j} \times \mathbf{B}$ heating and Brunel effect, respectively. C_1 and C_2 are semi-empirical parameters that depend on the laser intensity and polarization $\wp$. θ is the laser incidence angle, and f is a parameter accounting for the laser reflection.

2.3 Ion acceleration via Target Normal Sheath Acceleration (TNSA)

When an ultra-short (tens fs) super-intense ($I > 10^{18}\ \mathrm{W/cm^2}$) laser pulse interacts with a micrometric solid foil (i.e. targets), the acceleration of electrons and ions in the forward direction occurs [64, 65]. This phenomenon, observed for the first time in 2000, was reported in three independent works [66–68], and it is represented schematically in figure 2.3.a. The accelerated ions and electrons were characterized by a broad energy spectrum (see figure 2.3.b) with maximum energies up to 10s $\mathrm{MeV/u}$ and a number of accelerated particles between 10^9 and 10^{13} per laser shot. The ions bunch was directed orthogonally to the target surface with a broad angular distribution extending up to few tens of degrees.

The Target Normal Sheath Acceleration (TNSA) scheme was proposed to interpret the experimental observation. As explained in the previous Section, the interaction of the laser pulse with the target surface leads to the formation of an over-dense plasma. The pulse is reflected, and a population of supra-thermal electrons is generated through the Brunel effect and $\mathbf{j} \times \mathbf{B}$ heating. The hot electrons cross the target in the direction of the rear side. As a result, a return current of cold electrons moving in the opposite direction is formed. At the rear surface, the hot electrons leave the target creating an intense

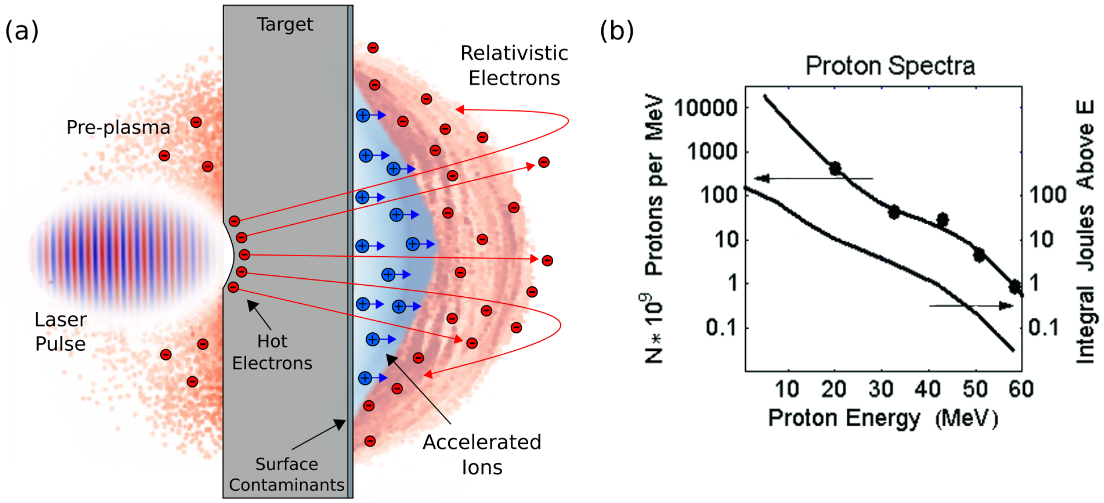

Figure 2.3: *(**a**) Scheme of the Target Normal Sheath Acceleration and (**b**) example of accelerated proton spectrum taken from [67].*

sheath electric field. The field accelerates the ions from the contaminants present on the rear surface of the foil.

The hot electron temperature can be evaluated using equation 2.7, which accounts for the physical phenomena responsible for the electron acceleration. However, the electron energy is also of the order of the cycle-averaged oscillation energy in the electric field of the laser, thus approximately equal to the ponderomotive potential. Accordingly, the electron temperature can be estimated as $T_h \approx m_e c^2 \sqrt{1 + a_0^2/\wp} - 1$. Assuming a laser irradiance $I\lambda^2 = 10^{20}\ \mu\mathrm{m}^2\mathrm{W/cm}^2$, the electron temperature results $T_h = 2.6$ MeV. Moreover, an energy flux balance between the laser pulse and the electrons can be written as $\eta I \approx n_h v_h T_h$, where η is the fraction of energy transferred from the laser to the hot electrons, n_h is the hot electron density, and v_h is the electron velocity. Considering $\eta = 0.1$ and $v_h \approx c$, we find $n_h \approx 8 \cdot 10^{20}\ \mathrm{cm}^{-3}$. We can also assume that the sheath field spacial extension is of the order of the Debye length of the electrons $L_s = \lambda_D = \sqrt{\frac{T_h}{4\pi e^2 n_h}} \approx 0.4\ \mu\mathrm{m}$. Finally, by imposing that the potential energy of the sheath field is equal to T_h, we can estimate the electrostatic field as $E_s \sim \frac{T_h}{eL_s} \sim 6 \cdot 10^{10}$ $\mathrm{V/cm}$. That is the magnitude of the field responsible for the ionization and acceleration of the ions from the target surface.

A rough scaling law for the maximum energy of the accelerated ions is $E_i^{max} \sim Z_i e E_s L_s = Z_i T_h$. Since the hot electron temperature scales with the square root of the laser intensity and linearly with the wavelength, the maximum proton energy should present the same dependences. Then, we can estimate the intensity as $I \propto \epsilon_p/\tau w^2$ where ϵ_p is the energy of the pulse and $\tau \propto \lambda/c$ is its temporal duration. Since $\omega \propto \tau$, the irradiance is directly proportional to the laser power and inversely proportional to the wavelength $I\lambda^2 \propto \epsilon_p c/\lambda$. Therefore, the ponderomotive scaling for the maximum ion energy is $E_i^{max} \propto \sqrt{P}$, where P is the laser power. It is worth pointing out that this scaling is in agreement with experimental data only for laser pulses with ps time duration. For $1 - 100$ fs time duration, the maximum proton energy shows a scaling law closer to a linear trend [69]. This discrepancy highlights the complexity of the phenomena in place and the necessity for more accurate descriptions.

Several models are available in the literature to estimate the most important properties of laser-driven accelerated ions. They can be classified as quasi-static [70], dynamic [71], and hybrid [72] models. A detailed description of these models is beyond the aims of this work. For this reason, only the following approximated relation [73] from the quasi-static model is reported:

$$E_p^{max} \approx T_h[\log\frac{n_h}{\tilde{n}} - 1] \tag{2.8}$$

Where E_p^{max} is the maximum proton energy and $\tilde{n}$ is a fitting parameter [73]. Equation 2.8 is valid only when the maximum electron energy is higher then T_h, which is a common condition.

2.3.1 Solid targets for TNSA

The number and energy of the accelerated ions are directly related to the hot electrons responsible for the sheath field formation. Therefore, controlling the hot electron temperature and density is the route to enhance the TNSA performances. As already mentioned, the hot electron current inside the target is counterbalanced by a return current of cold electrons. The currents are responsible for the generation of magnetic and electric fields, which can slow down the hot electrons. Moreover, electrons can undergo collisions with consequent loss of energy and broadening of their angular distribution.

A possible strategy is to reduce the target thickness (from 10s micrometers to 100s nanometers) to minimize the path of the electrons in the material. Experimental results demonstrate the feasibility of this approach. Indeed, an increment of a factor of ~ 2.0 for the maximum proton energy was observed, moving from 20 μm to 100 nm thicknesses [74–77]. The main drawback lies in the high thickness uncertainty of commercial sub-micrometric metallic sheets ($\pm 30\%$ of the nominal value, as commonly reported by manufacturers). They can also show the presence of defects like pinholes and ripples. Finally, the foils are clamped manually on perforated target holders with the risk of breakage and the formation of wrinkles. All these aspects affect the shot-to-shot reproducibility of the laser-driven source.

Another solution is to exploit *Reduced Mass Targets* characterized by a lateral dimension of the order of 10s μm. Because of the small lateral dimension, the recirculation effects allow better confinement of the hot electrons. Since the electron density is increased, the resulting TNSA process is more efficient. Again, an enhancement of a factor of ~ 1.5 for the maximum proton energy was observed [78].

To further increase the number of hot electrons, *grating targets* [79, 80] can be exploited. Indeed, the front side of these targets has a periodic surface modulation with spacial periodicity smaller than the laser wavelength. Both the energy and number of hot electrons are enhanced because of surface resonant wave excitation.

As previously mentioned, protons are accelerated from the contaminants present on the target rear side. This can lead to shot-to-shot fluctuations in the number of accelerated particles. The use of plastic foils instead of metallic targets allows stabilizing the proton beam current. On the other hand, dielectric foils exhibit an inhomogeneous spatial beam profile of laser-driven ions due to the onset of plasma instability [81]. This effect is suppressed with metallic (e.g. Al and Ti) foils or advanced dielectric (e.g. nanosphere

targets [82]) configurations.
Lastly, the use of near-critical *Double Layer Targets* (DLTs) is worthy of consideration. They consist of conventional solid foils covered by a low-density layer. If the actual density is comparable to the near-critical one, the laser pulse can propagate inside the plasma before reaching the solid foil surface. Indeed, the pulse digs a plasma channel pushing the electrons under the action of the ponderomotive force. The density gradient in the channel results in a radially dependent refractive index of the plasma which further focuses the laser pulse (i.e. *self-focusing* effect [83]). Because of the strong electron currents, very intense magnetic fields are formed, which push many electrons toward the rear side of the target [84]. The electrons are accelerated to super-ponderomotive energies through the Direct Laser Acceleration phenomenon (DLA) [85, 86] due to betatron resonance. These electrons contribute to the formation of a strong sheath field able to accelerate the ions and further enhancing their energies. Additional details about the pulse propagation and hot electrons generation in DLTs are provided in Section 2.3.3.
The materials required for DLTs must fulfill very stringent requirements like low density down to $\sim 10^{-3}$ $\mathrm{g/cm^3}$, thicknesses in the $1-10$ μm range, local spacial non-uniformity lower than the laser wavelength ($\sim$ μm), and mechanical compatibility with the solid substrates. Indeed, only a few porous materials like cellulose triacetate foams ($C_{12}H_{16}O_8$) [87], single-walled carbon nanotubes [88], and Carbon nanofoam (CNF) [89] (see figure 2.4) can satisfy the mentioned needs. The use of CNF for particle acceleration is of particular interest to the aims of this work. Therefore, it will be further discussed in the following Section.

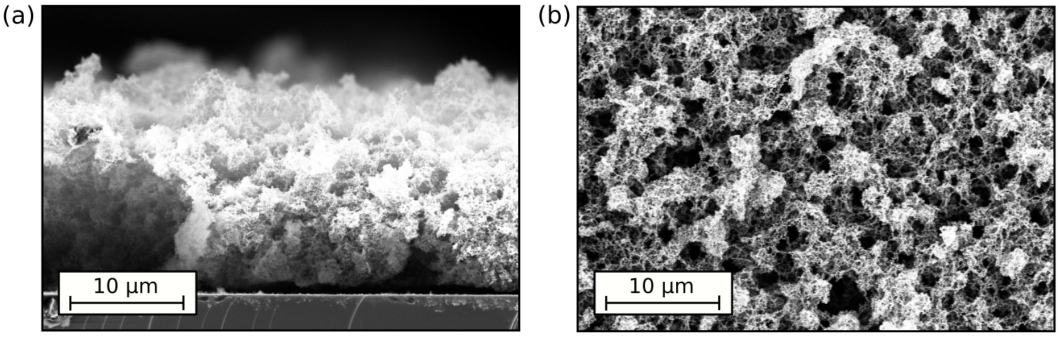

Figure 2.4: *SEM (**a**) cross section view and (**b**) top view of a near-critical Carbon nanofoam deposited at the NanoLab with the ns-Pulsed Laser Deposition technique.*

2.3.2 Enhanced TNSA with Near-critical Double Layer Targets (DLT)

Carbon nanofoams are porous materials that are successfully produced by Nanosecond-Pulsed Laser Deposition (ns-PLD) at the *Micro- and Nanostructured Materials Laboratory* (NanoLab), in the Politecnico di Milano. They are made of micrometer-sized aggregates of carbon nanoparticles. By controlling the ns-PLD deposition parameters (e.g. the working gas and pressure), it is possible to tune the average density down to the critical value [92].
Some experiments [90, 91, 93] have been performed to study ion acceleration via the super-intense laser interaction with Carbon foam-based DLTs. Here, we focus on the

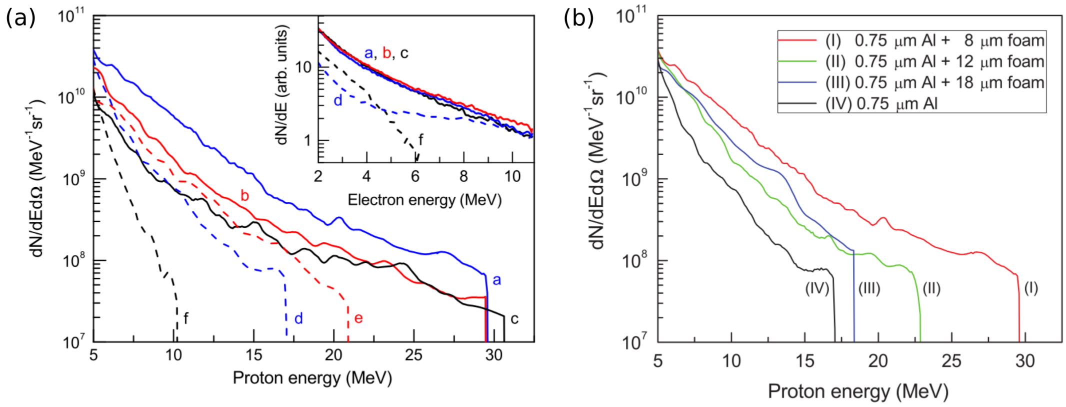

Figure 2.5: *(**a**) Proton energy spectra obtained with a laser intensity* $\sim 3.5-4\times10^{20}$ $\mathrm{W/cm^2}$ *for S-, P- and circular polarization with the bare target (the f, d, and e dotted lines) and the DLT (the a, b, and c continuous lines). The near-critical layer thickness of the DLT is equal to 8* μ*m. The inset plot shows the electron energy spectra for the bare and double-layer 12* μ*m thick targets for the different polarizations. From [90]. (**b**) Proton energy spectra for different foam thicknesses (8, 12, and 18* μ*m) deposited on a 0.75* μ*m thick Al substrate. The spectrum obtained with the bare target is also shown. From [91].*

experiment carried out at the *Center for Relativistic Laser Science* (CoReLS), *Institute for Basic Science* (IBS) in Korea. The campaign was performed with a petawatt Ti:Sapphire laser able to provide pulses with 7.4 J of energy and 5 μm focal spot with an angle of incidence of $30°$. Different irradiation conditions were tested considering linear (S and P) and circular polarization and laser intensities between 1 and 4.5×10^{20} $\mathrm{W/cm^2}$. Both bare and DLT targets with carbon foam thicknesses equal to 8, 12, 18, and 36 μm and density of 7 $\mathrm{mg/cm^3}$ were studied. The proton energy spectra were recorded exploiting a Thomson Parabola spectrometer placed along the target normal direction.

The experimental results highlight that the presence of the foam has a beneficial effect on the proton energy spectra. Indeed, as it is shown in figure 2.5.a, the maximum proton energy is increased by a factor of 2-3 with the DLT compare to the single-layer target case. The gain in terms of the number of accelerated particles is around 7 for P-polarization. Moreover, in absence of the foam, the spectra are greatly affected by the laser polarization because of the Brunel effect and the electron heating. On the other hand, this dependence is strongly mitigated with DLTs because of the volumetric electron heating. The electron energy spectra are reported in the inset graph of figure 2.5.a. Their number and temperature are significantly increased when the DLTs are exploited. Figure 2.5.b shows the proton spectra for various foam thicknesses. The trend is not monotonic, and the maximum proton energy and number were achieved with the 8 μm thick foam. Higher thicknesses have a detrimental effect on the properties of the accelerated particles. Thus, the foam thickness is a fundamental parameter that must be carefully chosen. To this aim, a model for the laser-driven electron and ion acceleration from DLTs has been developed within the framework of the ENSURE project (see Section 2.3.3 for details).

It is worth noting that the results considered here were obtained exploiting μm-thick substrates. Further improvements in terms of the particle energy and number could be achieved by decreasing the solid foil thickness or optimizing the near-critical layer density and thickness for the adopted laser parameters. Therefore, under the proper experimental conditions, DLTs can be considered one of the most powerful tools for the acceleration of both electrons and ions. That is confirmed also by other experimental observations using DLTs made of solid foils covered by nanotubes [94, 95].

2.3.3 Theoretical description of the laser-DLT interaction

The interaction between an ultra-intense laser pulse and a near-critical material is a non-trivial phenomenon characterized by several effects and high thermal non-equilibrium. Therefore, a plasma kinetic description should be adopted by solving the Vlasov equation [96]. However, with laser-driven particle acceleration, the solution cannot be found analytically because of the high complexity of the system.
A possible solution is to exploit numerical methods like Particle-In-Cell (PIC) simulations [97, 98]. The PIC approach allows realistically modeling the mechanisms involved in the interaction between the laser pulse and the plasma. An example of PIC output is provided in figure 2.6. However, this approach is very expensive from the computational point of view and it always requires exploiting Performance Computing resources. Moreover, the physical interpretation of the obtained results is not always straightforward. Further details about the PIC method will be provided in Section 3.3.
Nevertheless, a theoretical description of the physical phenomena in play is useful, both to perform predictions and to interpret experimental data. Because of the high degree of complexity of the involved physical phenomena, just the fundamental mechanisms for a sufficiently accurate description can be considered.
Here, the model proposed by *Pazzaglia et al.* [99] is briefly discussed since it represents one of the most recent and complete descriptions of the laser-driven ion and electron acceleration from near-critical double-layer targets. In addition, this model will be extensively exploited in Chapter 8.
The laser pulse profile is described with a $\cos^2$ temporal dependence and a Gaussian transverse shape. To model the self-focusing effect, the evolution of the beam waist $\omega(x)$ along the near-critical layer depth *x* is treated exploiting the thin-lens approximation:

$$\frac{\omega(\bar{x})}{\lambda} \approx \sqrt{\frac{1}{\pi^2 \bar{n}} + \left(\bar{x} - \frac{\omega_0}{\lambda}\right)^2} \tag{2.9}$$

where $\bar{x} = \sqrt{\bar{n} x/\lambda}$ is a normalized space variable, λ is the laser wavelength, and $\bar{n} = n_e/\gamma_0 n_c$ is a relativistic transparency factor. $\gamma_0 = \sqrt{1 + a_0^2/\wp}$ is the average Lorentz factor of the electron motion (with $\wp$ equal 1 and 2 for circular ad linear polarization, respectively). The hypotheses are that the beam waist keeps large compared to λ and its minimum value ω_m is significantly smaller than the initial one ω_0. The self-focusing effect in a near-critical plasma is evident in figure 2.6, obtained from a 3D PIC simulation. The pulse propagates inside the medium, heating electrons and losing energy accordingly to the ponderomotive scaling. The normalized energy loss is described as:

$$\frac{1}{\epsilon_{p0}} \frac{d\epsilon_p(x)}{dx} = -2 \left(\frac{2}{\pi}\right)^{D/2} V_{D-1} C_{nc} \frac{1}{\tau c} \frac{n_e}{a_0 n_c} \frac{\gamma(x) - 1}{a_0} \left(\frac{r_c \omega_x}{\omega_0}\right)^{D-1} \tag{2.10}$$

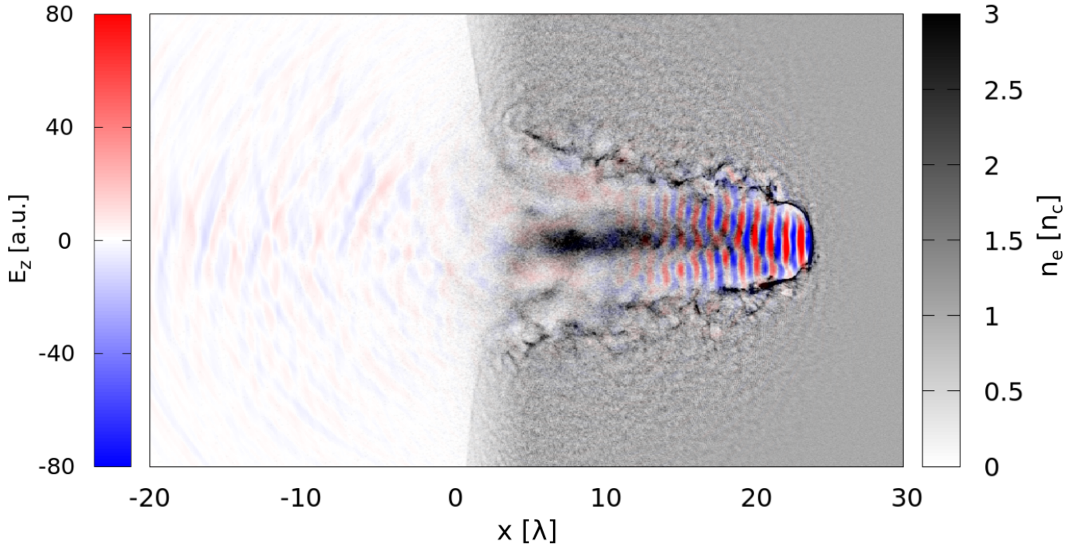

Figure 2.6: *3D PIC simulation output showing the transverse component of the electric field of an ultra-intense laser with $a_0 = 10$, propagating inside a uniform near-critical plasma with $n_e/n_c = 1$ at the time 40 λ/c after the beginning of the interaction. The simulation was performed with the Piccante code [100].*

where:

$$\epsilon_{p0} = \pi^{D/2} 2^{-D/2-1} m_e c^2 n_c a_0^2 \omega_0^{D-1} \tau c \tag{2.11}$$

is the initial energy of the Gaussian pulse in D-dimensions, τ is the field temporal duration, V^{D-1} is the volume of a $(D-1)$-dimension hypersphere with unitary radius, C_{nc} is a constant accounting for the details of the electron heating, $\gamma_x = \sqrt{1 + a(x)^2/\wp}$ is the local value of the Lorentz factor. r_c is the ratio of the plasma channel radius to the waist assumed to be constant. To solve equation 2.10, the pulse amplitude along the propagation length $a(x)$ is obtained from:

$$a_0(x) = a_0 \sqrt{\frac{\epsilon_p x/\epsilon_{p0}}{(\omega(x)/\omega_0)^{D-1}}} \tag{2.12}$$

Equations 2.12 and 2.10 describe the pulse propagation in the near-critical plasma, and they can be solved numerically with the finite difference method. In [99], the free parameters r_c and C_{nc} are evaluated by fitting the data obtained from 2D-PIC simulations with the model.

To describe the evolution of the hot electron population, the assumption that all the energy lost by the pulse is absorbed by the electrons is performed. This hypothesis is valid for short laser pulses (tens of fs) and $a_0 < 50$. The fraction of laser energy given to the electrons is:

$$\eta_{nc}(x) = \epsilon_p(x)/\epsilon_0 - R_D \tag{2.13}$$

where R_D is the reflectance of the plasma. The evaluation of R_D is not trivial, since its value depends on the considered region of the pulse. Indeed, close to the laser peak, the electrons are relativistic, and the plasma is near-critical allowing the pulse propagation. On the other hand, close to the tails, the electrons can be non-relativistic, resulting in an overcritical reflecting plasma. Considering the mentioned effects, an analytical expression for R_D in three dimensions is provided by the following relation:

$$R_{3D} = \mathrm{erf}(\sqrt{-2\log\bar{n}})\frac{4}{\sqrt{2\pi}}\bar{n}^2\sqrt{-\log\bar{n}} \tag{2.14}$$

The number of hot electrons in the near-critical layer $N_{nc}(x)$ is given by:

$$\frac{dN_{nc}(x)}{dx} = V_{D-1}n_e(r_c\omega(x))^{D-1} \tag{2.15}$$

From equation 2.13 and 2.15, the hot electron energy results:

$$E_{nc}(x) = \eta_{nc}(x)\epsilon_{p0}/N_{nc}(x) \tag{2.16}$$

When the pulse reaches the substrate, it generates hot electrons at the interface d_{nc} with energy:

$$E_s(d_{nc}) = C_s(\gamma(d_{nc}) - 1)m_ec^2 \tag{2.17}$$

where C_s collects all the effects at the interface. As far as the absorption efficiency at the interface is concerned, it is expressed as:

$$\eta_s = N_s(d_{nc})E_s(d_{nc})/\epsilon_p(d_{nc}) = 0.00388 \times a_0 + 0.0425 \tag{2.18}$$

where the coefficients of the linear relation are obtained from PIC simulations. Then, the overall electron energy $T_{DLT}(d_{nc})$ is retrieved by combining the contributions of the near-critical and substrate populations:

$$T_{DLT}(d_{nc}) = \frac{\eta_s\epsilon_p(d_{nc}) + \eta_{nc}(d_{nc})\epsilon_{p0}}{N_{tot}(d_{nc})} \tag{2.19}$$

where $N_{tot}(d_{nc}) = N_s(d_{nc}) + N_{nc}(d_{nc})$ is the total number of electrons.
Lastly, once the generation of the hot electrons is fully characterized, the energy of the accelerated ions is derived from equation 2.8. It is worth mentioning that the model has been further exploited to derive the optimal parameters of the DLT for ions acceleration considering several irradiation conditions. A detailed discussion of those results, which are beyond the aims of this thesis work, can be found in [99].

2.4 Laser-driven electron acceleration

As described in the previous Section, near-critical materials can be exploited for the efficient acceleration of electrons. The phenomenon, ascribable to the mentioned DLA mechanism, has been studied in several works [85, 86, 101–103]. For instance, the possibility to generate electron bunches with a total charge up to 5 μC has been demonstrated in [102]. The experiment was performed exploiting a polymer foam having 2 $\mathrm{mg/cm^3}$ density and up to 500 μm thickness. The near-critical plasma was produced by sending an ns laser pulse with 1-3 J of energy before the interaction with the main pulse. The second pulse was characterized by 750 fs time duration, total energy equal to 100 J and intensity $\sim 10^{19} - 10^{20}$ $\mathrm{W/cm^2}$.
Besides the high charge, the electrons accelerated with the near-critical material are characterized by exponential energy spectra with temperatures up to $\sim$ 12 MeV and

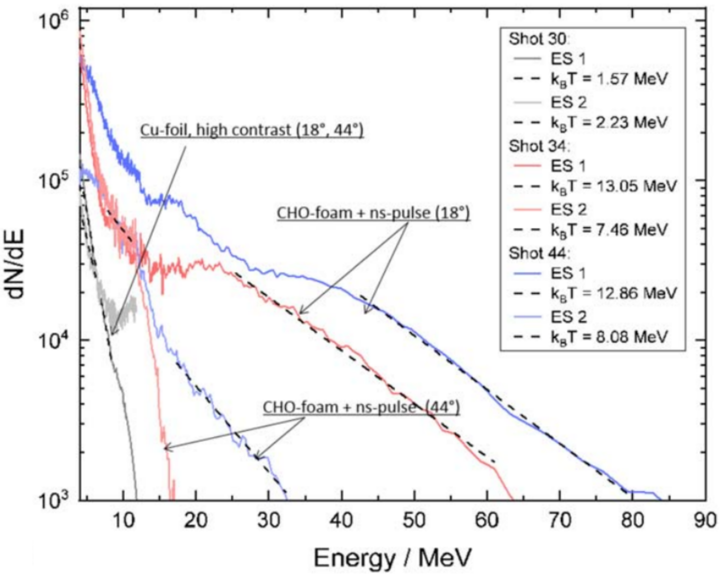

Figure 2.7: *Electron energy spectra at three emission angles accelerated with a near-critical material. From [102].*

maximum energy of the order of ~ 100 MeV. On the other hand, the electrons obtained from the irradiation of a conventional solid foil exhibit a temperature equal to 1-2 MeV and maximum energy of at least $\sim 10-20$ MeV. Figure 2.7 shows some examples of energy spectra for the aforementioned experimental conditions and different emission angles.

Clearly, in addition to the theoretical results, also the experimental evidence highlights the capabilities of near-critical targets for the generation of high-energy electron bunches. These electrons can interact with high Z materials and induce bremsstrahlung photon emission. Notably, the photons can activate target materials, and the delayed γ-ray emission can be used to characterize the primary electrons and bremsstrahlung radiation [104, 105]. However, the reference scenario for laser-driven electron acceleration exploits under-dense plasmas and the *laser wakefield acceleration* (lwfa) mechanism [106].

2.4.1 Laser wakefield acceleration (lwfa)

The gas-jet targets [107] are adopted to create an under-dense medium. They consist of a chamber filled with a gas (e.g. argon, hydrogen, or nitrogen). The gas is let out by a nozzle, which allows controlling the velocity and spatial profile of the flow. The gas emission is synchronized with the laser pulse using an electromagnetic valve. The resulting electron density is of the order of $10^{18}-10^{19}\ \mathrm{cm}^{-3}$.

When the laser pulse interacts with the gas-jet, it easily propagates through the under-dense plasma. Electrons are pushed toward regions where $|\mathbf{E}|^2$ is lower under the action of the pondermotive force. As a result, regions with a higher concentration of ions and electrons are created. Then, the electrons experience a strong attractive force back to the positively charged region. A wake (i.e. wakefield) is formed characterized by a high longitudinal and transverse electric field. The electrons trapped between the back and the middle of the wave are accelerated and focalized by the electric field.

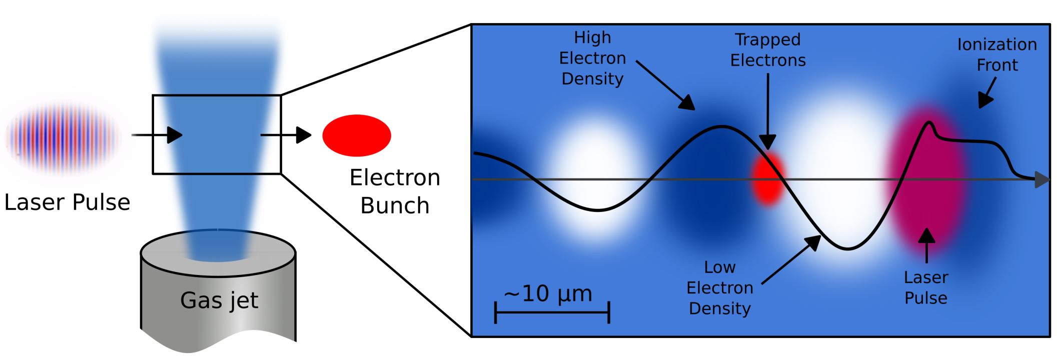

Figure 2.8: *Conceptual scheme of the laser wakefield acceleration mechanism.*

The best strategy to induce the wakefield formation is to exploit a laser wavelength of the order of the plasma wavelength. Under such a condition (also called *bubble* regime), the pulse energy is concentrated in a region smaller than the radius of the plasma wakefield. In this way, quasi-monoenergetic electron bunches are accelerated by electric field gradients of the order of 10s $\mathrm{GeV/m}$. The progressive increase in the mass of the relativistic electrons decreases the plasma frequency, leading to the saturation of the wakefield amplitude with no further acceleration. A schematic representation of the lwfa mechanism is reported in figure 2.8.

Since the first observation in 1985 [108], several experimental studies [109–112] have been performed. Exploiting $\sim 10-100$ TW lasers working at $1-10$ Hz repetition rate, electrons with energies up to several GeV of energy, angular divergence of few mrad, and $10-100$ pC of charge per laser shot have been accelerated. In addition, sub-TW laser drivers (i.e. 10s mJ of energy) have been successfully used to perform lwfa at kHz repetition rate [113]. In these experiments, the energy of the electrons is of the order of ~ 10 MeV with delivered currents of ~ 10 nA.

The acceleration gradients achieved with lwfa are 3 orders of magnitude higher than those exploited in conventional RF accelerators. Therefore, lwfa is considered one of the most promising strategies for future compact sources of electrons. Remarkably, a recent experiment [114] performed at the LUX beamline succeeded in operating a laser-plasma accelerator for more than a day exploiting a 48 TW laser working at 1 Hz repetition rate and providing electrons with 368 MeV of energy.

2.5 Applications of laser-driven particle sources

Laser-driven radiation sources can have potential advantages compared to conventional accelerators in terms of compactness and cost. Besides large PW class lasers, the existing technology provides table-top 10s TW class lasers. For instance, the possibility to accelerate protons up to MeV energies with such systems has been demonstrated [115, 116]. Moreover, a further reduction of costs and dimensions of superintense lasers is foreseen in the following years. Accordingly, several applications have been identified and tested for laser-driven proton and electron sources. They are extensively discussed in [117], and some of the most relevant ones are reported below.

Ion radiography and plasma probing

The peculiar properties of laser-driven protons are particularly suitable for radiography and imaging applications. They are characterized by a high degree of laminarity and spatial quality. Considering mm size objects, TNSA protons are emitted from a point-like source at the rear side of the target. Therefore, when laser-driven proton irradiation of a thin surface is performed, projection imaging is carried out from the detection of the transmitted particles [118]. The achievable resolution is of the order of a few μm.
Laser-driven protons have also been exploited to probe transient fields and density variations [119] in laser-plasma experiments, characterization of electric and magnetic fields in plasmas [120], observation of collisionless shock waves during laser-plasma interaction [121] and filamentation [122] in under-dense plasmas of interest for Inertial Confinement Fusion (ICF).

Warm dense matter production

Laser-driven ion sources can be exploited to heat solid matter via isochoric heating and induce the formation of the Warm Dense Matter (WDM) [123, 124]. WDM states are characterized by temperature (up to 100 eV) and density (from 1 to 10 times that of solids) conditions between condensed matter and hot plasma. This state is of great interest for astrophysics since it is present in the core of giant planets and small stars. It is also formed in ICF experiments during the solid-plasma phase transition.

Hadron therapy and Radioisotope production

Hadron therapy exploits protons and ions to carry out the irradiation of cancer tumours. Compared to common radiotherapy performed with X-rays, ions allow more precise irradiation of the region of interest, preventing the damage of the healthy tissues. Indeed, the ion range is well-defined, and the largest part of their energy is delivered in correspondence with the Bragg peak.
Laser-driven ion sources have been proposed for hadron therapy purposes [125, 126]. The research on the topic is one of the most active in the field of laser-driven ion acceleration. In the last years, the use of pulsed beams has shown significant advantages in terms of delivered dose rate to cancer tissues [127, 128]. In addition to the potential compactness compared to conventional accelerators, this observation makes laser-driven sources even more interesting for hadron therapy [129,130]. However, achieving laser-driven hadron therapy is a very challenging goal. Indeed, the accelerated proton energies achievable with a laser-driven source (i.e. $\sim 1 - 100$ MeV) are still far from that required for therapeutic purposes (i.e. between 60 and 250 MeV).
Radioisotopes production for Positron Emission Tomography (PET) is performed with cyclotrons and LINACs. As in the case of hadron therapy, laser-driven sources can be a suitable alternative to conventional ones with significant advantages in terms of costs, dimensions and radiation protection concerns. Therefore, the possibility to exploit laser-driven ion sources for PET radioisotopes production is under investigation [131–133]. The existing laser technology is not competitive yet with cyclotrons in terms of yields of the produced nuclides. However, in light of the aforementioned potential benefits, laser-driven sources could be relevant for the production of radioisotopes for preclinical studies in local hospitals and small facilities.

Nuclear physics

As already mentioned, laser-matter interaction is a suitable tool for the production of astrophysical plasmas at the laboratory scale. Laser-driven sources allow inducing nuclear reactions in plasmas and their study under astrophysical conditions [134, 135]. In the case of short-living radioisotopes, conventional accelerators are not able to provide adequate particle fluxes to produce a sufficient number of nuclei and place them inside a plasma. Moreover, the interaction of laser-driven ions with secondary targets can induce nuclear reactions suitable to monitor the beam properties [136]. It can also allow performing nuclear physics experiments in laser laboratories [137, 138] rather than in accelerator facilities.

Neutron production

Laser-driven particles have been exploited to generate high-energy neutrons (i.e. up to 100 MeV using ions) [139] through the interaction with converter materials. Laser-driven neutrons are still not competitive with accelerator-driven sources or nuclear reactors in terms of achievable fluxes. However, the growing research dealing with laser-driven neutron production testifies the interest in the topic [140–142]. Indeed, compact laser-driven neutron sources could be applied for several applications of social relevance like Fast Neutron Radiography and Neutron Resonance Spectroscopy for the inspection of cargo and containers, as well as for the active interrogation of sensitive nuclear materials.

Materials science

Laser-driven ion sources have been identified as a potential tool for materials processing applications, mainly for ion implantation [143–145]. Other uses of laser-driven ion sources in materials science are attracting attention only in very recent years. For instance, they have been proposed for the synthesis of metallic nanoparticles [146], micro-crystals and micro-structured surfaces [147]. As far as the characterization of materials is concerned, two studies [148, 149] have shown the possibility to exploit laser-driven source to analyze the composition of nanoparticles and pigments via In-Air Plasma-Induced Luminescence. Lastly, the identification of elements in materials using the characteristic X-ray emission induced by laser-driven particle irradiation has been performed by *Barberio et al.* [150]. It is worth mentioning that further studies dealing with the elemental characterization of materials with laser-driven radiation sources are not present in literature, which remains a substantially unexplored field.

CHAPTER 3

Thesis goals and methods

This Chapter contains the scopes and objectives beyond this PhD thesis work and the exploited methodologies. Specifically, the motivations and goals are highlighted in Section 3.1. Then, the Magnetron Sputtering deposition technique is described in Section 3.2, considering both the Direct Current Magnetron Sputtering (DCMS) and High Power Impulse Magnetron Sputtering (HiPIMS) regimes. Lastly, the Particle-In-Cell and Monte Carlo numerical methods for the description of the particle transport and laser-plasma interaction are presented in Section 3.4.

3.1 Thesis motivations, objectives and personal contribution

As extensively discussed in Chapter 1, atomic and nuclear analytical methods are among the most powerful tools for materials characterization. Despite their exceptional capabilities, many techniques are subject to significant limitations, preventing their large-scale diffusion. Indeed, as in the case of particle accelerators, the exploited radiation sources are large and expensive. Moreover, they can provide only one kind of particle. As a consequence, complementary techniques often require very different types of equipment. Lastly, when electrostatic accelerators are exploited, the energy is not easily tunable with detrimental consequences in terms of flexibility. Therefore, analytical techniques like Particle Induced X-ray Emission (PIXE), Energy Dispersive X-ray (EDX) spectroscopy and Photon Activation Analysis (PAA) can greatly benefit from the adoption of a more compact, cost-effective and multi-particle radiation source. In this respect, laser-driven particle acceleration presented in Chapter 2 could be an attractive alternative to conventional sources. Unlike conventionally accelerated particles, laser-driven electrons and ions are emitted quasi-simultaneously. Their energy can span from a few up to tens of MeV, and they are characterized by a broad momentum distribution. The particle energy can be easily tuned by changing the laser intensity or acting on the target properties. For instance, compared to conventional metallic foils, the adoption of near-critical double-layer targets allows enhancing both the energy and number of the accelerated particles. Because of their potential compactness and cheapness, several applications of laser-driven particle sources are the object of intense research. However, among the considered fields, the elemental characterization of materials is one of the least investigated. Indeed, only one work on this topic was present in literature before the start of this PhD thesis. Lastly, materials characterization techniques require excellent particle beam reliability. Considering laser-driven radiation sources, they are still subject to a certain degree of shot-to-shot instability. Nevertheless, the required reliability could be achieved by optimizing both the experimental setup and the particle detection system. Besides, the shot-to-shot reproducibility can be enhanced by improving the laser pulse stability and optimizing the target manufacture.

Within this framework, the present PhD work aims at investigating the possibility of exploiting laser-driven radiation sources for the elemental characterization of materials. The analytical techniques under investigation are PIXE, EDX and PAA (i.e. one for each of the families of methods introduced in Section 1.1). Among all possible laser-driven particle acceleration regimes, Target Normal Sheath Acceleration (TNSA) is considered because, while being recognized as one of the most stable and best-understood mechanisms, it provides both electrons and ions at the required energies. Besides, to ensure the particle energy and number demanded by the applications exploiting reduced laser requirements, the adoption of DLTs is considered.

In light of the mentioned goal, several important tasks must be accomplished. While the source stability can be raised acting on both the laser and target side, the present work focuses on the latter. Considering DLTs, the adopted sub-micrometric commercial substrates are affected by non-negligible local thickness uncertainty. Thus, a primary task of this work is to develop a strategy for the DLT substrates (or bare targets) manufacture, considering the sub-micrometre thickness range and achieving exceptional thickness uniformity. To this aim, the possibility to exploit the Magnetron Sputtering deposition technique is investigated. After the near-critical carbon foam deposition, the resulting DLTs should be the essential component of a laser-driven particle acceleration apparatus for materials characterization.

As previously mentioned, laser-driven radiation sources are intrinsically different compared to conventional ones. Therefore, another crucial task of this PhD thesis is to perform a theoretical instigation of the laser-driven PIXE, EDX and PAA feasibility. As it will be discussed in the following, this activity requires the exploitation of suitable numerical tools (e.g. Particle-In-Cell and Monte Carlo) and the development of theoretical models. Additional aims of this part of the work are the preliminary design of a compact laser-driven apparatus for materials science applications and to unveil the full potentials, in terms of analytical capabilities, of laser-driven PIXE, EDX and PAA.

Last, the possibility of performing different materials characterization techniques with a laser-driven radiation source must be experimentally demonstrated. Therefore, a further goal is to carry out a laser-driven PIXE and EDX proof-of-principle experiment at an international laser facility.

The first part of the PhD thesis deals with DLT substrate production. The Magnetron

Sputtering, able to operate both in Direct Current Magnetron Sputtering (DCMS) and High-Power Impulse Magnetron Sputtering (HiPIMS) regimes, is the ideal tool since it allows depositing compact films with controlled thicknesses (from 10 nm up to several μm) on large areas (e.g. several cm^2). The deposition apparatus was not present at the NanoLab laboratory in Politecnico di Milano before the beginning of this PhD work. The Magnetron Sputtering was installed at the Nanolab within the framework of the ERC-ENSURE project. A detailed description of the deposition technique and experimental apparatus is presented in Section 3.2. The investigated material is titanium (Ti) because it is a common target material in laser-driven ion acceleration experiments. I carried out a preliminary deposition and characterization campaign of Ti films, considering different working conditions. This activity aimed to understand the behaviour of the machine and to cover the lack of data in the literature about DCMS and HiPIMS deposition of Ti. The results are presented in Chapter 4. Then, I developed a strategy described in Chapter 5 to grow the Ti substrates directly on standardized target holders for laser-driven particle acceleration experiments. Both activities were carried out in close collaboration with two ENSURE team colleagues, Mr. Davide Vavassori and Dr. David Dellasega, and supported by a Master's Thesis in Nuclear Engineering of which I have been co-advisor. The Ti substrates production was performed within the context of the ERC-PoC project INTER (*Innovative Neutron source for non destructive TEsting and tReatments*) and in collaboration with the SourceLAB company. It is worth mentioning that the start-up of the laboratory required a time-consuming effort. Therefore, I carried out the activities presented in the first part of the thesis during the entire PhD period. The studies shown in the second part of the thesis have been performed in parallel, and in a coordinated fashion, with those described above. For instance, I exploited the knowledge acquired about Magnetron Sputtering to produce, with DCMS, the sample irradiated during the laser-driven PIXE and EDX experiment.

The second part of the thesis is entirely devoted to the numerical and experimental investigation of laser-driven radiation sources for PIXE, EDX and PAA. In Chapter 6, the theoretical description of PIXE is extended to include the presence of a non-monoenergetic proton source. Moreover, I developed a new numerical code to reconstruct the sample composition from the X-ray spectrum obtained with a laser-driven PIXE measurement. Then, I performed an extensive Monte Carlo simulation campaign of realistic laser-driven PIXE experiments. I also coupled the Monte Carlo with the output of 3D PIC simulations (made in collaboration with Dr. Luca Fedeli) to realistically describe the laser-driven source. The simulations are exploited to carry out a preliminary design of a laser-driven PIXE experimental apparatus, as well as to test the numerical code on 'synthetic' X-ray spectra. As far as laser-driven EDX is concerned, I performed other Monte Carlo simulations to study the characteristic X-ray emission from samples irradiated with laser-driven electrons.

Following the preliminary theoretical investigation, a proof-of-principle laser-driven EDX and quantitative PIXE experiment was performed. The campaign was conducted at the Centro de Láseres Pulsados (CLPU) with the Vega-2 laser system in collaboration with the other ENSURE team members, the group of Prof. Andrea Pola in Politecnico di Milano and the CLPU team. I took part in the campaign as a Local Principal Investigator, and I analyzed the collected data. The experiment and its outcomes are presented in Chapter 7.

Lastly, Chapter 8 shows a theoretical investigation of the laser-driven PAA feasibility. The first aim of this part of the work is to build a model for the comparison between conventional and laser-driven PAA performances. That was done by combining Monte Carlo simulations and a theoretical description (developed by Dr. Andrea Pazzaglia and presented in Section 2.3.3) of laser-driven electron acceleration in near-critical density media. The second task consists of a set of Monte Carlo simulations of conventional and laser-driven PAA experiments. The simulations were carried out considering both monoenergetic, pure exponential electron energy spectra and electron momentum distributions obtained from a PIC simulation. The PIC simulation was performed in collaboration with Dr. Arianna Formenti. Moreover, this activity was part of a Master's Thesis in Nuclear Engineering of which I have been co-advisor.

3.2 Magnetron Sputtering deposition techniques

The Magnetron Sputtering belongs to the Physical Vapour Deposition [151] family of techniques in which thin films are grown on substrates atom by atom. The atoms are sputtered or evaporated from a solid or liquid surface (i.e. condensed phase). They travel as vapour phase through the vacuum, a low-pressure gas or a plasma environment. When they reach the substrate surface, the atoms re-condense forming the film. PVD techniques are classified accordingly to the physical process responsible for the formation of the vapour phase. For instance, in *Vacuum Deposition*, the atoms (or molecules) are thermally evaporated by heating the material with a tungsten coil or high-energy electron beams. With *Arc Vapor Deposition*, the material is vaporized from an electrode subject to arcing conditions. On the other hand, when the vaporized particles are produced with a non-thermal process, the technique is called *Sputter Deposition*.

3.2.1 The sputtering process

The sputtering process [153] is carried out with energetic ions made to impinge on a target material and knock off the atoms. The process takes place inside a vacuum chamber filled with an inert gas (e.g. argon). A cathode (i.e. the target) and an anode (i.e. the substrate) are present in the chamber. A constant voltage is applied through a Direct Current (DC) power supply. The voltage application leads to the ignition of a glow discharge with the formation of a plasma. Since the target is placed at the negative voltage terminal, the positive gas ions are accelerated toward the cathode. Atoms are sputtered from the target surface by the ions, and they travel in the direction of the substrate. This simple scheme, represented in figure 3.1.a, is called DC diode glow discharge sputtering.

The minimum energy required for the ions to sputter the atoms from the target surface (also called *sputtering threshold*) ranges from 15 to 35 eV. According to the incident ion energy, three different sputtering regimes can be distinguished (see figure 3.1.b) [152]. In the single knock-on regime, the incident ion has just the energy to overcome the surface binding energy of a single atom. At higher energies, the incident ion can undergo a sequence of collisions in cascade with several atoms. It is the linear cascade regime in which only two-body interactions take place. Lastly, in the spike regime, the ion knocks out all the atoms along its path. In this case, the interaction occurs in the form of a many-body collision.

Table 3.1: *Examples of sputtering yields for 100, 200 and 300 eV energy Argon ions and several target elements. Extracted from [155].*

Ar^+ energy [eV]	Al	Ti	Cr	Fe	Cu	Mo	Ag	W	Au	U
100	0.11	0.081	0.30	0.20	0.48	0.13	0.63	0.068	0.32	0.14
200	0.35	0.22	0.67	0.53	1.10	0.40	1.58	0.29	1.07	0.35
300	0.65	0.33	0.87	0.76	1.59	0.58	2.20	0.40	1.65	0.59

Along with sputtering, the incident ion can be absorbed in the material without releasing an atom. Therefore, the sputtering yield must be introduced to describe the probability of the process (i.e. the fraction of emitted atoms per unit of incident ions). This quantity depends on the energy of the incident ion, the sputtered material and the angle of incidence of the impinging ions. Several analytical and semi-empirical formulas [152, 154] for the sputtering yield evaluation have been proposed for the mentioned energy regimes. Some values are reported in table 3.1 for different incident Ar ions and target elements.

Another relevant parameter is the deposition rate, expressed in terms of film thickness per unit deposition time. During the discharge, the ion current density is almost uniform over the target surface. A higher current density is required to increase the deposition rate, which could be achieved by increasing the pressure (up to $\sim 10^{-2}$ mbar) and voltage (from -2 to -3 kV). However, a higher pressure leads to a higher probability of collisions between the ions and the gas atoms with a reduction of their energy at the target surface. Therefore, to enhance the deposition rate, the unique strategy is to act on the applied voltage. Although, also many electrons are produced during the discharge, and they can reach the anode. The higher electron current density results in

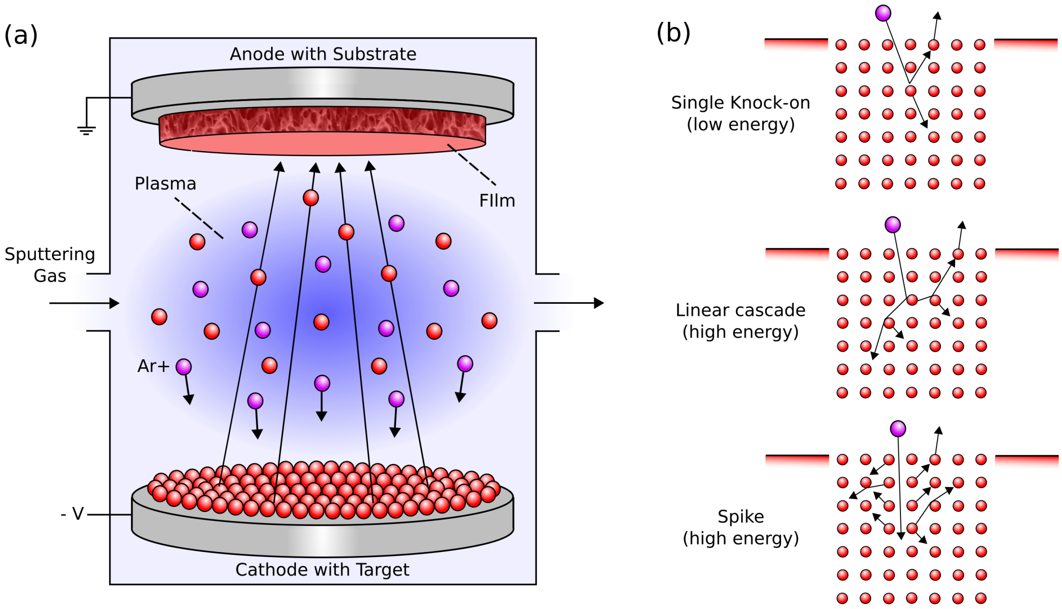

Figure 3.1: (***a***) *Schematic representation of the DC diode sputtering configuration.* (***b***) *Sputtering process representation for the single knock-on, linear cascade and spike regimes. Adapted from [152].*

a greater power released to the anode with consequent heating and substrate damage. The Magnetron Sputtering configuration is exploited to overcome this limitation.

3.2.2 Direct Current Magnetron Sputtering (DCMS)

Along with a constant voltage, in the Direct Current Magnetron Sputtering (DCMS) configuration [156], a constant magnetic field is applied to trap the electrons in the discharge. This allows increasing the ion current density by $1-2$ orders of magnitude and, as a consequence, to reduce the gas pressure (i.e. $\approx 10^{-3}$ mbar) and the applied voltage (i.e. ≈ -500 V). The ion energy at the target surface is higher with a significant increment of the deposition rate up to several $10\mathrm{s}$ of $\mathrm{nm/s}$.

The permanent magnets are located behind the target. As far as circular targets are concerned, one pole is placed at the centre of the disk. The other pole has an annular shape and is set in correspondence with the target corner. As a result, the magnetic field lines have a parabolic shape from the corner to the centre of the cathode, and the magnetic field has circular symmetry. The maximum field strength, of the order of a fraction of Tesla, is located where the magnetic fields lines are parallel to the surface. In this region, the plasma density is higher, and the ion current density at the target is maximized. Overall, the combination of the electric and magnetic field leads to a torus-shaped plasma where the electrons move with helicoidal trajectories along the magnetic field lines. The erosion of the target is maximized along the annular path, which is also called *race-track*. A schematic representation of the Magnetron Sputtering configuration and an example of a target are shown in figure 3.2.

It is worth mentioning that less than 50% of the target material is exploited with DCMS. Indeed, the target must be replaced before the erosion groove breaks through the material. Moreover, the erosion leads to a progressive increment of the magnetic field strength because the surface retreats towards the magnets. The magnetic field increment, in turn, leads to a gradual acceleration of erosion.

With the configuration reported in figure 3.2, the magnetic field lines are fully closed. This condition is called *balanced magnetron*, and the plasma is confined within ~ 6 cm from the target surface. Since the anode is usually placed farther from the target, the region close to the substrate is characterized by a low plasma density and ion cur-

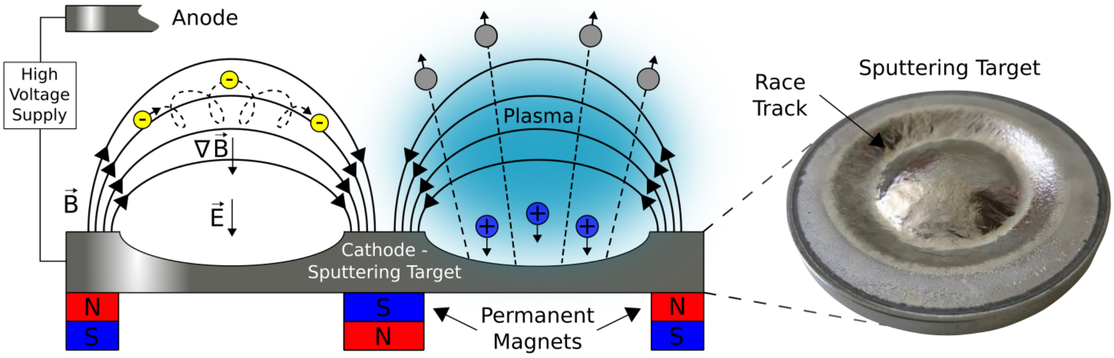

Figure 3.2: *Conceptual scheme of the balanced Magnetron Sputtering. The magnetic field configuration is shown, as well as an eroded Ti target.*

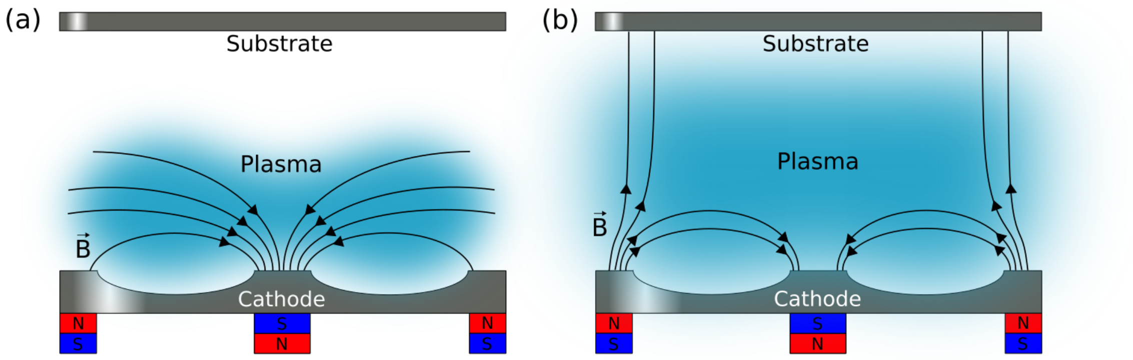

Figure 3.3: *Unbalanced Magnetron Sputtering in the (**a**) type-1 and (**b**) type-2 configuration.*

rent density lower than $1\ \mathrm{mA/cm^2}$. Such value of the current density will not affect the properties of the deposited film. Therefore, to grow denser films, the energies of the gas ions must be increased through the application of a negative bias voltage to the substrate. However, the high-energy ions can also enhance the intrinsic stresses in the film.

In addition to the balanced magnetron, two other configurations can be adopted: the *type-1* and *type-2 unbalanced magnetron*. In both cases, the magnetic field lines do not close between the magnets. They are shown in figure 3.3. In the Type-1 configuration, the central pole is strengthened compared to the outer. The field lines start from the wall of the chamber and converge to the centre of the cathode. In this case, the plasma density is more confined at the target than in the balanced configuration. Since the ion current at the substrate is lower, this scheme is recommended for the deposition of films that can be easily subject to damage because of internal stresses. On the other hand, in the type-2 configuration, the external magnet is stronger than the central one. Some magnetic field lines are directed towards the anode, and the plasma is less confined. Therefore, the substrate is subject to a higher ion current density (i.e. $2 - 10\ \mathrm{A/cm^2}$). This configuration is exploited to deposit denser films avoiding the use of a bias voltage and, thus, the onset of strong stresses.

With DCMS, the average surface power at the cathode is of the order of several $\mathrm{W/cm^2}$, with a resulting plasma density of $10^8 - 10^{10}\ \mathrm{cm^{-3}}$. The ionization degree of the plasma species and the ion flux to the substrate are relatively low [157]. Therefore, a high bias voltage (i.e. 100s of V) is required to affect the properties of the film. Moreover, when the sputtered atoms cross the plasma, only a small fraction of them undergo collisions with ionization [156]. As a consequence, the ion current associated with the substrate is mainly due to argon ions that, combined with the application of a bias, can cause argon implantation [158] in the film. Argon implantation can lead to the generation of lattice defects, degradation of the film quality and loss of adhesion.

A higher average power is needed to increase the ionization degree of the sputtered species. However, the maximum power is limited by the thermal load on the target caused by the ion bombardment. Therefore, a different strategy is required. In this respect, a novel technique called High Power Impulse Magnetron Sputtering (HiPIMS) has been developed, and it will be discussed in the next Section.

3.2.3 High Power Impulse Magnetron Sputtering (HiPIMS)

Having a higher ionization fraction of sputtered species is a viable strategy to control the energy of the film-forming species, and therefore, to finely tune the properties of the coating. In the HiPIMS [159] configuration, the power to the cathode is provided in short pulses of duration t_p typically within $10 - 100$ μs (i.e. on-time) and frequency of approximately 1 kHz (i.e. duty-cycle lower than 10%). The provided peak power is $\sim \mathrm{kW/cm^2}$ during the on-time, leading to plasma densities of the order of $10^{12} - 10^{13}$ $\mathrm{cm^{-3}}$. On the other hand, the average power is still comparable to that of DCMS (i.e. $\sim \mathrm{W/cm^2}$), preventing the target from overheating. Remarkably, the ionized fraction of sputtered species at the substrate in HiPIMS can reach values up to $70 - 90\%$. The high ionization fraction enables the deposition of smooth films characterized by high density and excellent adhesion to the substrate [160].

The energy of the particles can be controlled by electric fields (i.e. a bias voltage to the substrate). As it will be shown, the bias application allows tailoring the intrinsic stresses, the microstructure, the structural and mechanical properties of the film. Another advantage compared to conventional Magnetron Sputtering consists in the possibility of depositing homogeneous films on geometrically complex surfaces. While the trajectories of the neutral species in DCMS are determined only by their initial angular distribution, in biased HiPIMS, the charged particles will follow the electric field lines. Thus, the ions impinge almost orthogonally on the substrate surface, whatever its orientation to the source.

The main drawback of HiPIMS is the lower deposition rate ($\sim 30 - 80\%$) compared to DCMS [161]. It is ascribable to the considerably lower duty cycle and to the fact that part of the ionized metallic ions is drawn back to the cathode (thus, not contributing to the film growth).

The deposition system exploited in this work can operate both in DCMS and HiPIMS mode. The chamber is equipped with two cathodes to allow the co-deposition from different targets. The cathode rotates around the vertical axis up to a speed of 20 rpm to ensure uniform deposition. Moreover, it can be connected to an output of the power supply allowing bias application to the substrate. The generation of the pulses is performed by two Direct Current power suppliers connected to a pulsar with two output channels.

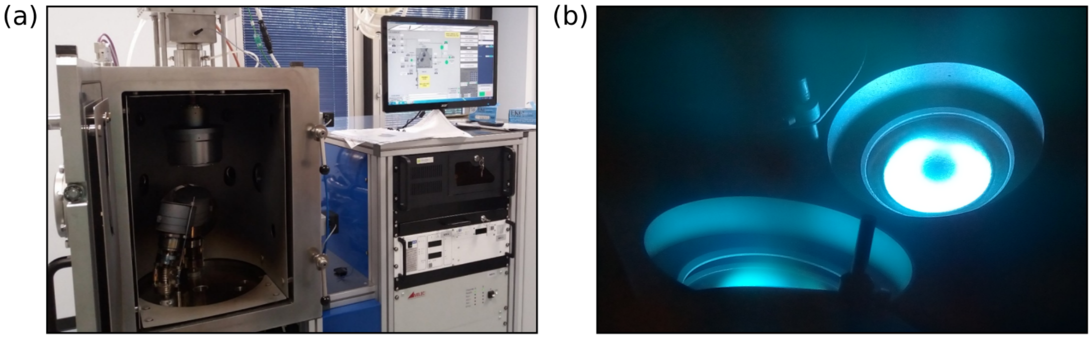

Figure 3.4: *Magnetron Sputtering deposition system at Nanolab in Politecnico di Milano. (**a**) Image of the machine. (**b**) Image of the anodes taken during the co-deposition from two Ti targets. The HiPIMS plasma is visible.*

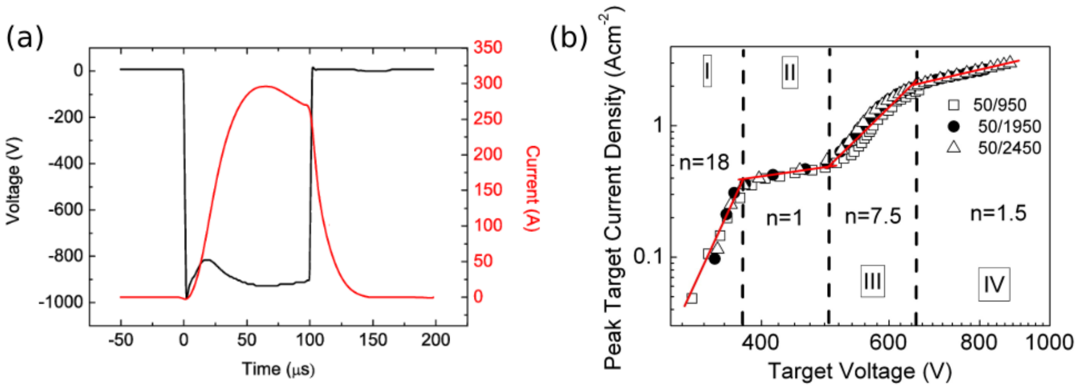

Figure 3.5: *(**a**) Example of experimental voltage and current waveforms taken from [163]. (**b**) The experimental trend of discharge peak current taken from [159]. The dashed black lines highlight the four regions of the HiPIMS operation.*

The pumping system is composed of a primary pump and a secondary turbomolecular pump. The primary pump allows us to reach the pre-vacuum condition (i.e. $\sim 8 \cdot 10^{-3}$ mbar) before start-up the secondary pump. The secondary pump brings the system in the final vacuum condition (i.e. $\sim 5 \cdot 10^{-7}$ mbar). This deposition system, which has been exploited in this PhD work, is shown in figure 3.4.a. An image of the HiPIMS plasma is also reported in figure 3.4.b.

The HiPIMS plasma discharge

The ion flux at the substrate depends principally on plasma density, target power and magnetic field configuration. In figure 3.5.a, an example of HiPIMS discharge voltage and current waveforms are shown. The discharge voltage waveform has a rectangular shape, while the discharge current increases and rapidly drops at the end of the voltage pulse. It is worth mentioning that the peak current (i.e. the maximum value of the current waveform) is usually three orders of magnitude higher compared to the DCMS current, and it exhibits a characteristic behaviour as a function of the applied voltage (see figure 3.5.b). The trend is independent of the pulse on- and off- times, and it is strongly related to the properties of the HiPIMS plasma.
The voltage V and peak current I_p are connected by the power low $V \propto I_p^n$. The actual value of n changes accordingly to the considered voltage range and HiPIMS configuration (e.g. the sputtered material and pressure). However, four regions can be identified that correspond to different plasma conditions [159, 162]. In region I, the power and target peak current are low. This behaviour is of DC-like plasmas. For a precise value of the discharge voltage, an increment in the plasma impedance is observed (i.e. region II). The increment corresponds to flux densities at the substrate $20 - 50$ times higher compared to DCMS conditions. The ionization further increases in region III with the onset of self-sputtering (i.e. sputtering by the target metal ions) and consequent decrease of the plasma impedance. The magnetic confinement is lost in region IV. The loss of magnetic confinement is due to the high azimuthal current, which results in a high induced magnetic field that screens the effect of the magnetron field.
In addition to the voltage, the pulse duration (i.e. the on-time) can strongly influence the fraction of ionized spices [163]. For $t_p < 50$ μs, the sputtering particles are mostly

Ar ions, and the self-sputtering is minimized. As the on-time increases (i.e. $50\ \mu$s $< t_p < 200\ \mu$s), a higher fraction of the ionized sputtered ions are attracted back to the target surface and contribute to the sputtering process. Due to the self-sputtering, less material reaches the substrate with a consequent reduction of the deposition rate. For longer pulses, the gas dissipation at the target surface may result in a drop of the discharge current unless the loss of gas ions is compensated by the self-sputtering ions from the target.

The plasma discharge in HiPIMS is a very complex phenomenon, influenced by several operating parameters. It is directly related to the flux and energy of the film-forming species, which are responsible for the properties of the deposited film. In the following, these aspects are briefly discussed with particular reference to the microstructure and phase composition.

Film processing with HiPIMS

The correlation between deposition parameters and microstructure evolution of polycrystalline films is described by the so-called Structure Zone Diagram (SZD). In PVD techniques, the microstructure is affected by the surface and bulk diffusion processes. These phenomena are related to the homologous temperature T_h (the film growth temperature normalized by the melting temperature of the material). According to this parameter, four different *Zones* can be identified [164]. In Zone 1 ($T_h < 0.15$), continuous nucleation of grains is observed because of the low adatom mobility. The resulting structure is characterized by thin columnar grains oriented in the direction of the flux and high porosity at the boundaries. In the so-called Zone T ($0.15 < T_h < 0.3$), the surface diffusion is enhanced while the diffusion at the grain boundary is suppressed. As a result, competitive grain growth takes place with V-shaped grains formation. Zone 2 ($0.3 < T_h < 0.5$) exhibits high surface and grain boundary diffusion with the formation of uniform columnar grains. Lastly, compact films with large grains are formed in Zone 3 ($T_h > 0.5$) because of the high bulk diffusion and recrystallization.

As far as DCMS is concerned, the gas pressure must be taken into account since it is directly related to the energy of the incident particles at the substrate. In this respect, Thornton proposed an SZD in which both the thermal effects (related to the homologous temperature) and kinetic effects (associate with the working pressure) are considered [165]. In the case of HiPIMS, also the influence of the ions needs to be considered. Therefore, the homologous temperature definition must be generalized (T^*), including temperature shifts caused by the potential energy. The pressure is replaced with a normalized energy E^* accounting for both the kinetic and the heating effects. The latter effects are caused by the bombarding particle kinetic energy. This extended representation of the SZD was proposed by *Anders et al.* [166], and it is reported in figure 3.6. It can be seen that the four Zones described above are still present, even if the diagram is associated with energetic depositions. The vertical axis is related to the film thickness t^* net of the film densification.

The large variety of microstructures depicted in the Anders diagram have significant implications on the mechanical and electrical performances of the films. In this respect, also the phase composition can affect the mentioned properties. The use of high-energy ion fluxes allows controlling the thermodynamic and kinetic conditions and, as a consequence, tailoring the phase composition. Indeed, energetic ions can trigger bulk and

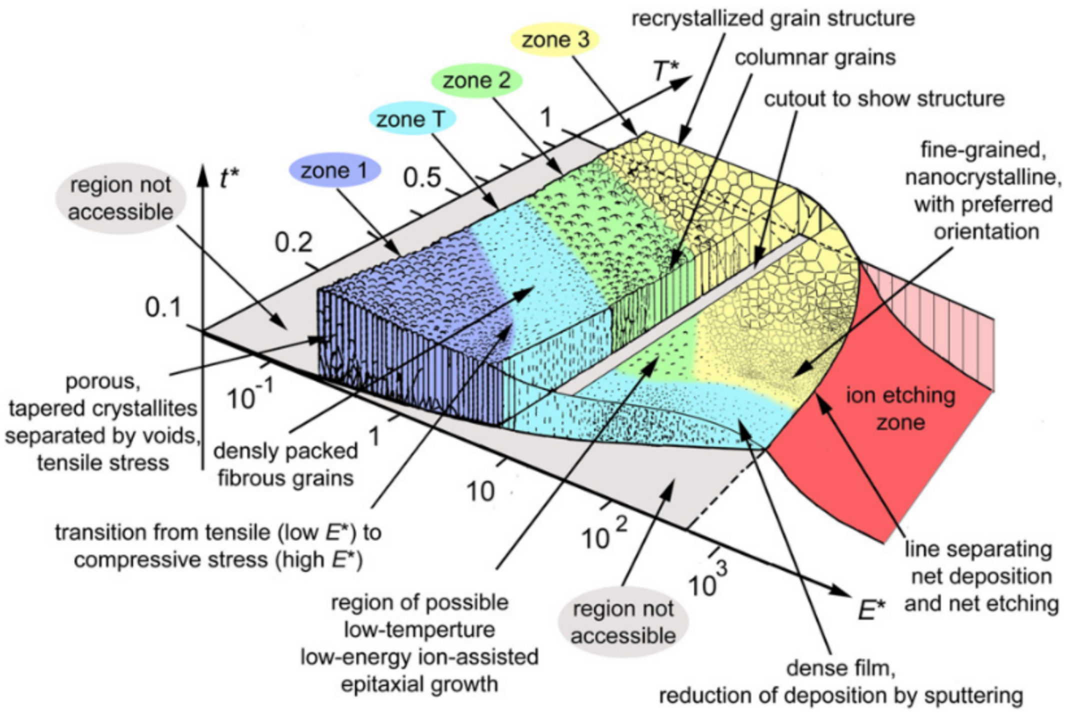
recrystallized grain structure
zone 3
columnar grains
zone 2
cutout to show structure
zone T
T*
1
fine-grained, nanocrystalline, with preferred orientation
region not accessible
t*
zone 1
0.5
0.2
0.1
porous, tapered crystallites separated by voids, tensile stress
10^-1
1
densly packed fibrous grains
ion etching zone
10
transition from tensile (low E*) to compressive stress (high E*)
10^2
10^3
line separating net deposition and net etching
E*
region of possible low-temperture low-energy ion-assisted epitaxial growth
region not accessible
dense film, reduction of deposition by sputtering

Figure 3.6: *Structure Zone Diagram for energetic depositions. Representative values of the normalized energy, generalized temperature and net thickness are reported on the axes. From [166].*

surface diffusion phenomena, as well as the formation of strong internal stresses [167]. For instance, the tailoring of the phase composition has been achieved in Ta films by controlling the magnitude of internal stresses [168]. As far as Ti films are concerned, the possibility of controlling its phase composition via Magnetron Sputtering and other PVD techniques is extensively discussed in the next Section.

The deposition of compound films can be achieved with HiPIMS by adding a reactive gas to the sputtering atmosphere. For instance, Titanium dioxide ($\mathrm{TiO_2}$) films deposition has been reported [169]. Also, in this case, the HiPIMS can be used to tune the phase composition of $\mathrm{TiO_2}$ from the conventional amorphous structure to the rutile crystalline phase. In addition to the transition metal oxides, reactive HiPIMS allows the deposition of many other classes of compounds [170] like transparent conducting oxides, binary and ternary transition metal nitrides.

3.2.4 Phase tailoring in titanium films with PVD techniques

Titanium is an appealing material for several applications in industrial engineering, aerospace and medicine because of its good corrosion resistance, high mechanical strength, excellent thermal stability and biocompatibility [171]. Moreover, Ti films are usually exploited in light detectors [172], as bolometers for infrared sensors [173], superconducting edge sensors in microcalorimeters [174], in large-scale integration technology and micro-electro-mechanical systems [175–177], single-electron transistors [178] and targets in laser-driven particle acceleration experiments [179].

Like the other transition metals of the IV group, Ti is characterized by different crystallographic structures. As clearly described by the phase diagram of Ti reported in figure 3.7, the formation of a specific structure depends on the temperature and pressure conditions [180]. At ambient pressure and temperature, Ti exhibits the α phase (also called *hcp*). Keeping the pressure constant and increasing the temperature, the conversion to the denser β phase (also called *bcc*) occurs. It is well-known that the β phase is more ductile than the α phase because it has a higher number of slip planes. Under high-pressure conditions, the formation of a hexagonal ω phase occurs. Its synthesis and properties are subject to intense research. It has been obtained both in bulk Ti via high-pressure torsion [181, 182] and through MeV energy particle beam irradiation [183–186]. In the second case, α phase Ti samples having a mixture of α and ω phases on their surface could exhibit improved mechanical properties like higher strength, hardness and fatigue resistance [187].

The phase tailoring in Ti films is not trivial since, often, high pressures and temperatures are not compatible with the substrate. Consequently, most Ti films show the α phase only. A viable strategy to trigger a new phase formation during a deposition is to exploit the affinity with the substrate inducing an epitaxial growth. The nucleation of the ω phase in Ti films was observed via electron beam evaporation on Fe (111) substrates [188]. At ~ 40 nm, the transition to the common α phase occurs. In addition, a face-centered-cubic (i.e. *fcc*) phase, not present in the Ti phase diagram, was observed in epitaxial films grown via evaporation on NaCl crystals [189], ceramic [190] and Al substrates [191]. In these cases, the transition to the α phase takes place at $\sim 1-20$ nm. Pure fcc films with thicknesses up to 220 nm were also produced by cathodic arc discharge on Si substrates [192]. The *fcc* phase formation is explained through the matching between the film and the substrate lattice. Indeed, the *fcc* phase exhibits the most compact orientation and stacking, allowing the minimization of the interfacial energy with the substrate.

Another strategy is to exploit an atom-by-atom deposition adding to the neutral species an ion field with hyperthermal energies (i.e. $10-100$ eV) [193]. Indeed, the ions are implanted in the surface layers (i.e. $1-3$ nm) of the film. The implantation causes the generation of point defects like interstitial, vacancies and substitutional atoms [194]. If sufficient energy is provided, the point defects can diffuse toward the closer under-

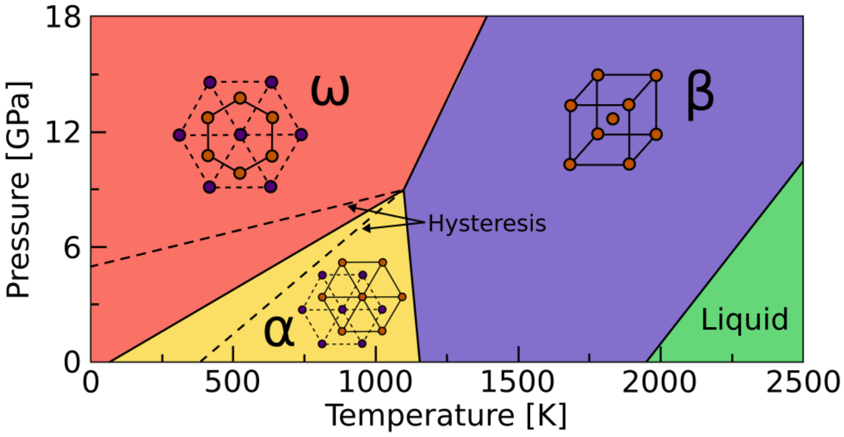

Figure 3.7: *Phase diagram of titanium. The regions associated with the α, ω, β and liquid phases are indicated.*

dense regions and be annihilated. This process allows altering the growth kinetics, morphology and structure of the films. In the case of Ti, few studies are present in the literature addressing the role of energetic ion species (mainly Ar) in determining the phase composition. The possibility of growing films containing a mixture of α and ω phases via arc-planting with a high bias voltage (i.e. 800 V) has been shown [195]. The high energy of the species, in conjunction with the low mobility of the atoms in the film, is suggested as a possible reason for the ω phase nucleation. Last, polycrystalline films containing both α and *fcc* phases have been deposited on Si substrates [196] with DCMS. Their thickness ranges from 140 nm to 720 nm. The *fcc* phase stability is explained with a thermodynamic stability model, and it is correlated with the state of stress in the films.
Overall, epitaxy can allow growing rather thin films containing both the α and unconventional phases of Ti. To improve the thickness, the use of energetic species seems to be a promising root. However, a detailed description of the role of the energetic ion species and deposition parameters is still missing in the existing literature.

3.3 Particle-In-Cell (PIC) method

The PIC method solves the relativistic Vlasov equation under the assumption of collisionless plasma, considering each particle species:

$$\partial_t f_i + \mathbf{v} \cdot \nabla_x f_i + q\left(\mathbf{E} + \frac{1}{c}\mathbf{v} \times \mathbf{B}\right) \cdot \nabla_p f_i = 0 \tag{3.1}$$

coupled with the Maxwell equations for the evaluation of the electromagnetic field:

$$\begin{cases} \nabla \times \mathbf{E} = -\frac{1}{c}\partial_t \mathbf{B} \\ \nabla \times \mathbf{B} = \frac{1}{c} + \partial_t \mathbf{E} + \frac{4\pi}{c}\mathbf{J} \\ \nabla \cdot \mathbf{E} = 4\pi\rho \\ \nabla \cdot \mathbf{B} = 0 \end{cases} \tag{3.2}$$

In equation 3.1, $f_i(\mathbf{x}, \mathbf{p}, t)$ is the phase-space distribution function of the i-th species. The idea is to describe the plasma as a collection of particles (e.g. ions and electrons) moving under the effect of external electromagnetic fields (e.g. the laser) and generated by the motion of the particles. The fields and currents are evaluated on a grid of spacing Δx. Since the system is formed by a huge number of real particles, electrons and ions are approximated as *macro-particles*. A macro-particle represents several real particles. This is possible since the Lorentz force depends on the charge-to-mass ratio. Therefore, the macro-particles trajectory is the same as the physical particles. Accordingly, f_i is approximated as:

$$f_i(\mathbf{x}, \mathbf{p}, t) = f_0 \sum_{j=1}^{N} S(\mathbf{x}, \mathbf{x}_j(t))\delta(\mathbf{p} - \mathbf{p}_j(t)) \tag{3.3}$$

where f_0 is a normalization constant. $\mathbf{x}_j$ and $\mathbf{p}_j$ are the position and momentum of the j-th macro-particle, respectively. $S(\mathbf{x}, \mathbf{x}_j(t))$ is a shape function representing the spacial extension of the macro-particles. A common choice is a triangular function of

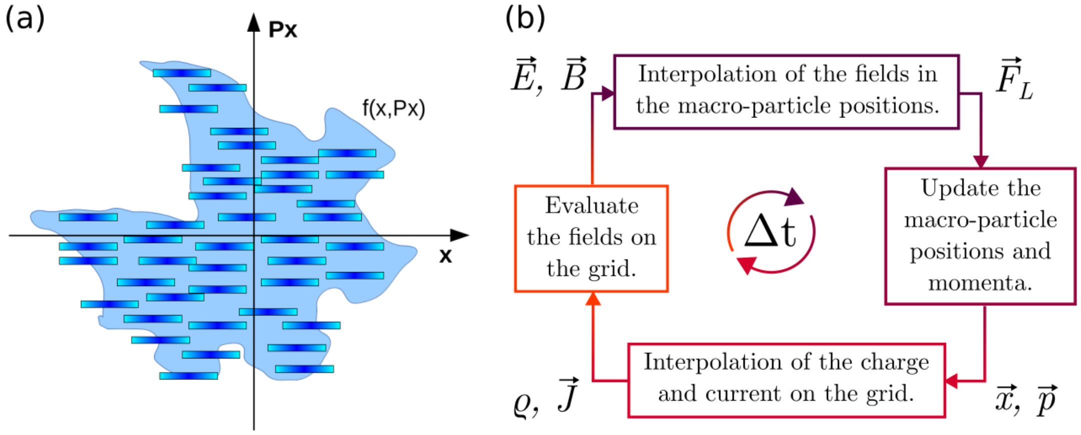
(a)
Px
f(x,Px)
x
(b)
$\vec{E}$, $\vec{B}$
Interpolation of the fields in the macro-particle positions.
$\vec{F}_L$
Update the macro-particle positions and momenta.
$\vec{x}$, $\vec{p}$
Interpolation of the charge and current on the grid.
ϱ, $\vec{J}$
Evaluate the fields on the grid.
Δt

Figure 3.8: *(**a**) Sampling of the plasma distribution function with macro-particles in the x-component of the phase space. From [197]. (**b**) Scheme of the Particle-In-Cell loop.*

size $2\Delta x$ in 1D, which can be easily projected to the 3D case. On the other hand, the macro-particles have defined momenta. This representation of the phase space distribution function is reported in figure 3.8.a.

The PIC simulation steps are summarized schematically in the flowchart of figure 3.8.b. The values of the electromagnetic field are interpolated in correspondence with all the macro-particle positions. The relativistic equation of motion is integrated for all macro-particles to advance their positions and momenta in time. Then, the charge densities and currents are evaluated on the grid nodes from the updated particle positions and momenta. Lastly, the fields are evaluated on the grid nodes solving the Maxwell equations. The cycle restarts with the field interpolation at the macro-particle positions.

The *Boris pusher* algorithm is exploited to advance the macro-particle positions. The evaluation of the current on the grid nodes can be done following two different strategies [198]: an energy-conserving algorithm and a charge-conserving algorithm (i.e. *Esirkepov* current deposition). The first strategy allows exact conservation of the energy at expense of the correct charge conservation. On the other hand, the charge-conserving algorithm ensures exact conservation of the total charge at expense of the energy. The Esirkepov strategy is more expensive from the computational point of view.

A really common Maxwell solver exploited in PIC codes is the second-order FDTD solver on a yee-lattice [199]. It is based on a spatial discretization on a staggered grid [200] and on a leap-frog scheme in time. The FDTD solver requires that the so-called *Courant condition* is satisfied to guarantee numerical stability:

$$\Delta t < \left[c\sqrt{\frac{1}{(\Delta x)^2} + \frac{1}{(\Delta y)^2} + \frac{1}{(\Delta z)^2}} \right]^{-1} \tag{3.4}$$

where Δt is the time step. The quantities Δx, Δy, and Δz are the grid spacing in the three directions.

In this work, the *piccante* [100] and *WarpX* [201] PIC codes have been used. They are open-source, massively parallel, fully relativistic codes that allow performing 3D simulations of laser-plasma interaction.

3.4 Monte Carlo method

Monte Carlo is a stochastic method for the simulation of real-world phenomena via random sampling. It is successfully applied in mathematics, physics, biology, finance and business. All problems that require the adoption of a Monte Carlo approach are characterized by a high degree of complexity. The idea behind this method is to consider a complex phenomenon as the result of simpler events for which the probability distribution functions are known.

For instance, in the case of radiation interaction with matter, particles can undergo many different processes. Each process is characterized by its probability. if the process takes place, the energy and trajectory of the particle will be affected by the current state and the physics of the process. Therefore, the *history* of a particle can be described as a series of *events* whose statistical behaviour is assumed to be known a priori. To this aim, pseudo-random number generator and sampling methods from statistical distributions are required.

The Monte Carlo approach never provides an exact solution, and it requires simulating a sufficiently high number of events to reduce the statistical uncertainty to an acceptable degree. Again, for particle transport, the final result consists of the superposition of the last states of many simulated particles. The fundamental hypothesis is that the interaction between the simulated particles is negligible.

In this PhD work, Monte Carlo is used to simulate the PIXE, EDX and PAA techniques exploiting laser-driven sources. To this aim, several codes are available [202–205]. Since the analytical methods under study involve different processes (see Chapter 1), a specific Monte Carlo must be selected accordingly to the reliability of the implemented physical models. Specifically, the Geant4 toolkit is adopted to simulate PIXE and EDX because of the accuracy of the ionization cross sections. On the other hand, the Fluka code is exploited to study PAA. As will be shown, the photonuclear reaction cross sections are better described compared to Geant4.

3.4.1 Geant4

Geant4 (Geometry and Tracking) [204, 206, 207] is an open-source C++ abstract-based class simulation toolkit for particle transport through matter. Released for the first time in 1998, it allows simulating the interaction of ions, electrons and photons with materials and the generation of secondary particles covering a wide range of energy (i.e. from eV to several PeV). Geant4 is the first Monte Carlo code exploiting object-oriented programming. Based on this paradigm, the toolkit provides a large variety of abstract classes and related methods for the definition of the main aspects of the simulation (i.e. the geometry and physics). The programmer constructs his code by creating the concrete classes that inherit all properties and methods of the abstract classes. The concrete classes can be modified by the user accordingly to the specific needs and, finally, the objects are instantiated.

Among the various abstract classes, three of them are mandatory classes that must be instantiated by the user (i.e. *user classes*) to build a working simulation.

1. The *G4VUserDetectorConstruction* class is used to set the geometry of the simulation and define the materials associated with each volume. Volumes can be defined with several shapes to build very complex geometries. The materials can

be selected from a list containing the elements and isotopic compositions present in the NIST database. Pure elements, compounds and mixtures can also be defined from scratch. Last, specific methods are available to create electromagnetic fields in different regions of the setup.

2. The *G4VUserPhysicsList* class allows registering all the particles and physical processes involved in the simulation. Some examples of physical processes are presented in the following. Different models are available to describe the same process, and they must be selected accordingly to the energy range of validity and the required degree of accuracy. Several pre-packaged physics lists are already within the Geant4 toolkit, and they include a large variety of processes. They are specific for applications like high-energy physics (e.g. *FTFP_BERT*) and medical applications (e.g. *QGSP_BIC_HP*). Moreover, Geant4 allows the user to build his physics list by adding the required processes.

3. The *G4VUserPrimaryGeneratorAction* class must be used to define the initial state of each particle during the simulation. Specifically, the type, position, direction and energy of the particles are required. They can also be extracted from complex distribution functions whenever a new primary particle is generated. Therefore, complex radiation fields can be simulated, as in the case of laser-driven electrons and ions.

A Geant4 simulation is conceptually divided into various levels. As an analogy with a real experiment, the *run* starts and ends with the first and last simulated particle, respectively. A run is composed of *events* containing primary particles. At the beginning of each event, primary particles are pushed into a *stack*, and the processing starts. When the *stack* is empty, the particles have been processed, and the event is finished. The *track* is a snapshot of the state of a particle (e.g. its energy and position). The particle travels within the geometry with a series of *steps*. The step contains transient information about the state of a particle (e.g. energy loss and time-of-flight). The information stored in the track is updated at every step.
In addition to the previously mentioned mandatory user classes, Geant4 also provides five optional user classes. They are not strictly required to build a simulation. However, they are needed to retrieve the data. The *G4UserRunAction*, *G4UserEventAction*, *G4UserTrackingAction* and *G4UserSteppingAction* classes are used to access and store information at the various levels of the simulation. The *G4UserStackingAction* allows the user to alter the priority of particles (primary and secondary) based on their properties.

Physical processes

For the aims of this work, several physical processes must be taken into account. As far as PIXE and EDX are concerned, the simulations involve the slowdown of the primary protons and electrons in the matter and the production of secondary radiation (i.e. photons, electrons and positrons) via electromagnetic processes. The secondary charged particles are tracked considering bremsstrahlung emission, ionization, multiple

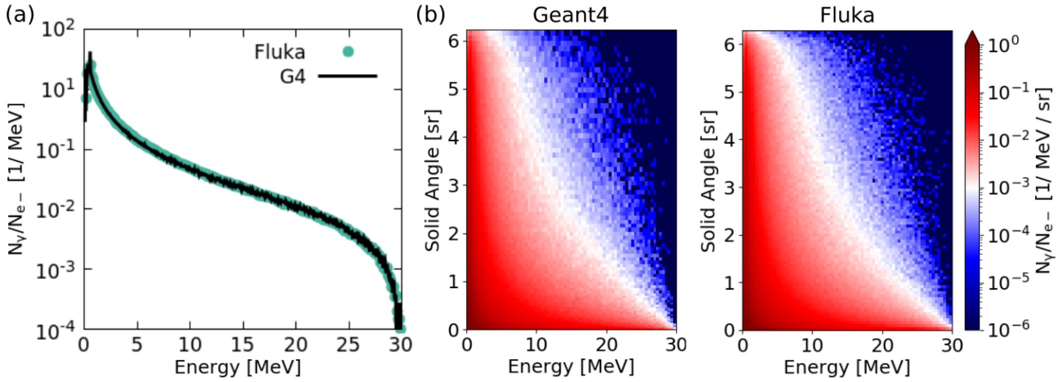

Figure 3.9: *Comparison between Geant4 and Fluka simulations of bremsstrahlung photon production from 30 MeV energy electrons interacting with a 3 mm thick tungsten plate. (**a**) Photon energy spectra. (**b**) Energy vs solid angle distribution for the photons emitted in the forward direction.*

scattering and Auger electron emission. The main processes considered, involving photons as secondary radiation, are the photoelectric effect, Compton scattering and pair production. All these events are activated with the *EmStandardPhysics_option3* module recommended by the Geant4 documentation for high accuracy with the electron, ion and photon tracking. Besides, the production cut for the secondary particles is set to 0.5 μm, meaning that all secondary particles with relatively low energy and whose ranges do not exceed the reported value are not created. The aim is to avoid infrared divergence and control the computing time.

Unlike other Monte Carlo codes, Geant4 allows the implementation of several cross section models for the K, L and M shells ionization by protons. The related libraries have also been extensively validated [208–211]. The cross section model exploited in this work for PIXE is the Energy-Loss Coulomb-Repulsion Perturbation-Stationary-State Relativistic Theory (ECPSSR).

Considering EDX simulations, the low-energy models for electrons, positrons and photons from the PENELOPE Monte Carlo code (PENetration and Energy LOss of Positrons and Electrons) are particularly suitable [212]. Their energy range of validity is between 100 eV and 1 GeV. They are activated with the *G4EmPenelopePhysics* module.

A PAA Monte Carlo simulation should account for the bremsstrahlung production of photons, the occurrence of photonuclear reactions, the decay of the activated nuclei and subsequent emission of characteristic γ-rays. The electron bremsstrahlung in high-Z materials is well-described in Geant4 by the *EmStandardPhysics_option3* physics list. For instance, consider the interaction of 30 MeV energy electrons with a 3 mm thick W converter. As shown in figure 3.9, the photon energy spectrum and angular distribution simulated with Geant4 agree with those obtained exploiting other Monte Carlo codes (i.e. Fluka). On the other hand, Geant4 photonuclear interaction cross sections, which are tabulated in the *G4PhotoNuclearCrossSection* class, are approximated for all nuclei and all energies [213]. Therefore, as shown in the following Section, Fluka is a better choice to perform PAA simulations [214].

3.4.2 Fluka

Fluka [203] is a closed-source Monte Carlo code written in the Fortran 77 language for particle transport and interaction with matter. It allows performing the propagation of about 60 different particles from keV up to hundreds TeV of energy. Fluka is characterized by a high degree of accuracy of the implemented physical models. Microscopic models are adopted whenever available, and the use of integral data is avoided. Thus, the correlation between different interactions and shower products is maintained at best.

While Geant4 provides a toolkit of classes and the source code of the simulation is written by the user, Fluka only requires an input ASCII file in which all the simulation parameters must be defined. The file contains a sequence of option lines (the so-called *cards*), sometimes followed by data cards containing specific options. They are used to define the primary particles, geometry and detectors. Concerning the physical processes, they are already implemented in the Fluka code. The user can only override the default settings with specific commands. The main options exploited to perform the simulations presented in this work are listed below.

1. The *BEAM* and *BEAMPOS* cards are used to define the primary particle type, energy, propagation direction and position of the source. When the primary particles are not monoenergetic, a user-defined routine (*source.f*) coupled with the *SOURCE* card is exploited to extract the energy from a distribution. Eventually, the irradiation conditions (i.e. time duration and current of primary particles) are set with the *IRRPROFILE* card.

2. The geometry definition starts with the *GEOBEGIN* card and finishes with the *GEOEND* card. Fluka exploits a combinatorial geometry meaning that simple convex shapes (e.g. spheres and cones) are combined to construct more complex regions via boolean operators (i.e. union, intersection and subtraction). Materials are defined with the *MATERIAL* and *COMPOUND* cards, and they are assigned to the various regions with the *ASSIGNMA* card.

3. The *PHOTONUC* card is activated to switch on the photonuclear reactions. The subsequent radioactive decay is implemented with the *RADDECAY* card. Moreover, the *PHYSICS* card with the *EVAPORAT* option is activated. It enables to describe the decay with the evaporation model, also considering heavy fragment evaporation. The mean free path of photons within the sample is reduced by a factor of 10^{-3} using the *LAMBIAS* card to enhance the statistical accuracy.

4. Detectors for scoring particles (i.e. electrons and γ-ray) crossing the boundary between volumes are defined with the *USRBDX* card. The *DCYTIMES* card is used to define the decay times for radioactive product scoring. They are associated with the detectors through the *DCYSCORE* card. Lastly, the number of activated nuclides in a material can be retrieved with the *RESNUCLE* card.

Fluka photonuclear cross sections and comparison with Geant4

While for the PIXE and EDX simulations the adopted Monte Carlo code is Geant4 because of the accuracy of the ionization cross sections, the choice of Fluka for the PAA simulation is guided by the reliability of the giant photonuclear cross sections [215].

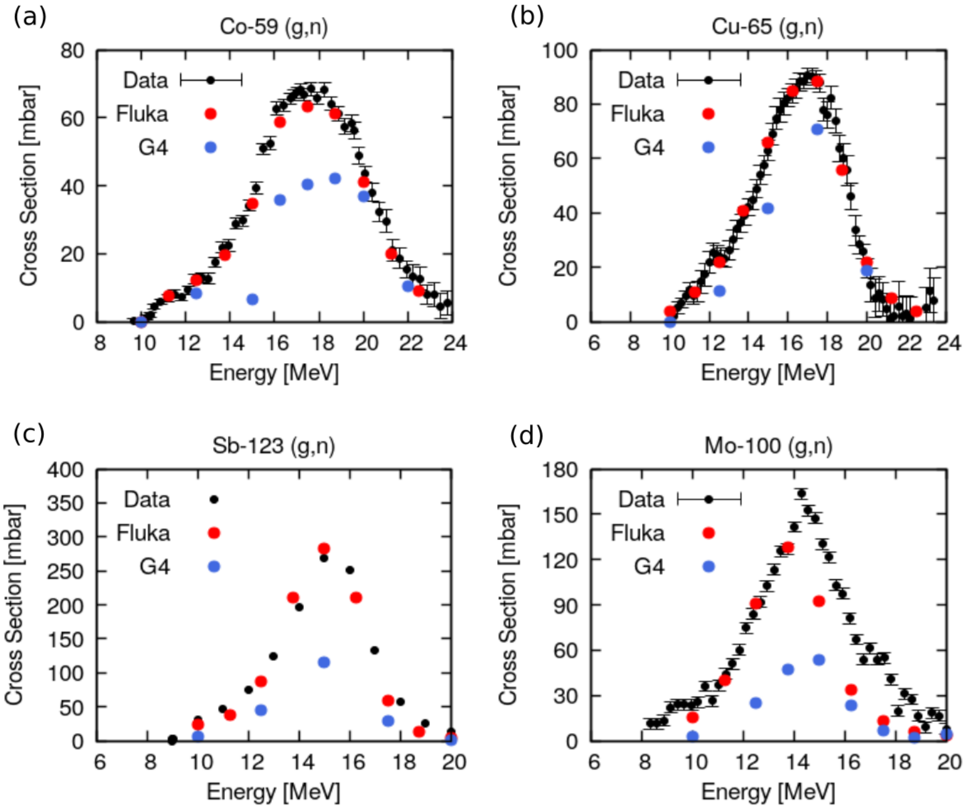

Figure 3.10: *Comparison between photonuclear reaction cross sections from the literature [216–218] and TENDL database [219] (black points) and simulated with Fluka (red points) and Geant4 (blue points) for the (**a**) Co-59, (**b**) Cu-65, (**c**) Sb-123 and (**d**) Mo-100 isotopes.*

The cross sections for several (γ, n) reactions at various photon energies have been retrieved for Fluka and Geant4. It was done with Monte Carlo simulations involving the irradiation of mono-elemental samples with pencil beams of monoenergetic photons. Assuming a sample sufficiently thin (i.e. 0.1 mm), the magnitude of the cross section σ_{ph} at specific photon energy is evaluated from the number of activated nuclides as:

$$\sigma_{ph} = \frac{N}{t\rho N_{av}} M_a \tag{3.5}$$

where N is the concentration of activated nuclides, t is the sample thickness, ρ is the sample density, N_{av} is the Avogadro's number and M_a is the atomic mass concentration. It is worth mentioning that equation 3.5 is valid only if the attenuation of the photon beam within the sample is negligible.

Many cross section values considering four photonuclear reactions in the giant dipole resonance energy region have been simulated with both codes. They are compared with experimental data available in literature in figure 3.10. The results shows that the accuracy of Fluka is superior to that of Geant4.

Part II

Production of solid targets for TNSA via Magnetron Sputtering

CHAPTER 4

DCMS and HiPIMS deposition of titanium (Ti) films and characterization

As discussed in Section 2.3.1, both sub-micrometric bare targets and DLTs are used for laser-driven particle acceleration. Solid foils having 100s nm thickness allow enhancing the energy of the accelerated ions compared to thicker (i.e. micrometric) targets. Moreover, additional improvement can be achieved by exploiting DLTs (see Section 2.3.2). However, to increase the shot-to-shot stability of the particle source, the local thickness uncertainty (i.e. up to $\pm$ 100s nm of tolerance) affecting rolled commercial sub-micrometric foils must be significantly reduced. To this aim, a new method for the production of metallic sheets is required, considering a suitable deposition technique.

The Magnetron Sputtering is the ideal choice because it allows depositing compact films in the considered thickness range with high planarity and on large areas. As extensively shown in Section 3.2, another advantage of this technique consists in the possibility of acting on a large number of deposition parameters. Consequently, films with very different morphological and structural properties can be obtained and adapted to the target requirements. However, considering Ti as deposition material, there is a non-negligible lack of knowledge in literature about the HiPIMS deposition of Ti films. Accordingly, this Chapter deals with the production and characterization of Ti coatings exploiting the DCMS and HiPIMS deposition techniques. The goal is to address the role of the ionized species, which are dominant in HiPIMS depositions, in determining the phase composition, morphology and state of stress of the films.

In Section 4.1, the deposition conditions and the procedure applied for the DCMS and HiPIMS plasma characterization are described. The microstructure, morphology and stress analyses are presented in Section 4.2. Last, Section 4.3 provides the interpretation of the results focusing on the phase composition and stress behaviour in the deposited films.

4.1 Experimental configuration and plasma characterization

The purpose of this Section is to characterize the plasma composition during DCMS and HiPIMS Ti depositions. The films were grown exploiting the Magnetron Sputtering system presented in Section 3.2.3. The Ti target (99.995% purity) has a circular shape with a diameter of 7.6 cm. The base pressure reached before the injection of the working gas was equal to $5 \cdot 10^{-4}$ Pa. During the deposition, the chamber was filled with Ar (99.999% purity) at a pressure of 0.5 Pa through continuous gas injection equal to 80 sccm.

During the HiPIMS depositions, the pulse duration, frequency and duty cycle were set equal to 50 μs, 350 Hz and 1.75%, respectively. Initially, the pulse voltage V_d was varied between 460 and 750 V. The goal was to investigate the role of this parameter in determining the plasma composition. The waveforms of both V_d and ion current at the target I during HiPIMS depositions were monitored with a Rigol DS4034 oscilloscope. As reported in figure 4.1.a, they have the typical rectangular and triangular shapes.

The peak discharge current at the target I_p (i.e. the maximum value reached by I during the discharge) as a function of V_d is shown in figure 4.1.b. As discussed in Section 3.2.3, the $I_p - V_d$ characteristic curve can be divided into four distinct regions, representative of different plasma regimes. Clearly, under the present experimental conditions (i.e. duty cycle and gas pressure), the applied voltage must be higher than $\sim$ 500 V to trigger a highly ionized HiPIMS discharge. As far as DCMS depositions are concerned, the voltage was kept within 300 V and 600 V to have average powers analogous to those provided during the HiPIMS depositions.

The plasma composition under both HiPIMS and DCMS conditions was characterized with Optical Emission Spectroscopy (OES) measurements in the $350 - 865$ nm wavelength range. In figure 4.2.a, the spectra recorded in HiPIMS and DCMS regimes at the same average power of ~ 450 W are shown. Two distinct subregions are present. In the first one (from 365 nm to 550 nm), most lines belong to neutral and ionized Ti

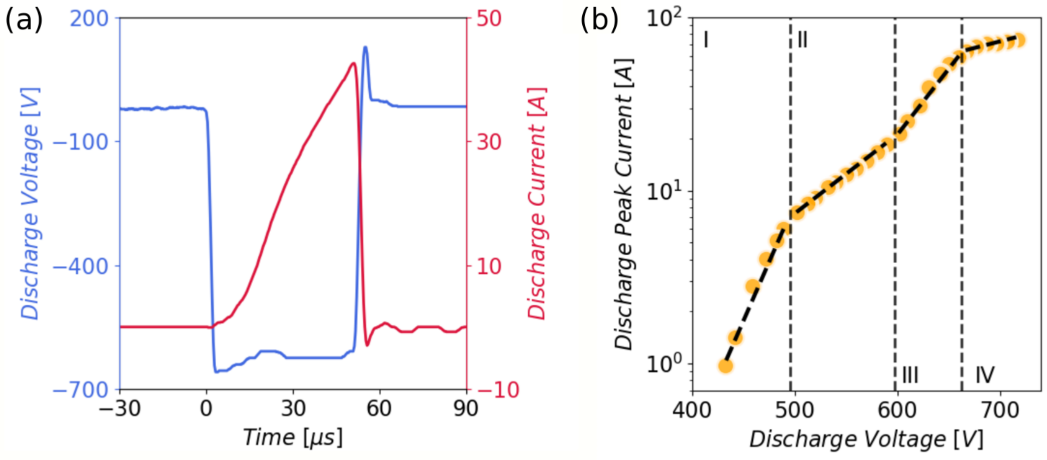

Figure 4.1: *(**a**) HiPIMS voltage and current waveforms measured at 0.5 Pa Ar pressure, 650 V applied voltage and 50 μs pulse duration. (**b**) Discharge peak current as a function of the discharge voltage at 0.5 Pa Ar pressure and 50 μs pulse duration. The vertical dashed lines delimit the four regions characterized by different plasma conditions.*

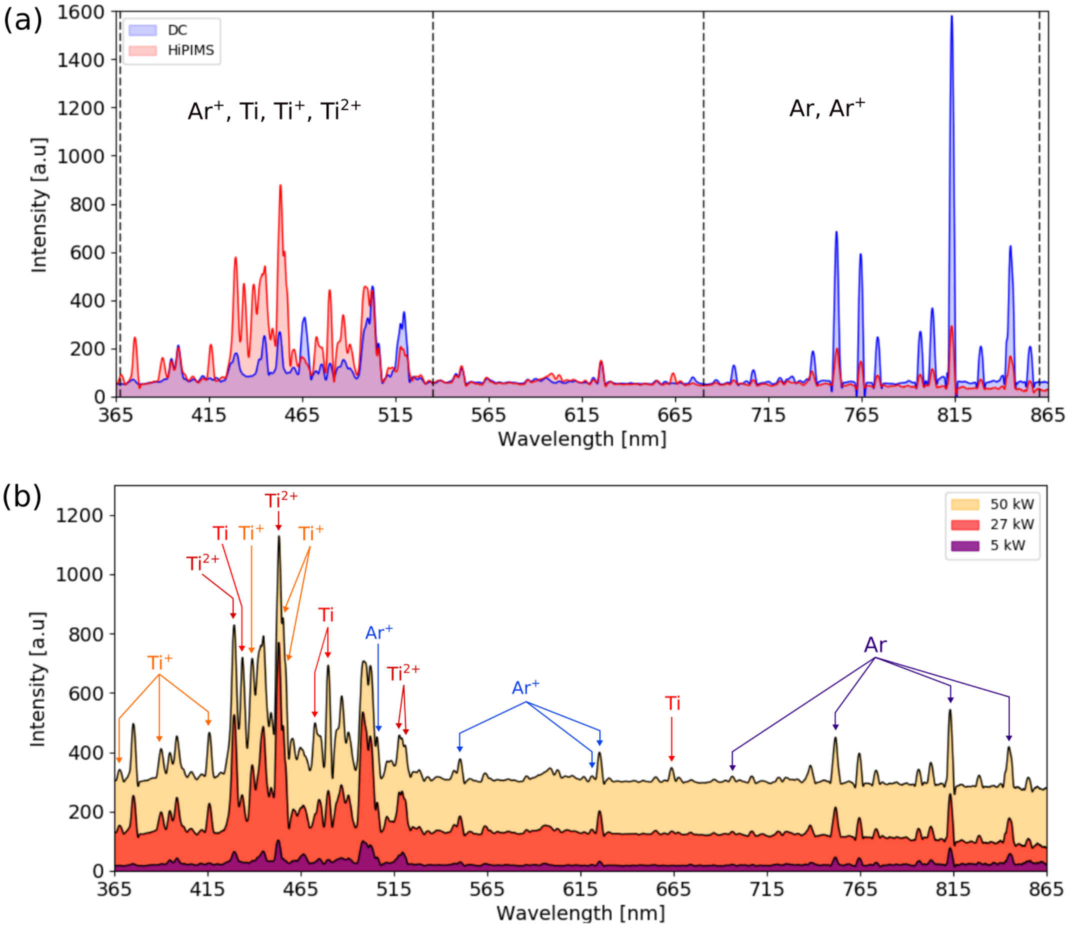

Figure 4.2: *(**a**) Optical emission spectra acquired in DCMS (blue) and HiPIMS (red) regimes at the same power of 450 W. The regions associated with Ti and Ar species are delimited with vertical dashed lines. (**b**) Optical emission spectra acquired in HiPIMS for 5 kW (purple), 27 kW (red) and 50 kW (yellow) peak powers. Peaks associated with the various species are pointed with arrows.*

atoms. On the other hand, the second subregion (from 680 nm to 865 nm) shows lines associated only with Ar species. Remarkably, the signals in the HiPIMS spectrum are mainly related to the Ti species, while the DCMS spectrum is dominated by peaks ascribable to Ar. These results are coherent with already published data [220].

As far as the HiPIMS plasma is concerned, the role of the applied voltage in determining the ionization fraction of the sputtered species must be clarified. To this aim, the peak power, defined as $P_{peak} = I_p \cdot V_d$, is worthy of consideration since it is strongly connected to the ions to atoms ratio [221, 222]. Accordingly, several OES measurements of the HiPIMS plasma were carried out at different P_{peak} values ranging from 5 kW to 50 kW. The investigated P_{peak} range coincides with the voltage interval considered in figure 4.1.b. Three OES spectra for P_{peak} values equal to 5, 27 and 50 kW are reported in figure 4.2.b. Overall, increasing the peak power, the peak intensities rise as a consequence of the higher plasma density.

Further insight can be achieved by observing how the intensity of specific peaks associated with different species varies as a function of P_{peak}. However, it is necessary to safely assign a certain number of peaks to each species (i.e. the arrows present over the peaks in figure 4.2.b). The association is not trivial since, according to the NIST database [223], the spectral signals belonging to Ti, Ti$^+$, Ti^{2+}, Ar and Ar$^+$ are very close, and many of them can lie within the wavelength interval subtended by one of the peaks in figure 4.2. Therefore, to identify the peaks belonging to a certain species, the procedure presented in the following Section was developed.

4.1.1 Optical Emission Spectroscopy analysis

A total number of spectra $n_p = 9$ at different P_{peak} values (identified by the i-index) was considered. For each P_{peak} value, local portions of the associated OES spectrum were fitted with the Levenberg-Marquardt least-square algorithm [224]. The fit was done assuming a Gaussian shape for the peaks and a linear function for the local background. The area subtended by the Gaussian function corresponds to the intensity $I_{i,j}$, where the j-index identifies a specific peak. Then, the following normalized peak intensity $\tilde{I}_{i,j}$ was evaluated for all the fitted peaks:

$$\tilde{I}_{i,j} = \frac{I_{i,j}}{\sum_{i=1}^{n_p} I_{i,j}} \tag{4.1}$$

Peaks associated with the same species will exhibit the same trend for $\tilde{I}_{i,j}$ as a function of P_{peak}. This criterion was applied to identify signals belonging to the same species. In figure 4.3, $\tilde{I}_{i,j}$ is plotted against P_{peak}, having already grouped peaks belonging to the same species. As expected, five distinct trends can be observed. Notice that the values of $\tilde{I}_{i,j}$, and therefore the density of the species, continuously increase with P_{peak}.

The identified emission lines are listed in table 4.1, and they are pointed with arrows in figure 4.2.b. It is worth mentioning that the reported results have been cross-checked with the data present in the NIST database. Notice that few peaks in figure 4.2.b are not indexed. For those signals, the procedure presented here did not allow performing safe discrimination. Indeed, superpositions between different lines can be present. In this respect, an improvement could be achieved using a detector with a higher energy resolution compared to that exploited in this work.

Once the intensities of several peaks, as well as the species to which they belong, have been retrieved, the next step consists of the evaluation of the ionization fraction for the

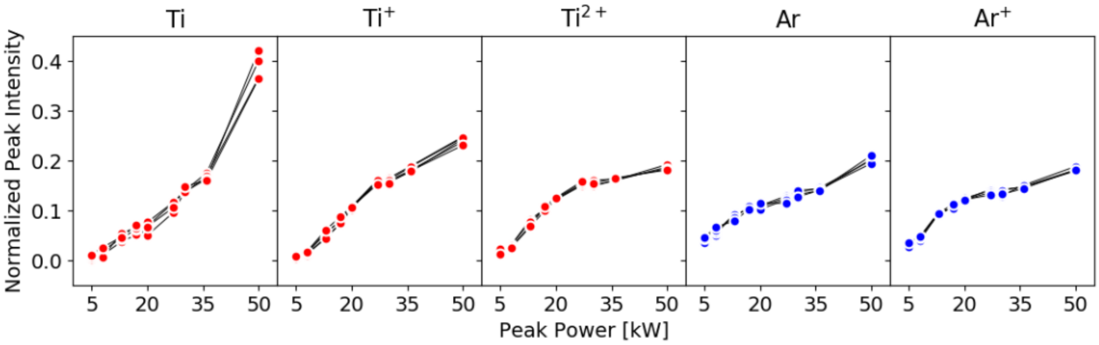

Figure 4.3: *Normalized OES peak intensity as a function of the peak power for Ti, Ti^+, Ti^{2+}, Ar and Ar^+ species.*

Table 4.1: *Wavelength λ and excitation energy E of the identified spectral lines for Ti, Ti^+, Ti^{2+}, Ar and Ar^+ species.*

Ti		Ti$^+$		Ti^{2+}		Ar		Ar$^+$	
λ [nm]	E [eV]	λ [nm]	E [eV]	λ [nm]	E [eV]	λ [nm]	E [eV]	λ [nm]	E [eV]
433.8	5.0	368.0	4.95	429.3	22.6	696.5	13.3	506.1	19.3
472.5	3.7	390.1	4.3	453.4	20.8	751.6	13.3	550.4	25.1
479.8	4.91	416	4.06	517.8	18.3	813	13.1	621.2	19.3
663.9	5.19	438.9	4.05	521.1	18.3	844.8	13.1	625.9	19.7
-	-	455.7	3.91	-	-	-	-	-	-
-	-	457.1	4.28	-	-	-	-	-	-

Ti and Ar species. For each value of P_{peak}, all peaks associated with the same species are considered and the average intensity is calculated from the $\tilde{I}_{i,j}$ values. This calculation was done for all the species and peak power values.

As a final step, the ratio between the average intensities associated with different species at equal P_{peak} is performed. For instance, the ratio between the average intensities of Ti and Ti$^+$ peaks is representative of the ionization fraction of titanium atoms in the HiPIMS plasma. The same also applies to the Ar and Ar$^+$ species. These ratios as a function of P_{peak} are reported in figure 4.4. Notably, the trends are not monotonic, and they show a maximum between 20 and 30 kW. Thus, while the overall number of sputtered species monotonically grows with the peak power, the ionization fraction of sputtered species (i.e. $\mathrm{Ti}^+/\mathrm{Ti}$ and $\mathrm{Ar}^+/\mathrm{Ar}$) is highest around $20 - 30$ kW.

It is worth noting that the previous considerations are valid only if the considered

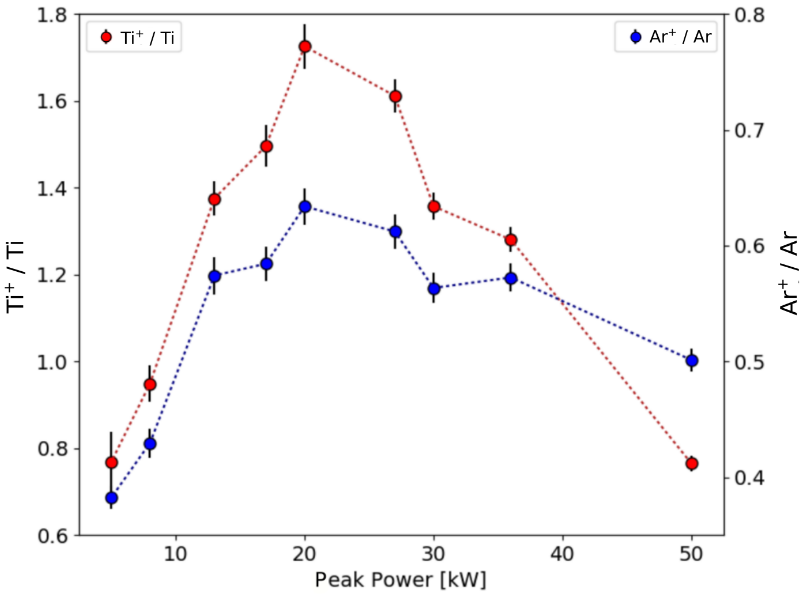

Figure 4.4: *Ratio of the average intensities for the* $\mathrm{Ti}^+/\mathrm{Ti}$ *(red points) and* $\mathrm{Ar}^+/\mathrm{Ar}$ *(blue points) as a function of the peak intensity.*

species have similar excitation energies [221, 222]. Indeed, the intensity ratio between different species depends on the excitation probabilities that are affected by the excitation energies. As reported in table 4.1, the excitation energies of the spectral lines associated with the Ti and Ti^{+} species are very close. Also, in the case of the Ar species, the excitation energies are similar, at least of the same order of magnitude. On the other hand, the Ti^{2+} species must be excluded from this analysis because their excitation energies are too high compared to those of Ti and Ti^{+} species.

4.2 Ti films characterization

This Chapter aims at characterizing Ti films deposited in both low and high ionization fraction environments exploiting the DCMS and HiPIMS techniques, respectively. As shown in the previous Section, the ions contribution compared to that of the neutral atoms during the HiPIMS depositions is maximum for P_{peak} around $20-30$ kW. Therefore, the HiPIMS depositions performed in the remaining part of this work were carried out by fixing the peak power value at 27 kW (i.e. around the maximum of the curve shown in figure 4.4). It is worth remembering that the DCMS depositions have been performed at the same average power as the HiPIMS ones.

Three values of bias voltage (i.e. $U_s =$ 0, 300 and 500 V) were applied to the substrate during HiPIMS depositions. The goal was to investigate different energy regimes of the deposited ions. Note that, even with $U_s = 0$ V, the substrate was subject to a floating potential between -10 V and -15 V because of the plasma sheath. Morphology, phase composition and stress state of the Ti films were characterized for thicknesses ranging from ~ 70 nm up to ~ 600 nm.

Both for HiPIMS and DCMS, the depositions lasted between 15 and 180 minutes. The films were deposited on 300 μm and 500 μm thick (100) silicon (Si) wafers cleaned with isopropanol and blown dry with nitrogen before the deposition. The substrate lateral dimensions were approximately 2×2 cm. The substrate holder was kept at $20-24°\mathrm{C}$, and no intentional heating of the Si substrate was applied.

4.2.1 Morphological characterization

The morphology of the films was investigated using a Zeiss Supra 40 field emission Scanning Electron Microscope (SEM) system, operated at an accelerating voltage of 5 kV. As shown in figure 4.5, Ti-DCMS and Ti-HiPIMS films exhibit different morphologies depending on the adopted deposition technique, energy regime and thickness.

Ti-DCMS films (see figure 4.5.a) are characterized by a columnar morphology with a pyramidal shape superficial pattern. This structure corresponds to the first zone in the Thornton diagram presented in Section 3.2.3 and extended for energetic depositions. Figure 4.5.b shows the morphology of Ti-HiPIMS films deposited at bias voltage equal to 0 V. All films exhibit a compact granular structure. The grain size increases with the film thickness up to a constant value of $\sim$ 50 nm. Ti-HiPIMS films grown with the application of 300 V and 500 V bias are reported in figures 4.5.c and 4.5.d, respectively. For thicknesses higher than $\sim$ 100 nm, elongated lamellar grains are formed. Their number and dimension increase with the film thickness. Besides, a higher value of the bias voltage seems to anticipate the onset of this structure.

The thicknesses of the films were evaluated using SEM cross-section images. They

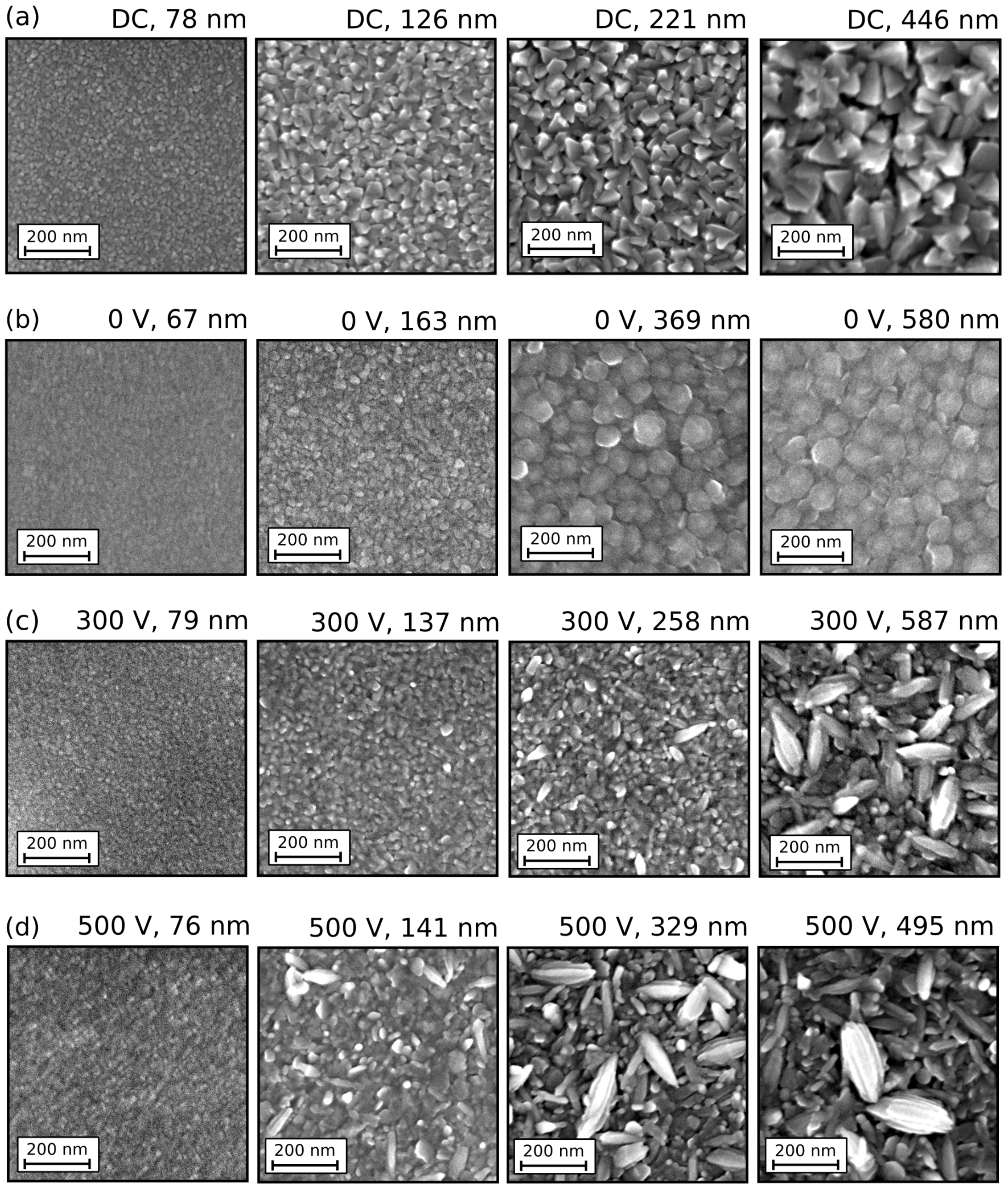
(a)
DC, 78 nm
DC, 126 nm
DC, 221 nm
DC, 446 nm
(b)
0 V, 67 nm
0 V, 163 nm
0 V, 369 nm
0 V, 580 nm
(c)
300 V, 79 nm
300 V, 137 nm
300 V, 258 nm
300 V, 587 nm
(d)
500 V, 76 nm
500 V, 141 nm
500 V, 329 nm
500 V, 495 nm
200 nm

Figure 4.5: *SEM top-views of (**a**) Ti-DCMS films, Ti-HiPIMS films deposited (**b**) without the application of the bias voltage, with the application of (**c**) 300 V and (**d**) 500 V bias. The film thickness is reported on the top of each panel.*

were measured in $4-5$ different sample points, and the average value was determined. The uncertainty was always within $\pm 10\%$ of the absolute thickness. The cross section views for the thickest films deposited under the four different deposition conditions are reported in figure 4.6. Comparing the Ti-DCMS and Ti-HiPIMS films, it is clear that the action of the higher fraction of ionized species leads to a more compact morphology. Considering only Ti-HiPIMS films, a progressive increment of the energy causes

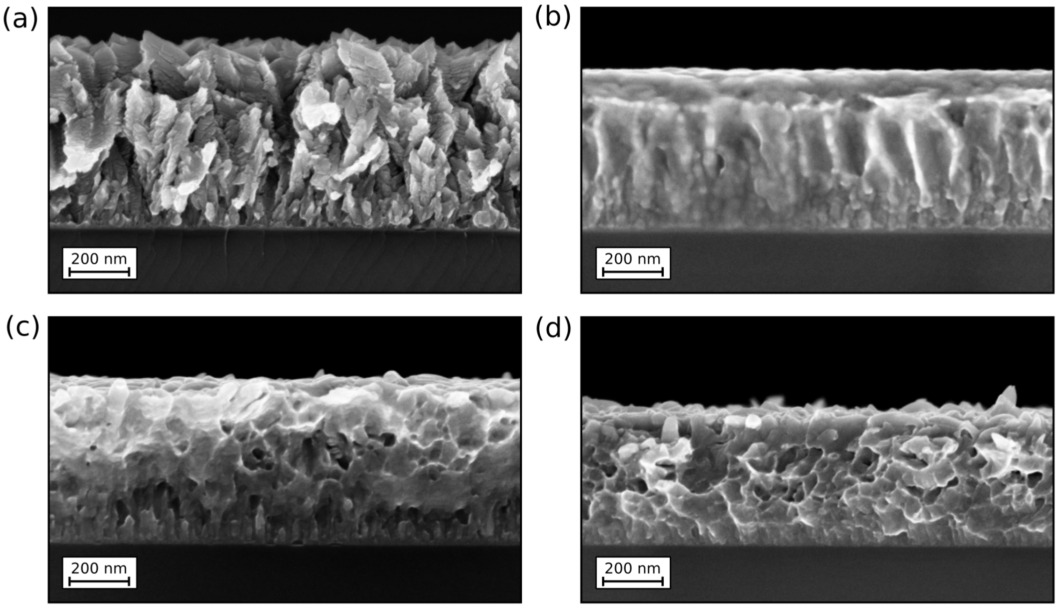

Figure 4.6: *SEM cross section views of (**a**) 658 nm thick Ti-DCMS film, (**b**) 580 nm thick Ti-HiPIMS film deposited without the application of the bias voltage, (**c**) 587 nm thick Ti-HiPIMS film deposited with 300 V bias and (**d**) 495 nm thick Ti-HiPIMS film deposited with 500 V bias.*

the formation of voids due to the growth of the randomly oriented lamellar structures. The formation of these peculiar submicrometric grains was never observed in the literature. As reported in figure 4.7.a, these structures completely cover the film. They protrude from the surface of approximately $\sim 50 - 100$ nm. A magnification of three grains is also shown in figure 4.7.b. They are composed of aligned structures.

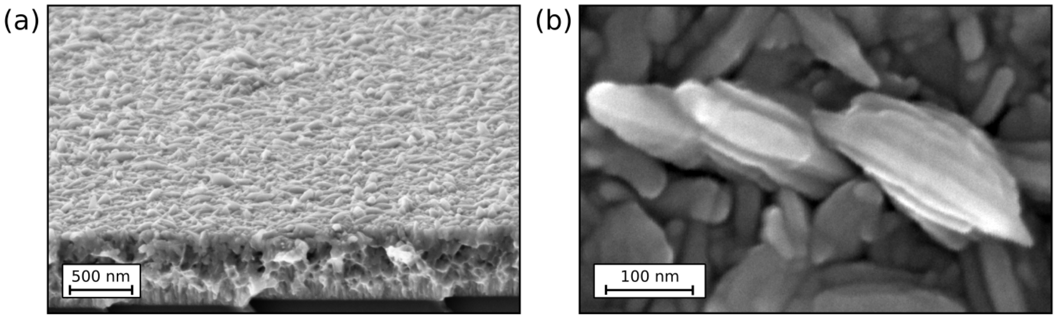

Figure 4.7: *(**a**) Cross section view tilted at $20°$ of the thickest Ti-HiPIMS film deposited with 500 V bias. (**b**) Magnification of the lamellar structures.*

4.2.2 Phase composition and crystallographic orientation

The crystalline phase evolution and crystallographic orientation of the films were assessed using X-ray Diffraction Spectroscopy (XRD) performed with a Panalytical X'Pert PRO X-ray diffractometer in $\theta/2\theta$ configuration.

The XRD spectra of the Ti-DCMS films are reported in figure 4.8.a for the thickness interval between 80 nm and 650 nm. For the thinnest film, no peaks are present in the spectrum. All the other films are characterized by peaks only related to the α phase of Ti, as already reported in other works [225–227]. For thicknesses between 100 nm and 200 nm, only the (002) reflection at $2\theta = 38.41°$ is present. The (100), (101) and (102) reflections at $2\theta = 35.07°$, $40.153°$ and $53.012°$ emerge at higher thickness.

Figure 4.8.b shows the spectra associated with the HiPIMS depositions without the application of the bias voltage. At 50 nm thickness, only one peak is present at $2\theta = 37.05°$. As reported in previous works [192, 196], this reflection corresponds to the (111) of the Ti *fcc* phase. For thicknesses greater than 100 nm, the (100) and (002) reflections of the α phase appear in the XRD spectra. The coexistence of the *fcc* and α phases maintains up to a thickness of 370 nm. For the thickest Ti sample, only the peaks associated with the α phase are present. Therefore, the complete $fcc \rightarrow \alpha$ transition occurs at a critical thickness between 370 nm and 580 nm.

The XRD spectra of Ti-HiPIMS films deposited with the application of 300 V and 500 V of bias are reported in figures 4.8.c and 4.8.d, respectively. For both deposition conditions, the spectra do not show peaks below a film thickness of $\sim$ 100 nm. For higher thicknesses, peaks associated with the α phase are present. Below 250 nm thickness,

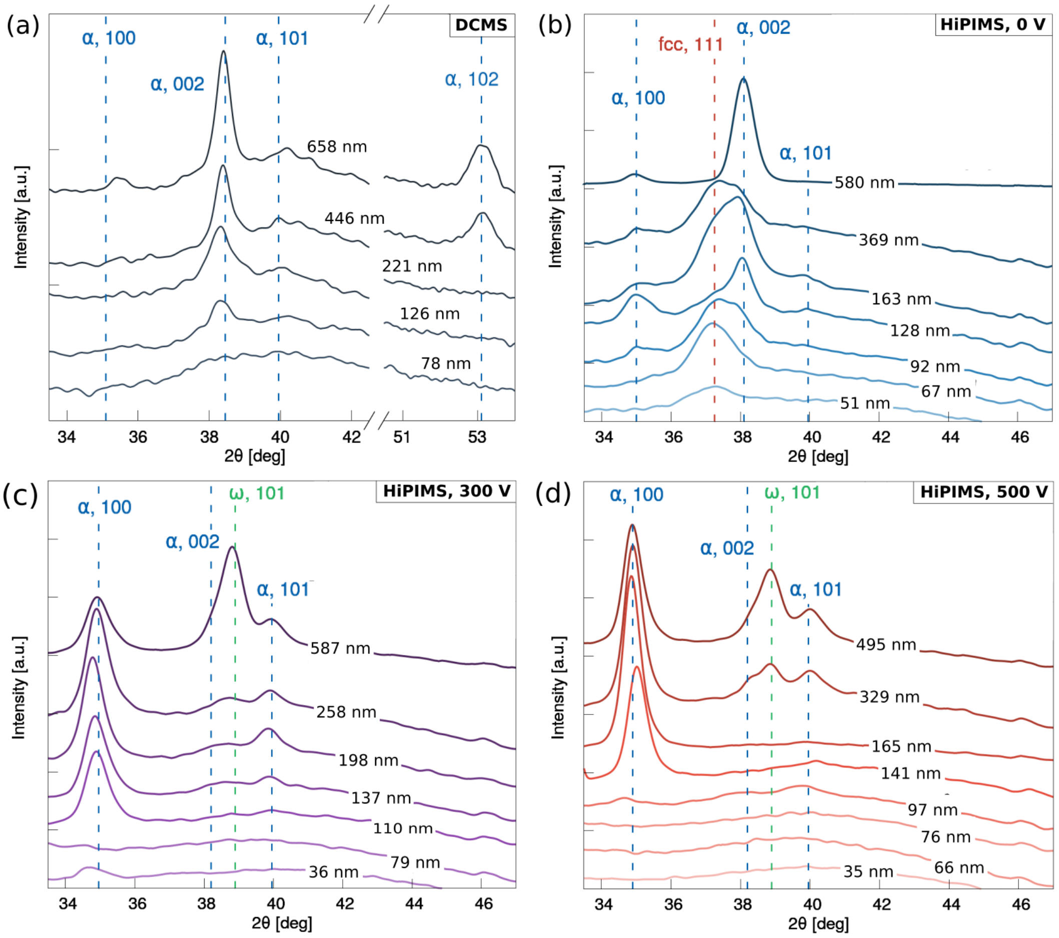

Figure 4.8: *XRD spectra of Ti films deposited in (**a**) DCMS and HiPIMS with an applied bias voltage of (**b**) 0 V, (**c**) 300 V and (**d**) 500 V. The thickness of the associated film is reported over each curve. The crystallographic orientations are marked with vertical dashed lines.*

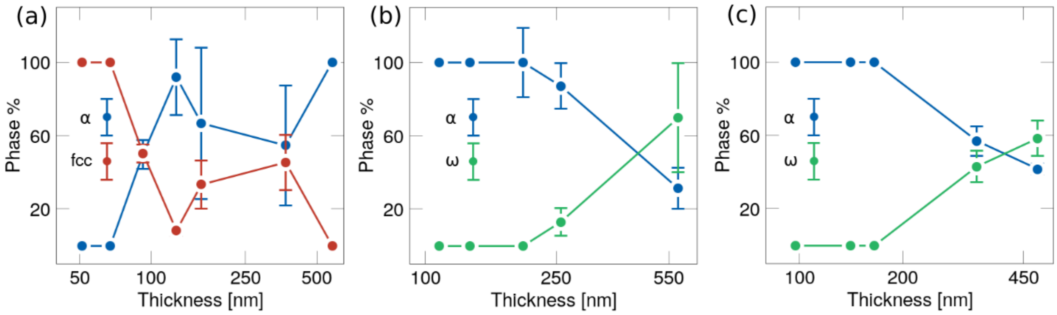

Figure 4.9: *fcc, α and ω phase concentrations as a function of the thickness in Ti-HiPIMS films deposited at (**a**) 0 V, (**b**) 300 V and (**c**) 500 V bias.*

the Ti film growth seems to be strongly oriented along the (100) orientation. Around 300 nm thickness, a new peak appears around $2\theta = 39.0°$. According to literature data [228], this peak is associated with the (101) reflection of the Ti ω phase.
The X-ray diffractograms were analyzed using the MAUD software [229] to obtain the phase fraction of *fcc*, α and ω phases. The behaviour of the phase composition as a function of the thickness is reported in figure 4.9 for the Ti-HiPIMS films deposited at different bias voltages. The analysis carried out with MAUD confirms the presence of the three phases. For 0 V of bias, the films initially contain only the *fcc* phase, while the thicker one is characterized only by the presence of the α phase. The transition starts at a thickness lower than 100 nm, and it proceeds with a non-monotonic behaviour. On the other hand, for the biased Ti-HiPIMS films, the $\alpha \rightarrow \omega$ phase transition starts around 250 nm, and the content of the ω phase monotonically increases with the film

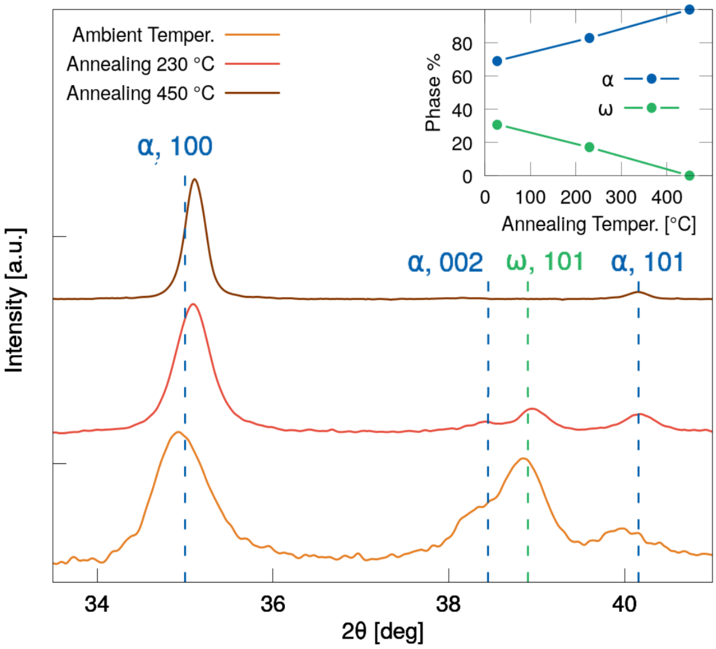

Figure 4.10: *XRD spectra of a Ti film containing ω phase before and after the vacuum annealing procedure. The inset graph shows the α and ω phase percentage as a function of the annealing temperature.*

thickness. It is worth noting that the ω phase formation is correlated to the appearance of the elongated lamellar grains shown in figure 4.7.
The temperature stability of the ω phase was assessed by vacuum annealing. Films characterized by the (101) orientation were annealed at two different temperatures of 230 °C and 450 °C. The XRD spectra associated with the annealed samples show a decrease up to the absence of the (101) peak associated with the ω phase (see figure 4.10). Coherently with already published works [181] and MAUD analysis (see the inset graph of figure 4.10), these observations correspond to a partial transformation in the α phase at 230 °C and a complete transition at 450 °C. The annealing provides further evidence of the ω phase presence in the thickest Ti-HiPIMS films grown with a bias voltage. Lastly, even if the ω phase disappears after annealing, the morphology remains unaltered, and the lamellar grains are still present.

4.2.3 Stress state evaluation

The residual stresses were evaluated using an optical implementation of the wafer curvature method. The experimental setup exploits a set of parallel laser beams to measure the curvature radius of the film-substrate system [230, 231]. The beams impinge on the uncoated substrate, and they are reflected by the surface. The reflected beams are collected by a high-frame-rate camera. The stresses are retrieved by evaluating the curvature variation of the uncoated surface of the silicon wafer before and after the film deposition. The residual stress σ_{res} is calculated with the Stoney equation [232] as:

$$\sigma_{res} = \frac{E_s}{1-\nu_s} \times \frac{t_s^2}{t_f} \times \frac{1}{6 \cdot R_c} \tag{4.2}$$

where E_s and ν_s are the Young's modulus and Poisson's ratio of the substrate, t_s and t_f are the substrate and film thicknesses, and R_c is the curvature radius of the system. It is worth pointing out that the substrate curvature method provides the average residual stresses. Even if the films can be characterized by a nonuniform stress state, the average stresses can be useful to identify trends as a function of the deposition parameters. The stresses as a function of the film thickness are reported in figure 4.11 for all the deposition conditions.
Ti-DCMS films show a tensile stress state of the order of a few GPa (see figure 4.11.a) for thicknesses lower than 200 nm. For higher thicknesses, the average stresses are close to zero. On the other hand, Ti-HiPIMS films are characterized by a completely different state of stress. At low energy of the film-forming species (i.e. 0 V bias), the initial growth stages are characterized by a stress state almost equal to zero (see figure 4.11.b). Around a thickness of 70 nm, the stresses are tensile. Then, increasing the thickness, the stresses rapidly become compressive, and they reach a value of -5 GPa around 130 nm. For higher thicknesses, a stabilization of the compressive stresses is observed around a value of -2.5 GPa.
Figures 4.11.c and 4.11.d show the stress state for the Ti-HiPIMS films deposited with bias voltage equal to 300 V and 500 V, respectively. At high Ti ion energies, the stresses start compressive (around -2 GPa and -5 GPa for 300 V and 500 V bias, respectively). They became tensile and, again, compressive increasing the thickness.

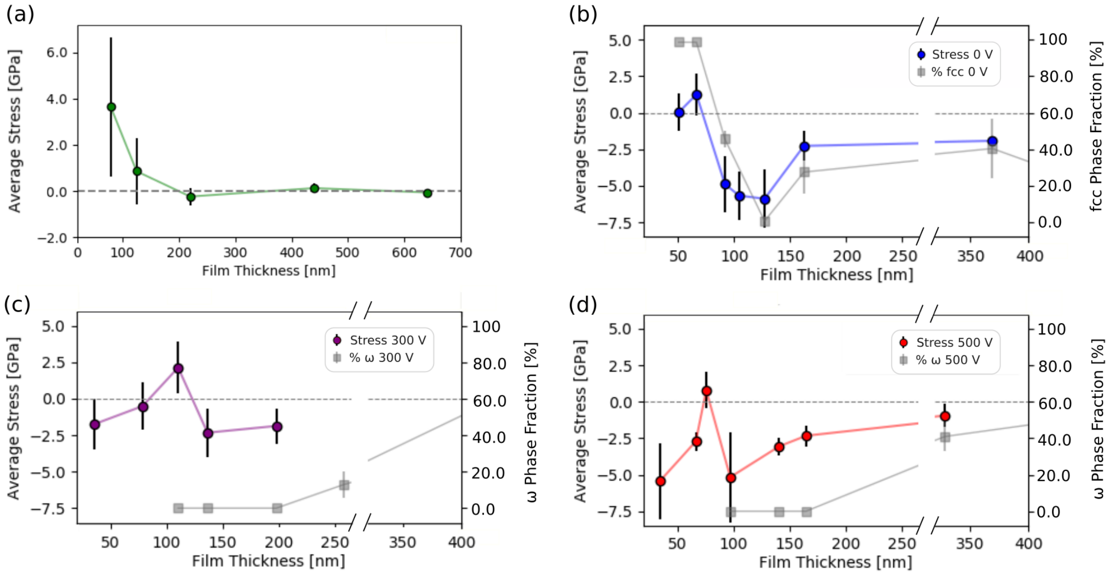

Figure 4.11: *(**a**) Average residual stresses for the Ti-DMCS films as a function of the thickness. (**b**) Average residual stresses for the Ti-HiPIMS films at 0 V of bias as a function of the thickness (blue points). The content of the fcc phase is reported as grey points. (**c**) Average residual stresses for the Ti-HiPIMS films at 300 V of bias as a function of the thickness (purple points). The content of the ω phase is reported as grey points. (**d**) Average residual stresses for the Ti-HiPIMS films at 500 V of bias as a function of the thickness (red points). The content of the ω phase is reported as grey points.*

4.3 Phase tailoring and stress behaviour in Ti films

The purpose of this Section is to discuss the conditions that lead to the formation of the crystalline phases observed with the XRD measurements, in conjunction with the observed stress state behaviour and morphology evolution. The production of unconventional phases of Ti, like the *fcc* and ω ones, could be of interest for several industrial and engineering applications. For this reason, many efforts have been made to produce these phases in the last two decades exploiting several deposition techniques (see Section 3.2.4). Moreover, suitably tailoring the Ti films phase composition can be of paramount importance even in innovative applications, as the production of engineered targets for laser-driven ion acceleration experiments, where peculiar and precise requirements on the final properties of the Ti films are demanded.

With Ti-DCMS films, the energy of the deposited species (mainly Ti and Ar neutrals) is of the order of 1-3 eV. Coherently with already published results [225–227, 233, 234], this energy regime leads to the formation of the α-phase with preferred (002) orientation because of the minimization of the surface energy [235]. The films follow a 3D Volmer-Weber growth [236], characterized by the nucleation of 3D islands on the substrate surface, subsequent growth and coalescence to form a continuous film. Depending on the mobility of the atoms, this growth mechanism is characterized by the onset of a different stress behaviour as a function of the film thickness. The fundamental parameter affecting mobility is the homologous temperature T_h (see Section 3.2.3). Usually, films deposited at $T_h < 0.2$ are characterized by low mobility of the adatoms, while $T_h > 0.2$ corresponds to the condition of high atomic mobility. For low atomic mobility, a tensile stress state develops as the islands coalesce. For the Ti-DCMS films considered in this work, T_h is equal to 0.15 by assuming the substrate at room temperature. Therefore, the observed tensile stress state is coherent with the proposed growth mechanism.

As far as Ti-HiPIMS films are concerned, in addition to the α phase, the *fcc* and ω phases are present. The nucleation of a specific phase is influenced by the energy of the particles striking the substrate, as well as by the type (i.e. ions or neutrals). Moreover, the substrate can contribute to determining the crystallographic structure during the first growth stages. Indeed, *Cemin et al.* [237, 238] showed that high energy Cu ions can cross the native Si oxide layer covering the substrate. As a result, epitaxial growth occurs onto the (100) Si substrate that leads to a change in the crystallographic orientation of Cu films from the (111) to the (002).

The penetration depth of Ti^+ ions in the native Si oxide layer was evaluated via SRIM simulations [27]. The goal is to exclude any contribution from the substrate to the *fcc* phase nucleation. The native Si oxide layer thickness can be estimated equal to $\sim 0.7 - 1.5$ nm [239]. Accordingly, two sets of simulations were performed assuming Si oxide layers of thicknesses equal to 0.7 nm and 1.5 nm on a semi-infinite Si substrate. Moreover, the third set of simulations was carried out considering a pure Ti target. The energy of the ions spans from 20 eV up to 500 eV. The results are reported in table 4.2.

Table 4.2: *Ranges of* Ti^+ *ions (from SRIM simulations) for five different initial energies travelling across Si oxide layers over semi-infinite Si substrates and in a semi-infinite Ti medium.*

Ti^+ Energy	SiO_2 (0.7 nm) + Si (inf.)	SiO_2 (1.5 nm) + Si (inf.)	Ti (inf.)
20 eV	0.8 ± 0.1 nm	0.9 ± 0.1 nm	0.5 ± 0.1 nm
30 eV	0.9 ± 0.2 nm	1.0 ± 0.2 nm	0.6 ± 0.2 nm
60 eV	1.1 ± 0.2 nm	1.2 ± 0.3 nm	0.7 ± 0.2 nm
300 eV	2.0 ± 0.7 nm	2.2 ± 0.6 nm	1.2 ± 0.6 nm
500 eV	2.5 ± 0.9 nm	2.7 ± 0.8 nm	1.6 ± 0.8 nm

For Ti^+ energies of 20 eV, the range is lower than the native Si oxide thickness. Therefore, in Ti-HiPIMS films deposited under unbiased conditions, the interaction with the underlying (100) Si crystal is negligible. On the other hand, with 300 eV and 500 eV of energies, the Ti^+ ions largely overcome the Si oxide. Thus, only in the high energy regime associated with the HiPIMS depositions with 300 V and 500 V of applied bias sputtering of the Si oxide and coupling with the Si substrate can not be excluded.

4.3.1 Low ion energy regime

While, in DCMS depositions, the film-forming species are mainly neutrals, the HiPIMS depositions are characterized by a high fraction of ionized species. In the second case, and for $U_s = 0$ V, the low energy ion flux leads to the nucleation of the *fcc* phase. As a first attempt, a pseudo-epitaxial growth involving the underlying (100) surface of the Si substrate can be claimed as a possible explanation. However, this mechanism cannot occur for the Ti-HIPIMS films with $U_s = 0$ V considered in this work. Indeed, as suggested by the SRIM simulations, the deposited species are not energetic enough to cross the Si oxide layer. Therefore, other mechanisms must be considered to explain the presence of the *fcc* phase.

In this respect, it is interesting to compare the *fcc* phase evolution with the results shown in the few works present in the literature. The first evidence of the *fcc* phase nucleation in Ti films under the effect of low energy ions and atoms via ion-beam sputtering was reported by *Yue et al.* [240]. In addition, *Fazio et al.* [192] observed the presence of the *fcc* phase in Ti films obtained with vacuum arc deposition. As for the Ti-HIPIMS films, a progressive $fcc \rightarrow \alpha$ transition increasing the thickness was observed. However, the complete transition to the α phase in their films occurs at approximately 220 nm, while Ti-HIPIMS films contain a certain amount of *fcc* phase still at 370 nm. From the thermodynamical point of view, they associate the *fcc* phase formation to the interfacial energy minimization at the film-substrate interface.

Although not present in the phase diagram, local stability of the *fcc* phase in Ti, Hf and Zr was theoretically demonstrated [241]. The total energy of the *fcc* phase is reported to be higher than that of the α and ω ones. Reasonably, the presence of an out of equilibrium condition (e.g. the growth in the form of a film), in conjunction with a suitably enhanced mobility of the impinging species, can lead to the *fcc* phase nucleation instead of the conventional, and more thermodynamic stable, α one. Further insight can be achieved by looking at the stress state associated with Ti-HiPIMS films. As shown in figure 4.11, it is different from that of Ti-DCMS films. The initial growth stages during HiPIMS depositions resemble a compressive-tensile-compressive (CTC) [237] stress behaviour. CTC is usually associated with high surface mobility metals (i.e. $T_h > 0.2$) following the Volmer-Weber growth. The growth stages are schematically reported in figure 4.12. Therefore, while Ti is a low mobility metal, it behaves like a high mobility one in the considered HiPIMS regime. This behaviour is possible if the deposition is characterized by a large flux of hyperthermal species (in the $10 - 100$ eV energy range) [194]. In this case, the migration of the adatoms at the underdense grain boundaries can be achieved. Evidently, because of the migrating adatoms contribution, the *fcc* phase nucleation is favoured compared to the α phase at low thicknesses.

Increasing the film thickness, a transition from the *fcc* to the α phase takes place. This behaviour was observed also in other literature works. *Chakraborty et al.* [196] proposed a thermodynamic explanation to address the $fcc \rightarrow \alpha$ phase transition through the bulk, surface and strain-free energy change. The increased stability of the α phase is ascribed to the bulk energy of the system, which rises with the film thickness. The predicted critical thickness for the *fcc* phase stability is 35 nm, but, as reported in the literature [192], this value depends on the deposition conditions (i.e. from few to ~ 100 nm). As far as the Ti-HiPIMS films deposited in this work are concerned, pure *fcc* phase up to a thickness of 67 nm and its coexistence with the α phase up to 370 nm are observed.

The progressive $fcc \rightarrow \alpha$ transition is strongly related to stress state behaviour. The connection is evident from figure 4.11.b where, in addition to the stresses, the *fcc* phase fraction as a function of the film thickness is reported. The high compressive stress state, observed around ~ 100 nm, can be explained as the result of several contributions. In this energy regime, adatoms mobility is possible, but it is not high. Moreover, the Ti ions implantation can result in the formation of interstitial defects. Last, the grain

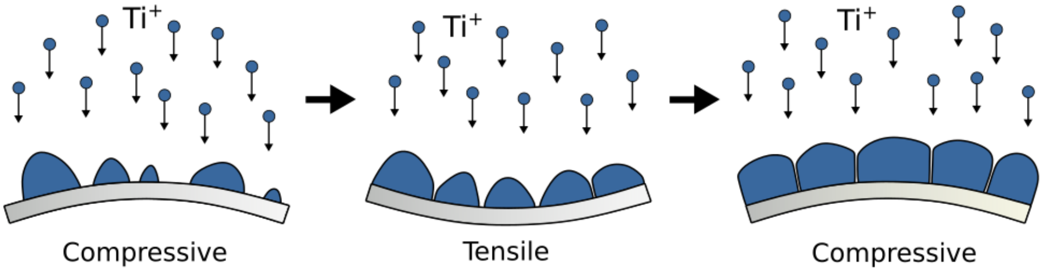

Figure 4.12: *Nucleation, coalescence and thickening of the film during Volmer-Weber growth with high surface mobility metals. Adapted from [242].*

boundary densification can further enhance the compressive stresses [194, 237]. As reported in a recent theoretical work [243], the onset of a compressive stress state leads to the formation of Schokley partial dislocations that slip the crystalline planes from the (111) orientation of the *fcc* phase to the (002) orientation of the α one. The onset of the transition is predicted at a stress value around 2.5 GPa. Remarkably, a significant reduction of the *fcc* phase in Ti-HiPIMS films starts when the stress state is close to this value.

As far as the α phase is concerned, the (002) peak for the thickest sample in figure 4.8.b is significantly shifted compared to the corresponding Ti-DCMS one in figure 4.8.a. The shift is approximately equal to $0.3°$, and it is probably due to the residual stress state.

Lastly, because of the low duty cycle of the HiPIMS regime and the relatively low energy of the impinging species, a significant increment of the growth temperature is not expected during the deposition. Therefore, it should not play a relevant role in determining the properties of the films.

To summarize, the ion field with energy in the hyperthermal range has a double effect on the growth dynamic of Ti films. During the first growth stages, it activates the adatoms mobility leading to the nucleation of the *fcc* phase. Afterwards, it induces the formation of defects resulting in the generation of strong compressive stresses. These stresses promote the transition to the α phase. It can be expected that the fine-tuning of the energy could lead to a further increment of the thickness at which the *fcc* phase is still present.

4.3.2 High ion energy regime

In the high energy regime, no phase identification is possible for a thickness lower than 100 nm. It is evident from the XRD spectra reported in figures 4.8.c and 4.8.d for the Ti-HiPIMS films deposited with $U_s = 300$ V and $U_s = 500$ V, respectively. From 100 nm to $200 - 250$ nm, only the (100) orientation of the α phase is observed. Its presence, at the expense of the (002) one, can be explained in light of the strain state of the system. Indeed, as reported by *Checchetto et al.* [235], the minimization of the surface energy when the strain contribution is negligible is achieved with the (200) orientation, while the minimization of the strain energy is correlated to the (001) orientation. The high energy ion field induces a stronger adhesion of the islands to the substrate due to the sputter etching of the Si oxide and atom intermixing. This induces the onset of a strong compressive stress state from the very first growth stages (i.e. below 50 nm thickness). As a result, an increment of the strain energy of the system is achieved, resulting in the development of the (100) orientation instead of the (002). Note that, in agreement with these considerations, the films deposited in this work and by *Chakraborty* et al. [196] with DCMS (i.e. in a low energy environment) shows the (002) crystallography orientation, while the depositions performed by cathodic arc [192] exhibit the (100) orientation.

In correspondence with the island impingement and coalescence, the stresses reach a tensile peak, followed by a transition to a compressive stress state associated with the continuous film growth. After the maximum compression at $\sim$ 130 nm and $\sim$ 100 nm for the $U_s = 300$ V and $U_s = 500$ V bias voltages, respectively, relaxation takes place. As shown in figures 4.11.c and 4.11.d, only the α phase is present during this CTC transition. Notably, there is a shift of the maximum tensile stress toward higher thicknesses for the samples deposited at $U_s = 300$ V compared to the $U_s = 0$ V case. The shift is ascribable to the higher adatoms mobility on the substrate surface [244]. On the other hand, the samples deposited at $U_s = 500$ V do not show the shift in the tensile peak. Therefore, the high-energy Ti ions lead to high production of defects and substrate sputtering rather than enhancing the adatoms mobility. Accordingly, the samples are more stressed, resulting in an enhancement of the (100) reflection (see figure 4.8.d) that, as already mentioned, minimizes the strain energy of the system.

Around 250 nm thickness, the (101) peak associated with the ω phase starts to be present in the XRD spectra shown in figures 4.8.c and 4.8.d. Two possible explanations can be provided to motivate its presence. As already demonstrated for bulk Ti and discussed in Section 3.2.4, the ω phase formation can be due to the onset of a high compressive stress state of the order of some GPa. However, from the XRD measurements, the ω phase seems to appear when the stress relaxation has already begun. Perhaps, its nucleation starts in correspondence with the maximum compression, but its content is not enough at that stage to be observed in the XRD spectra. Besides, a thermodynamic explanation can be provided to explain the nucleation of the ω phase. As shown in the last column of table 4.2, the high energy range of Ti ions in already deposited Ti is of the order of 1.5 nm, which means several atomic layers. This is associated with the high atom mobility responsible for the CTC stress behaviour, as well as with the formation of defects. An out of equilibrium condition could be the mechanism which leads to the evolution of one of the α phase orientation that, in the final unloading step of the CTC transition, finds a new energy minimum by rearranging itself to the structure of ω phase.

Lastly, because of the high ion energy and intense flux, especially at 500 V of bias, an increment of the growth temperature can not be excluded. Furthermore, the $\omega \rightarrow \alpha$ transition can start at relatively low temperatures, as shown by the annealing procedure at 230 °C. Therefore, at 500 V of bias, the ω phase nucleation and development could be hindered by the slight increase of the substrate temperature.

CHAPTER 5

Production of Ti substrates on perforated target holders

This Chapter describes the strategy developed to produce sub-micrometric bare targets and DLT substrates with controlled properties exploiting Magnetron Sputtering. Section 5.1 offers an overview of the procedure developed to deposit free-standing films on the holes of perforated target holders. In particular, the holder preparation before the film deposition is illustrated. Then, Section 5.2 focuses on the most important step of the process, i.e. the deposition of the Ti films performed with DCMS and HiPIMS modes. The results presented in Chapter 4 have been exploited to determine the optimal deposition conditions.

5.1 Strategy for the free-standing films deposition

To make laser-driven particle sources attractive for multiple applications, the target properties must be finely controlled. As far as DLTs are concerned, the parameters of interest are the thicknesses and densities of the near-critical layer and solid substrate, as well as their cohesion and overall integrity. The near-critical layer can be produced by exploiting the Pulsed Laser Deposition technique. As already described in Section 2.3.1, this technique allows depositing nanostructured carbon foams whose density can be tuned from the solid density down to the near-critical one (i.e. few $\mathrm{mg/cm^3}$).
Considering the solid substrates and bare targets, mainly commercial foils have been exploited until now. The available sub-micrometric sheets can be affected by significant disadvantages with detrimental consequences on the shot-to-shot stability of the laser-driven source. Usually, the production of metallic foils is carried out via rolling [245] techniques. Besides being available in a limited number of thicknesses and materials, rolled commercial sheets can be affected by high local thickness uncertainties, up to

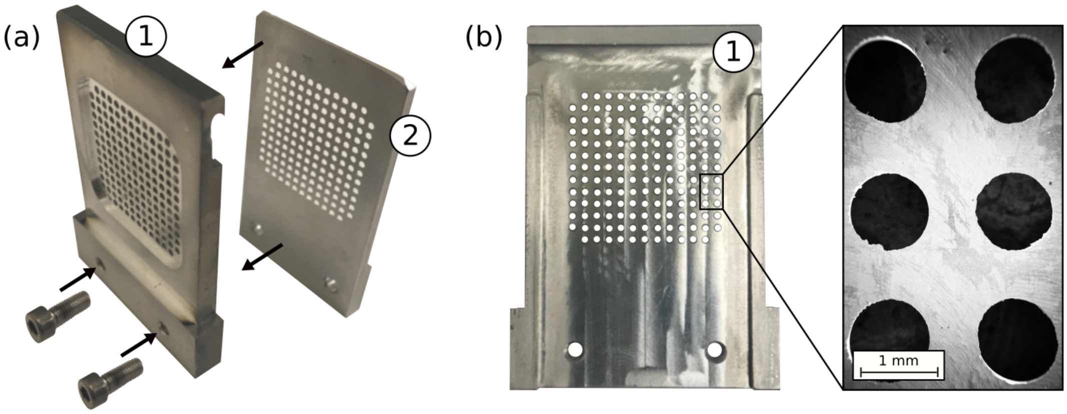

Figure 5.1: *(**a**) Target older disassembled in its two components. (**b**) The surface of the holder on which the Ti substrate is grown and SEM magnification image of six holed.*

$\pm 30\%$ of the nominal value. Moreover, the foils must be manually fixed or clamped on perforated target holders with the risk of breakage and formation of wrinkles and ripples.

To avoid all the mentioned drawbacks, a strategy for direct deposition of the metallic substrate on the holder must be developed. To this aim, a suitable deposition technique is Magnetron Sputtering since it allows depositing compact submicroscopic films on large surface areas (i.e. several cm^2) with a negligible variation of the thickness value. However, the deposition of films on a perforated surface is not trivial. To this aim, a suitable procedure must be developed.

The standardized holder considered in this work, provided by the SourceLAB company, is shown in figure 5.1. As already mentioned, usually, a foil can be clamped between the two masks. The perforated masks are made of stainless steel and are stuck together with two screws. A total number of 165 holes are present, arranged on a 13×13 grid. Their diameter and depth are equal to 1 mm. The mask on which the substrate is grown is identified with the number 1 in figure 5.1.a. The deposition surface is shown in figure 5.1.b. The other mask has a protective function during the laser-target interaction.

The entire procedure developed for the production of the DLTs is reported schematically in figure 5.2. The first step consists of the deposition of a drop of a liquid solution containing water as the solvent and a solid solute. As it will be shown, different solutes were tested (i.e. polymethyl methacrylate, sodium chloride and sucrose). The final choice of the filling material was the result of a compromise between several requirements like high solubility in water, low viscosity in solution, fast solidification and heat resistance. After the solidification, the holes are closed by a solid sacrificial layer.

With the second step, the metallic substrate is grown on the closed holes. The material selected for the deposition was Ti because of its excellent mechanical and thermal properties. Ti is a widely exploited target material in laser-driven ion acceleration experiments [179, 246, 247]. Indeed, it is a getter for H in the $25 - 400\ ^\circ\mathrm{C}$ temperature range. At higher temperatures, it can absorb also other gases of interest for laser-driven ion acceleration (e.g. O, CO_2 and N) [248]. In light of the results shown in the previous Chapter, depositions in different regimes were carried out exploiting both DCMS and HiPIMS modes. As it will be shown, the optimal deposition conditions must be se-

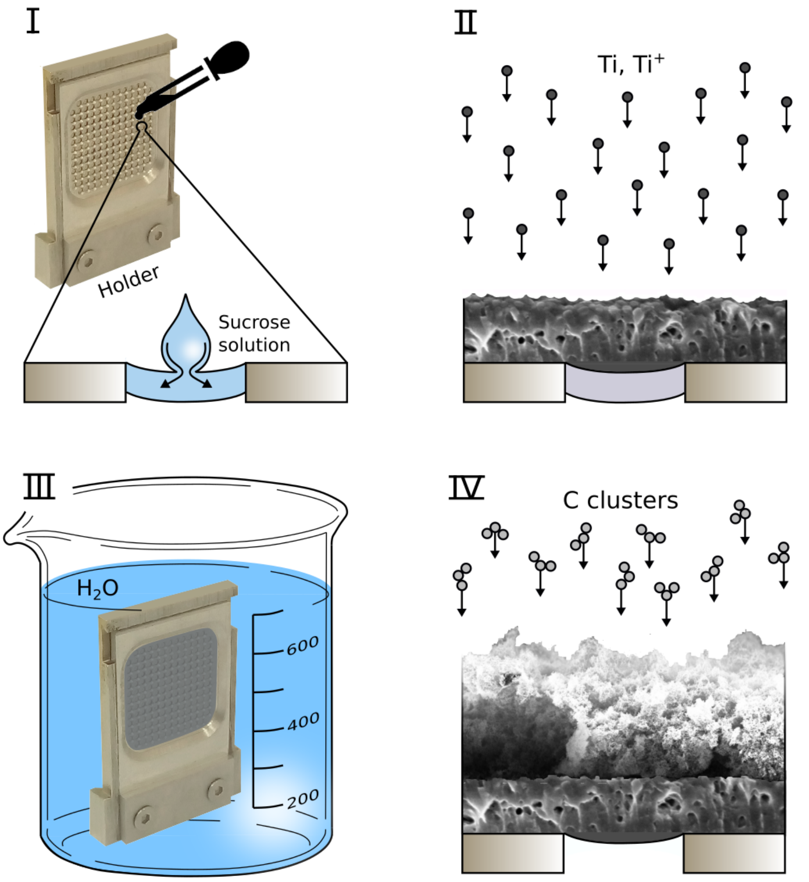

Figure 5.2: *Schematic representation of the step-by-step strategy developed for the DLT production. The procedure involves the holder holes filling (step I), substrate deposition (step II), dissolution of the sacrificial layer (step III) and carbon foam deposition (step IV).*

lected to grow very dense films and, at the same time, avoid the onset of strong stresses. To this aim, DCMS, unbiased and biased HiPIMS depositions have been carried out. When not specified, the adopted deposition parameters were the same already described in Section 4.1.

Following the Ti deposition, the sacrificial layer is removed via dissolution in water (i.e. the third step), and the substrate is ready for the near-critical carbon foam deposition via PLD (i.e. the fourth step). It is worth mentioning that, in the present work, the focus is on the production of the substrate. Therefore, the carbon foam deposition and characterization will not be discussed. Conversely, if the fourth step is not performed, the result is a bare target ready for laser-driven particle acceleration.

5.1.1 Holder preparation prior deposition

The drop of filling solution was deposited in the holes exploiting a micropipette. The diameter of the holes is sufficiently small to allow the drop to remain inside the holes because of capillarity. As already mentioned, the choice of the filling material must satisfy several requirements, among which the compatibility with the deposition tech-

nique is one of the most important.
First of all, the material must form a solution with a solvent available easily and not dangerous to handle. Therefore, several polymers that require dissolution in sulfuric acid can be excluded. The material solubility must be sufficiently high to guarantee the complete filling of the hole after the evaporation of the solvent. Besides, the evaporation should take place in a reasonable amount of time. Moreover, the viscosity of the solution has to be not excessively high to allow easy manipulation with the micropipette.
To grow targets with a flat front surface, the surface of the sacrificial layer must be as uniform as possible after the solidification. Lastly, during the HiPIMS deposition, a local temperature of $100-150$ °C can be reached at the interface between the filling material and the film. Therefore, the selected material must be able to withstand such a temperature without being damaged by heating.

Polymethyl Methacrylate (PMMA)

PMMA is an amorphous thermoplastic polymer formed via polymerization of the methyl methacrylate. It can be dissolved in acetone since it is not resistant to organic solvents. The resulting solution is characterized by low viscosity that allows simply controlling the drop. Acetone is a volatile material that evaporates very rapidly (i.e. few minutes). Since PMMA is an amorphous material, the resulting solid layer has a highly uniform and smooth surface without grain edges and irregularities.
The Ti film deposition on PMMA was performed with HiPMS without the application of the bias voltage. The deposition time was 120 minutes, resulting in a film thickness equal to approximately 500 nm. Following the dissolution of the PMMA sacrificial layer, the film broke over the holes. Moreover, evident wrinkles were present on its surface. The damage can be appreciated from figure 5.3.
PMMA is characterized by a relatively low glass transition temperature T_g (between 85 °C and 165 °C). Therefore, it starts to soften and expand during the deposition compromising the integrity of the Ti film. Moreover, the PMMA cools and retires, leading to the formation of breaks at the edges of the holes and to the formation of wrinkles. Since this behaviour is related to the temperature at the substrate, the same result is expected exploiting DCMS deposition and biased HiPIMS. Indeed, the average power (in this

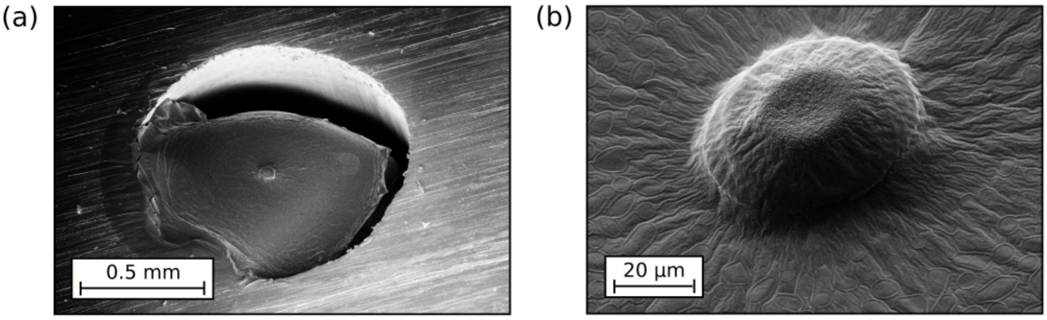

Figure 5.3: *(**a**) Example of a hole after HiPIMS deposition of the Ti film on PMMA. The damage at the border of the hole is evident. (**b**) Magnification of the wrinkle at the centre of the hole.*

case equal to 450 W) reached during HiPIMS and DCMS depositions is approximately the same, while the heat dissipation should be more efficient in HiPIMS because of the low duty cycle.
The conclusion is that, while it satisfies many of the mentioned requirements, PMMA is not suitable for the DLT substrates or bare targets production because of the incompatibility with the Magnetron Sputtering technique.

Sodium Chloride (NaCl)

Materials resistant to high temperatures must be selected to avoid the melting of the sacrificial layer during the deposition. In this respect, NaCl is a proper solution since it has a melting temperature of 801 °C. Once dissolved in water, it can be deposited easily inside the holder holes. However, after solidification, the NaCl crystals did not completely close the holes. This is due to its poor solubility in water (i.e. 35.8 g in 100 g of water at 20 °C). A second drop of solution was deposited to close the hole. Nevertheless, the crystals already present were dissolved, forcing to definitively exclude the use of NaCl.

Sucrose

Sucrose is an organic molecule that belongs to the family of disaccharides. It is formed by glucose and fructose monosaccharides. The sucrose melting temperature is equal to 186 °C, so it should withstand the temperatures reached at the substrate during the deposition. Its solubility of 210 g in 100 g of water at 20 °C is considerably higher than that of NaCl. Thus, being the volumes of liquid equal, more solute can be present in the solution. The main drawbacks of sucrose are the higher viscosity in solution and the long time required for the solidification.
With a 60% $\mathrm{w/w}$ sucrose solution, the formation of air bubbles in the sacrificial layer was observed. Their number increases with the sucrose concentration and, therefore, with the viscosity. The presence of bubbles must be avoided since, during the deposition, they can break and damage the Ti film. To this aim, the sucrose concentration was set at 40% $\mathrm{w/w}$. Moreover, a vacuum treatment was carried out by placing the holder in a dryer at a few mbars of pressure. Then, to accelerate the solidification of the sucrose, the holder was heated at a temperature of 95 °C.

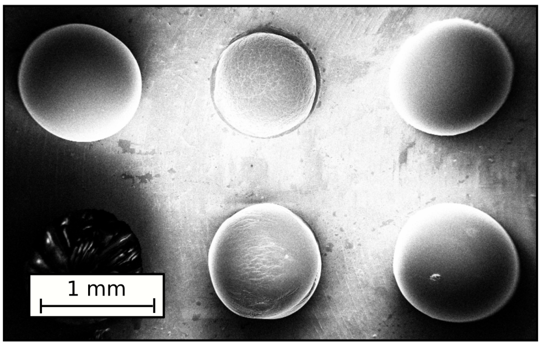

Figure 5.4: *Example of five holes after the filling with the liquid solution and solidification of the sucrose layer.*

The entire procedure lasts approximately 5 hours. To ensure that a sufficiently high quantity of sucrose to close the holes is deposited, the volume of the deposited solution was set equal to 1.25 μL. It corresponds to 160% of the volume of the holes. Some examples of holes following the sucrose solidification are reported in figure 5.4. Their surface satisfies the smoothness requirement.

5.2 Magnetron Sputtering deposition of Ti substrates.

The DCMS and HiPIMS deposition techniques were used to grow submicrometric substrates on the sucrose sacrificial layers. The deposition regimes are analogous to those presented in Chapter 4. As already mentioned, the same geometry configuration, working gas and pressure in the chamber, average and peak powers were kept.

The morphology and stress state of the films, already characterized in the previous Chapter, played a crucial role concerning the substrates structural integrity. The depositions were also performed on conventional Si substrates to take SEM cross section views of the films and retrieve their density. The density was measured with EDX spectroscopy and adopting the procedure described by *Pazzaglia et al.* [249].

DCMS depositions

Exploiting DCMS, homogeneous and intact Ti films were deposited on the sucrose layers. Because of the relatively high deposition rate (i.e. approximately 20 $\mathrm{nm/min.}$ compared to $3-4$ $\mathrm{nm/min.}$ in the HiPIMS regime), 1.0 μm thick films can be grown in less than one hour. However, after the removal of the sucrose layer, the collapse of the Ti films occurred. The resulting damage is shown in figure 5.5.a.

DCMS films are constituted by α phase with (002) preferred orientation, characterized by a low compact columnar structure having several macro-voids (see the cross section reported in figure 5.5.b). As a result, the film density is $\sim$ 70% of the bulk value of Ti. Consequently, after the dissolution of the sucrose layer, the film is not compact enough to self-sustain over the holes. Moreover, the loss of structural integrity can be due to a residual tensile stress state in the film. Therefore, DCMS films are not suited for substrates production because of their low density and poor compact structure.

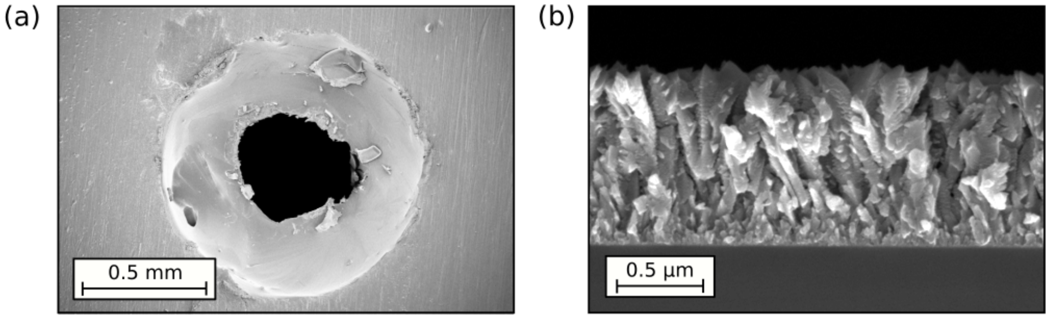

Figure 5.5: ***(a)*** *Example of a hole after the DCMS deposition of the Ti film and dissolution of the sucrose layer. The film is collapsed at the centre of the holder hole.* ***(b)*** *Cross section view of the Ti film deposited via DCMS on a Si substrate.*

HiPIMS depositions

HiPIMS depositions allow growing more compact films than DCMS because of the presence of the intense ion fluxes. The higher compactness can be appreciated from the cross section view reported in figure 5.6.a. Moreover, the density is 80% of the bulk value of Ti. Therefore, HiPIMS seems to be the proper choice to avoid the collapse of the films because of poor structural integrity. The only foreseeable drawback is related to the lower deposition rate compared to DCMS. For instance, the deposition of 1 μm Ti substrate should require more than five hours.

However, a different kind of damage was observed during HiPIMS depositions performed without the bias voltage application. For almost half of the holes, both the film and the underlying sucrose layer are strongly altered, as reported in figure 5.6.b. The damage of the structure can be partially due to the higher energy of the species at the sacrificial layer surface. Moreover, the generation of strong compressive stresses in the HiPIMS films (see the previous Chapter for a detailed discussion) can contribute to the deformation of the film-sucrose interface. Remarkably, despite the observed damage, the sucrose dissolution does not lead to film breakage.

The deposition strategy should share the advantages of both DCMS and HiPIMS modes while avoiding their drawbacks. Specifically, the deposition must be compatible with the substrate, as in the case of DCMS. On the other hand, it must grant the structural integrity of the free-standing Ti films after the sucrose dissolution, as obtained with HiPIMS depositions. Thus, to produce Ti films that meet the listed requirements, DCMS and HiPIMS depositions have been combined in multilayer structures. A significant advantage compared to single HiPIMS deposition is also expected in terms of deposition rate.

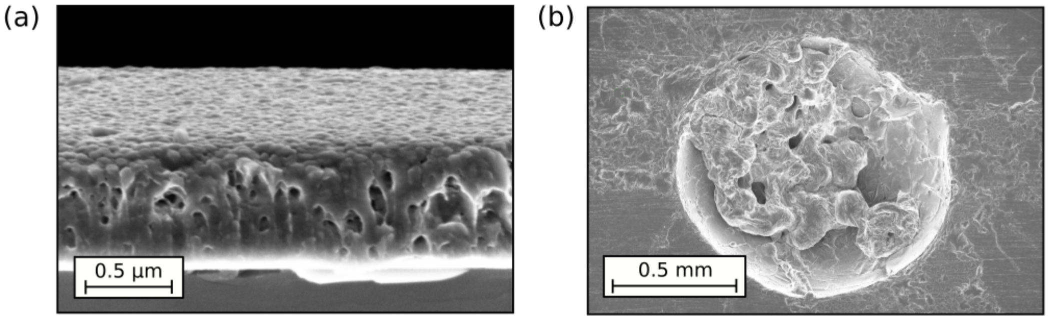

Figure 5.6: *(**a**) Cross section view of the Ti film deposited via HiPIMS on a Si substrate. (**b**) Example of damage of the Ti film and sucrose layer during HiPIMS deposition.*

5.2.1 Multilayer structures of DCMS and HiPIMS depositions

The first multilayer structure presented in this work was produced exploiting an initial deposition with DCMS and a second one with HiPIMS. The DCMS layer should guarantee compatibility with the substrate, while the second layer must provide the required structural integrity and avoid the collapse of the film after the sucrose removal. Moreover, the tensile stress state of the DCMS layer is expected to mitigate the compressive stresses present in the HiPIMS layer. The deposition times were selected to grow a 400 nm thick film where half of the thickness is ascribable to DCMS and half to HiPIMS.

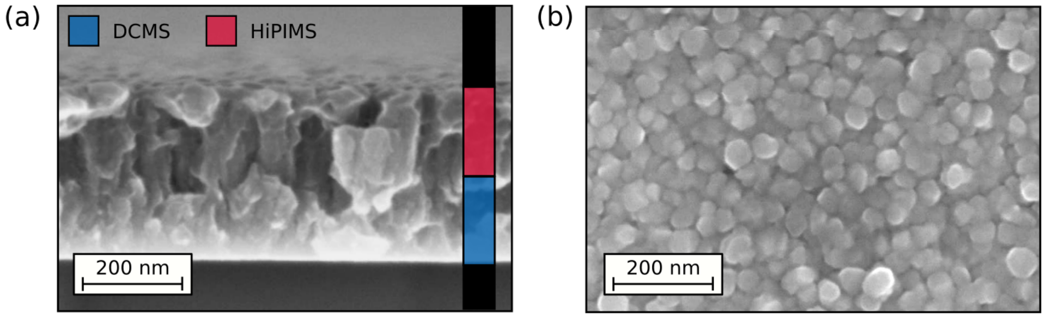

Figure 5.7: *SEM (**a**) cross section and (**b**) top views of the Ti film composed by one layer (half thickness) of DCMS and one layer (half thickness) of HiPIMS.*

The morphology of the film is reported as a cross section view in figure 5.7.a. The fractions of DCMS and HiPIMS in terms of thicknesses are reported as red and blue colour bars, respectively. The film appears uniform along the film thickness without an evident interface between the layers. Besides, the morphology does not resemble that of DCMS films nor that of HiPIMS ones. Indeed, the Ti ions reaching the film during the HiPIMS stage are deposited both on the surface of the DMCS layer and within the macro-voids of its columnar structure. As a result, a densification effect takes place, allowing for greater compactness of the entire structure. This consideration is confirmed by the resulting film thickness. Indeed, while the expected value was 400 nm, the measured thickness is equal to 350 nm. A fraction of the Ti species in the HiPIMS regime is deposited in the intra-columnar cavities instead of on the surface. As far as the planar view shown in figure 5.7.b is concerned, a granular structure similar to that reported in the previous Chapter for HiPIMS deposition without bias voltage is present. Probably, following an initial period during which the HiPIMS layer interpenetrates the DCMS layer, the conventional HiPIMS-like growth starts to be dominant. It is worth mentioning that the density is still around 80% of the bulk value.

Notably, about 80% of the holes were covered with smooth substrates without defects after the sucrose dissolution. This result suggests that the adopted deposition procedure is a viable route to produce the free-standing substrates. However, 20% of the holes still presented defects analogous to that shown in figure 5.6.b and caused by the HiPIMS deposition. A possible way to further reduce the number of damaged substrates is to decrease the fraction of HiPIMS. Moreover, an increment in the number of layers should allow maintaining the necessary compactness for structural integrity.

Accordingly, four multilayer films composed of two layers of Ti-DCMS and two layers of Ti-HiPIMS were deposited. All films are characterized by a thickness equal to ~ 600 nm. The fraction of HiPIMS (in terms of thickness percentage) has been set equal to 0%, 10%, 20% and 40%. Their cross section views are reported in figure 5.8.a. At 10% HiPIMS fraction, the morphology resembles that of the pure DCMS film. By increasing the HiPIMS fraction to 20%, the columnar structures are less evident, even if some macro-voids are still present. Last, considering the higher HiPIMS fraction, only traces of the columnar morphology are visible in favour of higher uniformity and compactness.

Figure 5.8.b reports the behaviour of the intrinsic stresses as a function of the HiPIMS

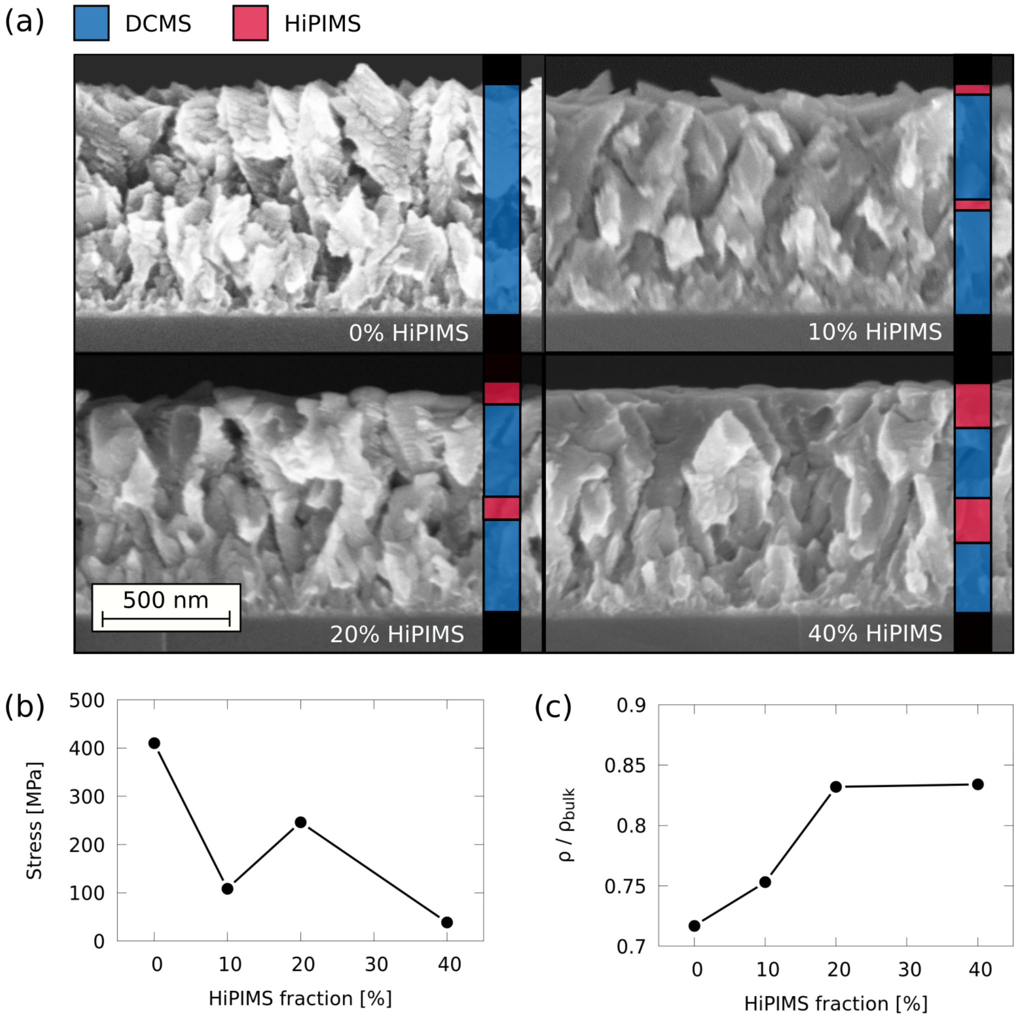

Figure 5.8: *Characterization of Ti films deposited with the alternation of DCMS and unbiased HiPIMS depositions. (**a**) SEM cross section views. The expected DCMS and HiPIMS contributions to the total thickness are reported as blue and red bars, respectively. The overall HiPIMS fraction is also reported on the bottom right of each panel. (**b**) Stress state and (**c**) density as a function of the HiPIMS fraction.*

fraction for the considered films. The pure DCMS film is characterized by a tensile stress state of the order of 400 MPa. This value is expected from the results presented in Section 4.2.3. Indeed, for 100s of μm thickness, the stress state of DCMS films oscillates around a few 100s of MPa. The stresses remain tensile and well below 400 MPa by increasing the HiPIMS fraction. Overall, they tend to decrease for higher fractions of HiPIMS. In parallel, a densification of the films takes place. The maximum density is reached around 20% HiPIMS fraction and, then, it keeps constant around 84% of the bulk density.

Figure 5.9.a shows the XRD spectra associated with the films. They further confirm that the alternation of DCMS and HiPIMS depositions does not result in a simple superposition of separated layers. Indeed, for a 10% HiPIMS fraction, the intensity of

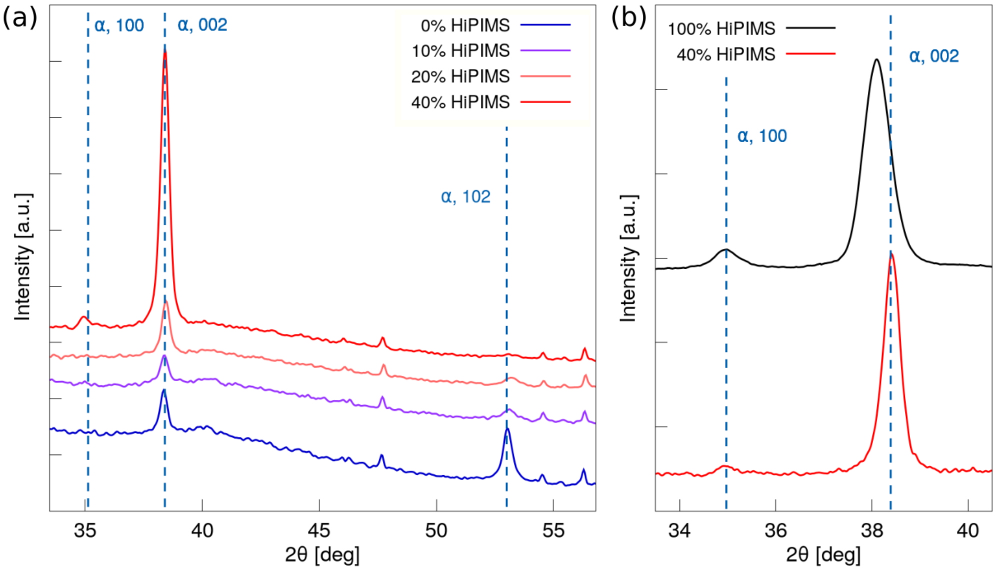

Figure 5.9: *(**a**) XRD spectra of Ti films deposited with the alternation of DCMS and HiPIMS depositions at an increasing fraction of the latter. (**b**) XRD spectra of Ti films deposited with* 40% *HiPIMS fraction and* 100% *HiPIMS.*

the (102) peak of the α phase associated with DCMS films (see Section 4.2.2) drastically decreases. For higher HiPIMS fractions, the (102) peak completely disappears, and the signal of the (002) plane increases. Considering a 40% HiPIMS fraction, the XRD spectrum shows the same features reported for the pure HiPIMS film of 600 nm thickness presented in Section 4.2.2. This result is a clear indication of the strong intermixing between the layers. Even if the DCMS fraction is still higher, the HiPIMS contribution to the microstructure evolution is dominant. Lastly, figure 5.9.b compares the (002) peak associated with the pure HiPIMS film (see again Section 4.2.2) and that of the 40% HiPIMS fraction film. In the second case, the (002) peak is not shifted, and its FWHM is considerably smaller. This is another clear indication of the lower stress state of the multilayer structure than that of the pure HiPIMS film.

In light of the obtained results, the proper HiPIMS fraction can be set approximately within the $20-40\%$ range. Under such condition, the morphology is more compact than that of DCMS films, and the density is the highest possible. Moreover, the fraction of HiPIMS is lower than 50%, allowing us to avoid the damage of the films.

To assess these points, two Ti substrates were deposited on the holder holes after being closed with the sucrose. In both cases, the total amount of the HiPIMS fraction was set equal to 25%. One film, of thickness equal to 300 nm, was grown with one deposition in DCMS and one in the HiPIMS regime. The other film was produced with four alternating depositions in DCMS and HiPIMS regimes, resulting in a total thickness of 600 nm. Their cross section views are reported in figures 5.10.a and 5.10.c. As expected, their morphology is similar to that reported in figure 5.8.a for the sample having 20% of HiPIMS fraction. In addition, their density is around $0.8-0.84\%$ of the bulk value. After the sucrose dissolution, both the 300 nm and 600 nm thick substrates were able to self-sustain over the holes. Two examples of the obtained targets are reported in figures 5.10.b and 5.10.d. No evident imperfections were present on their surface. Therefore,

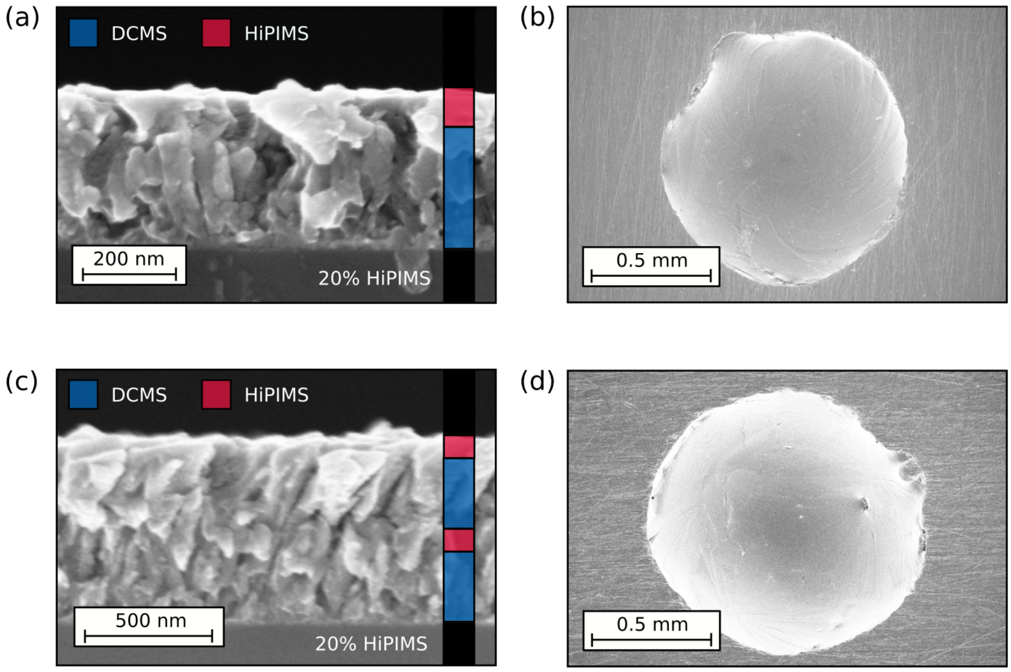

Figure 5.10: *(**a**) SEM cross section view of the 300 nm thick substrate deposited with one layer of DCMS and one layer of HiPIMS. (**b**) Example of a hole after the 300 nm thick substrate deposition and removal of the sucrose layer. (**c**) SEM cross section view of the 600 nm thick substrate deposited with two layers of DCMS and two layers of HiPIMS. (**d**) Example of a hole after the 600 nm thick substrate deposition and removal of the sucrose layer.*

exploiting the deposition strategy presented in this Section, a significant improvement in terms of structural integrity was achieved. However, observing the surface of the substrates at higher magnification, micro-cracks can be noticed. An example is shown in figure 5.11. They are in correspondence with the grain boundaries of the pre-existing sucrose layer. Their origin can be due to the relaxation of the small residual stress state affecting the film after the sucrose dissolution. While the micro-cracks do not prevent the integrity of the substrate, their presence could cause the breakage of the film when

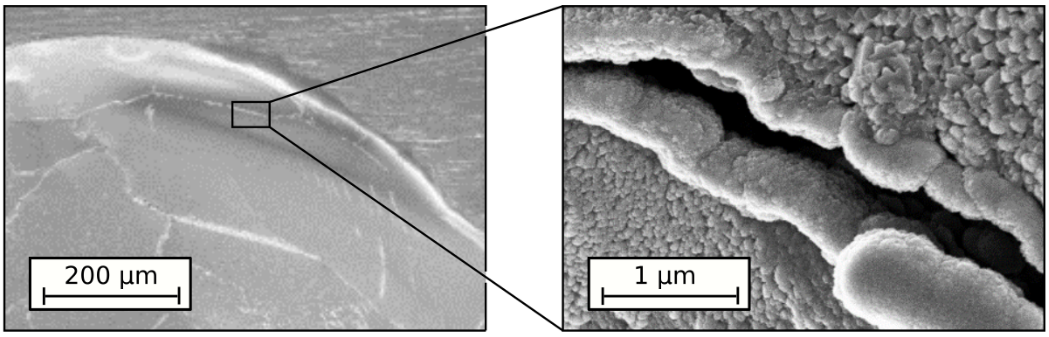

Figure 5.11: *Examples of grain boundaries and magnification of a film micro-crack formed after the sucrose layer dissolution.*

mechanically solicited (e.g. during the carbon foam deposition).

5.2.2 DCMS and HiPIMS depositions with bias application

Further densification of the Ti substrate is required to prevent the onset of micro-cracks while avoiding the formation of damages like that reported in figure 5.6.b. To this aim, the bias voltage application during HiPIMS depositions is needed since, as reported in Section 4.3.2, it will cause stronger adhesion and intermixing of the Ti islands. Moreover, the interpenetration between DCMS and HiPIMS layers should be further improved under the action of a high-energy ion field.

Accordingly, three Ti films were produced alternating DCMS and HiPIMS deposition. During the latter, a bias of 300 V was applied to the substrate. All films have an actual thickness of 600 nm obtained with an HiPIMS fraction equal to 40%. The amount of HiPIMS was slightly increased compared to the depositions performed without bias voltage application to enhance the effect of the energetic species. Lastly, the films were

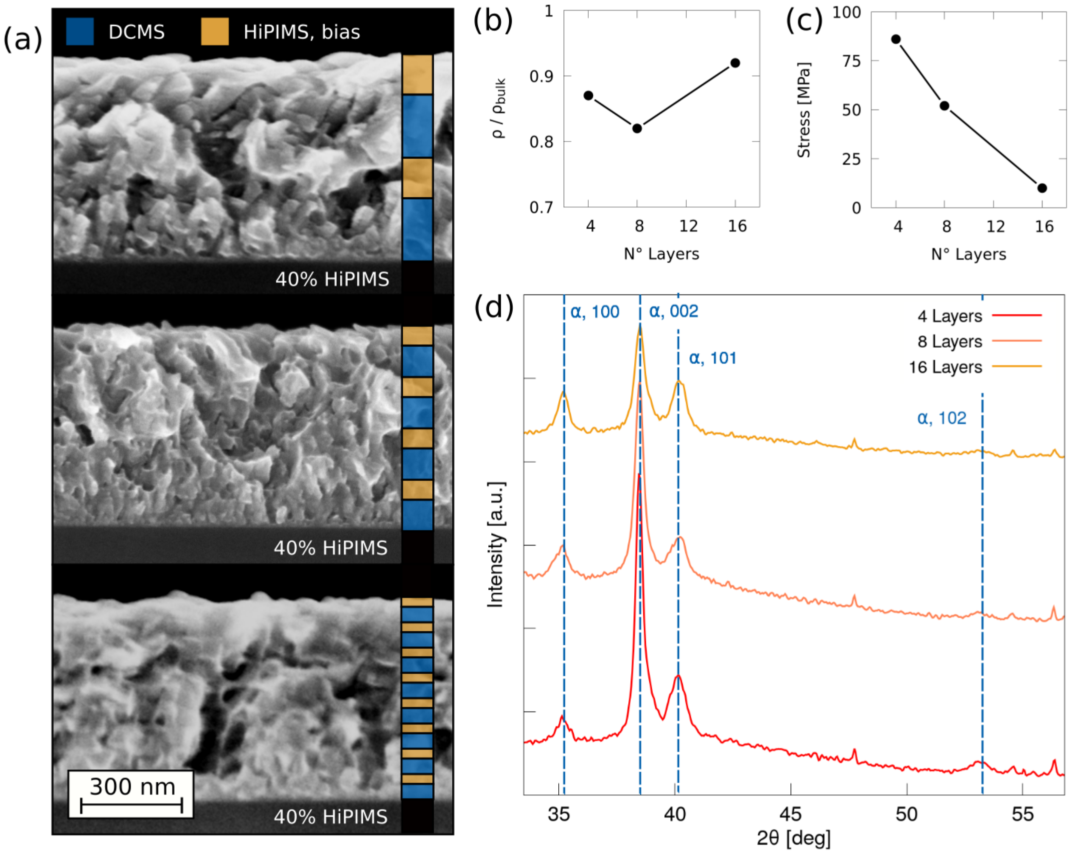

Figure 5.12: *Characterization of Ti films deposited with the alternation of DCMS and biased HiPIMS depositions. (**a**) SEM cross section views. The expected DCMS and HiPIMS contributions to the total thickness are reported as blue and yellow bars, respectively. The overall HiPIMS fraction is also reported on the bottom right of each panel. (**b**) Density and (**c**) stress state as a function of the HiPIMS fraction. (**d**) XRD spectra.*

grown with the alternation of 4, 8 and 16 DCMS and HiPIMS depositions. The aim is to investigate the effect of the number of layers on the morphology and density of the films.

The effect of the energy of the species on the morphology can be appreciated by comparing the cross section views reported in the fourth panel of figure 5.8.a (unbiased HiPIMS) and the first panel of figure 5.12.a (300 V biased HiPIMS). Both have been obtained with four layers and a 40% HiPIMS fraction. As previously mentioned, the film deposited without bias still has some traces of the columnar morphology associated with pure DCMS depositions. On the other hand, the application of the bias completely deletes any sign of the DCMS depositions. The density for the biased film is a little bit higher than for the unbiased case, passing from 84% to 87% of the bulk value.

The morphology evolution at an increased number of layers for the biased depositions can be observed in figure 5.12.a. The films tend to be more compact, evolving in a quasi-amorphous structure. Besides, their density keeps well above 80% of the bulk value, as reported in figure 5.12.b. Remarkably, the maximum density is equal to 92% of the bulk. This value, obtained for the film composed of 16 layers, represents a significant improvement compared to that achieved under unbiased conditions. For what concerns the stress state of these films, the average value as a function of the number of layers is reported in figure 5.12.c. Overall, they are tensile and always lower than 100 MPa. It is expected that the more compact morphology, higher density and negligible stress state can allow reducing the number of micro-cracks in the Ti substrates.

Lastly, figure 5.12.d shows the XRD spectra obtained for the considered samples. The (101) peak associated with the ω phase and observed in the previous Chapter for the thickest biased HiPIMS films is not present. The absence of ω phase can be due to the lack of the compressive stresses, which are necessary to trigger its nucleation. Moreover, the relative intensity of the (002) peak compared to that of the (101) peak associated with the α phase decreases as the number of layers increases. We can suppose that, for a higher number of layers, the growth along a well-defined preferential direction is

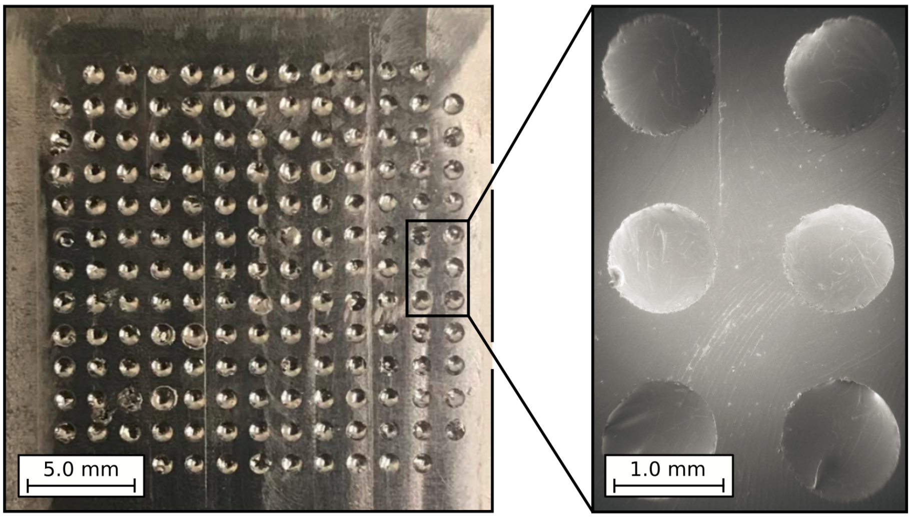

Figure 5.13: *Top view of the freestanding Ti substrates deposited on the perforated target holder and magnification in correspondence of six holes.*

inhibited in favour of a less crystalline and amorphous structure connected with the film densification.

In light of the obtained results, films grown with a series of biased HiPIMS and DCMS depositions are the most promising to produce the Ti substrates. Accordingly, a 600 nm thick substrate was grown on the perforated holder with an alternation of 16 depositions. The overall fraction of biased HiPIMS was equal to 40%, corresponding to the case shown in the last panel of figure 5.12.a. The surface of the holder after the sucrose dissolution and a magnification of six targets are reported in figure 5.13. After the sucrose layer dissolution, all the 165 substrates were able to self-sustain over the holes. Only a couple of them exhibit the damage associated with HiPIMS depositions and reported in figure 5.6.b. Besides, the micro-cracks observed without bias voltage have been reduced greatly in number and size. Indeed, in most of the substrates, none of them is present. It is worth mentioning that the maximum thickness uncertainty from one hole to another is $\sim 5\%$. This value is well below the $\sim 30\%$ thickness uncertainty affecting commercial submicrometric metallic targets.

It is possible to conclude that the strategy developed in this Chapter allows depositing targets in a controlled way, and it can be applied in the future for fully optimized DLT substrates production.

Part III

Investigation on laser-driven sources for materials characterization

CHAPTER 6

Theoretical study on laser-driven PIXE

In this Chapter, a theoretical and numerical investigation of the laser-driven PIXE feasibility is presented. Section 6.1 deals with the generalization of the PIXE theory to include the presence of a non-monoenergetic proton energy spectrum and the development of an iterative code for the sample composition reconstruction from a laser-driven PIXE measurement. In Section 6.2, the Monte Carlo and Particle In Cell tools are exploited to simulate realistic laser-driven PIXE experiments. In Section 6.3, the iterative code is applied to analyze the simulated X-ray spectra. The aim is to retrieve the sample composition set in the Monte Carlo simulation and check the reliability of the iterative code. Lastly, a numerical investigation via Monte Carlo simulations of the characteristic X-ray emission due to laser-driven electron irradiation is presented in Section 6.4.

6.1 Laser-driven PIXE modeling

In Section 1.3.2, the theoretical description of the physical phenomena involved in PIXE analysis has been presented. The model relates the characteristic X-ray line intensities to the material composition. Thus, it can be exploited to perform quantitative PIXE analysis (i.e. retrieve the elemental concentrations of homogeneous samples, the concentration depth profiles in non-homogeneous materials and the layer thicknesses in multilayer structures). To this aim, several commercial software have been developed. However, they rely on a theoretical description of PIXE that takes into account only monochromatic ion sources. On the other hand, laser-driven ions are invariably characterized by a broad energy distribution. The spectrum shape depends on the specific acceleration mechanism. Therefore, extending the theory for arbitrary energy distributions is the first crucial step to develop a quantitative laser-driven PIXE technique.

Consider a non-monoenergetic proton energy spectrum represented by a generic function:

$$f_p(E_p) = dN_p(E_p)/dE_p \tag{6.1}$$

The spectrum is different from zero in the energy interval from $E_{p,min}$ to $E_{p,max}$. The differential yield (i.e. the number of X-rays generated by incident protons with energy between E_p and $E_p + dE_p$) is equal to $dY_i = dN_p\Gamma_i = f_p\Gamma_i dE_p$, where the function Γ_i contains all the relevant physical quantities describing the proton-sample interaction and characteristic X-ray emission. The index i identifies a specific X-ray line and the associated element. Therefore, in the case of a homogeneous sample, the system of equations 1.4 can be generalized as follows:

$$Y_i = \frac{\Delta\Omega}{4\pi}\varepsilon_i \frac{N_{av}}{M_i} W_i \int_{E_{p,min}}^{E_{p,min}} f_p(E_p) \int_{E_p}^{0} \sigma_i(E)\omega_i e^{-\mu_i \int_{E_0}^{E'} \frac{dE'}{S(E')} \frac{\cos\theta}{\cos\phi}} \frac{dE}{S(E)} dE_p \tag{6.2}$$

All the relevant physical quantities present in equation 6.2 are already specified in Section 1.3.2. The considered irradiation geometry is reported schematically in figure 6.1.a. It is worth noting that, with the choice $f_p = N_p\delta(E_p - E_0)$ (i.e. a monoenergetic distribution), equation 6.2 reduces to equation 1.4, where N_p is the total number of incident protons.

Differential PIXE analysis is applied to retrieve the concentration depth profiles of the elements in non-homogeneous samples. In this case, the sample is split into a finite number of fictitious layers with mass thicknesses $\rho_j R_j$ and elemental concentrations $W_{i,j}$ (see figure 6.1.b). The differential PIXE analysis can be generalized considering K arbitrary proton energy distributions. Therefore, the system of equations 1.6 assumes the following form:

$$\begin{aligned} Y_i^k = {} & \frac{\Delta\Omega}{4\pi}\varepsilon_i \frac{N_{av}}{M_i} \sum_{j=1}^{J-1} W_{i,j} e^{-\sum_{l=1}^{j-1} (\frac{\mu}{\rho})_{i,l} \frac{\rho_l R_l - \rho_l R_{l-1}}{\cos\phi}} \times \\ & \times \int_{E_{p,min}^k}^{E_{p,max}^k} f_p^k(E_p) \int_{E_{p,j+1}^k}^{E_{p,j}^k} \sigma_i(E)\omega_i e^{-\mu_{i,j} \int_{E_p}^{E'} \frac{dE'}{S_j(E')} \frac{\cos\theta}{\cos\phi}} \frac{dE}{S_j(E)} dE_p \end{aligned} \tag{6.3}$$

Here, the quantities f_p^k, $E_{p,max}^k$ and $E_{p,min}^k$ refer to the k-th proton energy spectrum. Equation 6.3 suggests that, also with a non-monoenergetic source, the use of at least K

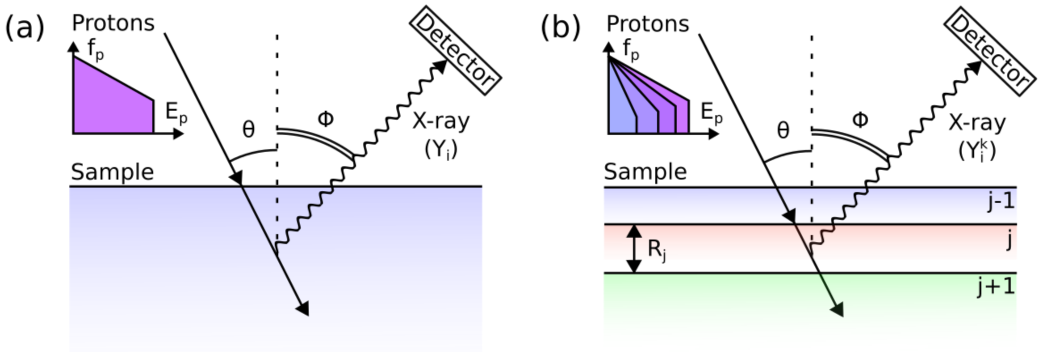

Figure 6.1: *Conceptual schemes for the* (***a***) *homogeneous and* (***b***) *non-homogeneous sample irradiation geometry in laser-driven PIXE.*

different spectra is required to perform differential PIXE.

As in conventional PIXE, the quantitative analysis can be performed by solving the non-linear systems of equations 6.2 and 6.3 for the homogeneous sample and differential PIXE analysis, respectively. The X-ray yields are obtained experimentally, and the unknowns are the properties of the sample (e.g. the concentrations W_i and the mass thicknesses $\rho_l R_l$).

If a laser-driven proton source is exploited, the proton energy spectrum $f_p(E_p)$ can take different forms according to the specific ion acceleration mechanism. As already discussed in Chapter 2, TNSA is arguably the most robust and well-understood process [250]. It has been achieved in high-repetition-rate operation [251]. Accordingly, TNSA is the optimal candidate to perform laser-driven PIXE. Other non-TNSA acceleration schemes, such as Radiation Pressure Acceleration (RPA) [252,253] and Collisionless Shock Acceleration (CSA) [254], are reported in the literature. They can provide a narrower proton energy distribution compared to TNSA. However, the energy spectrum is still much broader than that provided by conventional electrostatic accelerators, preventing the use of the standard algorithms for PIXE with monochromatic sources. Therefore, RPA or CSA are not more suitable than TNSA for laser-driven PIXE, and the approach described in this Section is valid also for RPA and CSA.

6.1.1 Iterative code for laser-driven PIXE quantitative analysis

As already mentioned, quantitative laser-driven PIXE analysis requires to solve the systems of equations 6.2 and 6.3. In the case of a homogeneous sample, the solution is found by minimizing the following χ^2-parameter:

$$\chi^2 = \sum_i \left(\frac{\tilde{Y}_i - \tilde{Y}_i^*}{\sqrt{\tilde{Y}_i^*}} \right)^2 \tag{6.4}$$

where $\tilde{Y}_i = Y_i / \sum_i Y_i$ and $\tilde{Y}_i^* = Y_i^* / \sum i Y_i^*$ are the normalized calculated and normalized experimental yields, respectively. This formulation allows performing a fast χ^2 minimization. Moreover, the knowledge of the total number of incident protons is not required, which is particularly interesting from the experimental point of view. The method exploited for the minimization relies on the *BOBYQA* algorithm present in the *dlib C++* library [255]. All the physical parameters (i.e. ionization cross sections, fluorescence yields, proton stopping power and X-ray attenuation coefficients) used in the algorithm are taken from standard libraries and codes (see Section 1.3.2 for details). As an initial guess, the elements are assumed to be equally concentrated.

As far as the differential PIXE analysis is concerned, the sample is split into five fictitious layers. The analysis demands an initial guess on both the elemental concentrations in each layer and on their thickness. The initial concentrations are selected following the procedure described in [33]. The guess on the mass thicknesses should consider the expected penetration depth of the protons and the expected scalelength of the inhomogeneities of the sample. We assume $[0.65\xi, 1.3\xi, 2.6\xi, 5.2\xi, \infty]$ $\mathrm{mg/cm^2}$, where ξ is a free parameter, its value is optimized during the iteration. It is constrained between 0.5 and 1.5, and the initial guess is set equal to 1.

Now, the χ^2-parameter must take into account also for the presence of at least $K = 5$

different measurements:

$$\chi^2 = \sum_{i,k} \left(\frac{Y_i^k - Y_i^{k,*}}{\sqrt{Y_i^{k,*}}} \right)^2 \tag{6.5}$$

In differential PIXE analysis, χ^2 is a function of the free parameter ξ and the elemental concentrations $W_{i,j}$ in the five layers. Since the minimization of such a function is particularly challenging, the procedure is subdivided into multiple steps. The minimization is performed for one element (and in all the layers) at a time and together with ξ. Then, the procedure is carried out for all the elements and repeated until convergence is reached. Moreover, the χ^2 is evaluated without the normalized X-ray yields. Indeed, the calculated Y_i^k and experimental $Y_i^{k,*}$ yields are considered in equation 6.5.
The formulation of the χ^2 minimization problem described until now is valid only if all the sample constituents emit characteristic X-rays. However, several samples are characterized by the presence of organic matrices. Their presence in the material can be known as a priori, but they do not exhibit any characteristic X-ray. Quantitative PIXE analysis can be done, but the additional constrain $\sum_i W_{i,j} = 1$ must be imposed. Therefore, equation 6.5 is modified as follows:

$$\chi^2 = \sum_{i,k} \left(\frac{Y_i^k - Y_i^{k,*}}{\sqrt{Y_i^{k,*}}} \right)^2 + \lambda \sum_j (1 - \sum_i W_{i,j})^2 \tag{6.6}$$

where λ is significantly larger compared to the first term on the right side of equation 6.6.

6.2 Simulations of laser-driven PIXE experiments

The goal of the present study is to assess the potentials of laser-driven PIXE in realistic scenarios. To this aim, a realistic experimental apparatus is proposed. It relies on a compact 10s TW class laser, a suitable beam handling system and an X-ray detector. Then, the iterative code presented in the previous Section must be applied to retrieve the composition of complex, realistic samples from the X-ray emission induced by the laser-driven proton source. For this purpose, no useful experimental data are available in the literature. Indeed, *Barberio et al.* [150] demonstrated the possibility to record an X-ray spectrum irradiating ceramic samples with a laser-driven particle source. They also assessed the absence of any damage to the material under irradiation. However, the elemental concentrations were not retrieved, and the reported data are too simplified to be considered for the goals of this work.
In this PhD thesis, a selection of samples relevant to cultural heritage studies was considered. They are naturally characterized by a multi-elemental, multi-layer composition. Therefore, their complexity represents an ideal testbed to demonstrate the general feasibility of laser-driven PIXE and Differential PIXE for many applications. Using Geant4 [204, 206, 207] Monte Carlo simulations, "synthetic" X-ray spectra (i.e. the experimental X-ray yields Y_i^* and $Y_i^{k,*}$) were generated. A comprehensive description of Geant4 and the implemented physical models for the PIXE Monte Carlo simulation are presented in Section 3.4.1. Three realistic laser-driven PIXE scenarios were simulated involving different samples and laser-driven proton sources. As already mentioned, the

proton sources are compatible with those achievable exploiting compact 10s TW class lasers. For each scenario, the x-ray spectra were analyzed with the iterative code to retrieve the composition of the samples. The results (i.e. the retrieved concentrations) are compared with the concentrations initially set in the Monte Carlo simulations (i.e. the actual concentrations from here on). The three scenarios are described briefly in the following paragraphs.

Metallic and homogeneous sample

The first scenario involves the laser-driven PIXE analysis of a homogeneous metallic sample in-vacuum performed with an idealized proton source. Indeed, primary protons were simulated in the Monte Carlo by extracting their initial energy from a simple exponential distribution $f_p(E_p) \sim e^{-E_p/T_p}$. The spectrum is characterized by a maximum cut-off energy $E_{p,max} = 5$ MeV and temperature $T_p = 0.7$ MeV. These values are realistic for a proton source driven by a 20 TW laser [256]. This simple description of the source allows us to carry out a sensitivity analysis. The analysis aims at addressing the effects of typical fluctuations of both $E_{p,max}$ and T_p on a laser-driven PIXE measurement. The simulated sample composition is representative of a Roman sword-scabbard (iron, copper, zinc, tin, and lead are present) [257].

Differential PIXE of a metallic sample

In the second scenario, the differential PIXE analysis of a non-homogeneous metallic sample in-vacuum is considered. Six Monte Carlo simulations were performed considering different pure exponential proton energy spectra. The values for $E_{p,max}$ and T_p are compatible with a laser system having a maximum power of 40 TW [256]. Indeed, the cut-off energies for the spectra range from 1 to 6 MeV. The sample composition is inspired by the elemental concentration profiles of a medieval broach [5]. It is composed of a superficial layer of thickness equal to 1.2 μm, an intermediate 1.3 μm thick layer and a semi-infinite substrate. The layers contain different concentrations of copper, zinc, silver, gold and mercury.

Differential PIXE of a painting

The third scenario, summarized in figure 6.2, deals with the differential PIXE analysis of a non-homogeneous sample in air. In this last case, the proton source exploits a 20 TW class laser, and it was realistically described using 3D Particle-In-Cell (PIC) simulations. In the PIC simulations, a double-layer target configuration (a solid foil coated with a homogeneous low-density foam) was used to enhance the laser-target coupling and increase the number and maximum energy of the accelerated protons. The PIC results and Monte Carlo simulation setup are extensively described in the following Sections. The sample composition is compatible with that of a Renaissance oil painting [33,258]. It is constituted by a 10.0 μm thick superficial layer of protective organic varnish. The second layer of thickness equal to 20 μm is present. It contains a red pigment (HgS, the so-called *Cinnabar*), a lead-based white pigment (the so-called *lead-white*), some impurities (Ca and Fe) and the organic binder. The thick substrate (the so-called *imprimitura*) is made by the lead-white and the organic binder.

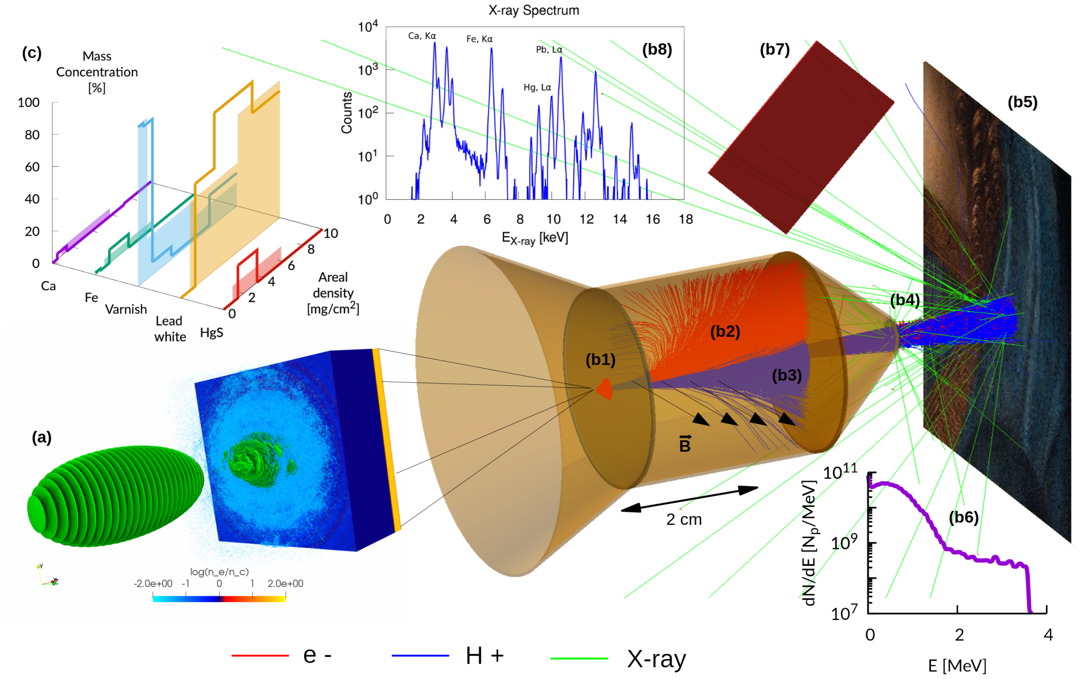

Figure 6.2: *Scheme of the laser-driven in-air PIXE analysis of a painting. (**a**) Laser-driven proton source composed of a double-layer target irradiated with an ultraintense laser pulse (snapshot from a PIC simulation). (**b**) Monte Carlo simulation setup: (b1) fist aperture slit; (b2) 0.15 T dipole magnet; (b3) second aperture slit; (b4) 1 µm thick Si_3N_4 exit window [259] (b5) sample placed in the air at 2 cm distance from the exit window; (b6) Example of proton energy spectrum at the sample surface; (b7) CCD camera (PI-LCX:1300) screen of dimensions $2.6 \times 2.68\ cm^2$. (b8) Example of X-ray energy spectrum recorded by the CCD. (**c**) retrieved elemental concentration profiles (solid lines) and actual profiles (filled regions).*

6.2.1 Monte Carlo simulation of laser-driven in-air PIXE

One of the goals of this work is to provide a first proof-of-principle design of a compact laser-driven source for PIXE analysis. To this aim, a realistic experimental apparatus was implemented in Geant4. The setup for the in-air PIXE analysis is illustrated in figure 6.2. As far as the first and second scenarios are concerned, they neglect the air and exit window, being otherwise identical.

Primary particles are emitted by a punctual source in-vacuum. In principle, protons, electrons and heavier ions should be considered. However, heavy ions were neglected in the Monte Carlo simulations since their number is usually orders of magnitude lower compared to protons in the TNSA regime [94, 260]. Moreover, their maximum energy per nucleon is lower, further reducing the X-ray emission due to heavier ions. As far as the electrons co-emitted with ions are concerned, they could lead to an unwanted X-ray signal from the sample. This aspect will be further investigated in Section 6.4. Nevertheless, the apparatus is designed to remove the electrons.

The particles cross an aperture slit (figure 6.2.b1) and pass through a dipole magnet (figure 6.2.b2). Magnets are standard components to manipulate the laser-driven particle path [261, 262]. Electrons are completely deflected by the magnetic field, and they are stopped by shielding. Protons undergo a smaller deflection ad they pass through a second slit (figure 6.2.b3). They cross an exit window separated from the vacuum by a thin membrane (figure 6.2.b4). Protons cross the air gap and reach the sample (figure 6.2.b5). An example of proton energy spectrum at the sample surface is reported in figure 6.2.b6. The X-ray detector was modelled as a commercial Charged Coupled Device (CCD) screen (figure 6.2.b7). The Monte Carlo simulations took into account the detection efficiency of the device. When the number of incident X-rays is lower than the number of pixels, CCDs can be exploited to perform single-shot photon spectroscopy [263]. Therefore, CCDs are the ideal choice to record the X-rays emitted by the sample during irradiation with laser-driven protons. An example of a simulated X-ray spectrum is reported in figure 6.2.b8.

The proton momenta distributions from PIC simulations $d^3N_p/dp_xdp_ydp_z$ (where p_x, p_y and p_z are the Cartesian components of the momentum) were provided as input to Geant4. The momentum components were extracted with the Inverse Transform Sampling method for each primary proton.

Many Geant4 simulations with different seeds of the Random Number Generator (RNG) were run in parallel (exploiting a user-defined routine) on the *Cineca* supercomputer, and the final results were aggregated. Overall, a few $10^{10} - 10^{11}$ primary particles were simulated for each proton energy spectrum. The *HepJamesRandom* generator was exploited, which implements the Marsaglia-Zaman RANMAR algorithm. This RNG has the fundamental property of providing a large number (i.e. $\sim 10^9$) of independent and very long sequences of pseudo-random numbers [264].

It is worth pointing out that possible collective effects are neglected because the Monte Carlo code simulates one particle at a time. This assumption should not affect the results because collective effects have been reported to be negligible in the considered regime [265].

6.2.2 Particle-In-Cell simulations of laser-driven proton acceleration

3D PIC simulations were performed with the open-source code *Piccante* [100] on the *Cineca* supercomputer. A general description of the PIC method is provided in Section 3.3. The aim is to obtain realistic energy and angular distributions of the accelerated protons.

The target is composed of a 0.8 μm thick solid foil with a density equal to 40 n_c (sampled with 8 macro-protons and 40 macro-electrons) covered by a near-critical 5.0 μm thick layer. The density of the near-critical layer is equal to 1.0 n_c (sampled with 1 macro-protons and 4 macro-electrons). On the rear side of the target, an 80 nm thick contaminant layer is present with a density equal to 5.0 n_c. The electron population was initialized cold (i.e. temperature equal to $\sim$ eV). The duration of the simulations is 267 fs. The time resolution is set equal to 98% of the Courant Limit. Periodic boundary conditions are set for both the macro-particles and fields. However, the box is sufficiently large to avoid unphysical effects due to recirculation.

The P-polarized laser pulse has a wavelength equal to 800 nm, 30 fs time duration, a $\cos^2$ temporal profile, a Gaussian transverse profile and normal incidence. A total number of six simulations were performed at different peak laser intensities a_0 equal to 2, 2.5, 3, 3.5, 4 and 4.5. They correspond to a focused intensity between $8.7 \cdot 10^{18}$ $\mathrm{W/cm^2}$ and $4.4 \cdot 10^{19}$ $\mathrm{W/cm^2}$. Such laser parameters are realistic for a tightly focused (waist of 3 μm) 20 TW Ti:Sapphire laser system. Indeed, they can be obtained by scaling down the parameters for a 200 TW laser, varying the intensity while keeping the waist

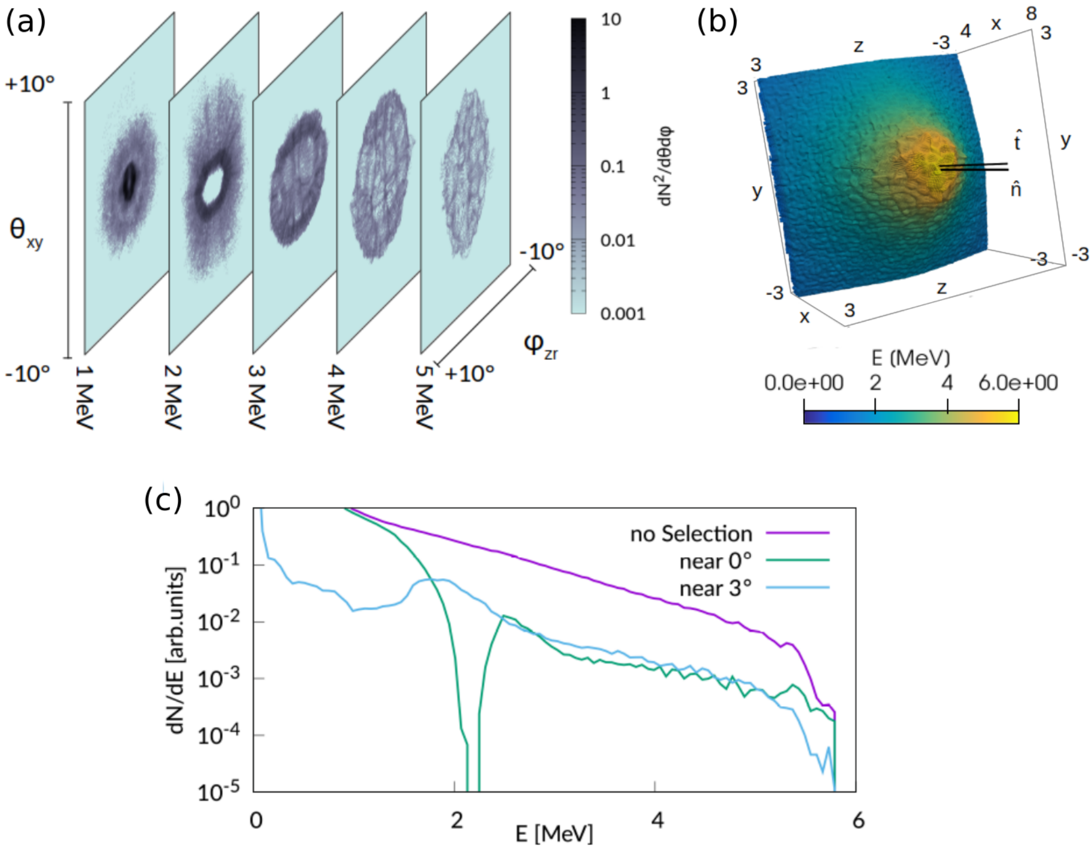

Figure 6.3: *3D Particle-In-Cell simulation results. (**a**) Angular and energy distribution of the protons for the* $a_0 = 4.0$ *case and retrieved at 267 fs. Each panel reports the angular distribution at the corresponding energy range. (**b**) Snapshot at 267 fs of the macro-protons for the* $a_0 = 4.0$ *case. Only the central region of the simulation box is shown, and the macro-protons are coloured according to their energy. The two black lines indicate the direction normal to the target surface (*$\tilde{n}$*) and the* 3° *tilted direction (*$\tilde{t}$*). (**c**) Energy spectra for all the protons (purple), for the protons propagating along* $\tilde{n}$ *(light blue) and* $\tilde{t}$ *(green).*

constant [266].

The main properties of the laser-driven proton source with $a_0 = 4$ are summarized in figure 6.3. The angular distributions in correspondence of different proton energies are shown in figure 6.3.a. At 2 MeV, a ring-like angular distribution is present, which results in a hole in the energy spectrum at 0° (see figure 6.3.c). Analogous distributions have been already observed in the literature [267]. The source was titled by 3° in the Monte Carlo simulation to irradiate the sample with a broader energy spectrum. It means that the laser pulse was at normal incidence at the target surface, but the laser axis (which corresponds to the target normal direction) was rotated by 3° to the beam handler axis.

The macro-proton positions and energies are reported in figure 6.3.b. They are forward peaked along the target normal direction. Lastly, figure 6.3.c shows the proton energy spectra at 0°, 3° and integrated over the emission angle. The cut-off energy is close to 6 MeV. To couple these results with the Monte Carlo, the macro-proton momentum distributions were retrieved for all the simulations.

6.3 Laser-driven PIXE quantitative analysis results

The quantitative PIXE analyses of the three scenarios described in Section 6.2 are presented. The compositions of the samples are reconstructed exploiting the χ^2 iterative algorithm discussed in Section 6.1.1.
Conventional PIXE measurements on delicate objects are carried out with beam currents of 10s of pA and irradiation times of 100s of seconds [268]. The $\sim 10^{10}$ total number of proton incident on the sample is coherent with actual beam parameters adopted in conventional PIXE. Considering protons with energy greater than 0.2 MeV, the transmission efficiency of the beam handling system is $\sim 10\%$. This value is evaluated assuming the case of in-air laser-driven PIXE and $a_0 = 2$, which is the most challenging condition. Thus, the laser-driven source should deliver 10^{11} protons with energy higher than 0.2 MeV at the laser-target interaction point. This condition is achievable with $\sim$ 10s of shots from a sub-100 TW laser working at high repetition (e.g. 1 Hz) [251]. In this scenario, the number of X-rays interacting with the CCD screen should be low enough to avoid the saturation of the instrument. A 10s TW class laser system can accelerate $\sim 10^9$ protons per laser shot. Thus, the massive Monte Carlo simulations are representative of a condition in which 10s of laser shots are integrated to collect the X-ray spectra.

6.3.1 Elemental concentrations in a homogeneous sample

The first scenario involves protons having a pure exponential energy spectrum (reported in figure 6.4.a) and few degrees of angular divergence. In figure 6.4.a, the actual concentrations and the retrieved ones are compared. For all the elements, the agreement is excellent and comparable to that of conventional PIXE, with a discrepancy always less than 1 %. However, this agreement has been achieved assuming perfect knowledge of the proton spectrum shape. Since laser-driven proton sources are affected by shot-to-shot fluctuations, they are characterized by a certain degree of uncertainty in the maximum energy and temperature. In principle, this uncertainty can limit the applicability of laser-driven PIXE. Therefore, its effect on the retrieved concentrations must be assessed. This evaluation can be easily performed for the simple case considered here.
By fixing the X-ray yields obtained from the Monte Carlo simulation and assuming different proton energy spectra, the iterative code was applied. More precisely, the proton energy spectrum was modelled as:

$$f_p(E_p, \alpha) = e^{-E_p/(\alpha \cdot T_{MC})} \Theta(E_p - \alpha E_{MC}) \tag{6.7}$$

Where E_{MC} and T_{MC} are the cut-off energy and temperature exploited in the Monte Carlo, respectively. The iterative code uses the correct proton energy spectrum with $\alpha = 1$. The value of α was varied between 0.8 and 1.2 to test the effects of the spectrum fluctuations (see figure 6.4.a) up to $\pm 20\%$. The results of this procedure are reported in figure 6.4.c. The graph shows the ratios between the concentrations obtained by varying α and those obtained with $\alpha = 1$. There is a mild dependence of the relative error as a function of the proton energy spectrum fluctuations. Indeed, even for $\pm 20\%$ error on the spectrum, the relative error on the retrieved concentrations keeps within $\pm 10\%$.

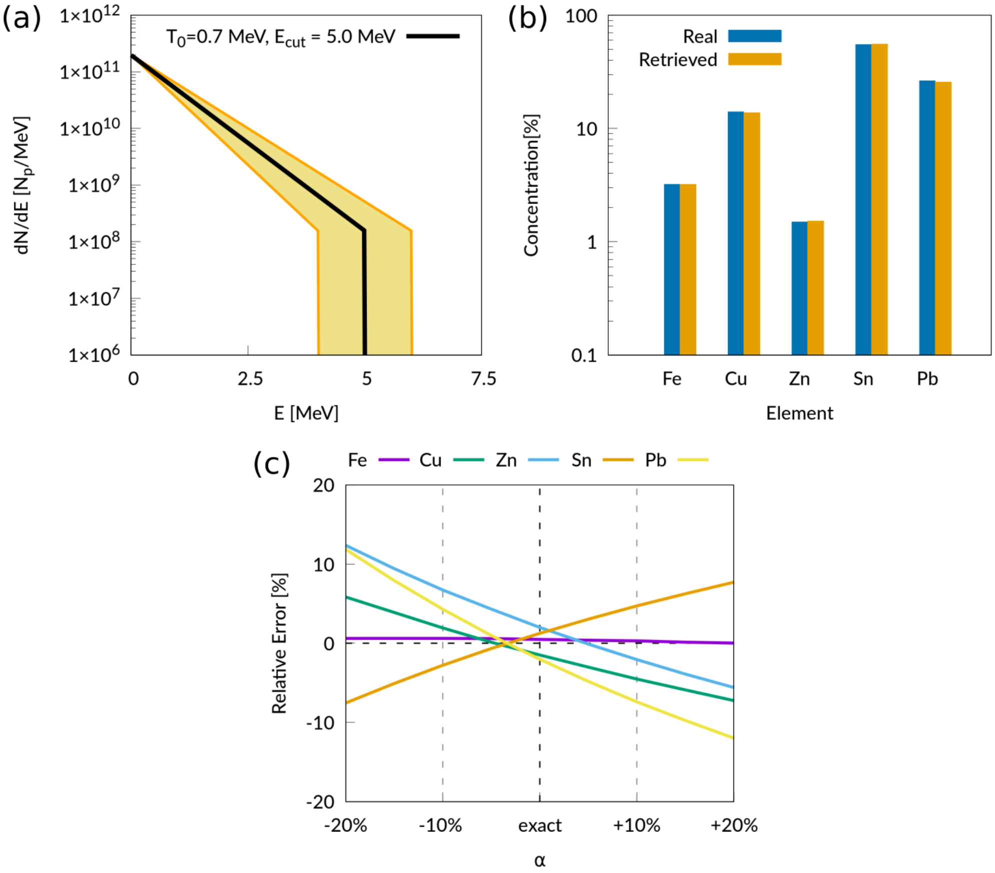

Figure 6.4: *Homogeneous sample analysis results. (**a**) Proton energy spectrum exploited for the Monte Carlo simulation (black line) and energy spectra interval used to obtain the elemental concentrations for the sensitivity analysis (yellow filled area). (**b**) Comparison between the retrieved and actual elemental concentrations. (**c**) The relative error for the retrieved concentrations as a function of the fluctuation parameter* α.

6.3.2 Differential PIXE analysis of non-homogeneous samples

In the second scenario, the proton source is represented by six different exponential energy spectra. The proton spectra at the sample surface are shown in figure 6.5.a. The inset graph reports the spot of the particles at the sample surface. The probed region on the sample is $\sim 1\ \mathrm{mm}^2$ (the result is identical for the homogeneous sample scenario). Such dimension is suitable for most of the applications [269]. Remarkably, the concentration profiles (see figures 6.5.b-f) show a good agreement with the original sample composition. Surface and bulk elements can be distinguished, and their concentrations are well predicted.

As previously discussed, the proton momentum distributions from six PIC simulations were used for the third scenario. The proton energy spectra and the particle spot size at the sample surface are reported in figure 6.6.a. As far as the concentration depth profile reconstruction considered here is concerned, the main difference compared to the previous case is that the X-ray peaks are associated with complex compounds rather than individual elements. Again, we have a satisfactory agreement (see figure 6.6.b-f).

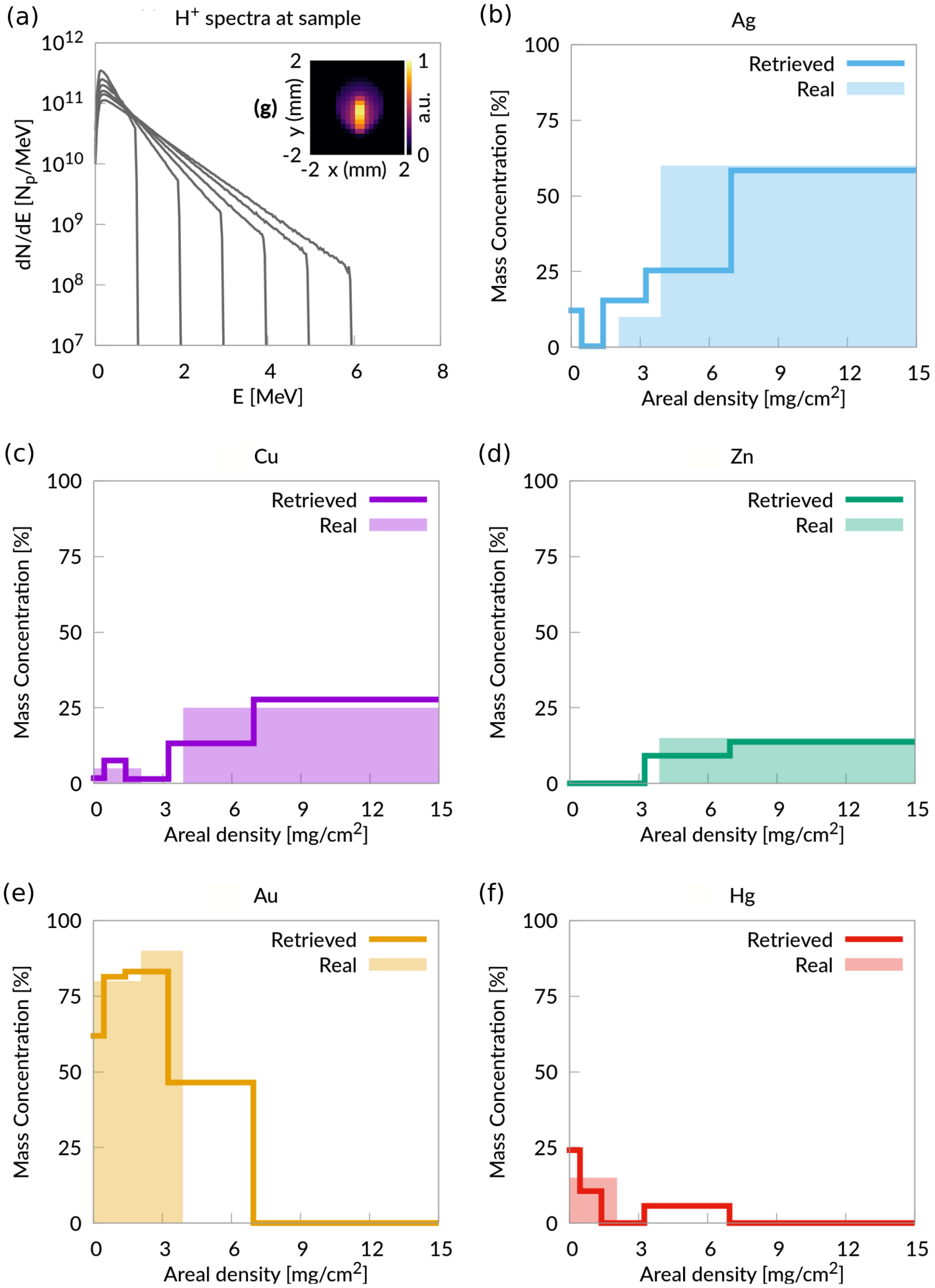

Figure 6.5: *Non-homogeneous metallic sample quantitative analysis. (**a**) Proton energy spectra at the sample surface. The inset graph reports the proton fluence at the surface of the sample. (**b-f**) Comparison between actual (filled regions) and retrieved (lines) concentration profiles.*

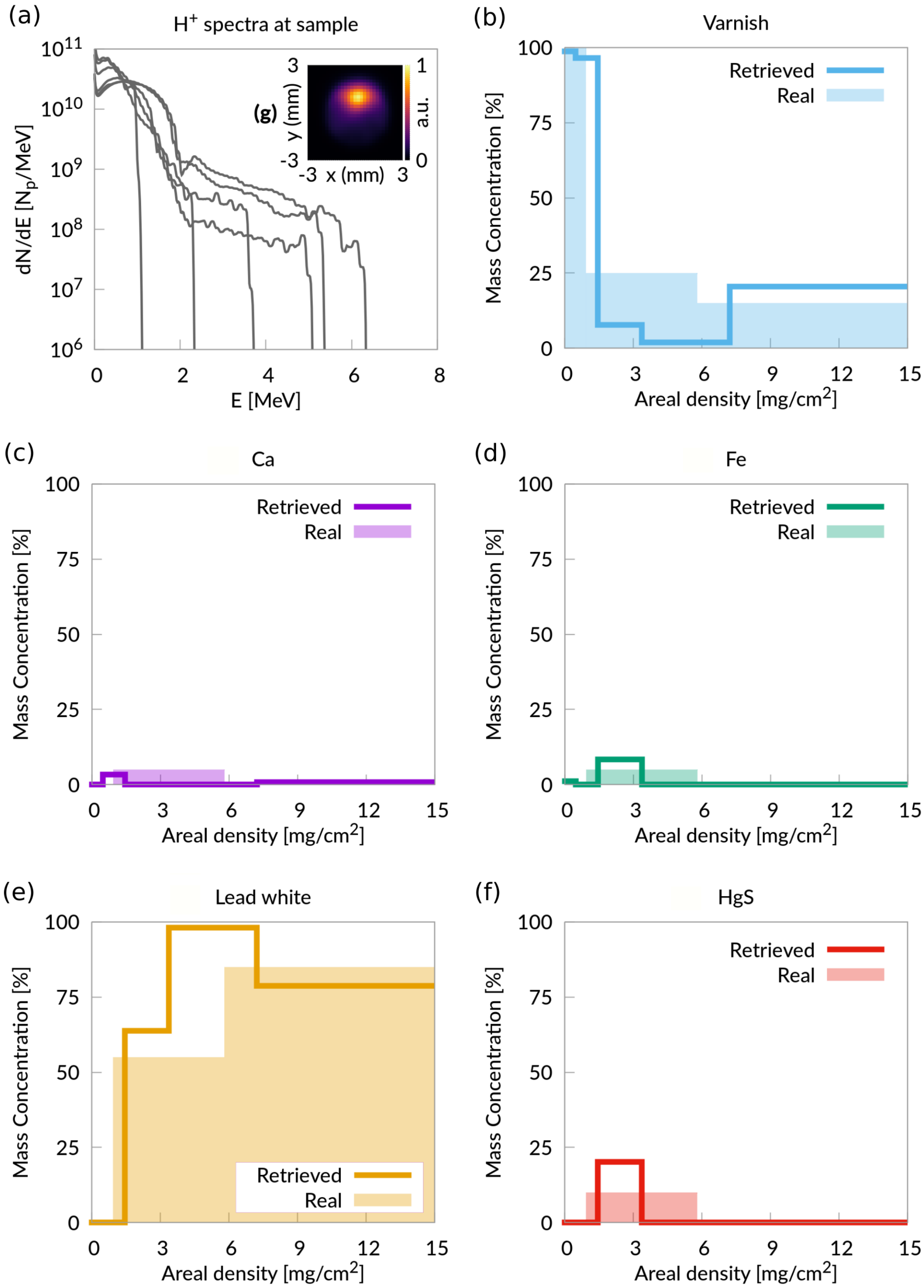

Figure 6.6: *Painting quantitative analysis. (**a**) Proton energy spectra at the sample surface. The inset graph reports the proton fluence at the surface of the sample. (**b-f**) Comparison between actual (filled regions) and retrieved (lines) concentration profiles.*

Indeed, the differential PIXE analysis allows identifying the superficial protective varnish, the intermediate layer where the pigment is present and the substrate. Thus, the considered setup, which relies on a 20 TW laser and a DLT, can be considered suitable for differential PIXE analysis of complex samples.
Lastly, the fact that the quantitative analysis converges to correct results for samples having very different structures (i.e. a metallic material and a painting) confirms the generality of the approach presented here.

6.4 Electron influence on laser-driven PIXE and laser-driven EDX

In addition to protons, laser-driven sources provide a large number of electrons. They are emitted with a broad angular distribution. The energy spectrum is quasi-exponential, extending from zero to several MeV (see Chapter 2 for details). The presence of electrons is a crucial aspect since, if not properly removed, they can induce characteristic X-ray emission, affecting the result of a laser-driven PIXE quantitative analysis. Therefore, Geant4 Monte Carlo simulations of sample irradiation with protons and electrons were performed to address this point. Two different setups were considered, i.e. in-vacuum and in-air sample irradiation. The second condition is reported schematically in figure 6.7.a.
The primary particles are generated 4 cm far from the sample. Protons are characterized by a pure exponential energy spectrum with temperature ad cut-off energy equal to 0.7 and 5 MeV, respectively. On the other hand, the exponential energy spectrum of the electrons has 5 MeV temperature and 15 MeV maximum energy. Protons and electrons have a uniform angular distribution between $\pm 10^\circ$ and $\pm 20^\circ$ to the sample normal direction, respectively. For each simulation, a total number of 10^9 protons and 10^8 electrons were considered. Between the source and sample, a protective 10.0 μm thick aluminium foil is present. The sample is constituted by a 2.25 μm thick chromium layer over a 1 mm thick copper substrate. The simulated setup includes a detection screen of lateral dimensions $2.5 \times 2.5 \text{ cm}^2$ for the detection of the emitted X-rays. It is placed 5 cm far from the sample tilted at 45° to the sample normal direction.
In figure 6.7.b, the simulated X-ray spectra in the $1 - 11$ keV energy range and obtained under proton and electron irradiation with the in-air setup are shown. They are normalized to the total number of incident electrons and protons. The X-ray emission due to the electrons covers the PIXE spectrum completely, both in terms of background and peaks. In addition, the bremsstrahlung background due to the electrons extends in the MeV energy range (see figure 6.7.c).
Lastly, figure 6.7.d summarizes the x-ray peak intensities for protons and electrons irradiation obtained both in-vacuum and in-air. Notably, the X-ray yields ascribable to the electrons are $1 - 2$ orders of magnitude higher than that due to protons. The reported results highlight that, if not removed, laser-driven electrons can irreparably distort the result of a laser-driven PIXE analysis. So, the removal of the electrons is mandatory and can be achieved by exploiting suitable dipole magnets (with magnetic field intensities of the order of a fraction of Tesla), as shown in the previous Section. This solution has been already tested in many experimental works [270–272].
Nevertheless, the co-emission of both ions and electrons is a peculiar feature of laser-driven radiation sources, which is not shared by conventional accelerators. This prop-

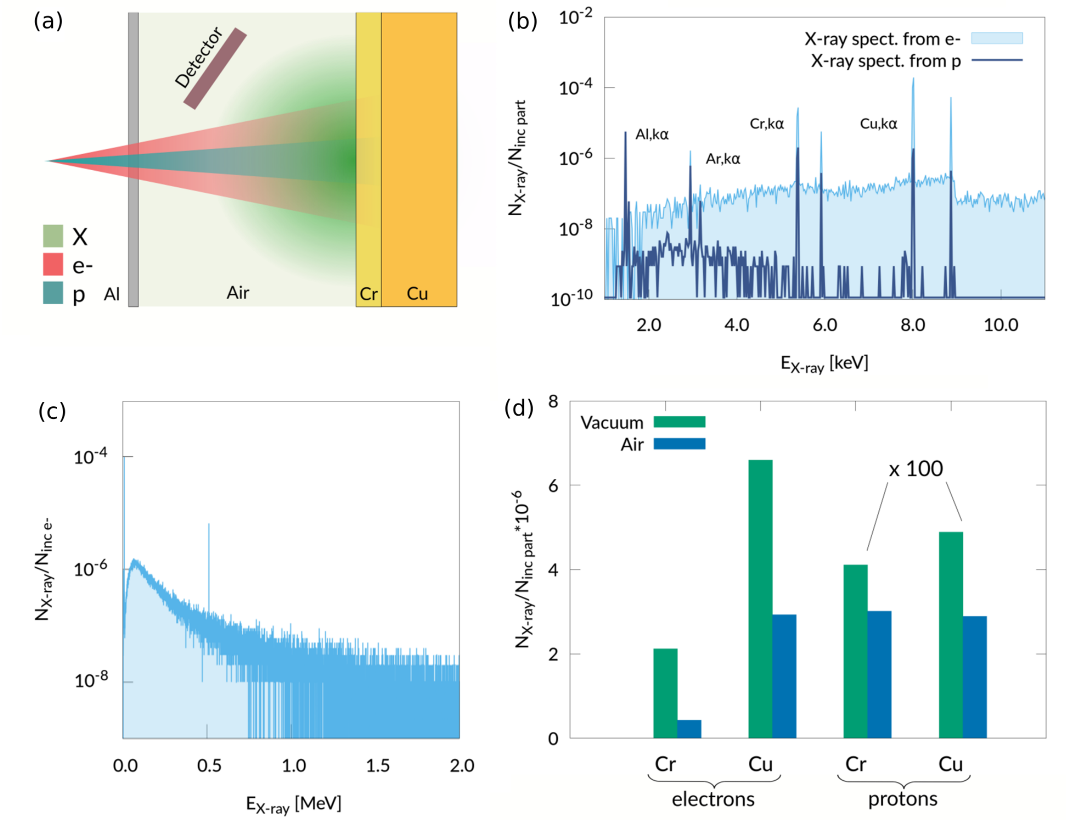

Figure 6.7: *(**a**) Simulation setup for laser-driven PIXE and electron irradiation in air. (**b**) Low energy region of the X-ray spectra from proton (dark blue) and electron (light blue) irradiation with the in-air setup. (**c**) Photon spectrum in the* $0-2$ *MeV energy range obtained by the simulation of electron irradiation in-air. (**d**) Comparison between the X-ray yields obtained under the different simulated irradiation conditions. The green and blue bars are related to the in-vacuum and in-air irradiation conditions, respectively.*

erty could be exploited for the elemental characterization of materials. Indeed, the characteristic X-ray emission induced by laser-driven electrons is exceptionally intense, paving the way for a faster element identification than that achievable with laser-driven PIXE. The irradiation with a mixed particle field should lead to a characteristic X-ray emission ascribable mainly to the electrons. Therefore, we call this configuration laser-driven EDX.

Compared to the state-of-the-art EDX analysis in which keV energy electrons are exploited, laser-driven EDX would be characterized by electrons in a wider range of energies (from keV up to several MeV). MeV electrons have a very long path length in gaseous materials (100s cm in the air). Thus, they could lead to the possibility of probing samples also in the air. Moreover, the wide range of MeV electrons in the solid matter can allow analyzing thick samples up to 100s μm thickness. At these energies, the electron impact ionization cross sections [273] for the Kα shells of heavy elements become considerably high. Besides, the associated X-rays are subject to weak attention in the material because their energies are of the order of several 10s of keV. These considerations suggest that laser-driven EDX could be exploited to identify heavy elements in light matrices down to mm depth, significantly expanding the capabilities of EDX. Compared to laser-driven PIXE and conventional EDX, the characterization of materials via laser-driven EDX might present some limitations. Indeed, the quantitative analysis requires a model to associate the X-ray yields, the composition of the material, and the energy spectrum of the primary particles. In the case of laser-driven electrons, the energy spectrum characterization is not trivial. Furthermore, MeV electrons are subject to many collisions, with continuous variation of their energy and direction. The collisions with orbital electrons result in the generation of secondary energetic electrons (δ-rays), while interactions with nuclei produce bremsstrahlung radiation emission. The unpredictability of the trajectories of the electrons and the generation of secondaries capable of inducing ionization do not allow easily describing the whole process. Thus, the X-ray spectrum obtained by a laser-driven EDX measurement can not be directly interpreted to retrieve quantitative information about the sample composition. To this aim, both reference samples and prior knowledge of the electron energy spectrum would be needed.

CHAPTER 7

Experimental investigation on laser-driven PIXE and laser-driven EDX

This Chapter describes the results of the proof-of-principle laser-driven EDX and PIXE experiment conducted during a three weeks experimental campaign at the Centro de Làseres Pulsados (CLPU) in Salamanca, Spain. The sample under investigation was constituted by a bi-layer structure (i.e. thick substrate covered by a thin film). The experiment was aimed at performing the identification of the elements (i.e. the elemental analysis) exploiting both laser-driven EDX and PIXE, as well as the measurement of the layer thickness (i.e. quantitative analysis) via laser-driven PIXE.
Section 7.1 presents the experimental setup, the sample under investigation, the diagnostics exploited to characterized the laser-driven protons and to detect the characteristic X-rays. In Section 7.2, the experimental results of the laser-driven EDX elemental analysis and laser-driven PIXE quantitative analysis are shown and discussed. Lastly, Section 7.3 describes a numerical investigation, via Monte Carlo simulations and analytical calculations, aimed at supporting and validating the experimental results.

7.1 Laser-driven EDX and PIXE experimental apparatus

Two in-vacuum irradiation setups were adopted to perform both laser-driven PIXE and EDX, exploiting at best the laser-driven charged particle source. With the so-called LD-EDX setup, the sample was co-irradiated with both electrons and protons. On the other hand, the LD-PIXE setup allows removing the electrons, and the material was irradiated mainly by protons.
Both experimental configurations exploit the 200 TW laser pulse provided by the Vega-2 laser system [274]. The pulse is characterized by a 30 fs time duration and P-polarization. The energy on target is 3 J, and the spot size full width at half maximum

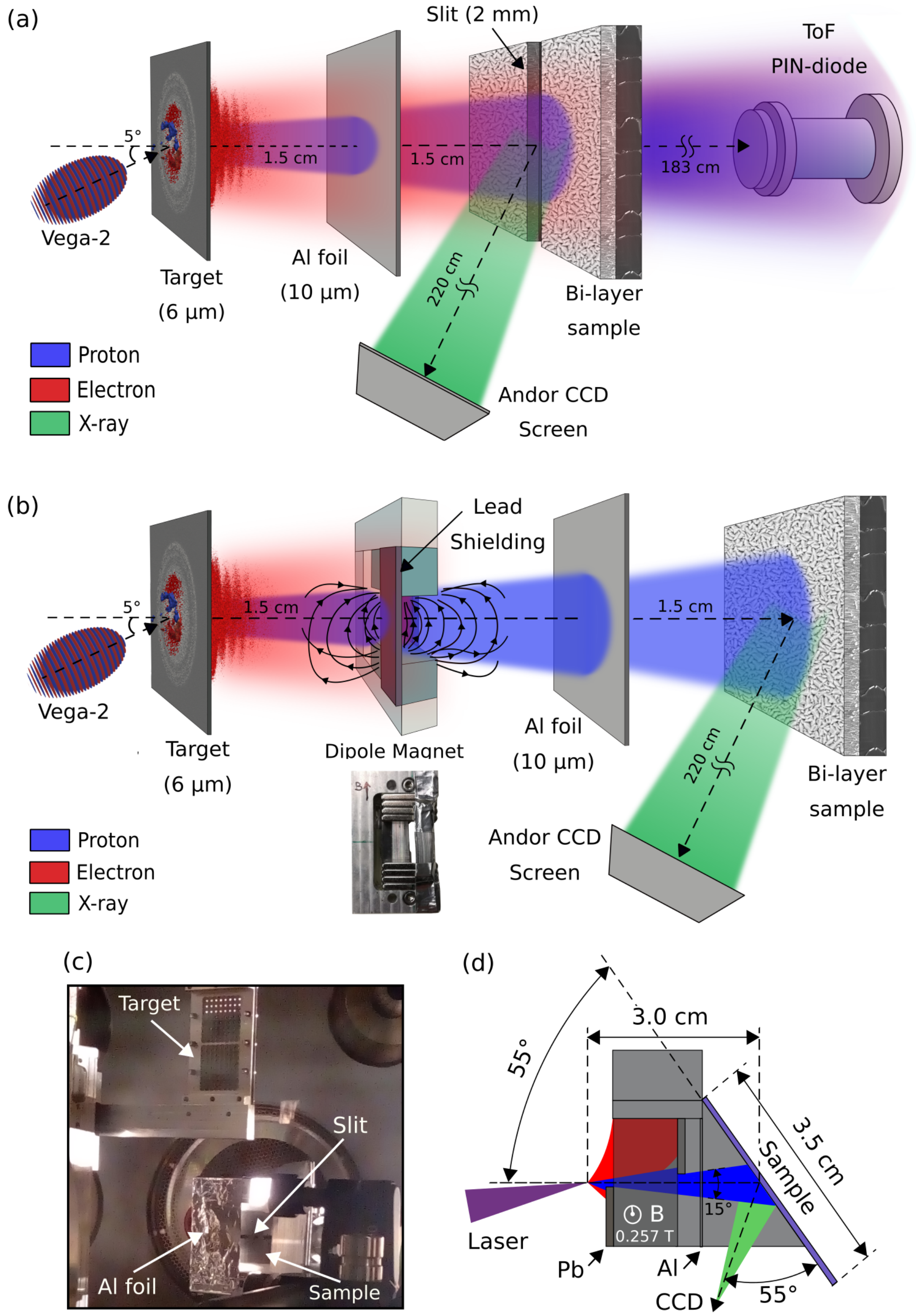
(a)
Slit (2 mm)
ToF
PIN-diode
5°
1.5 cm
1.5 cm
183 cm
Vega-2
Target
(6 µm)
Al foil
(10 µm)
220 cm
Bi-layer
sample
Andor CCD
Screen
🟦 Proton
🟥 Electron
🟩 X-ray
(b)
Lead
Shielding
5°
1.5 cm
1.5 cm
Vega-2
Target
(6 µm)
Dipole Magnet
Al foil
(10 µm)
220 cm
Bi-layer
sample
Andor CCD
Screen
🟦 Proton
🟥 Electron
🟩 X-ray
(c)
Target
Slit
Al foil
Sample
(d)
55°
3.0 cm
3.5 cm
Sample
B
0.257 T
15°
Laser
Pb
Al
CCD
55°

Figure 7.1: *Conceptual representations of the (**a**) LD-EDX and (**b**) LD-PIXE experimental setups. (**c**) Image of part of the LD-EDX setup. The movable target holder, protective Al foil, irradiated sample and aperture slit are pointed with arrows. (**d**) Top view scheme of the LD-PIXE setup. All distances and angles are reported.*

is 7.0 μm, resulting in an intensity equal to $\sim 2 \times 10^{20}$ $\mathrm{W/cm^2}$. The angle of incidence to the target normal direction is 5°.

The LD-EDX and LD-PIXE setups are schematically reported in figures 7.1.a and 7.1.b, respectively. In both cases, the pulse was made to interact with a 6.0 μm thick aluminium foil placed inside a target holder. Between the target and sample, we interposed a 10.0 μm thick aluminium foil to stop the debris produced by the laser-target interaction and the highly charged carbon ions. The characteristic X-rays emitted from the sample were detected employing a CCD camera. The experimental setups were designed to allow post-processing, single-photon counting spectrum reconstruction [263, 275].

The LD-EDX setup had the dual purpose of irradiating the sample and characterizing the accelerated protons. Therefore, a 2 mm aperture slit was present in the middle of the sample. So, a small fraction of protons could reach the ion diagnostics in the LD-EDX setup. The vacuum chamber region, where the target and sample were located, is shown in figure 7.1.c. The target, Al sheet and sample slit are visible. On the other hand, in the LD-PIXE setup, the sample is not split. Moreover, a 0.26 T dipole magnet combined with lead shields was present after the Al foil to remove the electrons. The dimensions of the components, distances and angles are reported in figure 7.1.d.

7.1.1 Sample production via DCMS

The sample is made of a 2.2 μm thick layer of chromium on a 1 mm thick substrate of pure copper. Oxygen is also present in the Cr layer with a percentage $\sim 7\%$ mass faction. The cross section and planar views of the sample are shown in figure 7.2.

To ensure a precise knowledge of the sample properties, the Cr layer was grown on the Cu substrate via the Magnetron Sputtering deposition system (operated in DCMS mode) exploited in the first part of this thesis for the Ti targets production. A description of the machine and general aspects of the DCMS deposition technique are provided in Section 3.2. DCMS allows growing planar films on large surface areas (i.e. several $\mathrm{cm^2}$). The deposition was performed with Argon as working gas at a pressure of $\sim 9 \times 10^{-3}$ mbar. The applied voltage, current and power were equal to 600 V, 2 A and 600 W, respectively. The deposition lasted 56 minutes. The overall process was broken into several steps to avoid the delamination of the film. Indeed, delamination can occur because of the onset of strong stresses [276] induced by a long deposition time.

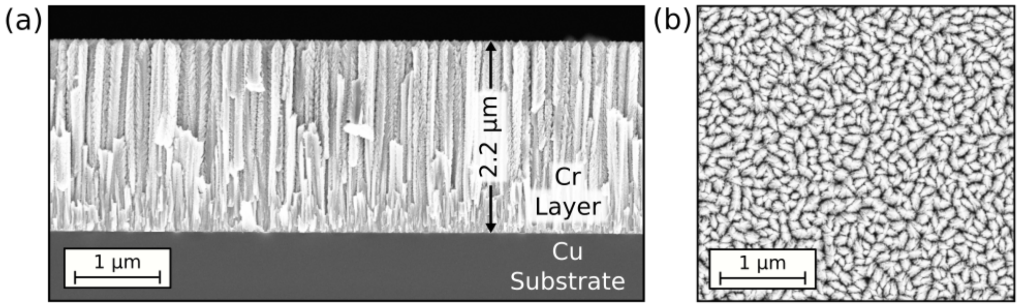

Figure 7.2: *SEM images of the sample. (**a**) Cross section view. The thickness is reported. (**b**) Planar view.*

The Cr layer density was measured exploiting two distinct methods, which provided the same result of 5.3 $\mathrm{g/cm^3}$. They are conventional EDX [249], and the weight difference between the sample and bare substrate. The actual thickness, planarity and morphology were characterized employing SEM images (see figure 7.2). The sample exhibits the columnar structure typical of metallic films deposited using the DCMS technique.

7.1.2 Proton energy spectra characterization

The proton energy spectra were characterized by exploiting a Time-of-Flight (ToF) spectrometer placed along the target normal direction and aligned with the sample slit in the LD-EDX setup (see figure 7.1.a). The diagnostic is constituted by a 1.0 ns time-resolved pin diode detector placed at $L = 186$ cm far from the target. An overall number of 166 ToF measurements were taken from as many shots. The proton energy spectra were reconstructed from each signal following the approach provided by *Milluzzo et al.* [277] and valid for semiconductor detectors.
Figure 7.3.a shows an example of ToF signal. The photopeak due to UV radiation and low energy X-rays is used to set the instant of time t at which the particles are emitted

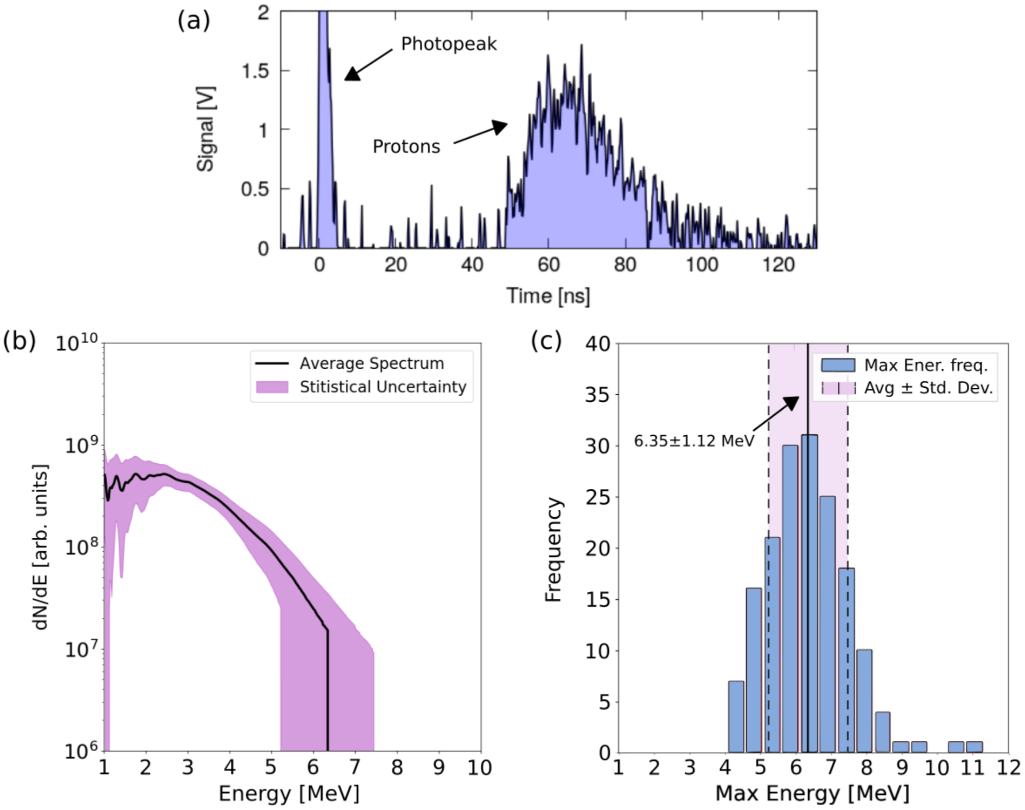

Figure 7.3: *(**a**) Example of ToF signal acquired during the experiment. The photopeak and the proton signal are pointed with arrows. (**b**) Proton energy spectrum recorded with the ToF diagnostic. The continuous black line is the average spectrum, while the purple area is the statistical uncertainty. (**c**) Frequency distribution of the maximum proton energy. The continuous vertical line is the average value. The purple bandwidth is equal to two times the standard deviation.*

equal to zero. Following the reasoning in [277], the energy spectrum is evaluated as:

$$\frac{dN}{dE_p} \propto \frac{V(t)}{E_p}\left(-\frac{1}{2}t - \delta t\right) \tag{7.1}$$

Where $V(t)$ is ToF signal, E_p is the proton energy, and δt is time step. The proton energies is derived from:

$$E_p = m\left(\frac{1}{\sqrt{1-\beta^2}} - 1\right) \tag{7.2}$$

with $\beta = L/(ct)$, where c is the speed of light, and m is the proton mass. It is worth noting that, in equation 7.1, the energy spectrum is only proportional to the ToF signal. Indeed, the detector absolute calibration was not provided. Therefore, the number of collected particles was not retrieved. However, the total number of protons is not required to perform the quantitative laser-driven PIXE analysis. To this aim, only the shape of the spectrum is needed.

The proton energy spectrum averaged over the 166 shots is shown in figure 7.3.b. Coherently with the mentioned consideration, no absolute calibration is provided on the vertical axis. The uncertainty is reported as the superposition of two contributions, i.e. the uncertainty on the signal for each energy value and the uncertainty on the maximum proton energy. In addition, figure 7.3.c shows the maximum proton energy distribution. It is centred in 6.35 MeV, and its statistical uncertainty is equal to 1.12 MeV (evaluated as 2σ, where σ is the standard deviation).

7.1.3 X-ray spectra reconstruction and CCD energy calibration

CCDs are widely exploited for spectroscopy in laser-plasma interaction experiments [263, 278, 279]. Here, the CCD was an Andor IKon-M D0934P-BN CCD camera with 1024×1024 pixels. The CCD screen was protected with lead shields from the flash radiation emitted at the laser-target interaction point. The screen was further protected by a 2.0 μm thick Mylar and a 6.0 μm thick aluminium foil. A magnification of a CCD image is shown in figure 7.4.a. Single-pixel events can be distinguished. They correspond to photons that release all their energy in the active volume of single pixels. The photons are converted into electron-hole pairs, and the charge is turned into a voltage signal.

The spectrum reconstruction was performed considering the 3×3 pixels surrounding a chip whose intensity (i.e. the collected charge converted to signal voltage) is higher than a given threshold (see figure 7.4.b). The threshold was set equal to 3σ, where σ is the standard deviation of the Gaussian distribution of all pixel intensities. With this threshold, the probability of distinguishing a significant event from the dark noise is 99.7%. Only single-pixel events were considered. Indeed, multi-pixel events (i.e. photons interacting with more than one pixel) are extremely rare. Moreover, they are associated mainly with X-rays having energies higher than 10 keV. These photons are not of interest to the aims of this work.

The CCD energy calibration was performed exploiting the LD-EDX setup and a pure Cu sample. The average spectrum recorded with 16 shots is reported in figure 7.4.c. The local background distribution was evaluated for each single-pixel event (i.e. the average intensity related to the eight surrounding pixels). The distribution is shown in

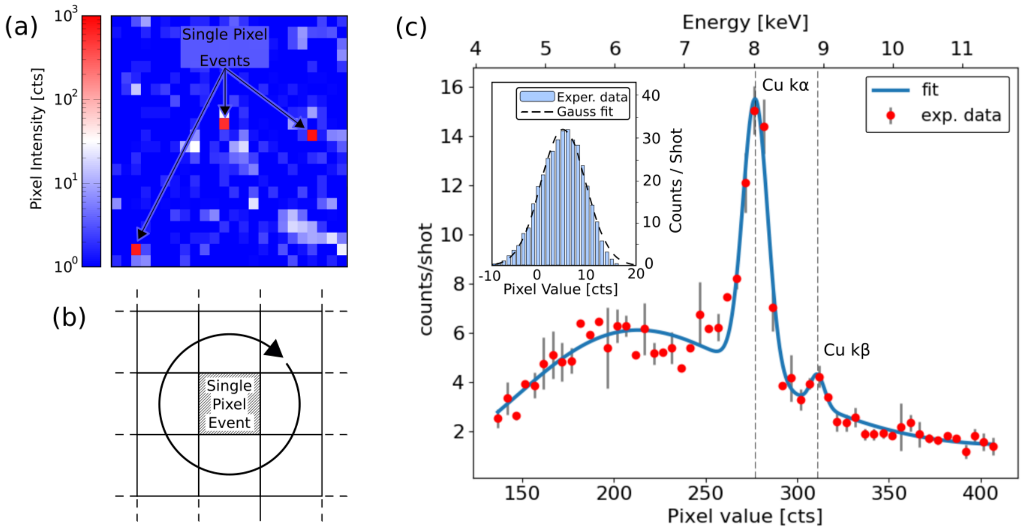

Figure 7.4: *(**a**) Magnification of a recorded CCD image. Single-pixel events are pointed with arrows. (**b**) Representation of the single-pixel event and surrounding pixels considered for the spectrum reconstruction. (**c**) X-ray spectrum obtained from the Cu sample irradiation and exploited for the CCD energy calibration. The inset plot shows the intensity distribution of the local background around single-pixel events.*

figure 7.4.c as an inset graph. As expected, it has a Gaussian shape centred around $0 - 10$ cts (i.e. charge to signal voltage). Since the characteristic X-ray peak intensities are at 100s of cts, the local background contribution was neglected, and the CCD was calibrated considering the absolute position of the $\mathrm{k}\alpha$ peak of Cu at 8.048 keV. The resulting calibration factor is equal to $8.048\ \mathrm{keV}/277\ \mathrm{cts} = 0.029\ \mathrm{keV}/\mathrm{cts}$.

7.2 Laser-driven EDX and PIXE experimental results

This Section starts with the discussion of the laser-driven EDX spectrum. The aim is to identify the elements present in the sample (i.e. elemental analysis). Then, the laser-driven PIXE quantitative analysis is shown. As extensively described in the previous Chapter, laser-driven PIXE can provide much information about the sample structure. Here, since the superficial layer and the substrate are monoelemental, the quantitative analysis was performed to retrieve the Cr layer thickness. Thus, for this specific case, the procedure is called stratigraphic analysis.

7.2.1 Elemental analysis

The sample was irradiated with 42 particle bunches exploiting the LD-EDX setup. Figure 7.5.a shows the recorded X-ray spectrum per unit of shots. Clear peaks rise over the continuous background. The spectrum was fitted with the Levenberg-Marquardt least-squares fitting algorithm [224], which is a standard method for the spectra interpolation in X-ray spectroscopy. The X-ray peaks were modelled as Gaussian functions. The background was fitted with an exponential polynomial of third-order [280]. The fitted peaks after the background subtraction are also plotted.

In the case of Cu, both the $\mathrm{k}\alpha$ and $\mathrm{k}\beta$ lines are present. On the other hand, the Cr $\mathrm{k}\beta$

peak cannot be distinguished because of the partial superposition with the kα line and the presence of a strong background. As far as the oxygen is concerned, the detection efficiency of the shielded CCD is too low at the X-ray energy corresponding to the kα line of this element. The energies of the X-ray peaks are listed in figure 7.5.b. They are very close to the values reported in the literature (the relative error is always less than 2%). The elements are identified uniquely from the peak energies and, therefore, laser-driven EDX provides a correct elemental analysis.

As extensively discussed in Section 6.4, laser-driven EDX cannot be directly exploited to retrieve quantitative (e.g. stratigraphic) information about the sample composition. To this aim, a laser-driven PIXE analysis must be carried out. The laser-driven PIXE spectrum obtained with 16 laser shots is reported in figure 7.5.c. In addition to the Cr and Cu characteristic peaks, the Pb kα line is also present. It is due to the lead shields added in the LD-PIXE setup to stop the electrons. Moreover, a weak signal at 6.3 keV can be recognized, probably related to the iron in the magnet.

Again in the case of laser-driven PIXE, both the Cr and Cu elements are recognized correctly. However, the X-ray peak intensities per laser shot are $\sim$ 10 times lower than those obtained with laser-driven EDX. This result is coherent with the analysis

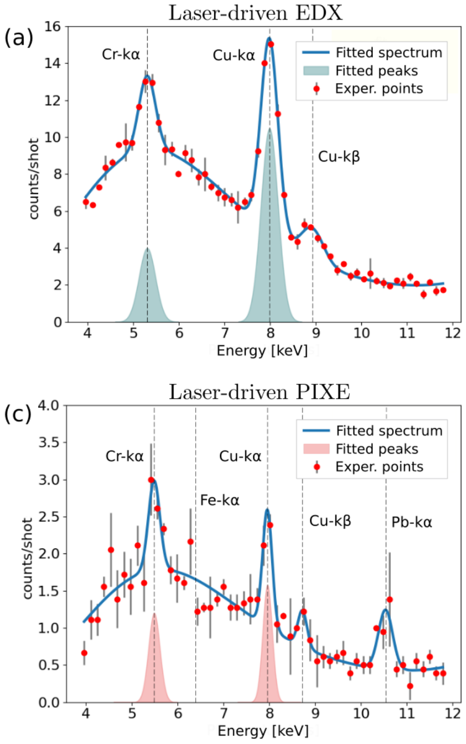

(b)

X-ray lines [keV]	Literature energies [keV]	LD-EDX (Cu)	LD-EDX (Cr, Cu)	LD-PIXE (Cr, Cu)
Cr-Kα	5.414	∼	5.31	5.49
Cr-Kβ	5.94	∼	∼	∼
Cu-Kα	8.048	8.048	7.99	7.95
Cu-Kβ	8.905	8.94	8.94	8.72
Pb-Kα	10.551	∼	∼	10.54
Intensity ratio (Cr/Cu)	∼	∼	0.37 ± 0.0207	0.91 ± 0.1687

Figure 7.5: *Laser-driven EDX and PIXE results. (**a**) X-ray spectrum obtained with the LD-EDX setup. The red points are the average over the shots of the photon counts at each energy. The error bars are evaluated as two times the standard deviation. The fit is represented as a blue line. The filled curves are the Gaussian fits of the peaks. (**b**) Summary of the X-ray peak energies and intensity ratios of Cr and Cu* kα *peaks. In the first column, the expected X-ray energies from the literature are reported. The second, third and fourth columns are associated with the X-ray spectra exploited for the CCD energy calibration and from the sample irradiation with the LD-EDX and LD-PIXE setups, respectively. (**c**) X-ray spectrum obtained with the LD-PIXE setup.*

described in Section 6.4. Thus, laser-driven EDX allows performing the elemental analysis with a lower number of shots than laser-driven PIXE.

7.2.2 Stratigraphic analysis

The model and the iterative procedure described in Section 6.1 were exploited to perform the stratigraphic analysis. For the specific case considered here, the ratio between the X-ray yields (see equation 6.1 for the general form) can be evaluated as:

$$\frac{Y_{Cr}}{Y_{Cu}} = \frac{\epsilon_{Cr}\cdot M_{Cu}\cdot W_{Cr}}{\epsilon_{Cu}\cdot M_{Cr}\cdot W_{Cu}} \times \frac{\int_{E_{p,max}}^{E_{p,min}} f_p \int_{E_{p,outCr}}^{E_p} \sigma_{Cr}\omega_{Cr}A_{Cr}\frac{dE}{S_{Cr}}dE_p}{B\cdot\int_{E_{p,max}}^{E_{p,min}} f_p \int_0^{E_{p,outCr}} \sigma_{Cu}\omega_{Cu}A_{Cu}\frac{dE}{S_{Cu}}dE_p} \tag{7.3}$$

where Y_{Cr}/Y_{Cu} is the ratio between the areas of the Cr and Cu $\mathrm{k}\alpha$ peaks. Except for A_{Cr} and B, the general definitions of the involved physical quantities have been already provided in Section 1.3.2. They are specified for the Cr and Cu elements with subscripts in equation 7.3. The proton spectrum shape is reported in figure 7.3. The A_{Cr} term represents the attenuation of the X-rays in the Cr layer, and its expression is:

$$A_{Cr}(E) = e^{-\mu_{Cr}\int_E^{E_p}\frac{dE'}{S_{Cr}(E'}\cdot\frac{\cos\theta}{\cos\phi}} \tag{7.4}$$

where $\theta = 35°$ is the proton incidence angle, and $\phi = 35°$ is the X-ray emission angle to the target normal direction. The attenuation of the Cu X-rays in the Cr film is modelled as:

$$B = e^{-\left(\frac{\mu}{\rho}\right)_{Cr-Cu}\frac{(\rho t)_{Cr}}{\cos\phi}} \tag{7.5}$$

and $(\mu/\rho)_{Cr-Cu}$ is the mass attenuation coefficient of the Cu X-rays in the Cr film. Since both Y_{Cr}/Y_{Cu} and f_p are known as experimental data, the iterative code can be applied to find the mass thickness $(\rho t)_{Cr}$ of the Cr layer. Y_{Cr} and Y_{Cu} were evaluated as the areas subtended by the Gaussian peaks after background subtraction. Their ratio is reported in the last row of figure 7.5.

The comparison between the sample cross section and the retrieved thickness from the laser-driven PIXE analysis is shown in figure 7.6. Assuming a pure Cr film and Cu substrate (i.e. neglecting the oxygen in the film), the layer thickness results in 1.90 ± 0.39 μm. On the other hand, considering a film composed of 7% O and 93% Cr, the thickness is estimated to be equal to 2.01 ± 0.39 μm, which is even closer to the actual value of 2.2 μm. The laser-driven PIXE measurement provides a satisfying estimation of the layer thickness. As described in the following Section, the error was calculated accounting for the uncertainties on the X-ray yields and the proton spectrum.

In figure 7.6, the thickness obtained considering the yield ratio from the laser-driven EDX measurement (see figure 7.5.c) is reported as well. The procedure for the thickness evaluation is the same, but under the assumption of ignoring the electron contribution in the laser-driven PIXE measurement. In this case, the estimated thickness results 0.98 ± 0.16 μm, strongly underestimating the actual value. This result is because electrons travel in the matter for longer distances compared to the proton path length. Therefore, they generate X-rays deeper in the sample, and they unbalance the yield ratio in favour of Cu.

The results presented in this Section provide experimental confirmation of many of the

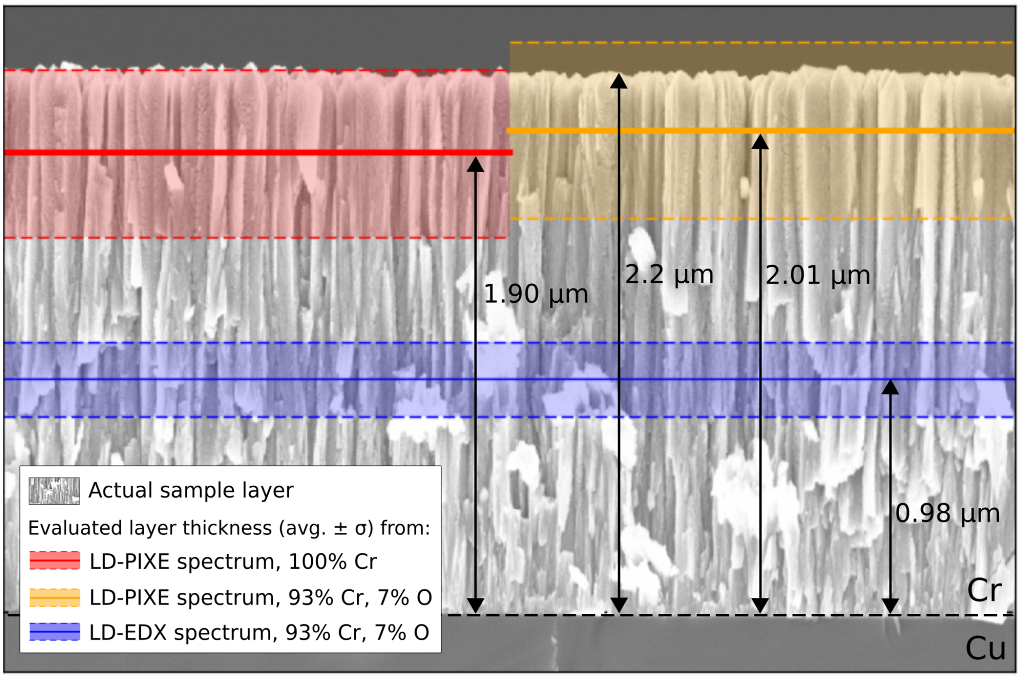

Figure 7.6: *Laser-driven PIXE stratigraphic analysis results. The red and yellow lines represent the layer thicknesses obtained assuming a pure Cr film and a 93% Cr plus 7% O film, respectively. The blue line is the thickness retrieved with the yield ratio from the laser-driven EDX measurement. The colour-filled regions are the statistical uncertainties.*

considerations made in the previous Chapter. First of all, because of the strong X-ray signal, the recommended technique for a fast elemental analysis is laser-driven EDX. Because of the high energy electrons, it should allow also recognizing the presence of elements deeper inside samples compared to laser-driven PIXE.

On the other hand, quantitative analysis can be achieved via laser-driven PIXE, and the removal of the electrons is mandatory. The knowledge of the total number of incident protons is not required to perform the quantitative analysis. Lastly, thanks to a suitable theoretical description of laser-driven PIXE, the monochromaticity of the accelerated protons is no longer necessary.

It is worth noting that the results obtained with a 200 TW laser could be replicated exploiting compact 10s TW class lasers [74, 116] and advanced target configurations (e.g. the DLTs presented in Section 2.3.2). Indeed, they can accelerate protons up to maximum energies $\sim$ 6 MeV with 10s TW systems.

As shown in Chapter 2, laser-driven radiation sources offer many solutions to tune the energy of the accelerated ions. For instance, the maximum energy and temperature can be reduced by decreasing the laser intensity [256] or fixing the laser power and increasing the target thickness [74]. In addition, the maximum energy and number of accelerated particles can be enhanced by exploiting the DLTs. Therefore, the possibility to modify the proton energy spectrum could be exploited to perform differential PIXE on complex samples, as shown in the previous Chapter.

Uncertainty evaluation via Monte Carlo approach

To properly combine the uncertainties on the proton spectrum $f_p(E_p)$ and yield ratio Y_{Cr}/Y_{Cu}, the error on the layer thickness was retrieved exploiting a Monte Carlo approach. The thickness was evaluated many times with the iterative code. At each evaluation, the input $f_p(E_p)$ and Y_{Cr}/Y_{Cu} are varied according to their uncertainties. The $f_p(E_p)$ were extracted from the set of experimental spectra. The values for Y_{Cr}/Y_{Cu} were sampled from a Gaussian distribution. The average values are 0.91 and 0.37, and the standard deviations are 0.1687 and 0.0207 for the laser-driven PIXE and laser-driven EDX, respectively. The thickness statistical distribution was obtained with 10^3 Monte Carlo cycles. It is shown in figure 7.7.a for the laser-driven PIXE measurement. In agreement with the central limit theorem, the distribution tends to a Gaussian function. Its standard deviation is the thickness error.

All data obtained with the Monte Carlo procedure are represented with a scatter plot in figure 7.7.b. The representation is particularly suitable to compare the different contributions from $f_p(E_p)$ and Y_{Cr}/Y_{Cu} to the total uncertainty. Thicknesses obtained in correspondence of the average proton spectrum (red dots) and average yield ratio (green dots) are plotted over the heat map. The thickness ranges covered by the green and red points along the vertical axis are similar. Accordingly, the uncertainties on $f_p(E_p)$ and Y_{Cr}/Y_{Cu} contribute evenly to the thickness error.

In light of these results, the error can be reduced by performing a longer measurement (i.e. increase the number of shots), optimizing the X-ray detection system or improving the proton source reproducibility. The latter can be done by optimizing the target and increasing the shot-to-shot stabilization of the laser pulse. An additional small source of error is due to the partial superposition of the kα and kβ X-ray peaks of Cr. A detector with better energy resolution must be exploited to avoid this issue.

Lastly, a small fraction of the electrons could still interact with the sample during the laser-driven PIXE measurement. They could slightly contribute to the X-ray yields and

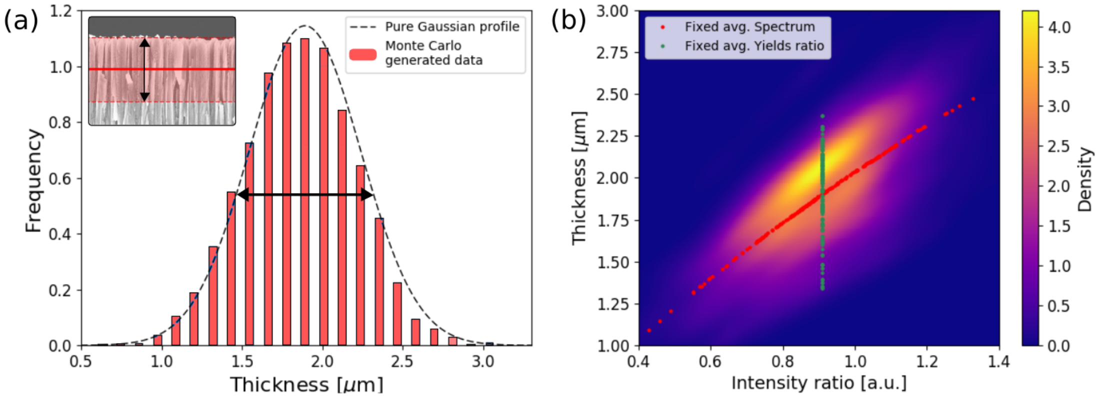

Figure 7.7: *Thickness uncertainty evaluation for the laser-driven PIXE measurement. (**a**) Frequency distribution of the thickness. The related uncertainty is reported in the inset graph. (**b**) Heat-map representing the scattered data from the Monte Carlo. The horizontal axis reports the intensity ratio, while the evaluated thickness is located on the vertical axis. The colour scale represents the number of occurrences. The green dots were obtained at fixed intensity ratio (equal to the average value). The red dots were obtained at a fixed proton energy spectrum (the average one).*

alter the calculated thickness. This point is addressed in the following Section exploiting Geant4 Monte Carlo simulations and analytical calculations.

7.3 Evaluation of the electron influence on laser-driven PIXE

In light of the results shown in the previous Section, a detailed characterization of the system used to remove the electrons in the LD-PIXE setup is required. Indeed, the calculated thickness underestimates the real one of $\sim 10\%$. As previously mentioned, few electrons could pass through the magnet without being stopped by the lead shielding. Thus, the fraction of characteristic X-rays generated by the electrons compared to the amount due to protons must be evaluated. To this aim, Geant4 simulations of the electron and proton propagation in both setups, the interaction with the sample and X-ray generation were performed.

To correctly describe the particle propagation in the LD-PIXE setup, the Geant4 simulations must include the realistic magnetic field configuration. Accordingly, the 3D magnetic field distribution was calculated with a magnetostatic Finite Elemental Analysis (mFEA) simulation.

7.3.1 Finite Element Analysis of the magnetic field configuration

The static magnetic field generated by the structure reported in figure 7.8.a was simulated in 3D with the finite element library Sparselizard [281]. An example of a magnetostatic problem solved in 2D is present in the code libraries. Briefly, without currents, the Maxwell equations give $\nabla \times \mathbf{H} = 0$, where $\mathbf{H}$ is the magnetic field intensity. The magnetic scalar potential ϕ can be defined as $\mathbf{H} = \nabla\phi$. Since $\nabla \cdot \mathbf{B} = 0$, the scalar potential can be derived from:

$$\nabla \cdot (\mu(-\nabla\phi)) = 0 \tag{7.6}$$

with $\mathbf{B} = \mu\mathbf{H}$, where μ is the permeability of the medium. Inside the magnet, the assumption is that the material is pre-magnetized by a magnetization vector $\mathbf{M}$ and,

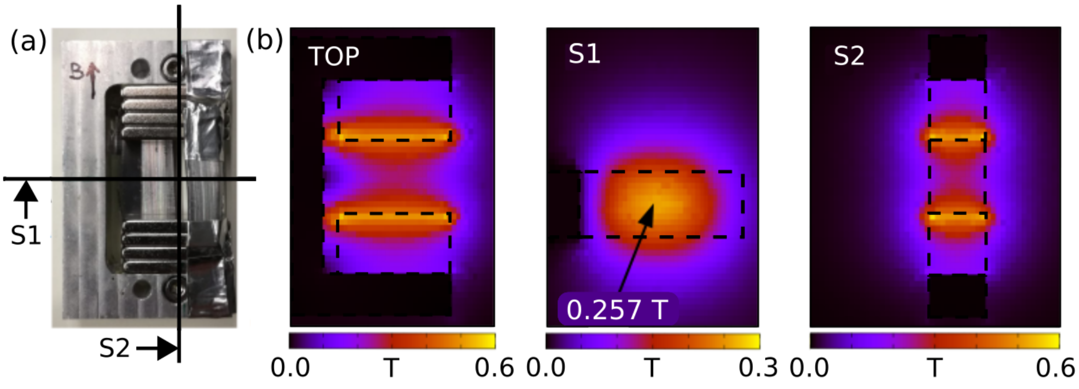

Figure 7.8: *(**a**) Top view of the component for the removal of the electrons and (**b**) slices of the magnetic field intensity distribution calculated with the mFEA simulation. The TOP slice is parallel to the top view, and it crosses the centre of the magnet. In the first panel, the position of the S1 and S2 slices are pointed with arrows.*

therefore:

$$\nabla \cdot (\mu_0(-\nabla\phi) + \mu_0 \cdot \mathbf{M}) = 0 \tag{7.7}$$

The magnets were characterized by a magnetization equal to 8.0×10^5 A/m. The permeability was $4\pi \times 10^{-7}$ H/m in the vacuum and the magnets. In the metallic support, a value equal to $4\pi \times 10^{-4}$ H/m was assumed. The structure was placed at the centre of a $10 \times 10 \times 10\ cm^3$ cubic box. The spacial mesh of $\sim 2 \times 10^5$ nodes was generated with the Gmsh code [282]. The magnetic scalar potential was fixed equal to zero in one node at the corner of the metallic support. This boundary condition is necessary to have a well-posed problem.

Figure 7.8.b shows the calculated magnetic field intensity in three different sections. The value at the centre of the system is equal to 0.26 T, and it coincides with the intensity measured experimentally.

7.3.2 Monte Carlo simulations of the experimental setups

The Monte Carlo simulations of the LD-EDX and LD-PIXE setups were performed by considering both electrons and protons as primary particles. They are shown in figures 7.9.a and 7.9.b, respectively. All the main components (i.e. the metallic support, the magnets, Al foil, lead shields and sample) present in the experimental configuration are considered. The simulations were carried out with the same number (i.e. 10^8) of primary electrons and protons. Particles are emitted by a point-like source with a uniform angular distribution between $\pm 20°$. In this way, the sample surface is entirely hit by the particles. The primary proton energies were sampled from the experimental energy distribution reported in figure 7.3.b.

As far as the simulations with electrons as primary particles are concerned, two sets of simulations were carried out. In both cases, the electron energies were extracted from a pure exponential distribution with maximum energy equal to 10 MeV. However, two different electron temperatures of 0.67 MeV and 1.0 MeV were considered. The first value was calculated from the laser parameters while using the generalized ponderomotive scaling from equation 2.7 and presented in Section 2.2. The second temperature was retrieved by matching the theoretical estimation (equation 2.8 of Section 2.3) of

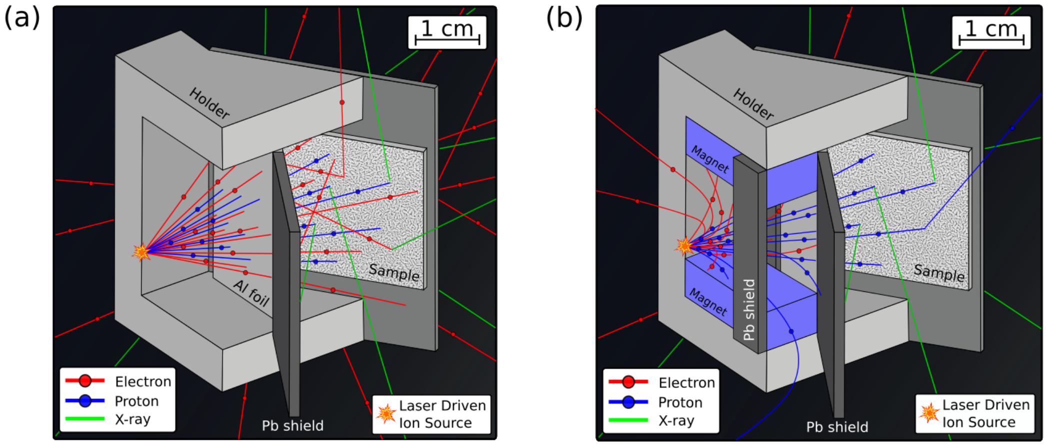

Figure 7.9: *Snapshots of (**a**) the laser-driven EDX and (**b**) laser-driven PIXE Monte Carlo simulations.*

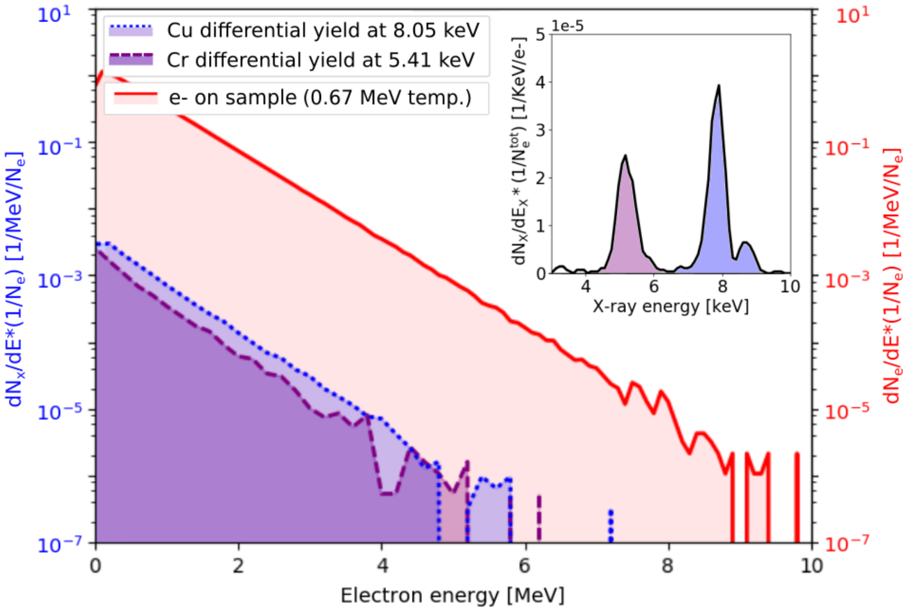

Figure 7.10: *Laser-driven EDX Monte Carlo simulation outputs with electrons of 0.67 MeV temperature as primary particles. The filled red curve is the electron energy spectrum at the sample surface. The filled blue areas are the X-ray differential yields. The inset plot is the simulated X-ray spectrum.*

the proton cut-off energy and the obtained experimental value of 6.35 MeV.

The magnetic field intensity distribution was evaluated on a $10 \times 10 \times 10$ grid located between the magnetic plates. With this choice, the magnetic field covers the region of interest where the electrons and protons can travel and be deflected. The grid is fed into the Monte Carlo simulation of the LD-PIXE setup.

We start discussing the simulations with electrons as primary particles. The simulated electron energy spectrum at the sample surface in the LD-EDX setup is shown in figure 7.10. The data refer to the 0.67 MeV electron temperature case and they are normalized to the total number of simulated electrons. Since in the LD-EDX setup the particles were not deflected, the incident electrons on the sample are characterized by an exponential spectrum equal to that of the primary particles.

Figure 7.10 also reports the X-ray differential yields of Cr and Cu. The differential yield is defined as the number of characteristic X-rays leaving the sample as a function of the incident electron energy. The differential yields extend up to the MeV energy range. Therefore, also the high-energy electrons contributed to the X-ray generation because the substrate is thick enough to let them slow down.

On the other hand, the electron spectrum at the sample surface in the LD-PIXE setup is reported in figure 7.11. In this case, the number of electrons reaching the sample is lowered drastically because of the presence of the magnet. Indeed, 98% of the incident electrons are removed if the 0.67 MeV electron temperature case is considered. With a temperature equal to 1 MeV, this fraction is 96.3% of the total simulated electrons. Moreover, both the electron spectrum and differential X-ray yields are no longer exponential because the trajectories of the electrons through the magnet depend on their energy. In other words, the effectiveness of the magnet in removing the electrons de-

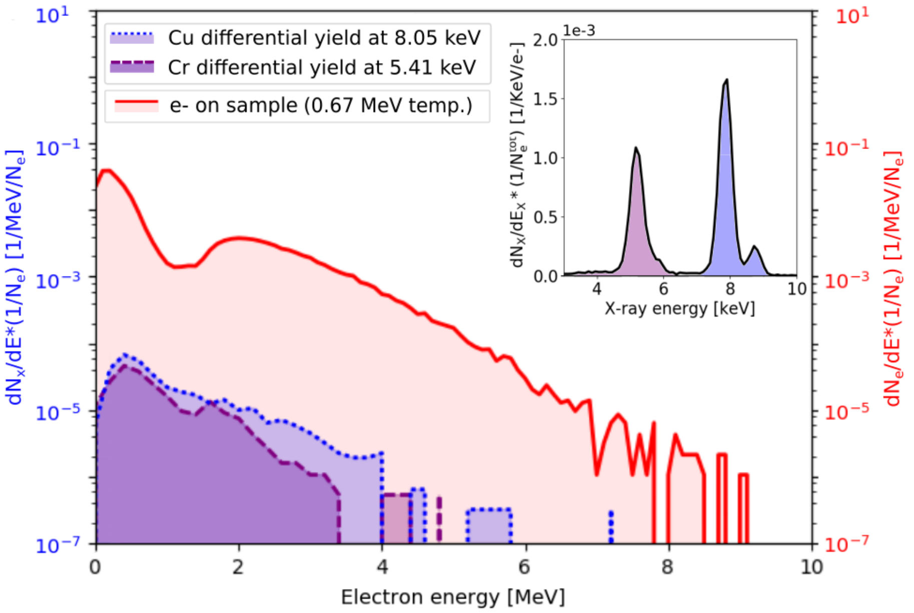

Figure 7.11: *Laser-driven PIXE Monte Carlo simulation outputs with electrons of 0.67 MeV temperature as primary particles. The filled red curve is the electron energy spectrum at the sample surface. The filled blue areas are the X-ray differential yields. The inset plot is the simulated X-ray spectrum.*

pends on the energy of the particles.

Exploiting the experimental and simulated results, a conservative estimation of the fraction of X-rays due to electron irradiation in the laser-driven PIXE experiment can be provided. The calculations are shown for the 0.67 MeV electron temperature case. From the Monte Carlo simulations, the ratio between the X-ray yields due to electrons in the LD-PIXE and LD-EDX setup is:

$$\frac{Y_{LD-PIXE,e}}{Y_{LD-EDX,e}} = 0.02 \tag{7.8}$$

The experimental ratio between the total yields (due to both electrons and protons) in the LD-EDX and LD-PIXE setups is:

$$\frac{Y_{LD-EDX,e} + Y_{LD-EDX,p}}{Y_{LD-PIXE,e} + Y_{LD-PIXE,p}} = 8.6 \tag{7.9}$$

The X-ray yield due to electrons in the LD-EDX setup $Y_{LD-EDX,e}$ can be expressed in terms of $Y_{LD-PIXE,e}$ by inverting equation 7.8. With substitution in equation 7.9 and simple manipulations, an expression for the fraction of X-rays due to the electron irradiation in the LD-PIXE experiment can be obtained:

$$\frac{Y_{LD-PIXE,e}}{Y_{LD-PIXE,e} + Y_{LD-PIXE,p}} = 0.17 \times \left(1 - \frac{0.02 \times Y_{LD-EDX,p}}{Y_{LD-PIXE,e} + Y_{LD-PIXE,p}}\right) \tag{7.10}$$

The right side of equation 7.10 is maximized and equal to 0.17 by assuming to neglect the proton contribution to the X-ray yield in the laser-driven EDX measurement $Y_{LD-EDX,p}$. However, since this contribution is higher than zero, 17% can be considered an upper threshold for the fraction of X-rays due to surviving electrons in the

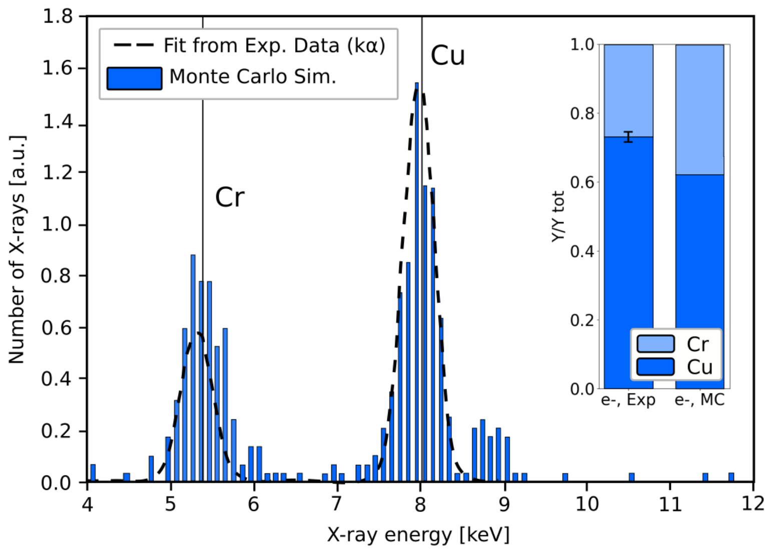

Figure 7.12: *Comparison between the simulated and experimental fitted X-ray peaks for laser-driven EDX. The inset bar plot compares the experimental and simulated X-ray yields.*

LD-PIXE measurement. The value is equal to 30% considering the 1.0 MeV electron temperature case. These results are coherent with the 10% underestimation of the Cr layer thickness obtained in the previous Section.

In figure 7.12, the fit of the experimental kα peaks obtained from the laser-driven EDX measurement is compared with the simulated spectrum. The counts at each energy are normalized to the total number of X-rays for both the elements combined. Again, the results are referred to the 0.67 MeV electron temperature case. The proton contribution is neglected in the Mote Carlo simulation. The inset graph provides a direct comparison between the experimental and simulated yield ratios. The same comparison is performed for the laser-driven PIXE experimental results and the corresponding Monte Carlo simulation. It is reported in figure 7.13. The agreement between experimental data and Monte Carlo simulations is quite reasonable, giving further evidence that laser-driven EDX is dominated by the electron contribution, while, in laser-driven PIXE, the protons play a relevant role. Therefore, the proof-of-principle laser-driven PIXE experiment presented in this Chapter is a good starting point for the design of an optimized beam handling system. It is worth mentioning that this is an essential point for the development of a reliable laser-driven PIXE analysis.

7.3.3 Post hoc evaluation of the electron temperature

An estimation of the electron temperature can be done by exploiting the simulated and experimental yield ratios. From the Monte Carlo simulations, the ratio between the Cu yields due to the electrons in the LD-PIXE and LD-EDX setups can be expressed as a linear function of the electron temperature T_e.

$$\frac{Y^{Cu}_{LD-PIXE,e}}{Y^{Cu}_{LD-EDX,e}} = 0.035 \times T_e + 0.0034 \tag{7.11}$$

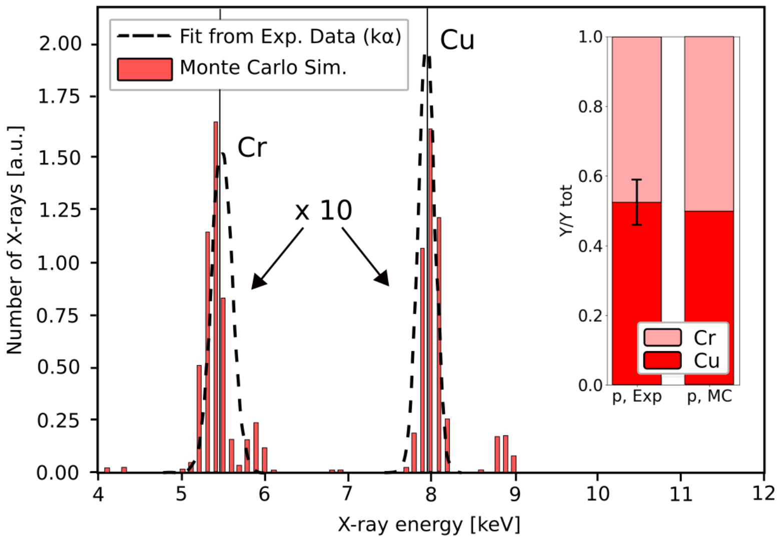

Figure 7.13: *Comparison between the simulated and experimental fitted X-ray peaks for laser-driven PIXE. The inset bar plot compares the experimental and simulated X-ray yields.*

This linear fit is also reported in figure 7.14. From the Monte Carlo simulations, the ratio between the Cr and Cu X-ray yields ascribable to electrons in the LD-PIXE setup is equal to:

$$a = \frac{Y^{Cr}_{LD-PIXE,e}}{Y^{Cu}_{LD-PIXE,e}} = 0.65 \tag{7.12}$$

For reasonable values of T_e, the value of a keeps constant. Again from the Monte Carlo results, the ratio between the Cr and Cu X-ray yields due to protons in the LD-PIXE setup can be evaluated:

$$b = \frac{Y^{Cr}_{LD-PIXE,p}}{Y^{Cu}_{LD-PIXE,p}} = 1.023 \tag{7.13}$$

The experimental data provide the ratio between the X-ray yields of Cr and Cu in the laser-driven PIXE measurement:

$$c = \frac{Y^{Cr}_{LD-PIXE,e} + Y^{Cr}_{LD-PIXE,p}}{Y^{Cu}_{LD-PIXE,e} + Y^{Cu}_{LD-PIXE,p}} = 0.91 \pm 0.169 \tag{7.14}$$

By neglecting the proton contribution to the X-ray spectrum in the experimental laser-driven EDX spectrum:

$$d = \frac{Y^{Cu}_{LD-PIXE,e} + Y^{Cu}_{LD-PIXE,p}}{Y^{Cu}_{LD-EDX,e}} = 0.083 \pm 0.011 \tag{7.15}$$

By combining equations 7.11 to 7.15, the following expression for the electron temperature can be derived:

$$T_e = 28.63 \times d \times \frac{b-c}{b-a} - 0.096 \tag{7.16}$$

With equation 7.16, the temperature results 0.63 ± 0.49 MeV. The corresponding Cu X-ray yield ratio in the LD-PIXE and LD-EDX setups is equal to 0.025 ± 0.017. This point

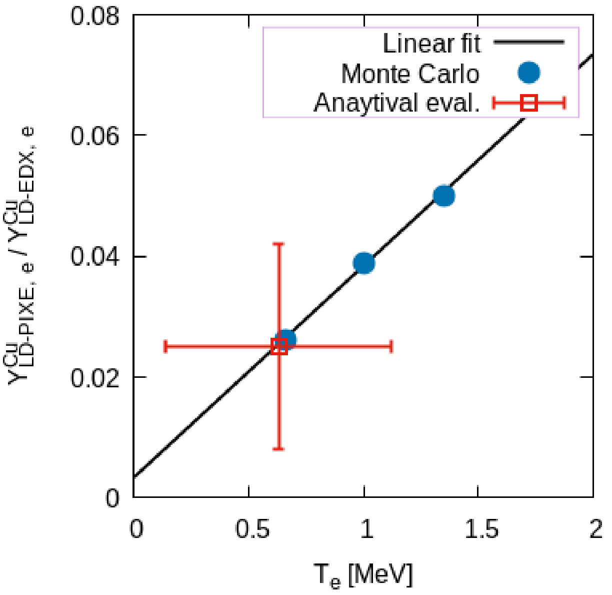

Figure 7.14: *Linear fit (black line) of the X-ray yields ratio due to electrons in the laser-driven PIXE and EDX measurements as a function of the electron temperature* T_e*. The data exploited for the fit are reported as blue points. The red marker is the ratio of the yields obtained from the fit in correspondence with* $T_e = 0.63 \pm 0.49$ *MeV.*

is reported in figure 7.14. The calculated temperature is very close to the 0.67 MeV value from the ponderomotive scaling, while the 1.0 MeV estimation falls within its uncertainty. Despite the large statistical uncertainty, this result supports the theoretical estimations of the electron temperature assumed in the Monte Carlo simulations.

CHAPTER 8

Theoretical study on Laser-driven PAA

This Chapter aims at assessing, exploiting theoretical and numerical tools, whether laser-driven electron sources could be used for Photon Activation Analysis (PAA). A model for the description of conventional PAA (i.e. performed with monoenergetic electron sources) is provided in Section 8.1. In the same Section, an analogous model developed for laser-driven PAA is presented. A near-critical material is considered for the generation of hot electrons. The theoretical description of laser-driven PAA is exploited to retrieve the optimal laser-driven electron source parameters, i.e. the target properties that maximize the characteristic γ-ray emission from the irradiated sample. Then, in Section 8.2, both models are used to compare the laser-driven PAA performances and that accomplished exploiting conventional accelerators. Monte Carlo simulations of conventional and laser-driven PAA experiments are carried out in Section 8.3 to check the reliability of the models. At this step, pure exponential electron energy spectra are considered for the laser-driven source. Lastly, Section 8.4 presents a combined PIC-Monte Carlo simulation of a realistic laser-driven PAA case study.

8.1 Theoretical description for the conventional and laser-driven PAA

Unlike PIXE and EDX, PAA relies on a multi-step procedure that involves the intermediate conversion of the primary electrons into high-energy photons and the subsequent activation of the sample. This technique has been extensively described in Section 1.4. At present, laser-driven electron sources have never been considered to carry out PAA. Therefore, an investigation of the laser-driven PAA feasibility requires preliminary estimating its capabilities and comparing its performances with that achievable with conventional electron accelerators. To this aim, multi-stage theoretical models must be developed for both conventional PAA and laser-driven PAA.

In the conventional PAA scenario, the input parameters to the model are the electron energy and current delivered by the accelerator. Then, the bremsstrahlung production of photons and the photonuclear interactions in the sample are taken into account via Monte Carlo simulations and a suitable parametrization of the cross sections, respectively. The model output consists of the sample activation rate, a quantity directly related to the number of emitted characteristic γ-rays. This model was exploited initially to obtain the optimal converter thickness as a function of the incident electron energy in conventional PAA.

As far as the laser-driven PAA model is concerned, the input quantities are the laser operating parameters, i.e. the intensity and repetition rate. Considering the target, even if both laser wakefield acceleration (lwfa) and near-critical solid media are suitable for electron acceleration, only the second configuration is adopted because of the higher delivered charge per laser shot (see Section 2.4.1 for details). Therefore, the overall target consists of a low-density material, e.g. a foam, for the electron acceleration, attached to an $\sim \mathrm{mm}$ thick tungsten (W) converter for the production of high-energy photons. This peculiar DLT configuration is compatible with the experimental setup for ion acceleration based on thin solid targets. Therefore, another advantage over lwfa consists in the possibility of switching from proton acceleration to photon production with minimum variations to the experimental apparatus.

A schematic representation of the laser-driven PAA setup proposed and investigated in this work is reported in figure 8.1. Since the near-critical solid medium is attached to the converter material, the electrons generated in the first layer are directly accelerated

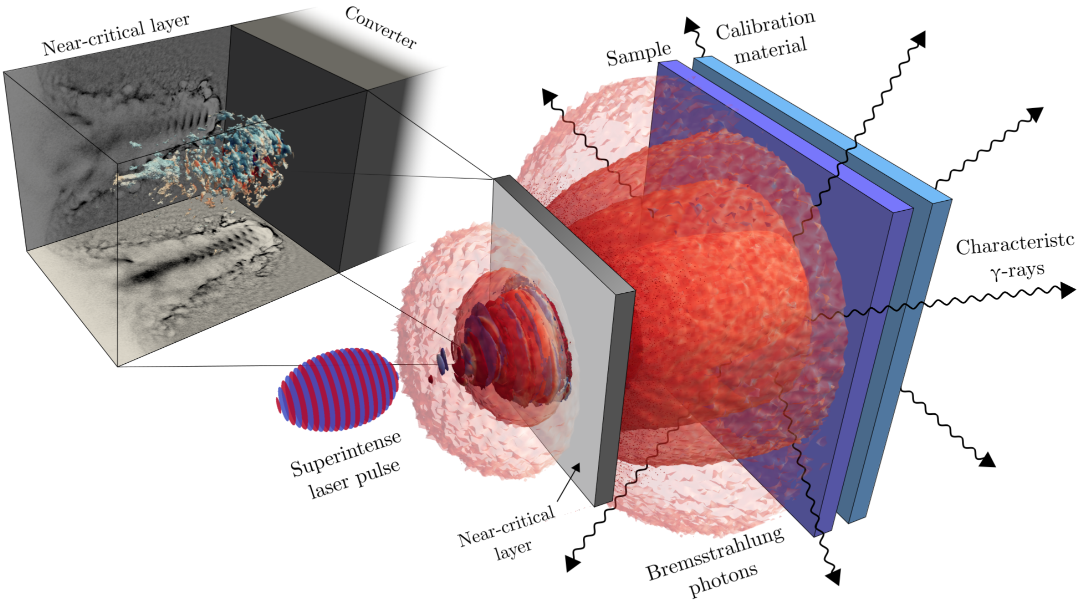

Figure 8.1: *Conceptual scheme of the laser-driven PAA setup. The near-critical material is located on the rear side of the mm thick converter material. A magnification of the laser propagating in the near-critical medium is shown (from a 3D PIC simulation). The hot electrons interact with the converter, and they generate bremsstrahlung photons. The photons irradiate a sample and a calibration material. The subsequent emission of characteristic γ-rays is reported as black wavy arrows.*

in the converter with the consequent generation of bremsstrahlung photons. The model for laser-driven PAA, whose output consists again in the sample activation rate, was initially used to retrieve the optimal near-critical layer density and thickness as a function of the laser intensity.

8.1.1 Model for conventional PAA

To correctly describe the PAA technique, the bremsstrahlung production of photons from 10s of MeV electrons and the probability of inducing photonuclear reactions in the sample must be considered.

The bremsstrahlung photon spectrum $f(E) = (1/N_e)dN_\gamma/dE$ per unit of incident electrons N_e depends on the energy of the electrons, the converter material and thickness. It can be obtained by exploiting analytical formulas [283] or Monte Carlo simulations [284]. The first approach is recommended when quick estimations are needed. However, it requires the adoption of simplifying assumptions which, in some cases, can lead to a non-acceptable degree of error. Indeed, a Monte Carlo description of the bremsstrahlung is often required for several applications, as for PAA modelling [285]. Accordingly, a set of 49 Monte Carlo simulations were performed with Fluka [203].

In each simulation, electrons with different energies E_e (i.e. 10, 15, 20, 25, 30, 35 and 40 MeV) were made to interact with a W rectangular converter having variable thickness l (i.e. 1, 2, 3, 4, 5, 7, 10 mm). The EMFCUT card associated with this volume was activated. This option allows reducing the computational time by setting 100 keV and 1 MeV energy thresholds for the photon and pair production, respectively. Further details about the Fluka simulations are provided in Section 3.4.2. The photon energy spectra were recorded performing 5 cycles with 10^7 primary electrons per cycle for each simulation. The electrons energies and W thicknesses cover the ranges usually adopted in PAA experiments. Some examples of bremsstrahlung spectra are reported in figures 8.2.a and 8.2.b for different primary electron energies and converter thicknesses, respectively.

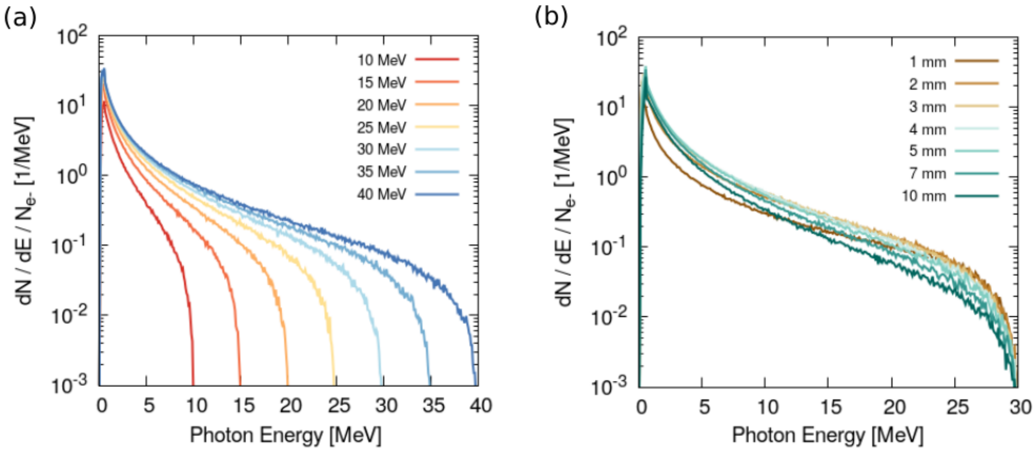

Figure 8.2: *Bremsstrahlung spectra simulated with Fluka for (**a**) different values of the primary electron energy and fixed converter thickness (i.e. 3 mm); (**b**) different values of the converter thickness and fixed primary electron energy (i.e. 30 MeV). The spectra are normalized to the total number of primary electrons.*

Even if (γ, p), $(\gamma, 2n)$, $(\gamma, 3n)$ reactions can occur in the sample during irradiation, the (γ, n) reactions are the most commonly exploited in PAA [20] studies. Therefore, they are the only king of photonuclear reactions considered in this work. The associated cross sections are well-described by a bell-shaped function centred around 15-20 MeV. Their magnitude can range from few tens up to hundreds of mbarn. Figure 8.3.a shows some cross sections whose areas have been normalized to unity. The position of the maximum is weakly dependent on the considered isotope. Accordingly, the cross section can be modelled as:

$$\sigma(E) = \sigma_{int} \cdot \tilde{\sigma}(E) \tag{8.1}$$

where σ_{int} is the total area, and $\tilde{\sigma}(E)$ is a normalized Gaussian function (i.e. normalized cross section). Figure 8.3.a reports $\tilde{\sigma}(E)$ centred in $E = 17$ MeV and having Full With Half Maximum (FWHM) equal to 7 MeV. $\tilde{\sigma}(E)$ will be exploited instead of $\sigma(E)$ in the discussion to generalize the description.

For all the bremsstrahlung spectra obtained with the Fluka simulations, the following integral was evaluated:

$$Y(E_e, l) = \int_E f(E_e, l; E)\tilde{\sigma}(E)dE \tag{8.2}$$

and assuming the mentioned parameters for $\tilde{\sigma}(E)$. The resulting values are the normalized reaction yields $Y(E_e, l)$ for the discrete primary electron energies and converter thicknesses. They are proportional to the actual reaction yields, except for a multiplication constant that depends on the specific composition and size of the sample, adopted irradiation geometry (e.g. the source-sample distance) and the number of electrons.

Then, the discrete values were fitted with a fourth-order polynomial in the variables E_e and l. In this way, the normalized reaction yield was expressed as a continuous function of two setup parameters (i.e. E_e and l). This function is reported as a blue contour plot

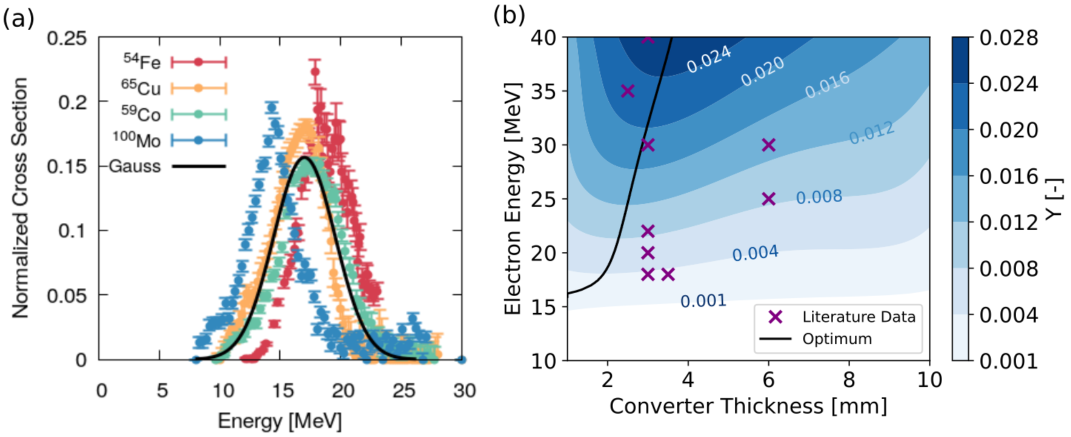

Figure 8.3: *(**a**) Comparison between normalized experimental photonuclear cross sections and a Gaussian function centred in 17 MeV and having Full Width Half Maximum equal to 7 MeV. (**b**) Contour plot representing the normalized yield as a function of the primary electron energy and converter thickness. The continuous black line marks the locus of optimal converter thickness for each value of electron energy. The purple markers are in correspondence with experimental conditions reported in the literature [286–292].*

in figure 8.3.b.

The optimal converter thickness t_{opt} as a function of the incident electron energy can be evaluated as:

$$l_{opt}(E_e) = \arg\max_{l} Y(E_e, l) \tag{8.3}$$

and the corresponding normalized yield is $Y_{max}(E_e) = Y(E_e, l_{opt}(E_e))$. In figure 8.3.b, the function $l_{opt}(E_e)$ is superimposed to the contour plot as a black line. Moreover, some experimental conditions reported in the literature are identified with cross markers.

The obtained results show that the performances of PAA, expressed in terms of normalized reaction yield, are weekly dependent on the converter thickness. The optimum for the considered E_e range lies between 2 and 4 mm. Accordingly, several converter thicknesses adopted in the literature are within this interval. On the other hand, the dependence of $Y(E_e, l)$ on E_e is more pronounced. Below a critical value of ~ 15 MeV electron energy, the normalized yield tends to zero because the bremsstrahlung spectrum does not cover the region where the cross section is located. As a consequence, $l_{opt}(E_e)$ asymptotically tends to zero around the reported critical value. In other words, no photons useful for PAA are produced for $E_e < 15$ MeV, whatever the value of the converter thickness.

Lastly, it is worth noting that the electron current I_e, a relevant operating parameter in PAA, was not considered here. The reason is that the electron energy and current are independent parameters. Therefore, the optimal converter thickness can be retrieved without taking into account the current. Anyhow, the electron current will enter the discussion in Section 8.2.

8.1.2 Model for laser-driven PAA

Laser-driven electrons accelerated exploiting near-critical density targets have a quasi-exponential energy distribution. Accordingly, pure exponential energy spectra were considered, and the maximum energy was set equal to 40 MeV. With this choice of the cut-off value, the resulting bremsstrahlung photon energy spectra cover the region of non-vanishing photonuclear cross sections. The selected maximum electron energy is reasonable for sufficiently intense laser pulses (i.e. normalized intensity $a_0 \approx 10$) and near-critical targets [94]. However, since the electron spectrum is exponential, very few bremsstrahlung photons are generated by the cut-off electrons. Thus, the exact value of the maximum electron energy has a negligible effect on the number of activated nuclei, while the temperature plays a crucial role. The electron energy spectra were provided as input to the Fluka simulations exploiting a user-defined routine.

A total of 35 Fluka Monte Carlo simulations were carried out considering several electron temperatures T_e (i.e. 5, 10, 15, 20 and 25 MeV) and converter thicknesses l (i.e. 1, 2, 3, 4, 5, 7 and 10 mm). Then, the same integration and interpolation procedure described in the previous Section were applied to retrieve the normalized reaction yields. $Y(T_e, l)$ and the optimal converter thickness $l_{opt}(T_e)$ are reported in figure 8.4.a. Here, the maximum normalized yield is a function of the electron temperature since $Y_{opt}(T_e) = Y(T_e, l_{opt}(T_e))$.

The electron temperature is determined by the laser operating parameters and target properties. Therefore, to proceed, Y_{opt} must be expressed in terms of the normalized

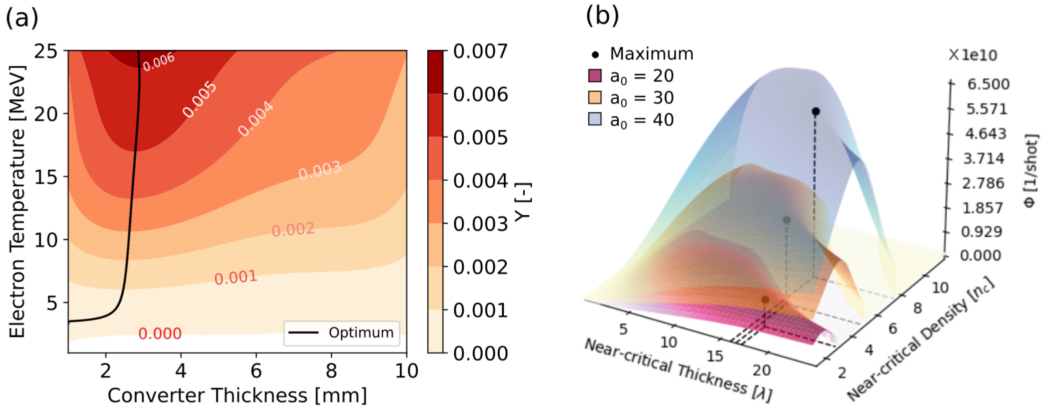

Figure 8.4: *(**a**) Contour plot representing the normalized yield as a function of the laser-driven electron temperature and converter thickness. The continuous black line is in correspondence with the maximum normalized yield for each electron temperature. (**b**) Normalized yields per laser shot for three values of a_0 (i.e. 20, 30, and 40) as a function of the target near-critical layer density and thickness. The maxima are marked with a black dot, and they are projected on the horizontal plane at $\Phi = 0$.*

laser intensity a_0 and near-critical layer density n and thickness x. To this aim, the model developed by *A. Pazzaglia et al.* [99] and presented in Section 2.3.3 was exploited. It allows describing the propagation of a super-intense laser pulse in a near-critical material and the generation of hot electrons. Assuming a linearly polarized laser pulse with normal incidence, wavelength $\lambda = 0.8\ \mu$m, and waist $FWHM = 4.7\ \mu$m, this model was used to express the electron temperature as a function of the aforementioned operating parameters. As a consequence, also the maximum normalized yield has the same dependencies being $Y_{opt}(a_0, n, x) = Y_{opt}(T_e(a_0, n, x))$.
At this step, the number of accelerated electrons per laser shot N_e must be considered. Like the temperature, its value can be determined using the mentioned model and as a function of the laser and target parameters. A new quantity $\Phi(x, n, a_0)$ was defined to include N_e in the description:

$$\Phi(x, n, a_0) = Y_{max}(T_e(x, n, a_0)) \times N_e(x, n, a_0) \tag{8.4}$$

The quantity $\Phi(x, n, a_0)$ is reported in figure 8.4.b as a function of the near-critical target properties x and n and three different values of a_0. The maximum of this function identifies the optimal near-critical target density and thickness for a specific value of laser intensity (i.e. the thickness and density that maximizes the sample activation per laser shot). This condition can be expressed as:

$$x_{opt}(a_0), n_{opt}(a_0) = \arg\max_{n,x} \Phi(x, n, a_0) \tag{8.5}$$

The corresponding values for $a_0 = 20$, 30 and 40 are marked in figure 8.4.b with black points. Equation 8.5 was evaluated for a_0 ranging from 10 to 50, and the resulting optimal target parameters are reported in figure 8.5.a. The optimal thickness and density are expressed in units of laser wavelength and critical density n_c, respectively. The optimal thickness slightly decreases while increasing the laser intensity. However, its value keeps within $\sim 14 - 18\ \lambda$. On the other hand, the optimal density progressively

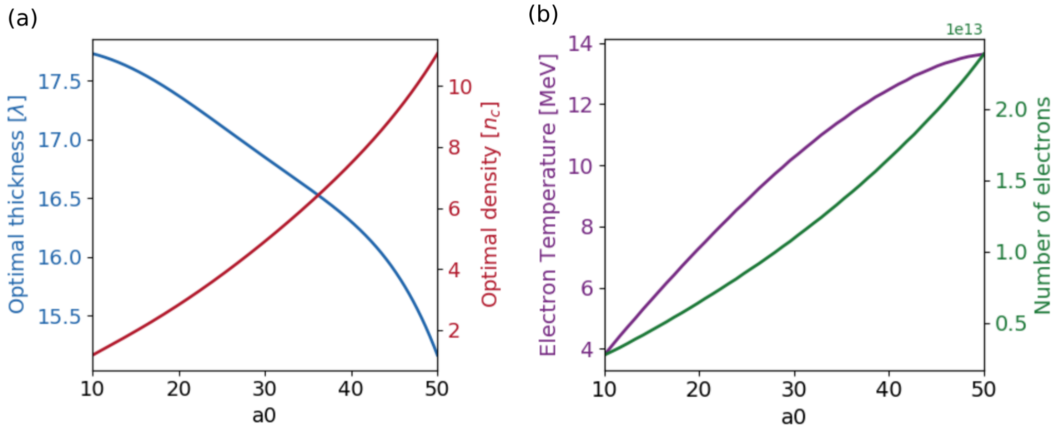

Figure 8.5: *(**a**) Optimal near-critical layer density and thickness as a function of the normalized laser intensity. (**b**) Laser-driven electron temperature and number per shot as a function of the laser intensity at the optimal target conditions.*

increases with a_0 allowing greater absorption of the laser pulse by the near-critical material. Overall, the maximum of the Φ function, and therefore the corresponding target parameters, is the result of a trade-off between the accelerated electron temperature and number, which in turn affects the bremsstrahlung photon spectrum and the sample activation in cascade.

The electron temperature and number under the optimal condition for the sample activation are a function of the laser intensity:

$$T_{e,opt}(a_0) = T_e(x_{opt}(a_0), n_{opt}(a_0), a_0) \tag{8.6}$$

$$N_{e,opt}(a_0) = N_e(x_{opt}(a_0), n_{opt}(a_0), a_0) \tag{8.7}$$

They are shown in figure 8.5.b. As expected, the electron temperature and number monotonically increase with the laser intensity. Last, the corresponding values for the normalized yield per laser shot

$$\Phi_{max}(a_0) = \Phi(x_{opt}(a_0), n_{opt}(a_0), a_0) \tag{8.8}$$

can be obtained.

8.2 Comparison between conventional PAA and laser-driven PAA performances

In the previous Section, the optimal parameters for conventional PAA (i.e. the converter thickness as a function of the electron density) and laser-driven PAA (i.e. the converter thickness, the foam thickness and density as a function of the laser intensity) were obtained. The goal of this Section is to compare the performance of PAA, expressed in terms of sample activation rate, carried out with conventional accelerators and laser-driven electron sources. In both cases, the optimal conditions were considered. To this aim, the normalized yield per unit of impinging electron $Y_{max}(E_e)$ must be multiplied by the electron current I_e delivered by the accelerator. On the other hand, the normalized yield per laser shot must be multiplied by the repetition rate RR of the laser.

The activation rate associated with the laser-driven source $\Phi_{max} \cdot RR$ is shown in figure 8.6 as a red colour map as a function of a_0 and RR in the ranges $10 - 50$ and $1 - 100$ Hz, respectively. On the upper x-axis, the corresponding values of T_e obtained in the previous Section are reported. Moreover, some isolines representing the activation rate achievable with existing conventional electron sources are superimposed to the map. Their locations are identified by the condition:

$$\Phi_{max}(a_0) \cdot RR = Y_{max}(E_e) \cdot I_e \tag{8.9}$$

Each isoline for a monoenergetic electron source lies in the correspondence of several possible equivalent laser systems for PAA. The reliability of this comparison will be carefully checked in the following Section. Here, the goal is to discuss the feasibility of laser-driven PAA.

To generate enough bremsstrahlung photons to significantly activate the sample, both the laser intensity (and therefore the electron temperature and number per shot) and the repetition rate must be considered. The performances of laser-driven PAA will be determined by a trade-off between these two operating parameters. The existing super-intense laser technology already provides lasers able to work in the entire intensity range considered here. However, the maximum nominal repetition rate they can currently achieve is $\sim 1 - 10$ Hz [59, 60]. Therefore, the top half of the map in figure 8.6

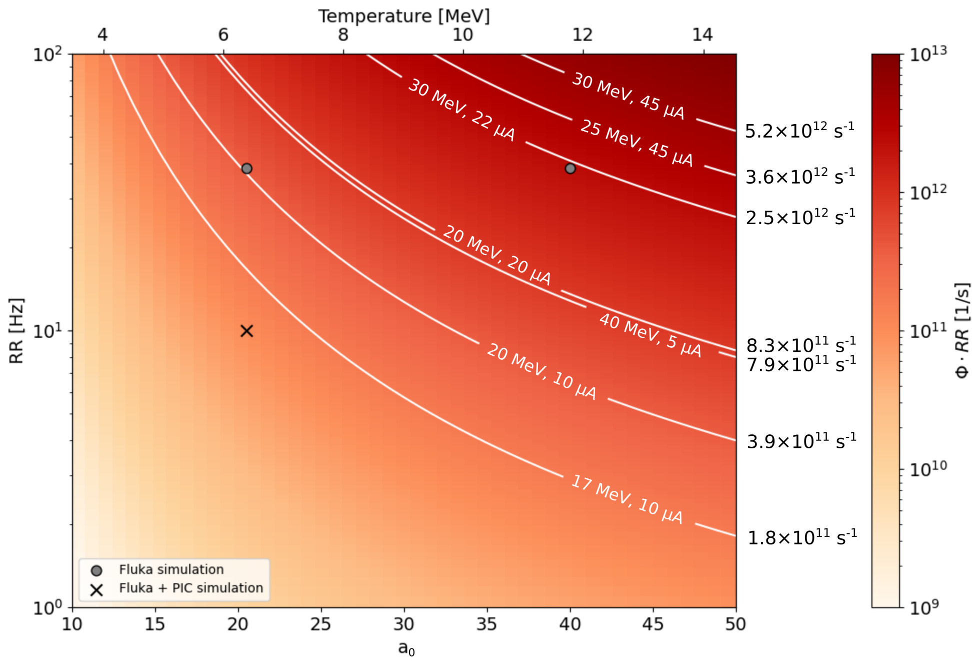

Figure 8.6: *Comparison between monoenergetic and laser-driven sources for PAA. The read heat-map is the normalized activation rate associated with the laser-driven source as a function of the laser intensity and repetition rate. The isolines are in correspondence with the normalized activation rate achievable with conventional accelerators working at the reported electron energies and currents (from the literature [286, 288]). The normalized activation rates corresponding to the isolines are reported on the right side of the map. The grey points are in correspondence with two PAA experimental conditions simulated with the Monte Carlo and presented in Section 8.3. The cross marker identifies the laser parameters for the PIC-Monte Carlo laser-driven PAA simulation shown in Section 8.4.*

can not be achieved with the currently available laser systems. In that region, the most powerful LINACs are located. Nevertheless, looking at the lower zone of the map, the performances of laser-driven PAA carried out with 100s TW class lasers can approach those achievable with some conventional accelerators.

To that aim, working at high repetition rates (HRR) for hour-long irradiation time is necessary. Currently, achieving HRR is challenging because of issues related to the laser-target interaction. HRR demands fast target refreshing, positioning, alignment and screening of the optics and neighbouring targets from the debris. Since many potential applications of laser-driven radiation sources require HRR, several efforts have been done to satisfy the mentioned needs [293]. Indeed, fast target delivery systems [294–296] and rapid alignment components [297] have been developed. In addition, various strategies have been found to protect the optical components from debris [293,298]. Lastly, the near-critical layer covering the W converter can be damaged because of the re-deposition of evaporated material. Therefore, a grid should be present to protect the regions adjacent to the interaction point. All these strategies are required to achieve the best laser-driven PAA performances.

The sample-converter distance, irradiation time, rest time and measurement time are assumed to be equal in laser-driven and conventional PAA. Such a condition allows performing a general comparison. Nevertheless, the setup parameters should be modified accordingly to the actual irradiation condition and irradiated material. For instance, a way of improving the laser-driven PAA performances is to decrease the converter-sample distance. As a result, the photon flux on the sample surface will increase.

In addition, it is worth pointing out that super-intense laser technology is still a very active research field. In this respect, further improvements in terms of repetition rate and a reduction of dimension and costs are foreseen in the following years. Therefore, laser-driven electron sources based on near-critical solid targets could be on their way to becoming competitive with conventional accelerators for applications like PAA.

8.3 Monte Carlo simulation of PAA experiments

This Section deals with Monte Carlo simulations of PAA experiments performed with monoenergetic and purely exponential (i.e. laser-driven like) electron energy spectra. As shown in Section 3.4.2, Fluka is the proper Monte Carlo code to simulate PAA experiments because of the reliability of the photonuclear cross sections. The simulations account for the bremsstrahlung photon production in the converter material, the photonuclear reactions in the sample, the decay and delayed emission of characteristic γ-rays. The aim is to exploit the results of these simulations to validate the comparison presented in the previous Section.

8.3.1 Simulation setup

Four different experimental conditions were considered. Two conditions (called S1 and S2) consist of conventional PAA experiments performed with monoenergetic electrons with energies equal to 30 MeV and 20 MeV and currents of 22 μA and 10 μA. For both of them, the equivalent PAA experiments carried out with laser-driven electrons were simulated (called S3 and S4). The experimental conditions are reported as grey points in figure 8.6 and summarized in table 8.1.

Each simulation was performed in two steps. In the first step, pencil-beam electrons interact with the W converter generating the bremsstrahlung photons. The photon energy spectra are retrieved. The total number of simulated electrons was 10^7 for each simulation. In the second step, the spectra are provided as input to Fluka simulations that account for the activation of the sample and subsequent decay. Since no photonuclear reactions of interest can occur below 5 MeV energy, the primary photon energies were extracted above this threshold. In the second step, a total number of 10^8 primary events were set for each simulation.

The sample has a thickness of 3 mm, and it is placed 10 cm far from the photon source in all the simulations. Its composition is reported in table 8.2, expressed in terms of mass concentrations of the elements. It is comparable to a bronze sculpture (1550-1400 BC) reported in [299] and analyzed by Prompt Gamma Activation Analysis and Neutron Imaging. As far as the activation is concerned, the present analysis focused on the Cu, Na, Fe, Pb, Ni and Ca elements.

For all the simulations, the photon irradiation lasted 3 hours. As far as the laser-driven sources are concerned, the current set in the simulation was obtained from the product of the repetition rate and the number of electrons accelerated per shot. Then, a cooling time of 12 hours was set before the start of the activity measurement. The measurement time was 3 hours. These conditions are coherent with those exploited in actual PAA experiments (see Section 1.4). The DCYTIMES and USRDBX cards are exploited to obtain the characteristic γ-ray spectra collected during the measurement. Since Fluka does not allow to retrieve straightforwardly the energy spectra integrated along a time interval, activity spectra were recorded at many successive instants of time within the overall measurement period. Then, the spectra were integrated in time to obtain the signal collected during the entire measurement period. It is worth noting that this procedure is valid only if the time sampling is significantly smaller compared to the shorter half-life of the activated isotopes. By way of example, the characteristic γ-ray spectrum

Table 8.1: *Summary of the source parameters for the conventional and laser-driven PAA experiments selected to be simulated.*

Source	Monoenergetic		Laser-driven	
Simulation	S1	S2	S3	S4
Electron energy (E_e) [MeV]	30	20	-	-
Electron current (I) [μA]	22	10	-	-
Laser intensity (a_0) [-]	-	-	40	20.5
Laser repetition rate (RR) [Hz]	-	-	38.6	38.6
Near-critical density (n) [n_c]	-	-	7.5	2.92
Near-critical thickness (x) [λ]	-	-	16.3	17.34
Electron temperature (T_e) [MeV]	-	-	12.5	7.5
Electrons per shot (N_e) [-]	-	-	1.6×10^{13}	6.4×10^{12}
Converter thickness (t) [mm]	3	2.41	2.73	2.58

Table 8.2: *Elemental mass concentrations of the sample.*

Element	Cu	Ca	Ni	Ma	Cl	Fe	Pb	Z	Al	Si	Na	Po
Concentration [%]	40.4	0.5	0.1	1.0	1.2	30.0	8.0	11.0	2.0	2.8	2.0	1.0

obtained from the S1 simulation is reported in figure 8.7.

8.3.2 Assessment of the comparison

In order to assess the feasibility of the comparison shown in Section 8.2, the ratio between the peak intensities retrieved from the S1, S2, S3 and S4 simulations were performed. In particular, for each simulation, the peaks marked in figure 8.7 were considered. Then, the ratios from the simulations were compared with the corresponding values predicted by the comparison.

The intensity ratios are independent of several parameters like the sample mass, thickness and elemental concentrations, the specific values of σ_{int}, the irradiation, measurement and cooling times. Therefore, the ratios between line intensities (from the Monte Carlo) can be directly compared with the ratios between normalized activation rates (from the theoretical model).

Consider the ratios between the peak intensities obtained from the S1 and S2 (i.e. $\mathrm{S1/S2}$) and the S3 and S4 (i.e. $\mathrm{S3/S4}$) simulations. Therefore, the comparison is made between the monoenergetic sources and between the laser-driven ones corresponding to different points of the map in figure 8.6. The $\mathrm{S1/S2}$ and $\mathrm{S3/S4}$ ratios for all the considered elements are reported in figure 8.8.a with blue and yellow points, respectively. Considering a normalized cross section $\tilde{\sigma}(E)$ centred in 17 MeV, the predicted ratio is 6.2. In addition, assuming $\tilde{\sigma}(E)$ centred in 15 MeV and 20 MeV, the expected ratio results in 4.9 and 9.8, respectively. The predicted ratio depends on the choice of the parameters for the cross section. This is also confirmed by the different ratios obtained from the simulations for the various elements. Nevertheless, almost all the points lie between the region identified by the lower and upper values (i.e. the red dashed lines

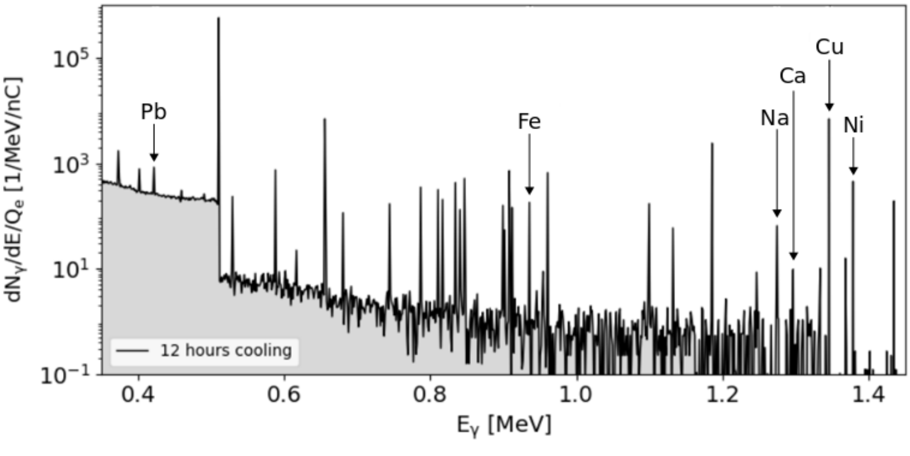

Figure 8.7: *Example of γ-ray energy spectrum from the S1 simulation. The characteristic γ-ray peaks associated with the considered elements are marked.*

in figure 8.8.a) predicted by the model. Thus, both in the case of conventional and laser-driven PAA, the model well-predicts how the peak intensities scale changing the operating parameters of the sources.
Besides, the ratios between the peak intensities obtained from the S1 and S3 (i.e. $\mathrm{S1}/\mathrm{S3}$) and the S2 and S4 (i.e. $\mathrm{S2}/\mathrm{S4}$) simulations are considered. They are reported in figure 8.8.b as green and red points. Since the ratios involve the intensities of the conventional sources and the equivalent laser-driven ones, the expected theoretical result is 1 (the continuous black line). Remarkably, with the only exception of Ca, all the points are in a region close to the expected value. Indeed, on average, the discrepancy is of the order of 20%. Therefore, the model allows establishing a comparison between conventional and laser-driven sources with an adequate degree of reliability.
Lastly, it is worth noting that the points associated with the Fe peak are not present in figure 8.8.a. Indeed, the bremsstrahlung photons in the S2 and S4 simulations are not energetic enough to induce sufficient photonuclear reactions for this element.

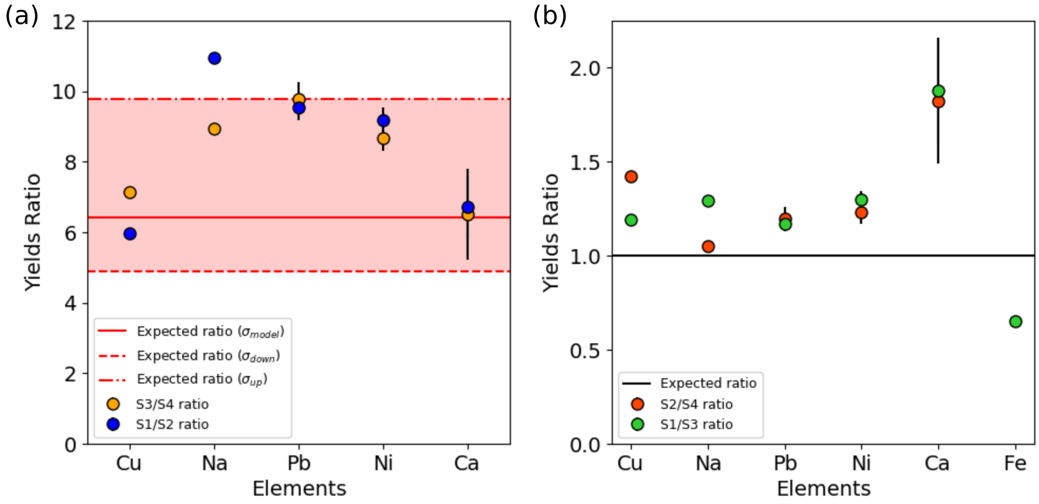

Figure 8.8: *(**a**) The ratio between the intensities from simulations* $\mathrm{S1}/\mathrm{S2}$ *and* $\mathrm{S3}/\mathrm{S4}$ *for each element. The continuous red line is the ratio predicted by the model by assuming a normalized cross section centred in 17 MeV. The dashed upper and lower red lines are the ratios predicted by the model by assuming normalized cross sections centred in 20 MeV and 15 MeV, respectively. (**b**) The ratio between the intensities from simulations* $\mathrm{S1}/\mathrm{S3}$ *and* $\mathrm{S2}/\mathrm{S4}$ *for each element. The black line corresponds to the value predicted by the model.*

8.4 Combined PIC-Monte Carlo simulation of a laser-driven PAA experiment

The goal of this Section is to carry out a realistic laser-driven PAA simulation selecting laser parameters compatible with state-of-the-art laser technology. The laser intensity and the repetition rate are 20.5 and 10 Hz, respectively. This operating condition is identified with a cross marker in figure 8.6. The target parameters were retrieved from the model presented in Section 8.1.2. The near-critical layer density and thickness are $2.92\ n_c$ and $17.34\ \lambda$, respectively. The electrons generated in the near-critical layer travel across a W converter having a thickness equal to 2.58 mm. The absence of a gap separating the low-density layer and converter allows avoiding geometrical losses. Moreover, the establishing of the TNSA process is suppressed. The absence of TNSA is convenient since a small part of the electron energy would be transferred to the ions with a consequent reduction of photon generation due to electron bremsstrahlung.

From the structural point of view, the proposed configuration (see figure 8.1) is quite robust. Compared to DLTs exploiting thin substrates, an mm thick target does not require encapsulation in a perforated holder. The laser can be focused rapidly at any point on the surface, aiding the high repetition rate operation. Lastly, such a target-converter component can be easily produced. Indeed, the surface of a W plate could be covered with a C-foam exploiting the PLD technique.

The sample position and composition are equal to those already described in the previous Section (see table 8.2). Here, a calibration material was added to the setup and placed behind the sample. They are separated by a 1 mm gap. The calibration material composition is reported in table 8.3. The aim is to simulate the co-irradiation of both sample and calibration material and exploit the characteristic γ-ray spectra to retrieve the composition of the first.

The irradiation time was assumed to be again three hours. However, three different measurement times (i.e. 2, 8 and 24 hours) preceded by increasing cooling times (0.5, 7 and 30 days) were set. The choice of stepwise increasing cooling periods allows excluding spectral interference by short-lived nuclides and enhancing the signal from long-lived nuclides.

8.4.1 Particle-In-Cell simulations of laser-driven electron acceleration

In order to provide a realistic description of the laser-driven electron source, a 3D PIC simulation of the laser interaction with the near-critical material was performed with the WarpX code [201]. A general description of the PIC method is provided in Section 3.3.

The laser is at normal incidence to the target surface. It is linearly polarized with $\lambda = 0.8\ \mu$m and waist $FWHM = 4.7\ \mu$m. The computational box has dimensions equal to $75\lambda \times 75\lambda \times 75\lambda$ with a spatial resolution of 20 points per unit λ in all directions. The time resolution was set at 98% of the Courant limit. Both the transverse and longitudinal laser profiles are Gaussian.

The target was sampled with 4 macro-electrons and 2 macro-ions with $Z = 6$ and $A = 12$. The electron population was initialized with a Maxell-Boltzmann momentum distribution with a temperature of 10 eV. The ion population was initially cold. The front target-vacuum interface was at 25λ. The overall simulation time was equal to 300 fs. The actual target thickness set in the PIC simulation is 25λ, so larger than 17.34λ. Indeed, a dense converter layer (even just a few microns) cannot be included

Table 8.3: *Elemental mass concentrations of the calibration material.*

Element	Cu	Ca	Ni	Ma	Cl	Fe	Pb	Z	Al	Si	Na	Po
Concentration [%]	33.0	1.37	0.03	0.6	3.6	0.025	19.0	7.4	4.7	1.8	1.5	2.0

in the simulation because it would require unbearable computational resources. Therefore, a near-critical layer thicker than the actual one was considered to avoid electron expansion in vacuum at the rear side of the medium. Then, the output was retrieved at the instant of time at which the laser front is at 17.34λ within the target (i.e. after 143 fs from the start of the simulation). Figure 8.9 shows the electron density and z-component of the magnetic field. The self-focusing of the laser pulse due to the ponderomotive and relativistic effects is evident. As described in Section 2.3.2, electrons are pushed outside the high electromagnetic field intensity regions under the action of the ponderomotive force. Together, the peak fields accelerate the electrons at relativistic energies.

At the considered instant of time, the momentum distribution $d^3N/dp_xdp_ydp_z$ associated to the macro-electron phase-space was retrieved, and the further propagation of the laser was not considered. The d^2N/dp_ydp_z, d^2N/dp_xdp_y and d^2N/dp_xdp_z distributions integrated along the missing component are reported in figures 8.10.a-c. Electron momenta are characterized by a symmetric distribution in the $p_y - p_z$ plane, while being forward peaked along the p_x component (i.e. the laser propagation direction). Figure 8.10.d reports the electron energy spectrum. The maximum energy extends up to ~ 110

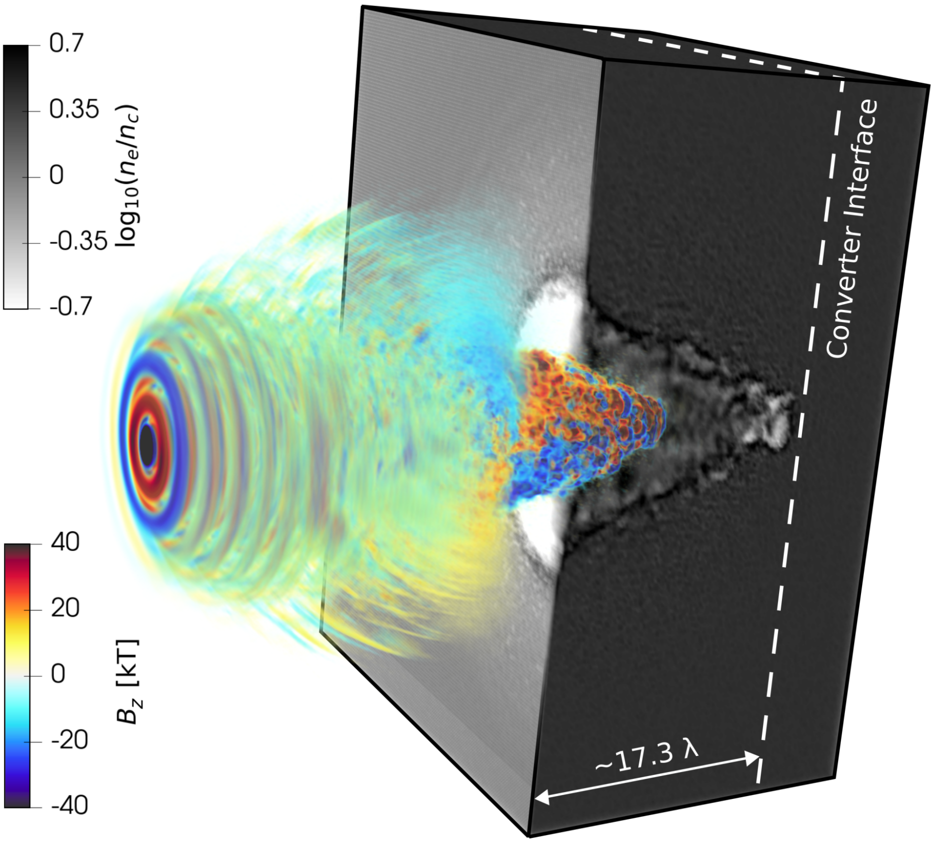

Figure 8.9: *Three-dimensional exploded view of the electron density and z-component of the magnetic field obtained from the 3D PIC simulation. They are retrieved at the instant of time at which the laser front reaches the rear side of the near-critical layer. The fictitious interface with the converter is marked with a dashed line.*

MeV while its temperature is ~ 7.8 MeV. Remarkably, this value is in absolute agreement with the 7.5 MeV temperature predicted by the model.
At the considered instant of time, about 60% of the initial laser energy (equal to 8.6 J) is transferred to the electrons. The total number of accelerated electrons was evaluated as the ratio between the energy absorbed by the hot electrons and the temperature. The resulting value is 4×10^{12}, which agrees with the 6.4×10^{12} electrons accelerated per laser shot predicted by the model. The slight overestimation of the temperature and overestimation of the number of accelerated electrons is ascribable to the fact that, in the PIC simulation, the reflection of the laser at the interface with the converter is neglected. However, its contribution can be considered negligible, as also stated in [99].

8.4.2 Monte Carlo simulation and sample composition reconstruction

The momentum distribution from the PIC simulation was provided as input to the Monte Carlo. At the beginning of each event, the momentum components of the primary electron are extracted with the Inverse Transform Sampling method, and they are used to define the initial energy and propagation direction.
The Monte Carlo simulation setup and its implementation are similar to those of the S1-

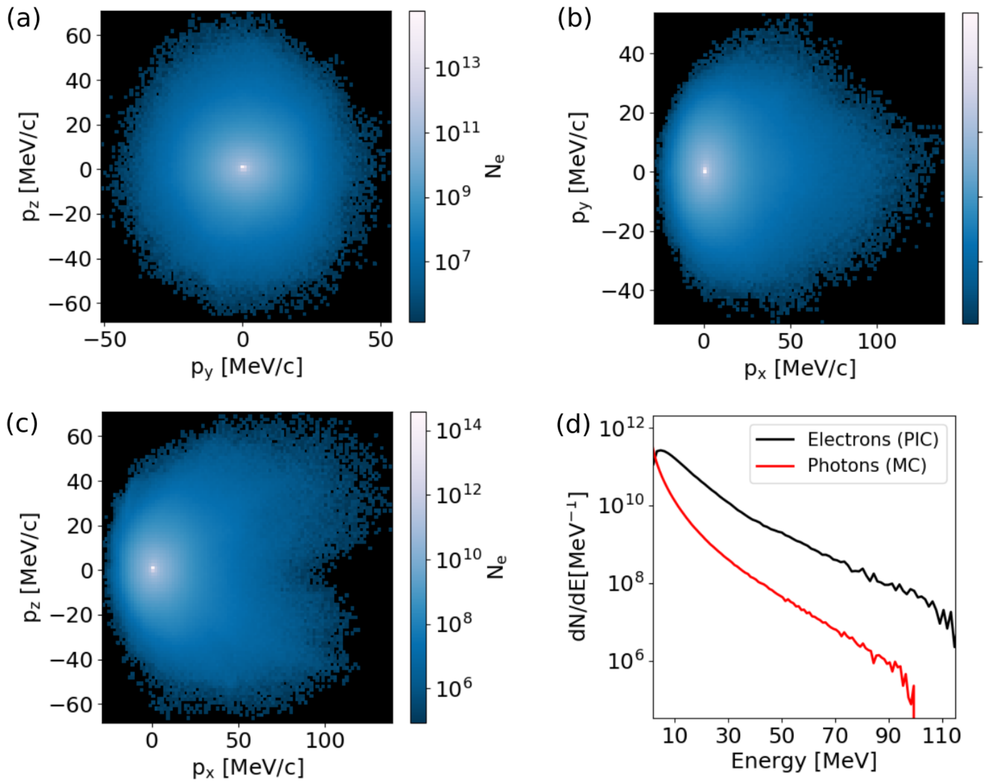

Figure 8.10: *(**a-c**) Electron momentum distributions retrieved from the PIC simulation after 143 fs. The 2D distributions are integrated along one momentum component and plotted in the other two. (**d**) Electron energy spectrum from the PIC simulation and bremsstrahlung photon spectrum from the Monte Carlo simulation.*

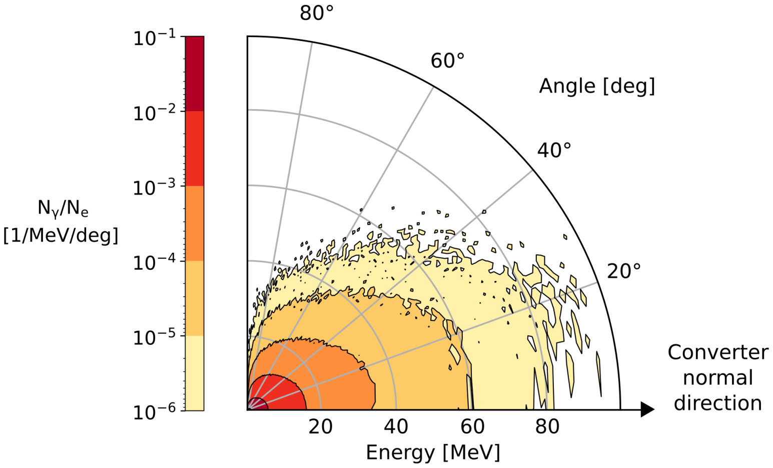

Figure 8.11: *Polar plot of the energy vs angular distribution of the bremsstrahlung photons. The colour scale is the number of photons normalized to the number of electrons.*

S4 simulations presented in the previous Section. The only difference is that, as already mentioned, the calibration material was added to the present setup. The bremsstrahlung photon energy spectrum is reported in figure 8.10.d. As expected, its shape is quasi-exponential, and the maximum energy approaches that of the primary electrons.

As in conventional PAA, the photons from the rear side of the converter are characterized by a broad angular distribution peaked in the forward direction. The energy-angle distribution is reported in figure 8.11. The highest energy photons have a maximum angular aperture equal to $\sim 20°$. The angular spread increases progressively, up to $\sim 80°$ for 20 MeV energy photons. As a consequence of the broad electron momentum distribution, the photon angular spread is higher than that observed in conventional PAA. Therefore, laser-driven PAA allows more uniform irradiation conditions than conventional PAA (assuming equal distance between sample and converter). The sample can be placed closer to the photon source in laser-driven PAA, increasing the average photon flux while maintaining uniform irradiation and avoiding overheating the material under investigation.

The characteristic γ-rays emitted from the sample were collected in the spectra reported in figure 8.12.a for the three considered cooling times. As in the previous cases, the characteristic peaks emerge over the continuous background. Moreover, the progressive disappearance of lines associated with short-lived nuclides increasing the cooling time can be appreciated.

Lastly, exploiting the characteristic γ-ray intensities emitted by the sample Y_γ^{sm} and calibration material Y_γ^{cl}, the sample elemental concentrations W^{sm} can be retrieved. The procedure has been already described in Section 1.4. However, since the irradiation, cooling and measurement times are assumed to be equal for both sample and standard, equation 1.8 simplifies as:

$$W^{sm} = \frac{W^{cl} Y_\gamma^{sm} Ar^{sm}}{Y_\gamma^{cl} Ar^{cl}} \tag{8.10}$$

The resulting concentrations are reported in figure 8.12.b, and they are compared with those set in the Monte Carlo simulation. The agreement is excellent, proving that the

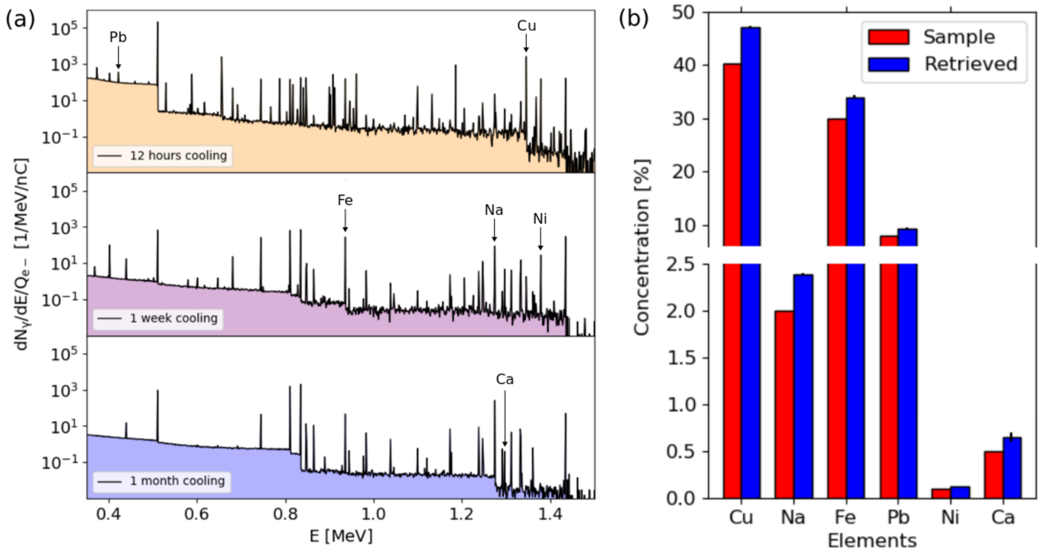

Figure 8.12: *(**a**) Simulated γ-ray energy spectra emitted following the activation of the sample and retrieved after three different cooling times. (**b**) Comparison between the retrieved elemental concentrations from the simulated γ-ray spectra and the values set in the Monte Carlo code.*

laser-driven PAA experiment has been successfully simulated.

Notice that, for all the elements, the retrieved concentrations slightly overestimate the original ones. The overestimation is because the sample is in front of the comparative material in the Monte Carlo setup. Therefore, the photon flux seen by the second is attenuated partially by the first, leading to a slight reduction of the calibration material activation. As already described in Section 1.4, this effect is also shared by conventional PAA, and it can be avoided by exploiting a flux monitor.

Overall, this analysis suggests that laser-driven PAA can be already performed in existing ultra-intense laser facilities hosting 100s TW class lasers. Indeed, the adoption of near-critical targets covering thick converters allows the efficient generation of photons in the $1-100$ MeV energy range. Therefore, the subject of this Chapter represents a further step toward the development of a multi-radiation source for different materials science studies. The developed theoretical framework allows us to identify the optimal target and converter parameters in a wide range of laser intensities. Moreover, it can be helpful for the evaluation of the laser-driven source performances (in terms of activated nuclei). Lastly, it is worth mentioning that the approach presented here could be applied to assess the potential of laser-based photon sources for other exciting applications like the production of medical radioisotopes.

Part IV

Conclusions and future perspectives

Conclusions and future perspectives

In this PhD thesis, performed within the framework of the ENSURE project, the possibility to exploit laser-driven radiation sources for the elemental characterization of materials has been theoretically and experimentally investigated. Moreover, the production of bare targets and Double Layer Target (DLT) substrates with controlled properties via Magnetron Sputtering for laser-driven ion acceleration experiments has been achieved.

As introduced in Chapter 1, atomic and nuclear analytical methods are indispensable tools for the elemental characterization of materials. These techniques allow probing the composition of a large variety of samples in a non-destructive way exploiting various kinds of radiation sources. They are inherently complementary since, depending on the primary particles and detected secondary radiation, different kinds of information can be retrieved (e.g. the elemental concentrations on the surface of homogeneous samples, the distribution as a function of the thickness in non-homogeneous materials, stratigraphic analysis and bulk composition in centimetre-thick objects). However, the wide use of techniques like Energy Dispersive X-ray (EDX), Particle Induced X-ray Emission (PIXE) and Photon Activation Analysis (PAA) is hindered by the limitations of the exploited radiation sources. Indeed, they are large and expensive. Moreover, only one kind of radiation is provided, and, as in the case of electrostatic accelerators for PIXE, they do not allow tuning easily the particle energy.

Laser-driven radiation sources, extensively described in Chapter 2, represent a promising alternative to the conventional ones because of their cheapness and compactness. Particles are accelerated through the interaction of ultrashort and superintense laser pulses with targets of different nature. Among the others, the use of micrometric solid foils represents a robust solution to co-accelerate electrons and ions in the $1-10$ MeV energy range. Particles are characterized by ultra-fast dynamics and broad energy spectra. Notably, their type and properties can be tuned by acting on the laser parameters and target configuration. For instance, decreasing the target thickness down to ~ 100 nm allows increasing the energy and number of the accelerated particles. DLTs, where the solid foils are coated with near-critical materials, are a viable route to further enhance the laser-driven source performances. Despite the growing effort invested in developing these novel accelerators, they are still subject to a certain degree of instability.

Indeed, sub-micrometric metallic foils are subject to a non-negligible local thickness uncertainty, which can strongly affect the shot-to-shot reproducibility.

In this framework, this PhD work aimed to bring off two fundamental goals: the preliminary study of Ti films deposition with Direct Current Magnetron Sputtering (DCMS) and High Power Impulse Magnetron Sputtering (HiPIMS) and subsequent production of Ti sub-micrometric targets on perforated target holders (Part II); the investigation with numerical and experimental methods of the laser-driven radiation source compatibility with the PIXE, EDX and PAA techniques (Part III). As mentioned in Section 3.1, these tasks have been addressed in parallel during the entire PhD period. Even if the targets developed in Part II were not exploited in the studies presented in Part III, the activities are coordinated toward the same goal. Indeed, producing high-quality targets with controlled properties is mandatory to achieve the high particle beam stability demanded by the investigated laser-driven analytical techniques.

In more detail, Chapter 4 dealt with the production and characterization of Ti films with DCMS, unbiased and biased HiPIMS. The plasma composition was characterized preliminarily with Optical Emission Spectroscopy measurements. The aim was to exploit at best the features of the considered deposition techniques. The film morphology, phase composition and stress state were retrieved with the Scanning Electron Microscope, X-Ray Diffraction and Wafer Curvature Method. Their evolution was interpreted in light of the explored atom and ion energy regimes characterizing DCMS and HiPIMS depositions. DCMS films exhibit a columnar morphology with several macro-voids. On the other hand, HiPIMS samples are characterized by a more compact granular structure. Notably, while the DCMS samples had the conventional α crystallographic phase only, the exotic *fcc* and ω phases were observed in unbiased and biased HiPIMS films, respectively. Their presence and evolution are strongly connected to the stress state of the Ti films. Overall, the stresses are tensile with DCMS depositions, and they are mainly compressive, up to several GPa, with HiPIMS depositions. From these results, we can conclude that Magnetron Sputtering allows depositing Ti films with very different morphology, crystallographic structure and state of stress. All these properties can be finely tuned acting on the deposition parameters. The high degree of versatility suggests that HiPIMS and DCMS could be suitable to carry out the production of engineered targets for laser-driven ion acceleration experiments. Moreover, tuning the phase composition of Ti films could be of interest to improve the performances of Ti coatings for various existing industrial and engineering applications.

Considering the mentioned results, a strategy for the deposition of sub-micrometric Ti foils on perforated target holders was developed and presented in Chapter 5. The procedure starts with the hole filling with a liquid solution containing sucrose. The choice of the filling material is a compromise between requirements like high solubility in water, heat resistance during deposition and moderate viscosity in solution. After solidification, the Ti film is deposited on the holes, and then the sucrose layer is removed via dissolution in water. With DCMS depositions, the substrates collapsed in the holes after the sucrose removal. Essentially, the film was not compact enough to self-support on the hole. Contrarily, the formation of significant damages of the sucrose during HiPIMS depositions was observed because of the high compressive stress state. Finally, to grow compact and stress-free films, DCMS and HiPIMS depositions were combined in a multi-layer structure. The resulting targets were characterized by $300 - 600$ nm thickness, high-density values (i.e. up to 90% of the bulk), very compact morphology (quasi-amorphous) and negligible stresses (i.e. $10 - 100$ MPa in compression). Therefore, they were able to self-sustain over the holes after the sucrose dissolution. It is worth mentioning that the obtained targets were charactered by a significantly lower thickness uncertainty (i.e. less than 5%) than rolled commercial sheets. In conclusion, the developed strategy allows producing bare targets and DLT substrates with optimal features in terms of thickness and planarity. This result is enabled by the alternation of low and high-energy Magnetron Sputtering regimes, such as the HiPIMS and DCMS, respectively.

Part III of this PhD thesis starts with a numerical investigation of the laser-driven PIXE feasibility. While the available codes for the analysis of PIXE measurements account only for the presence of a monoenergetic proton spectrum, the energy spectra of laser-driven particles are characterized by a quasi-exponential shape. Therefore, in Chapter 6, the theoretical framework of conventional PIXE analysis was extended to account for the presence of a non-monoenergetic proton source. Based on the model, a code for the analysis of the laser-driven PIXE X-ray spectra and the sample composition reconstruction was developed. Then, realistic laser-driven PIXE experiments were simulated through the PIC and Monte Carlo tools. With the simulations, two important goals were achieved: perform a preliminary design of a compact laser-driven PIXE experimental apparatus considering compact ~ 10 TW class lasers and DLTs; obtain 'synthetic', but realistic, X-ray spectra. The spectra were provided as input to the developed software, and the compositions of the samples originally set in the Monte Carlo simulations were correctly reconstructed. In light of these results, we can conclude that the theoretical description of laser-driven PIXE and the software for the X-ray spectra analysis can be used for quantitative characterization without the need for comparative materials. Combined PIC and Monte Carlo simulations indicate that compact lasers and DLTs allow satisfying the energy and current requirements for cultural heritage PIXE studies. Lastly, simulations concerning laser-driven electron irradiation suggested that laser-driven EDX is suitable to recognize the elements in solid samples.

The natural development of the aforementioned theoretical activities is the realization of the first quantitative laser-driven PIXE and EDX experiment. The campaign was carried out at the Centro de Láseres Pulsados (CLPU) in Salamanca with the 200 TW VEGA-2 laser system, and the achievements are presented in Chapter 7. Two setups were exploited to irradiate a sample composed of a micrometric thick Cr layer covering a thick Cu substrate. In the first setup, the so-called EDX setup, the sample irradiation was performed with both electrons and protons. In the second configuration, i.e. the PIXE setup, the electrons are deflected with a dipole magnet and stopped by lead shielding, ensuring that the particle field reaching the sample is mainly composed of protons. The results confirm that the X-ray production due to electrons is 10 times higher than that due to protons. Therefore, laser-driven EDX can be used to successfully identify the elements with fewer shots compared to laser-driven PIXE. Because of the higher range of laser-driven electrons in the matter than that of protons, the probed thickness is larger. On the other hand, we can conclude that laser-driven PIXE allows performing the quantitative stratigraphic analysis of non-homogeneous samples. This possibility was assessed by applying the software for the sample composition reconstruction to the recorder X-ray spectrum in the laser-driven PIXE measurement. Indeed, the code was able to retrieve the correct Cr layer thickness. These achievements confirm that laser-driven PIXE and EDX are complementary techniques that can be effectively performed with minimum changes to the experimental setup.

The last activity carried out with this PhD work and presented in Chapter 8 consists of a theoretical and numerical investigation of the laser-driven PAA feasibility. In particular, two models were developed for the description of PAA performed with both monoenergetic and laser-driven electron sources. In the second scenario, a near-critical material covering a thick converter was considered for the bremsstrahlung photon generation. Exploiting the laser-driven PAA model, the optimal near-critical layer and converter parameters were retrieved in a wide range of laser intensities. Then, both models were used to compare the performances PAA performed with laser-driven sources and electron LINACs. The results confirm that the potentials of laser-driven PAA, carried out with 100s TW class lasers and near-critical targets, are not far from the capabilities of conventional PAA. Remarkably, PAA could be already performed in existing super-intense laser facilities. These conclusions have been further assessed through Monte Carlo and 3D PIC simulations of conventional and laser-driven PAA experiments.

Laser-driven particle sources have been a thriving research topic in the last two decades, thanks to their many foreseen applications in a large number of scientific, technological and societal fields. While for most of such applications significant challenges still need to be tackled, the achievements presented in this PhD thesis for laser-driven PIXE, EDX and PAA demonstrate the feasibility of a compact, versatile, laser-based multi-radiation platform for different materials science studies. This goal can be achieved by combining several activities, i.e. (I) a thorough numerical approach for the system design, taking into account the most recent advanced laser-driven particle acceleration schemes and state-of-the-art laser systems; (II) experimental campaigns of laser-driven particle acceleration oriented toward materials characterization; (III) fabrication of advanced targets with controlled properties to mitigate the laser requirements and improve the particle source stability.

Starting from the activities presented in Part II of this work, the mechanical properties of the Ti films and targets presented in Chapters 4 and 5 must be characterized. For instance, Brillouin spectroscopy and nanoindentation can be used for the elastic modulus and the hardness, respectively. Indeed, these quantities, whose knowledge is crucial for several applications, are still missing in literature for the *fcc* and ω phases of Ti. Besides, they can be helpful to improve the properties of Ti targets produced via Magnetron Sputtering. In parallel, the thickness range of the targets should be extended from $\sim$ 100 nm to several micrometres. Indeed, changing the target thickness is an easy way to tune the energy of the accelerated particles. Moreover, the deposition of other materials like Aluminum, Copper, and Iron can be performed. As far as DLTs are concerned, the next step is the near-critical carbon foam deposition via Pulsed Laser Deposition on the Ti substrates. The final result will be a fully optimized DLT whose properties can be controlled from the solid foil and near-critical layer side. These targets must be tested in a laser-driven ion acceleration campaign and, finally, be used in laser-driven PIXE and EDX experiments with compact 10s TW class lasers.

Considering the results presented in Part III of this work, the experimental setups developed for laser-driven PIXE, EDX and PAA are suitable starting points for further optimizations. For instance, the simple system for the removal of the electrons in PIXE can be considerably improved. The setup optimization cannot disregard the use of compact 10s TW class lasers and advanced DLTs. Then, exploiting the new configuration, further laser-driven PIXE and EDX experiments should be performed. In these experiments, the quantitative PIXE analysis of more complex multi-elemental and non-homogeneous samples will be carried out. In addition, both laser-driven PIXE and EDX measurements on large materials could be achieved in-air. To this aim, a dedicated setup might be designed and implemented. This point is crucial to apply laser-driven PIXE to the study of cultural heritage samples, which is one of the most fascinating applications. As far as laser-driven PAA is concerned, the next step consists of the first proof-of-principle experiment carried out with a 100s TW class laser system and the target-converter configuration proposed in this work. Lastly, other atomic and nuclear analytical methods like X-ray Fluorescence Spectroscopy and Neutron Activation Analysis are worthy of consideration as potential applications of laser-driven radiation sources. Therefore, the number of laser-driven materials characterization techniques under investigation might increase in the coming years.

List of Figures

1.1 Schematic representation of (**a**) X-ray emission spectroscopy, (**b**) creation of the vacancy in the inner shell and (**c**) atomic relaxation with X-ray emission. 10
1.2 Schematic representation of (**a**) Rutherford Backscattering Spectroscopy and (**b**) Elastic Recoil Detection Analysis. 11
1.3 (**a**) Conceptual scheme of EDX spectroscopy and (**b**) an example of EDX spectrum obtained from a stainless steel sample coated with a 1.0 μm thick Ti layer. The accelerating voltage was set equal to 8 kV. . . . 13
1.4 Example of a typical PIXE spectrum from [24]. The elements and the atomic transitions are reported in correspondence with the peaks. 14
1.5 Scheme of the vacuum chamber for PIXE analysis. From [1]. 15
1.6 Examples of (**a**) K-shell and (**b**) L1-shell ionization cross sections for different values of atomic number Z. (**c**) Behaviour of the fluorescence yields for the K and L shells. 16
1.7 Conceptual schemes for the (**a**) homogeneous and (**b**) non-homogeneous sample irradiation geometry. 18
1.8 Example of differential PIXE analysis result from [5]. The concentration profiles of the elements in an Early Medieval brooch are shown. The object under investigation is reported as an inset image in the right panel. 19
1.9 Typical PAA irradiation geometry. The inset plot shows the bremsstrahlung photon energy spectrum (red line) obtained from the irradiation of a 3 mm tungsten converter with 30 MeV energy electrons and three photonuclear reaction cross sections (from the EXFOR database [40]). . . . 20
1.10 Representation of the total photon absorption cross section. Energy regions associated with the different (γ, γ') and (γ, xn) reactions are highlighted. From [20]. 22
1.11 Example of PAA spectrum. From [22]. 23
1.12 Conceptual schemes of (**a**) the single-ended Van de Graaff, (**b**) cyclotron and (**c**) LINAC accelerators. 25

2.1 Schematic representation of the Chirped Pulse Amplification working principle. 28
2.2 Scheme of the electron heating processes in the interaction of an ultra-intense laser pulse with an over-dense plasma. Adapted from [62]. . . . 30
2.3 (**a**) Scheme of the Target Normal Sheath Acceleration and (**b**) example of accelerated proton spectrum taken from [67]. 32
2.4 SEM (**a**) cross section view and (**b**) top view of a near-critical Carbon nanofoam deposited at the NanoLab with the ns-Pulsed Laser Deposition technique. 34
2.5 (**a**) Proton energy spectra obtained with a laser intensity $\sim 3.5 - 4 \times 10^{20}\ \mathrm{W/cm^2}$ for S-, P- and circular polarization with the bare target (the f, d, and e dotted lines) and the DLT (the a, b, and c continuous lines). The near-critical layer thickness of the DLT is equal to 8 μm. The inset plot shows the electron energy spectra for the bare and double-layer 12 μm thick targets for the different polarizations. From [90]. (**b**) Proton energy spectra for different foam thicknesses (8, 12, and 18 μm) deposited on a 0.75 μm thick Al substrate. The spectrum obtained with the bare target is also shown. From [91]. 35
2.6 3D PIC simulation output showing the transverse component of the electric field of an ultra-intense laser with $a_0 = 10$, propagating inside a uniform near-critical plasma with $n_e/n_c = 1$ at the time 40 λ/c after the beginning of the interaction. The simulation was performed with the Piccante code [100]. 37
2.7 Electron energy spectra at three emission angles accelerated with a near-critical material. From [102]. 39
2.8 Conceptual scheme of the laser wakefield acceleration mechanism. . . . 40

3.1 (**a**) Schematic representation of the DC diode sputtering configuration. (**b**) Sputtering process representation for the single knock-on, linear cascade and spike regimes. Adapted from [152]. 47
3.2 Conceptual scheme of the balanced Magnetron Sputtering. The magnetic field configuration is shown, as well as an eroded Ti target. 48
3.3 Unbalanced Magnetron Sputtering in the (**a**) type-1 and (**b**) type-2 configuration. 49
3.4 Magnetron Sputtering deposition system at Nanolab in Politecnico di Milano. (**a**) Image of the machine. (**b**) Image of the anodes taken during the co-deposition from two Ti targets. The HiPIMS plasma is visible. . 50
3.5 (**a**) Example of experimental voltage and current waveforms taken from [163]. (**b**) The experimental trend of discharge peak current taken from [159]. The dashed black lines highlight the four regions of the HiPIMS operation. 51
3.6 Structure Zone Diagram for energetic depositions. Representative values of the normalized energy, generalized temperature and net thickness are reported on the axes. From [166]. 53
3.7 Phase diagram of titanium. The regions associated with the α, ω, β and liquid phases are indicated. 54

3.8 (**a**) Sampling of the plasma distribution function with macro-particles in the x-component of the phase space. From [197]. (**b**) Scheme of the Particle-In-Cell loop. 56
3.9 Comparison between Geant4 and Fluka simulations of bremsstrahlung photon production from 30 MeV energy electrons interacting with a 3 mm thick tungsten plate. (**a**) Photon energy spectra. (**b**) Energy vs solid angle distribution for the photons emitted in the forward direction. . . . 59
3.10 Comparison between photonuclear reaction cross sections from the literature [216–218] and TENDL database [219] (black points) and simulated with Fluka (red points) and Geant4 (blue points) for the (**a**) Co-59, (**b**) Cu-65, (**c**) Sb-123 and (**d**) Mo-100 isotopes. 61

4.1 (**a**) HiPIMS voltage and current waveforms measured at 0.5 Pa Ar pressure, 650 V applied voltage and 50 μs pulse duration. (**b**) Discharge peak current as a function of the discharge voltage at 0.5 Pa Ar pressure and 50 μs pulse duration. The vertical dashed lines delimit the four regions characterized by different plasma conditions. 66
4.2 (**a**) Optical emission spectra acquired in DCMS (blue) and HiPIMS (red) regimes at the same power of 450 W. The regions associated with Ti and Ar species are delimited with vertical dashed lines. (**b**) Optical emission spectra acquired in HiPIMS for 5 kW (purple), 27 kW (red) and 50 kW (yellow) peak powers. Peaks associated with the various species are pointed with arrows. 67
4.3 Normalized OES peak intensity as a function of the peak power for Ti, Ti^+, Ti^{2+}, Ar and Ar^+ species. 68
4.4 Ratio of the average intensities for the $\mathrm{Ti}^+/\mathrm{Ti}$ (red points) and $\mathrm{Ar}^+/\mathrm{Ar}$ (blue points) as a function of the peak intensity. 69
4.5 SEM top-views of (**a**) Ti-DCMS films, Ti-HiPIMS films deposited (**b**) without the application of the bias voltage, with the application of (**c**) 300 V and (**d**) 500 V bias. The film thickness is reported on the top of each panel. 71
4.6 SEM cross section views of (**a**) 658 nm thick Ti-DCMS film, (**b**) 580 nm thick Ti-HiPIMS film deposited without the application of the bias voltage, (**c**) 587 nm thick Ti-HiPIMS film deposited with 300 V bias and (**d**) 495 nm thick Ti-HiPIMS film deposited with 500 V bias. 72
4.7 (**a**) Cross section view tilted at 20° of the thickest Ti-HiPIMS film deposited with 500 V bias. (**b**) Magnification of the lamellar structures. . 72
4.8 XRD spectra of Ti films deposited in (**a**) DCMS and HiPIMS with an applied bias voltage of (**b**) 0 V, (**c**) 300 V and (**d**) 500 V. The thickness of the associated film is reported over each curve. The crystallographic orientations are marked with vertical dashed lines. 73
4.9 fcc, α and ω phase concentrations as a function of the thickness in Ti-HiPIMS films deposited at (**a**) 0 V, (**b**) 300 V and (**c**) 500 V bias. 74
4.10 XRD spectra of a Ti film containing ω phase before and after the vacuum annealing procedure. The inset graph shows the α and ω phase percentage as a function of the annealing temperature. 74

4.11 (**a**) Average residual stresses for the Ti-DMCS films as a function of the thickness. (**b**) Average residual stresses for the Ti-HiPIMS films at 0 V of bias as a function of the thickness (blue points). The content of the *fcc* phase is reported as grey points. (**c**) Average residual stresses for the Ti-HiPIMS films at 300 V of bias as a function of the thickness (purple points). The content of the ω phase is reported as grey points. (**d**) Average residual stresses for the Ti-HiPIMS films at 500 V of bias as a function of the thickness (red points). The content of the ω phase is reported as grey points. 76

4.12 Nucleation, coalescence and thickening of the film during Volmer-Weber growth with high surface mobility metals. Adapted from [242]. 79

5.1 (**a**) Target older disassembled in its two components. (**b**) The surface of the holder on which the Ti substrate is grown and SEM magnification image of six holed. 82

5.2 Schematic representation of the step-by-step strategy developed for the DLT production. The procedure involves the holder holes filling (step I), substrate deposition (step II), dissolution of the sacrificial layer (step III) and carbon foam deposition (step IV). 83

5.3 (**a**) Example of a hole after HiPIMS deposition of the Ti film on PMMA. The damage at the border of the hole is evident. (**b**) Magnification of the wrinkle at the centre of the hole. 84

5.4 Example of five holes after the filling with the liquid solution and solidification of the sucrose layer. 85

5.5 (**a**) Example of a hole after the DCMS deposition of the Ti film and dissolution of the sucrose layer. The film is collapsed at the centre of the holder hole. (**b**) Cross section view of the Ti film deposited via DCMS on a Si substrate. 86

5.6 (**a**) Cross section view of the Ti film deposited via HiPIMS on a Si substrate. (**b**) Example of damage of the Ti film and sucrose layer during HiPIMS deposition. 87

5.7 SEM (**a**) cross section and (**b**) top views of the Ti film composed by one layer (half thickness) of DCMS and one layer (half thickness) of HiPIMS. 88

5.8 Characterization of Ti films deposited with the alternation of DCMS and unbiased HiPIMS depositions. (**a**) SEM cross section views. The expected DCMS and HiPIMS contributions to the total thickness are reported as blue and red bars, respectively. The overall HiPIMS fraction is also reported on the bottom right of each panel. (**b**) Stress state and (**c**) density as a function of the HiPIMS fraction. 89

5.9 (**a**) XRD spectra of Ti films deposited with the alternation of DCMS and HiPIMS depositions at an increasing fraction of the latter. (**b**) XRD spectra of Ti films deposited with 40% HiPIMS fraction and 100% HiPIMS. 90

5.10 (**a**) SEM cross section view of the 300 nm thick substrate deposited with one layer of DCMS and one layer of HiPIMS. (**b**) Example of a hole after the 300 nm thick substrate deposition and removal of the sucrose layer. (**c**) SEM cross section view of the 600 nm thick substrate deposited with two layers of DCMS and two layers of HiPIMS. (**d**) Example of a hole after the 600 nm thick substrate deposition and removal of the sucrose layer. 91

5.11 Examples of grain boundaries and magnification of a film micro-crack formed after the sucrose layer dissolution. 91

5.12 Characterization of Ti films deposited with the alternation of DCMS and biased HiPIMS depositions. (**a**) SEM cross section views. The expected DCMS and HiPIMS contributions to the total thickness are reported as blue and yellow bars, respectively. The overall HiPIMS fraction is also reported on the bottom right of each panel. (**b**) Density and (**c**) stress state as a function of the HiPIMS fraction. (**d**) XRD spectra. 92

5.13 Top view of the freestanding Ti substrates deposited on the perforated target holder and magnification in correspondence of six holes. 93

6.1 Conceptual schemes for the (**a**) homogeneous and (**b**) non-homogeneous sample irradiation geometry in laser-driven PIXE. 98

6.2 Scheme of the laser-driven in-air PIXE analysis of a painting. (**a**) Laser-driven proton source composed of a double-layer target irradiated with an ultraintense laser pulse (snapshot from a PIC simulation). (**b**) Monte Carlo simulation setup: (b1) fist aperture slit; (b2) 0.15 T dipole magnet; (b3) second aperture slit; (b4) 1 μm thick Si_3N_4 exit window [259] (b5) sample placed in the air at 2 cm distance from the exit window; (b6) Example of proton energy spectrum at the sample surface; (b7) CCD camera (PI-LCX:1300) screen of dimensions $2.6 \times 2.68\ cm^2$. (b8) Example of X-ray energy spectrum recorded by the CCD. (**c**) retrieved elemental concentration profiles (solid lines) and actual profiles (filled regions). . 102

6.3 3D Particle-In-Cell simulation results. (**a**) Angular and energy distribution of the protons for the $a_0 = 4.0$ case and retrieved at 267 fs. Each panel reports the angular distribution at the corresponding energy range. (**b**) Snapshot at 267 fs of the macro-protons for the $a_0 = 4.0$ case. Only the central region of the simulation box is shown, and the macro-protons are coloured according to their energy. The two black lines indicate the direction normal to the target surface ($\tilde{n}$) and the 3° tilted direction ($\tilde{t}$). (**c**) Energy spectra for all the protons (purple), for the protons propagating along $\tilde{n}$ (light blue) and $\tilde{t}$ (green). 104

6.4 Homogeneous sample analysis results. (**a**) Proton energy spectrum exploited for the Monte Carlo simulation (black line) and energy spectra interval used to obtain the elemental concentrations for the sensitivity analysis (yellow filled area). (**b**) Comparison between the retrieved and actual elemental concentrations. (**c**) The relative error for the retrieved concentrations as a function of the fluctuation parameter α. 106

6.5 Non-homogeneous metallic sample quantitative analysis. (**a**) Proton energy spectra at the sample surface. The inset graph reports the proton fluence at the surface of the sample. (**b-f**) Comparison between actual (filled regions) and retrieved (lines) concentration profiles. 107

6.6 Painting quantitative analysis. (**a**) Proton energy spectra at the sample surface. The inset graph reports the proton fluence at the surface of the sample. (**b-f**) Comparison between actual (filled regions) and retrieved (lines) concentration profiles. 108

6.7 (**a**) Simulation setup for laser-driven PIXE and electron irradiation in air. (**b**) Low energy region of the X-ray spectra from proton (dark blue) and electron (light blue) irradiation with the in-air setup. (**c**) Photon spectrum in the $0-2$ MeV energy range obtained by the simulation of electron irradiation in-air. (**d**) Comparison between the X-ray yields obtained under the different simulated irradiation conditions. The green and blue bars are related to the in-vacuum and in-air irradiation conditions, respectively. 110

7.1 Conceptual representations of the (**a**) LD-EDX and (**b**) LD-PIXE experimental setups. (**c**) Image of part of the LD-EDX setup. The movable target holder, protective Al foil, irradiated sample and aperture slit are pointed with arrows. (**d**) Top view scheme of the LD-PIXE setup. All distances and angles are reported. 114

7.2 SEM images of the sample. (**a**) Cross section view. The thickness is reported. (**b**) Planar view. 115

7.3 (**a**) Example of ToF signal acquired during the experiment. The photopeak and the proton signal are pointed with arrows. (**b**) Proton energy spectrum recorded with the ToF diagnostic. The continuous black line is the average spectrum, while the purple area is the statistical uncertainty. (**c**) Frequency distribution of the maximum proton energy. The continuous vertical line is the average value. The purple bandwidth is equal to two times the standard deviation. 116

7.4 (**a**) Magnification of a recorded CCD image. Single-pixel events are pointed with arrows. (**b**) Representation of the single-pixel event and surrounding pixels considered for the spectrum reconstruction. (**c**) X-ray spectrum obtained from the Cu sample irradiation and exploited for the CCD energy calibration. The inset plot shows the intensity distribution of the local background around single-pixel events. 118

7.5 Laser-driven EDX and PIXE results. (**a**) X-ray spectrum obtained with the LD-EDX setup. The red points are the average over the shots of the photon counts at each energy. The error bars are evaluated as two times the standard deviation. The fit is represented as a blue line. The filled curves are the Gaussian fits of the peaks. (**b**) Summary of the X-ray peak energies and intensity ratios of Cr and Cu $\mathrm{k}\alpha$ peaks. In the first column, the expected X-ray energies from the literature are reported. The second, third and fourth columns are associated with the X-ray spectra exploited for the CCD energy calibration and from the sample irradiation with the LD-EDX and LD-PIXE setups, respectively. (**c**) X-ray spectrum obtained with the LD-PIXE setup. 119

7.6 Laser-driven PIXE stratigraphic analysis results. The red and yellow lines represent the layer thicknesses obtained assuming a pure Cr film and a 93% Cr plus 7% O film, respectively. The blue line is the thickness retrieved with the yield ratio from the laser-driven EDX measurement. The colour-filled regions are the statistical uncertainties. 121

7.7 Thickness uncertainty evaluation for the laser-driven PIXE measurement. (**a**) Frequency distribution of the thickness. The related uncertainty is reported in the inset graph. (**b**) Heat-map representing the scattered data from the Monte Carlo. The horizontal axis reports the intensity ratio, while the evaluated thickness is located on the vertical axis. The colour scale represents the number of occurrences. The green dots were obtained at fixed intensity ratio (equal to the average value). The red dots were obtained at a fixed proton energy spectrum (the average one). 122

7.8 (**a**) Top view of the component for the removal of the electrons and (**b**) slices of the magnetic field intensity distribution calculated with the mFEA simulation. The TOP slice is parallel to the top view, and it crosses the centre of the magnet. In the first panel, the position of the S1 and S2 slices are pointed with arrows. 123

7.9 Snapshots of (**a**) the laser-driven EDX and (**b**) laser-driven PIXE Monte Carlo simulations. 124

7.10 Laser-driven EDX Monte Carlo simulation outputs with electrons of 0.67 MeV temperature as primary particles. The filled red curve is the electron energy spectrum at the sample surface. The filled blue areas are the X-ray differential yields. The inset plot is the simulated X-ray spectrum. 125

7.11 Laser-driven PIXE Monte Carlo simulation outputs with electrons of 0.67 MeV temperature as primary particles. The filled red curve is the electron energy spectrum at the sample surface. The filled blue areas are the X-ray differential yields. The inset plot is the simulated X-ray spectrum. 126

7.12 Comparison between the simulated and experimental fitted X-ray peaks for laser-driven EDX. The inset bar plot compares the experimental and simulated X-ray yields. 127

7.13 Comparison between the simulated and experimental fitted X-ray peaks for laser-driven PIXE. The inset bar plot compares the experimental and simulated X-ray yields. 128

7.14 Linear fit (black line) of the X-ray yields ratio due to electrons in the laser-driven PIXE and EDX measurements as a function of the electron temperature T_e. The data exploited for the fit are reported as blue points. The red marker is the ratio of the yields obtained from the fit in correspondence with $T_e = 0.63 \pm 0.49$ MeV. 129

8.1 Conceptual scheme of the laser-driven PAA setup. The near-critical material is located on the rear side of the mm thick converter material. A magnification of the laser propagating in the near-critical medium is shown (from a 3D PIC simulation). The hot electrons interact with the converter, and they generate bremsstrahlung photons. The photons irradiate a sample and a calibration material. The subsequent emission of characteristic γ-rays is reported as black wavy arrows. 132

8.2 Bremsstrahlung spectra simulated with Fluka for (**a**) different values of the primary electron energy and fixed converter thickness (i.e. 3 mm); (**b**) different values of the converter thickness and fixed primary electron energy (i.e. 30 MeV). The spectra are normalized to the total number of primary electrons. 133

8.3 (**a**) Comparison between normalized experimental photonuclear cross sections and a Gaussian function centred in 17 MeV and having Full Width Half Maximum equal to 7 MeV. (**b**) Contour plot representing the normalized yield as a function of the primary electron energy and converter thickness. The continuous black line marks the locus of optimal converter thickness for each value of electron energy. The purple markers are in correspondence with experimental conditions reported in the literature [286–292]. 134

8.4 (**a**) Contour plot representing the normalized yield as a function of the laser-driven electron temperature and converter thickness. The continuous black line is in correspondence with the maximum normalized yield for each electron temperature. (**b**) Normalized yields per laser shot for three values of a_0 (i.e. 20, 30, and 40) as a function of the target near-critical layer density and thickness. The maxima are marked with a black dot, and they are projected on the horizontal plane at $\Phi = 0$. 136

8.5 (**a**) Optimal near-critical layer density and thickness as a function of the normalized laser intensity. (**b**) Laser-driven electron temperature and number per shot as a function of the laser intensity at the optimal target conditions. 137

8.6 Comparison between monoenergetic and laser-driven sources for PAA. The read heat-map is the normalized activation rate associated with the laser-driven source as a function of the laser intensity and repetition rate. The isolines are in correspondence with the normalized activation rate achievable with conventional accelerators working at the reported electron energies and currents (from the literature [286, 288]). The normalized activation rates corresponding to the isolines are reported on the right side of the map. The grey points are in correspondence with two PAA experimental conditions simulated with the Monte Carlo and presented in Section 8.3. The cross marker identifies the laser parameters for the PIC-Monte Carlo laser-driven PAA simulation shown in Section 8.4. 138

8.7 Example of γ-ray energy spectrum from the S1 simulation. The characteristic γ-ray peaks associated with the considered elements are marked. 141

8.8 (**a**) The ratio between the intensities from simulations $\mathrm{S1/S2}$ and $\mathrm{S3/S4}$ for each element. The continuous red line is the ratio predicted by the model by assuming a normalized cross section centred in 17 MeV. The dashed upper and lower red lines are the ratios predicted by the model by assuming normalized cross sections centred in 20 MeV and 15 MeV, respectively. (**b**) The ratio between the intensities from simulations $\mathrm{S1/S3}$ and $\mathrm{S2/S4}$ for each element. The black line corresponds to the value predicted by the model. 142

8.9 Three-dimensional exploded view of the electron density and z-component of the magnetic field obtained from the 3D PIC simulation. They are retrieved at the instant of time at which the laser front reaches the rear side of the near-critical layer. The fictitious interface with the converter is marked with a dashed line. 144

8.10 (**a-c**) Electron momentum distributions retrieved from the PIC simulation after 143 fs. The 2D distributions are integrated along one momentum component and plotted in the other two. (**d**) Electron energy spectrum from the PIC simulation and bremsstrahlung photon spectrum from the Monte Carlo simulation. 145

8.11 Polar plot of the energy vs angular distribution of the bremsstrahlung photons. The colour scale is the number of photons normalized to the number of electrons. 146

8.12 (**a**) Simulated γ-ray energy spectra emitted following the activation of the sample and retrieved after three different cooling times. (**b**) Comparison between the retrieved elemental concentrations from the simulated γ-ray spectra and the values set in the Monte Carlo code. 147

List of Tables

1.1 Examples of nuclear reactions exploited in PAA. 22

3.1 Examples of sputtering yields for 100, 200 and 300 eV energy Argon ions and several target elements. Extracted from [155]. 47

4.1 Wavelength λ and excitation energy E of the identified spectral lines for Ti, Ti^+, Ti^{2+}, Ar and Ar^+ species. 69
4.2 Ranges of Ti^+ ions (from SRIM simulations) for five different initial energies travelling across Si oxide layers over semi-infinite Si substrates and in a semi-infinite Ti medium. 77

8.1 Summary of the source parameters for the conventional and laser-driven PAA experiments selected to be simulated. 140
8.2 Elemental mass concentrations of the sample. 141
8.3 Elemental mass concentrations of the calibration material. 143

Bibliography

[1] H. R. Verma. *Atomic and nuclear analytical methods*. Springer, 2007.

[2] R. Jenkins. *X-ray fluorescence spectrometry*, volume 2. Wiley New York, 1999.

[3] D. C. Bell and A. J. Garratt-Reed. *Energy dispersive X-ray analysis in the electron microscope*, volume 49. Garland Science, 2003.

[4] S. A. Johansson, J. L. Campbell, and K. G. Malmqvist. *Particle-induced X-ray emission spectrometry (PIXE)*, volume 133. Wiley New York, 1995.

[5] Ž. Šmit, J. Istenič, and T. Knific. Plating of archaeological metallic objects–studies by differential pixe. *Nuclear Instruments and Methods in Physics Research Section B: Beam Interactions with Materials and Atoms*, 266(10):2329–2333, 2008.

[6] A. G. Karydas, C. Streeck, I. Bogdanovic Radovic, C. Kaufmann, T. Rissom, B. Beckhoff, M. Jaksic, and N. P. Barradas. Ion beam analysis of Cu(In, Ga)Se2 thin film solar cells. *Applied Surface Science*, 356:631–638, 2015.

[7] D. Nam, A. S. Opanasyuk, P. V. Koval, A. G. Ponomarev, A. R. Jeong, G. Y. Kim, W. Jo, and H. Cheong. Composition variations in cu2znsnse4 thin films analyzed by x-ray diffraction, energy dispersive x-ray spectroscopy, particle induced x-ray emission, photoluminescence, and raman spectroscopy. *Thin Solid Films*, 562:109–113, 2014.

[8] T. Z. Hossain and J. K. Lowell. Method and apparatus for the detection of light elements on the surface of a semiconductor substrate using x-ray fluorescence (xrf), July 7 1998. US Patent 5,778,039.

[9] C. Q. Orsini and L. C. Boueres. A pixe system for air pollution studies in south america. *Nuclear Instruments and Methods*, 142(1-2):27–32, 1977.

[10] E. Wyroba, S. Suski, K. Miller, and R. Bartosiewicz. Biomedical and agricultural applications of energy dispersive x-ray spectroscopy in electron microscopy. *Cellular and Molecular Biology Letters*, 20(3):488–509, 2015.

[11] D. C. Weindorf, Y. Zhu, S. Chakraborty, N. Bakr, and B. Huang. Use of portable x-ray fluorescence spectrometry for environmental quality assessment of peri-urban agriculture. *Environmental Monitoring and Assessment*, 184(1):217–227, 2012.

[12] P. A. Mandò, M. E. Fedi, N. Grassi, and A. Migliori. Differential pixe for investigating the layer structure of paintings. *Nuclear Instruments and Methods in Physics Research Section B: Beam Interactions with Materials and Atoms*, 239(1-2):71–76, 2005.

[13] A. G. Shen, X. H. Wang, W. Xie, J. Shen, H. Y. Li, Z. A. Liu, and J. M. Hu. Pigment identification of colored drawings from wuying hall of the imperial palace by micro-raman spectroscopy and energy dispersive x-ray spectroscopy. *Journal of Raman Spectroscopy: An International Journal for Original Work in all Aspects of Raman Spectroscopy, Including Higher Order Processes, and also Brillouin and Rayleigh Scattering*, 37(1-3):230–234, 2006.

[14] M. Mantler and M. Schreiner. X-ray fluorescence spectrometry in art and archaeology. *X-Ray Spectrometry: An International Journal*, 29(1):3–17, 2000.

[15] M. Rubel, J. P. Coad, D. Hole, JET-EFDA Contributors, et al. Accelerator-based ion beam analysis of fusion reactor materials. *Vacuum*, 78(2-4):255–261, 2005.

[16] M. Lungu, C. Dobrea, and I Tiseanu. Enhanced xrf methods for investigating the erosion-resistant functional coatings. *Coatings*, 9(12):847, 2019.

[17] R. W. Hamm and M. E. Hamm. *Industrial accelerators and their applications*. World Scientific, 2012.

[18] J. Salomon, D. C. Dran, T. Guillou, B. Moignard, L. Pichon, P. Walter, and F. Mathis. Present and future role of ion beam analysis in the study of cultural heritage materials: The example of the aglae facility. *Nuclear Instruments and Methods in Physics Research Section B: Beam Interactions with Materials and Atoms*, 266(10):2273–2278, 2008.

[19] R. R. Greenberg, P. Bode, and E. A D. N. Fernandes. Neutron activation analysis: a primary method of measurement. *Spectrochimica Acta Part B: Atomic Spectroscopy*, 66(3-4):193–241, 2011.

[20] C. Segebade and A. Berger. Photon activation analysis. *Encyclopedia of Analytical Chemistry: Applications, Theory and Instrumentation*, 2006.

[21] E. Witkowska, K. Szczepaniak, and M. Biziuk. Some applications of neutron activation analysis. *Journal of Radioanalytical and Nuclear Chemistry*, 265(1):141–150, 2005.

[22] C. Segebade, V. N. Starovoitova, T. Borgwardt, and D. Wells. Principles, methodologies, and applications of photon activation analysis: a review. *Journal of Radioanalytical and Nuclear Chemistry*, 312(3):443–459, 2017.

[23] G. F. Knoll. *Radiation detection and measurement*. John Wiley & Sons, 2010.

[24] G. Quarta, L. Calcagnile, and M. Vidale. Integrating non-destructive ion beam analysis methods and ams radiocarbon dating for the study of ancient bronze statues. *Radiocarbon*, 54(3-4):801–812, 2012.

[25] J. A. Maxwell, W. J. Teesdale, and J. L. Campbell. The guelph pixe software package ii. *Nuclear Instruments and Methods in Physics Research Section B: Beam Interactions with Materials and Atoms*, 95(3):407–421, 1995.

[26] C. G. Ryan, D. R. Cousens, S. H. Sie, and W. L. Griffin. Quantitative analysis of pixe spectra in geoscience applications. *Nuclear Instruments and Methods in Physics Research Section B: Beam Interactions with Materials and Atoms*, 49(1-4):271–276, 1990.

[27] J. F. Ziegler, M. D. Ziegler, and J. P. Biersack. Srim–the stopping and range of ions in matter (2010). *Nuclear Instruments and Methods in Physics Research Section B: Beam Interactions with Materials and Atoms*, 268(11-12):1818–1823, 2010.

[28] W. Brandt and G. Lapicki. L-shell coulomb ionization by heavy charged particles. *Physical Review A*, 20(2):465, 1979.

[29] W. Brandt and G. Lapicki. Energy-loss effect in inner-shell coulomb ionization by heavy charged particles. *Physical Review A*, 23(4):1717, 1981.

[30] A. Kahoul, A. Abassi, B. Deghfel, and M. Nekkab. K-shell fluorescence yields for elements with $6 \leq z \leq 99$. *Radiation Physics and Chemistry*, 80(3):369–377, 2011.

[31] M. J. Berger, J. H. Hubbell, S. M. Seltzer, J. Chang, J. S. Coursey, R. Sukumar, D. S. Zucker, and K. Olsen. Xcom: photon cross section database (version 1.5),[online] available: http://physics. nist. gov/xcom, national institute of standards and technology, gaithersburg. *Gaithersburg, MD*, 2005.

[32] W. Reuter, A. Lurio, F. Cardone, and J. F. Ziegler. Quantitative analysis of complex targets by proton-induced x rays. *Journal of Applied Physics*, 46(7):3194–3202, 1975.

[33] Ž. Šmit, M. Uršič, P. Pelicon, T. Trček-Pečak, B. Šeme, A. Smrekar, I. Langus, I. Nemec, and K. Kavkler. Concentration profiles in paint layers studied by differential pixe. *Nuclear Instruments and Methods in Physics Research Section B: Beam Interactions with Materials and Atoms*, 266(9):2047–2059, 2008.

[34] N. Grassi, A. Migliori, P. A. Mandò, and H. Calvo Del Castillo. Differential pixe measurements for the stratigraphic analysis of the painting madonna dei fusi by leonardo da vinci. *X-Ray Spectrometry: An International Journal*, 34(4):306–309, 2005.

[35] W. Maenhaut, L. De Reu, H. A. Van Rinsvelt, J. Cafmeyer, and P. Van Espen. Particle-induced x-ray emission (pixe) analysis of biological materials: Precision, accuracy and application to cancer tissues. *Nuclear Instruments and Methods*, 168(1-3):557–562, 1980.

[36] H. J. Annegarn and S. Bauman. Geological and mineralogical applications of pixe: A review. *Nuclear Instruments and Methods in Physics Research Section B: Beam Interactions with Materials and Atoms*, 49(1-4):264–270, 1990.

[37] T. Calligaro. Pixe in the study of archaeological and historical glass. *X-Ray Spectrometry: An International Journal*, 37(2):169–177, 2008.

[38] D. D. Cohen, G. M. Bailey, and R. Kondepudi. Elemental analysis by pixe and other iba techniques and their application to source fingerprinting of atmospheric fine particle pollution. *Nuclear Instruments and Methods in Physics Research Section B: Beam Interactions with Materials and Atoms*, 109:218–226, 1996.

[39] I. O. Mitu, G. Floare, D. G. Ghiţă, D. V. Moşu, and G. Căta-Danil. Radiological protection evaluation of the bucharest tandetron 3 mv accelerator. *Journal of Radiological Protection*, 35(2):285, 2015.

[40] V. V. Zerkin and B. Pritychenko. The experimental nuclear reaction data (exfor): Extended computer database and web retrieval system. *Nuclear Instruments and Methods in Physics Research Section A: Accelerators, Spectrometers, Detectors and Associated Equipment*, 888:31–43, 2018.

[41] S. M. Seltzer and M. J. Berger. Bremsstrahlung spectra from electron interactions with screened atomic nuclei and orbital electrons. *Nuclear Instruments and Methods in Physics Research Section B: Beam Interactions with Materials and Atoms*, 12(1):95–134, 1985.

[42] K. Masumoto, T. Ohtsuki, Y. Miyamoto, J. Zaidi, A. Kajikawa, H. Hab, and K. Sakamoto. Photon activation analysis of iodine, thallium and uranium in environmental materials. *Journal of radioanalytical and nuclear chemistry*, 239(3):495–500, 1999.

[43] Z. Řanda, J. Kučera, J. Mizera, and J. Frána. Comparison of the role of photon and neutron activation analyses for elemental characterization of geological, biological and environmental materials. *Journal of radioanalytical and nuclear chemistry*, 271(3):589–596, 2007.

[44] T. Kato, N. Sato, and N. Suzuki. Multielement photon activation analysis of biological materials. *Analytica Chimica Acta*, 81(2):337–347, 1976.

[45] B. F. Schmitt and H. U. Fusban. Analysis of carbon, nitrogen and oxygen in refractory metals with the aid of photon activation. *Metall*, 33(12):1265–1269, 1979.

[46] P. Reimers, G. Z. Lutz, and C. Segebade. The non-destructive determination of gold, silver and copper by photon activation analysis of coins and art objects. *Archaeometry*, 19(pt. 2):167–172, 1977.

[47] R. J. Van De Graaff, K. T. Compton, and L. C. Van Atta. The electrostatic production of high voltage for nuclear investigations. *Physical Review*, 43(3):149, 1933.

[48] J. D. Cockcroft and E. T. S. Walton. Artificial production of fast protons. *nature*, 129(3250):242–242, 1932.

[49] E. O. Lawrence. Method and apparatus for the acceleration of ions, February 20 1934. US Patent 1,948,384.

[50] R. Wideröe. Über ein neues prinzip zur herstellung hoher spannungen. In *Arbeiten aus dem Elektrotechnischen Institut der Technischen Hochschule Aachen*, pages 157–176. Springer, 1929.

[51] W. Scharf. *Particle accelerators and their uses*. CRC Press, 1986.

[52] R. J. Van de Graaff. Tandem electrostatic accelerators. *Nuclear Instruments and Methods*, 8(2):195–202, 1960.

[53] Z. Alfassi and M. Peisach. *Elemental analysis by particle accelerators*. CRC Press, 2020.

[54] T. H. Maiman. Stimulated optical radiation in ruby. *nature*, 187(4736):493–494, 1960.

[55] F. J. McClung and R. W. Hellwarth. Giant optical pulsations from ruby. *Journal of Applied Physics*, 33(3):828–829, 1962.

[56] L. E. Hargrove, R. L. Fork, and M. A. Pollack. Locking of he–ne laser modes induced by synchronous intracavity modulation. *Applied Physics Letters*, 5(1):4–5, 1964.

[57] D. Strickland and G. Mourou. Compression of amplified chirped optical pulses. *Optics communications*, 56(3):219–221, 1985.

[58] J. W. Yoon, C. Jeon, J. Shin, S. K. Lee, H. W. Lee, I. W. Choi, H. T. Kim, J. H. Sung, and C. H. Nam. Achieving the laser intensity of 5.5× 10 22 w/cm 2 with a wavefront-corrected multi-pw laser. *Optics express*, 27(15):20412–20420, 2019.

[59] C. Danson, D. Hillier, N. Hopps, and D. Neely. Petawatt class lasers worldwide. *High power laser science and engineering*, 3, 2015.

[60] C. N. Danson, C. Haefner, J. Bromage, T. Butcher, J.-C. F.Chanteloup, E. A. Chowdhury, A. Galvanauskas, L. A. Gizzi, J. Hein, D. I. Hillier, et al. Petawatt and exawatt class lasers worldwide. *High Power Laser Science and Engineering*, 7, 2019.

[61] G. A. Mourou and D. Umstadter. Extreme light. *Scientific American*, 286(5):80–86, 2002.

[62] A. Pazzaglia. Investigation on near-critical double-layer targets for enhanced laser-driven ion acceleration. 2020.

[63] L. Cialfi, L. Fedeli, and M. Passoni. Electron heating in subpicosecond laser interaction with overdense and near-critical plasmas. *Physical Review E*, 94(5):053201, 2016.

[64] A. Macchi, M. Borghesi, and M. Passoni. Ion acceleration by superintense laser-plasma interaction. *Reviews of Modern Physics*, 85(2):751, 2013.

[65] H. Daido, M. Nishiuchi, and A. S. Pirozhkov. Review of laser-driven ion sources and their applications. *Reports on progress in physics*, 75(5):056401, 2012.

[66] A. Maksimchuk, S. Gu, K. Flippo, D. Umstadter, and V. Y. Bychenkov. Forward ion acceleration in thin films driven by a high-intensity laser. *Physical Review Letters*, 84(18):4108, 2000.

[67] R. A. Snavely, M. H Key, S. P. Hatchett, T. E. Cowan, M. Roth, T. W. Phillips, M. A. Stoyer, E. A. Henry, T. C. Sangster, M. S. Singh, et al. Intense high-energy proton beams from petawatt-laser irradiation of solids. *Physical review letters*, 85(14):2945, 2000.

[68] S. P. Hatchett, C. G. Brown, T. E. Cowan, E. A. Henry, J. S. Johnson, M. H. Key, J. A. Koch, A. B. Langdon, B. F. Lasinski, R. W. Lee, et al. Electron, photon, and ion beams from the relativistic interaction of petawatt laser pulses with solid targets. *Physics of Plasmas*, 7(5):2076–2082, 2000.

[69] M. Borghesi, A. Bigongiari, S. Kar, A. Macchi, L. Romagnani, P. Audebert, J. Fuchs, T. Toncian, O. Willi, S. V. Bulanov, et al. Laser-driven proton acceleration: source optimization and radiographic applications. *Plasma Physics and Controlled Fusion*, 50(12):124040, 2008.

[70] M. Passoni and M. Lontano. Theory of light-ion acceleration driven by a strong charge separation. *Physical review letters*, 101(11):115001, 2008.

[71] P. Mora. Thin-foil expansion into a vacuum. *Physical Review E*, 72(5):056401, 2005.

[72] B. J. Albright, L. Yin, B. M. Hegelich, K. J. Bowers, T. J. K. Kwan, and J. C. Fernández. Theory of laser acceleration of light-ion beams from interaction of ultrahigh-intensity lasers with layered targets. *Physical review letters*, 97(11):115002, 2006.

[73] M. Passoni, C. Perego, A. Sgattoni, and D. Batani. Advances in target normal sheath acceleration theory. *Physics of Plasmas*, 20(6):060701, 2013.

[74] T. Ceccotti, A. Lévy, H. Popescu, F. Réau, P. d'Oliveira, P. Monot, J. P. Geindre, E. Lefebvre, and P. Martin. Proton acceleration with high-intensity ultrahigh-contrast laser pulses. *Physical review letters*, 99(18):185002, 2007.

[75] J. Fuchs, P. Antici, E. d'Humières, E. Lefebvre, M. Borghesi, E. Brambrink, C. A. Cecchetti, M. Kaluza, V. Malka, M. Manclossi, et al. Laser-driven proton scaling laws and new paths towards energy increase. *Nature physics*, 2(1):48–54, 2006.

[76] D. Neely, P. Foster, A. Robinson, F. Lindau, O. Lundh, A. Persson, C.-G. Wahlström, and P. McKenna. Enhanced proton beams from ultrathin targets driven by high contrast laser pulses. *Applied Physics Letters*, 89(2):021502, 2006.

[77] A. Flacco, F. Sylla, M. Veltcheva, M. Carrié, R. Nuter, E. Lefebvre, D. Batani, and V. Malka. Dependence on pulse duration and foil thickness in high-contrast-laser proton acceleration. *Physical Review E*, 81(3):036405, 2010.

[78] K. Zeil, J. Metzkes, T. Kluge, M. Bussmann, T. E. Cowan, S. D. Kraft, R. Sauerbrey, B. Schmidt, M. Zier, and U. Schramm. Robust energy enhancement of ultrashort pulse laser accelerated protons from reduced mass targets. *Plasma Physics and Controlled Fusion*, 56(8):084004, 2014.

[79] L. Fedeli, A. Sgattoni, G. Cantono, D. Garzella, F. Réau, I. Prencipe, M. Passoni, M. Raynaud, M. Květoň, J. Proska, et al. Electron acceleration by relativistic surface plasmons in laser-grating interaction. *Physical review letters*, 116(1):015001, 2016.

[80] T. Ceccotti, V. Floquet, A. Sgattoni, A. Bigongiari, O. Klimo, M. Raynaud, C. Riconda, A. Heron, F. Baffigi, L. Labate, et al. Evidence of resonant surface-wave excitation in the relativistic regime through measurements of proton acceleration from grating targets. *Physical review letters*, 111(18):185001, 2013.

[81] M. Manclossi, J. J. Santos, D. Batani, J. Faure, A. Debayle, V. T. Tikhonchuk, and V. Malka. Study of ultraintense laser-produced fast-electron propagation and filamentation in insulator and metal foil targets by optical emission diagnostics. *Physical review letters*, 96(12):125002, 2006.

[82] D. Margarone, I. J. Kim Jong, J. Psikal, J. Kaufman, T. Mocek, I. W. Choi, L. Stolcova, J. Proska, A. Choukourov, M. Melnichuk, et al. Laser-driven high-energy proton beam with homogeneous spatial profile from a nanosphere target. *Physical Review Special Topics-Accelerators and Beams*, 18(7):071304, 2015.

[83] H. Y. Wang, C. Lin, Z. M. Sheng, B. Liu, S. Zhao, Z. Y. Guo, Y. R. Lu, X. T. He, J. E. Chen, and X. Q. Yan. Laser shaping of a relativistic intense, short gaussian pulse by a plasma lens. *Physical review letters*, 107(26):265002, 2011.

[84] T. Nakamura, S. V. Bulanov, T. Z. Esirkepov, and M. Kando. High-energy ions from near-critical density plasmas via magnetic vortex acceleration. *Physical review letters*, 105(13):135002, 2010.

[85] A. Pukhov, Z. M. Sheng, and J. Meyer ter Vehn. Particle acceleration in relativistic laser channels. *Physics of Plasmas*, 6(7):2847–2854, 1999.

[86] A. Sgattoni, P. Londrillo, A. Macchi, and M. Passoni. Laser ion acceleration using a solid target coupled with a low-density layer. *Physical Review E*, 85(3):036405, 2012.

[87] N. G. Borisenko, A. M. Khalenkov, V. Kmetik, J. Limpouch, Y. A. Merkuliev, and V. G. Pimenov. Plastic aerogel targets and optical transparency of undercritical microheterogeneous plasma. *Fusion science and technology*, 51(4):655–664, 2007.

[88] W. Ma, L. Song, R. Yang, T. Zhang, Y. Zhao, L. Sun, Y. Ren, D. Liu, L. Liu, J. Shen, et al. Directly synthesized strong, highly conducting, transparent single-walled carbon nanotube films. *Nano Letters*, 7(8):2307–2311, 2007.

[89] A. Zani, D. Dellasega, V. Russo, and M. Passoni. Ultra-low density carbon foams produced by pulsed laser deposition. *Carbon*, 56:358–365, 2013.

[90] M. Passoni, A. Sgattoni, I. Prencipe, L. Fedeli, D. Dellasega, L Cialfi, I. W. Choi, I. J. Kim, K. A. Janulewicz, H. W. Lee, et al. Toward high-energy laser-driven ion beams: Nanostructured double-layer targets. *Physical Review Accelerators and Beams*, 19(6):061301, 2016.

[91] I. Prencipe, A. Sgattoni, D. Dellasega, L. Fedeli, L. Cialfi, I. W. Choi, I. J. Kim, K. A. Janulewicz, K. F. Kakolee, H. W. Lee, et al. Development of foam-based layered targets for laser-driven ion beam production. *Plasma Physics and Controlled Fusion*, 58(3):034019, 2016.

[92] A. Maffini, A. Pazzaglia, D. Dellasega, V. Russo, and M. Passoni. Growth dynamics of pulsed laser deposited nanofoams. *Physical Review Materials*, 3(8):083404, 2019.

[93] Passoni M, A. Zani, A. Sgattoni, D. Dellasega, A. Macchi, I. Prencipe, V. Floquet, P. Martin, T. V. Liseykina, and T. Ceccotti. Energetic ions at moderate laser intensities using foam-based multi-layered targets. *Plasma Physics and Controlled Fusion*, 56(4):045001, 2014.

[94] J. H. Bin, M. Yeung, Z. Gong, H. Y. Wang, C. Kreuzer, M. L. Zhou, M. J. V. Streeter, P. S. Foster, S. Cousens, B. Dromey, et al. Enhanced laser-driven ion acceleration by superponderomotive electrons generated from near-critical-density plasma. *Physical review letters*, 120(7):074801, 2018.

[95] W. J. Ma, I. J. Kim, J. Q. Yu, I. W. Choi, P. K. Singh, H. W. Lee, J. H. Sung, S. K. Lee, C. Lin, Q. Liao, et al. Laser acceleration of highly energetic carbon ions using a double-layer target composed of slightly underdense plasma and ultrathin foil. *Physical review letters*, 122(1):014803, 2019.

[96] W. Kruer. *The physics of laser plasma interactions*. CRC Press, 2019.

[97] C. K. Birdsall and A. B. Langdon. *Plasma physics via computer simulation*. CRC press, 2004.

[98] T. D. Arber, K. Bennett, C. S. Brady, A. Lawrence-Douglas, M. G. Ramsay, N. J. Sircombe, P. Gillies, R. G. Evans, H. Schmitz, A. R. Bell, et al. Contemporary particle-in-cell approach to laser-plasma modelling. *Plasma Physics and Controlled Fusion*, 57(11):113001, 2015.

[99] A. Pazzaglia, L. Fedeli, A. Formenti, A. Maffini, and M. Passoni. A theoretical model of laser-driven ion acceleration from near-critical double-layer targets. *Communications Physics*, 3(1):1–13, 2020.

[100] A. Sgattoni, L. Fedeli, S. Sinigardi, A. Marocchino, A. Macchi, V. Weinberg, and A. Karmakar. Optimising piccante-an open source particle-in-cell code for advanced simulations on tier-0 systems. *arXiv preprint arXiv:1503.02464*, 2015.

[101] T. Toncian, C. Wang, E. McCary, A. Meadows, A. V. Arefiev, J. Blakeney, K. Serratto, D. Kuk, C. Chester, R. Roycroft, et al. Non-maxwellian electron distributions resulting from direct laser acceleration in near-critical plasmas. *Matter and Radiation at Extremes*, 1(1):82–87, 2016.

[102] O. N. Rosmej, N. E. Andreev, S. Zaehter, N. Zahn, P. Christ, B. Borm, T. Radon, A. Sokolov, L. P. Pugachev, D. Khaghani, et al. Interaction of relativistically intense laser pulses with long-scale near critical plasmas for optimization of laser based sources of mev electrons and gamma-rays. *New Journal of Physics*, 21(4):043044, 2019.

[103] O. N. Rosmej, M. Gyrdymov, M. M. Günther, N. E. Andreev, P. Tavana, P. Neumayer, S. Zähter, N Zahn, V. S. Popov, N. G. Borisenko, et al. High-current laser-driven beams of relativistic electrons for high energy density research. *Plasma Physics and Controlled Fusion*, 62(11):115024, 2020.

[104] M. M. Günther, K. Sonnabend, E. Brambrink, K. Vog, V. Bagnoud, K. Harres, and M. Roth. A novel nuclear pyrometry for the characterization of high-energy bremsstrahlung and electrons produced in relativistic laser-plasma interactions. *Physics of Plasmas*, 18(8):083102, 2011.

[105] O. N. Rosmej, M. Gyrdymov, M. M. Günther, N. E. Andreev, P. Tavana, P. Neumayer, S. Zähter, N. Zahn, V. S. Popov N. G., Borisenko, et al. High-current laser-driven beams of relativistic electrons for high energy density research. *Plasma Physics and Controlled Fusion*, 62(11):115024, 2020.

[106] V. Malka, J. Faure, Y. A. Gauduel, E. Lefebvre, A. Rousse, and K. T. Phuoc. Principles and applications of compact laser–plasma accelerators. *Nature physics*, 4(6):447–453, 2008.

[107] S. Semushin and V. Malka. High density gas jet nozzle design for laser target production. *Review of Scientific Instruments*, 72(7):2961–2965, 2001.

[108] C. E. Clayton, C. Joshi, C. Darrow, and D. Umstadter. Relativistic plasma-wave excitation by collinear optical mixing. *Physical review letters*, 54(21):2343, 1985.

[109] W. P. Leemans, B. Nagler, A. J. Gonsalves, C. Tóth, K. Nakamura, C. G. R. Geddes, E. S. C. B. Esarey, C. B. Schroeder, and S. M. Hooker. Gev electron beams from a centimetre-scale accelerator. *Nature physics*, 2(10):696–699, 2006.

[110] H. K. Kim, K. H. Pae, H. J. Cha, I. J. Kim, T. J. Yu, J. H. Sung, S. K. Lee, T. M. Jeong, and L. Lee. Enhancement of electron energy to the multi-gev regime by a dual-stage laser-wakefield accelerator pumped by petawatt laser pulses. *Physical review letters*, 111(16):165002, 2013.

[111] N. A. M. Hafz, T. M. Jeong, I. W. Choi, S. K. Lee, K. H. Pae, V. V. Kulagin, J. H. Sung, T. J. Yu, K. H. Hong, T. Hosokai, et al. Stable generation of gev-class electron beams from self-guided laser–plasma channels. *Nature Photonics*, 2(9):571–577, 2008.

[112] A. J. Gonsalves, K. Nakamura, J. Daniels, C. Benedettiand C. Pieronek, T. C. H. De Raadt, S. Steinke, J. H. Bin, S. S. Bulanov, J. Van Tilborg, et al. Petawatt laser guiding and electron beam acceleration to 8 gev in a laser-heated capillary discharge waveguide. *Physical review letters*, 122(8):084801, 2019.

[113] F. Gustas, D. Guénot, A. Vernier, S. Dutt, F. Böhle, R. Lopez-Martens, A. Lifschitz, and J. Faure. High-charge relativistic electron bunches from a khz laser-plasma accelerator. *Physical Review Accelerators and Beams*, 21(1):013401, 2018.

[114] A. R. Maier, N. M. Delbos, T. Eichner, L. Hübner, S. Jalas, L. Jeppe, S. W. Jolly, M. Kirchen, V. Leroux, P. Messner, et al. Decoding sources of energy variability in a laser-plasma accelerator. *Physical Review X*, 10(3):031039, 2020.

[115] T. Ceccotti, A. Lévy, H. Popescu, F. Réau, P. d'Oliveira, P. Monot, J. P. Geindre, E. Lefebvre, and P. Martin. Proton acceleration with high-intensity ultrahigh-contrast laser pulses. *Physical review letters*, 99(18):185002, 2007.

[116] D. Neely, P. Foster, A. Robinson, F. Lindau, O. Lundh, A. Persson, C. G. Wahlström, and P. McKenna. Enhanced proton beams from ultrathin targets driven by high contrast laser pulses. *Applied Physics Letters*, 89(2):021502, 2006.

[117] P. Bolton, K. Parodi, and J. Schreiber. *Applications of laser-driven particle acceleration*. CRC Press, 2018.

[118] J. A. Cobble, R. P. Johnson, T. E. Cowan, N. Renard-Le Galloudec, and M. Allen. High resolution laser-driven proton radiography. *Journal of applied physics*, 92(4):1775–1779, 2002.

[119] A. J. Mackinnon, P. K. Patel, R. P. Town, M. J. Edwards, T. Phillips, S. C. Lerner, D. W. Price, D. Hicks, M. H. Key, S. Hatchett, et al. Proton radiography as an electromagnetic field and density perturbation diagnostic. *Review of Scientific Instruments*, 75(10):3531–3536, 2004.

[120] M. Borghesi, D. H. Campbell, A. Schiavi, M. G. Haines, O. Willi, A. J. MacKinnon, P. Patel, L. A. Gizzi, M. Galimberti, R. J. Clarke, et al. Electric field detection in laser-plasma interaction experiments via the proton imaging technique. *Physics of Plasmas*, 9(5):2214–2220, 2002.

[121] L. Romagnani, S. V. Bulanov, M. Borghesi, P. Audebert, J. C. Gauthier, K. Löwenbrück, A. J. Mackinnon, P. Patel, G. Pretzler, T. Toncian, et al. Observation of collisionless shocks in laser-plasma experiments. *Physical review letters*, 101(2):025004, 2008.

[122] G. Sarri, C. A. Cecchetti, R. Jung, P. Hobbs, S. James, J. Lockyear, R. M. Stevenson, D. Doria, D. J. Hoarty, O. Willi, et al. Spatially resolved measurements of laser filamentation in long scale length underdense plasmas with and without beam smoothing. *Physical review letters*, 106(9):095001, 2011.

[123] P. K. Patel, A. J. Mackinnon, M. H. Key, T. E. Cowan, M. E. Foord, M. Allen, D. F. Price, H. Ruhl, P. T. Springer, and R. Stephens. Isochoric heating of solid-density matter with an ultrafast proton beam. *Physical review letters*, 91(12):125004, 2003.

[124] Y. Ping, A. A. Correa, T. Ogitsu, E. Draeger, E. Schwegler, T. Ao, K. Widmann, D. F. Price, E. Lee, H. Tam, et al. Warm dense matter created by isochoric laser heating. *High Energy Density Physics*, 6(2):246–257, 2010.

[125] S. V. Bulanov, T. Z. Esirkepov, V. S. Khoroshkov, A. V. Kuznetsov, and F. Pegoraro. Oncological hadrontherapy with laser ion accelerators. *Physics Letters A*, 299(2-3):240–247, 2002.

[126] K. W. D. Ledingham, P. R. Bolton, N. Shikazono, and C. M. C. Ma. Towards laser driven hadron cancer radiotherapy: A review of progress. *Applied Sciences*, 4(3):402–443, 2014.

[127] V. Favaudon, L. Caplier, V. Monceau, F. Pouzoulet, M. Sayarath, C. Fouillade, M. F. Poupon, I. Brito, P. Hupé, J Bourhis, et al. Ultrahigh dose-rate flash irradiation increases the differential response between normal and tumor tissue in mice. *Science translational medicine*, 6(245):245ra93–245ra93, 2014.

[128] M. C. Vozenin, P. De Fornel, K. Petersson, V. Favaudon, M. Jaccard, J. F. Germond, B. Petit, M. Burki, G. Ferrand, D. Patin, et al. The advantage of flash radiotherapy confirmed in mini-pig and cat-cancer patients. *Clinical Cancer Research*, 25(1):35–42, 2019.

[129] M. Durante, E. Bräuer-Krisch, and M. Hill. Faster and safer? flash ultra-high dose rate in radiotherapy. *The British journal of radiology*, 91(1082):20170628, 2018.

[130] F. Romano, A. Subiel, M. McManus andN. D. Lee, H. Palmans, R. Thomas, S. McCallum, G. Milluzzo, M. Borghesi, A. McIlvenny, et al. Challenges in dosimetry of particle beams with ultra-high pulse dose rates. In *Journal of Physics: Conference Series*, volume 1662, page 012028. IOP Publishing, 2020.

[131] S. Fritzler, V. Malka, G. Grillon, J. P. Rousseau, F. Burgy, E. Lefebvre, E. d'Humieres, P. McKenna, and K. W. D. Ledingham. Proton beams generated with high-intensity lasers: Applications to medical isotope production. *Applied physics letters*, 83(15):3039–3041, 2003.

[132] K. W. D. Ledingham, P. McKenna, T. McCanny, S. Shimizu, J. M. Yang, L. Robson, J. Zweit, J. M. Gillies, J. Bailey, G. M. Chimon, et al. High power laser production of short-lived isotopes for positron emission tomography. *Journal of Physics D: Applied Physics*, 37(16):2341, 2004.

[133] V. Y. Bychenkov, A. V. Brantov, and G. Mourou. Tc-99m production with ultrashort intense laser pulses. *Laser and Particle Beams*, 32(4):605, 2014.

[134] H. Takabe. Astrophysics with intense and ultra-intense lasers "laser astrophysics". *Progress of Theoretical Physics Supplement*, 143:202–265, 2001.

[135] D. Mascali, S. Tudisco, A. Bonanno, N. Gambino, S. Ivanovski, A. Anzalone, S. Gammino, R. Miracoli, and F. Musumeci. Colliding laser-produced plasmas: a new tool for nuclear astrophysics studies. *Radiation Effects & Defects in Solids: Incorporating Plasma Science & Plasma Technology*, 165(6-10):730–736, 2010.

[136] L. Willingale, S. R. Nagel, A. G. R. Thomas, C. Bellei, R. J. Clarke, A. E. Dangor, R. Heathcote, M. C. Kaluza, C. Kamperidis, S. Kneip, et al. Characterization of laser-driven proton beams from near-critical density targets using copper activation. *Journal of Plasma Physics*, 81(LLNL-JRNL-741116), 2014.

[137] D. Habs, P. G. Thirolf, M. Gross, K. Allinger, J. Bin, A. Henig, D. Kiefer, W. Ma, and J. Schreiber. Introducing the fission–fusion reaction process: using a laser-accelerated th beam to produce neutron-rich nuclei towards the n= 126 waiting point of the r-process. *Applied Physics B*, 103(2):471–484, 2011.

[138] K. W. D. Ledingham, P. McKenna, and R. P. Singhal. Applications for nuclear phenomena generated by ultra-intense lasers. *Science*, 300(5622):1107–1111, 2003.

[139] M. Roth, D. Jung, K. Falk andN. Guler, O. Deppert, M. Devlin, A. Favalli, J. Fernandez, D. Gautier, M. Geissel, et al. Bright laser-driven neutron source based on the relativistic transparency of solids. *Physical review letters*, 110(4):044802, 2013.

[140] K. L. Lancaster, S. Karsch, H. Habara, F. N. Beg, E. L. Clark, R. Freeman, M. H. Key, J. A. King, R. Kodama, K. Krushelnick, et al. Characterization of 7 li (p, n) 7 be neutron yields from laser produced ion beams for fast neutron radiography. *Physics of plasmas*, 11(7):3404–3408, 2004.

[141] C. M. Brenner, S. R. Mirfayzi, D. R. Rusby, C. Armstrong, A. Alejo, L. A. Wilson, R. Clarke, H. Ahmed, N. M. H. Butler, D. Haddock, et al. Laser-driven x-ray and neutron source development for industrial applications of plasma accelerators. *Plasma Physics and Controlled Fusion*, 58(1):014039, 2015.

[142] L. Fedeli, A. Formenti, A. Pazzaglia, F. M. Arioli, A. Tentori, and M. Passoni. Enhanced laser-driven hadron sources with nanostructured double-layer targets. *New Journal of Physics*, 22(3):033045, 2020.

[143] F. P. Boody, R. Höpfl, H. Hora, and J. K. Kelly. Laser-driven ion source for reduced-cost implantation of metal ions for strong reduction of dry friction and increased durability. *Laser and Particle Beams*, 14(3):443–448, 1996.

[144] L. Torrisi, S. Gammino, A. M. Mezzasalma, J. Badziak, P. Parys, J. Wolowski, E. Woryna, J. Krasa, L. Laska, M. Pfeifer, et al. Implantation of ions produced by the use of high power iodine laser. *Applied surface science*, 217(1-4):319–331, 2003.

[145] R. Ahmad, M. S. Rafique, M. B. Tahir, and H. Malik. Implantation of various energy metallic ions on aluminium substrate using a table top laser driven ion source. *Laser and Particle Beams*, 32(2):261, 2014.

[146] M. Barberio, S. Giusepponi, S. Vallières, M. Scisció, M. Celino, and P. Antici. Ultra-fast high-precision metallic nanoparticle synthesis using laser-accelerated protons. *Scientific Reports*, 10(1):1–17, 2020.

[147] M. Barberio, M. Scisciò, S. Vallières, S. Veltri, A. Morabito, and P. Antici. Laser-generated proton beams for high-precision ultra-fast crystal synthesis. *Scientific Reports*, 7(1):1–9, 2017.

[148] M. Barberio, E. Skantzakis, and P. Antici. Material analysis using laser-plasma driven luminescence spectroscopy. *Journal of Luminescence*, 214:116603, 2019.

[149] M. Barberio, E. Skantzakis, S. Sorieul, and P. Antici. Pigment darkening as case study of in-air plasma-induced luminescence. *Science advances*, 5(6):eaar6228, 2019.

[150] M. Barberio, S. Veltri, M. Scisciò, and P. Antici. Laser-accelerated proton beams as diagnostics for cultural heritage. *Scientific Reports*, 7:40415, 2017.

[151] J. E. Mahan. Physical vapor deposition of thin films. 2000.

[152] P. Sigmund. Theory of sputtering. i. sputtering yield of amorphous and polycrystalline targets. *Physical review*, 184(2):383, 1969.

[153] P. Sigmund. Sputtering by ion bombardment theoretical concepts. In *Sputtering by particle bombardment I*, pages 9–71. Springer, 1981.

[154] Y. Yamamura and H. Tawara. Energy dependence of ion-induced sputtering yields from monatomic solids at normal incidence. *Atomic data and nuclear data tables*, 62(2):149–253, 1996.

[155] N. Laegreid and G. K. Wehner. Sputtering yields of metals for ar+ and ne+ ions with energies from 50 to 600 ev. *Journal of Applied Physics*, 32(3):365–369, 1961.

[156] P. J. Kelly and R. D. Arnell. Magnetron sputtering: a review of recent developments and applications. *Vacuum*, 56(3):159–172, 2000.

[157] C. Christou and Z. H. Barber. Ionization of sputtered material in a planar magnetron discharge. *Journal of Vacuum Science & Technology A: Vacuum, Surfaces, and Films*, 18(6):2897–2907, 2000.

[158] Y. Lifshitz, S. R. Kasi, and J. W. Rabalais. Subplantation model for film growth from hyperthermal species: Application to diamond. *Physical review letters*, 62(11):1290, 1989.

[159] K. Sarakinos, J. Alami, and S. Konstantinidis. High power pulsed magnetron sputtering: A review on scientific and engineering state of the art. *Surface and Coatings Technology*, 204(11):1661–1684, 2010.

[160] J. Alami, P. O. Persson, D. Music, J. T. Gudmundsson, J. Bohlmark, and U. Helmersson. Ion-assisted physical vapor deposition for enhanced film properties on nonflat surfaces. *Journal of Vacuum Science & Technology A: Vacuum, Surfaces, and Films*, 23(2):278–280, 2005.

[161] M. Samuelsson, D. Lundin, J. Jensen, M. A. Raadu, J. T. Gudmundsson, and U. Helmersson. On the film density using high power impulse magnetron sputtering. *Surface and Coatings Technology*, 205(2):591–596, 2010.

[162] J. Alami, K. Sarakinos, G. Mark, and M. Wuttig. On the deposition rate in a high power pulsed magnetron sputtering discharge. *Applied physics letters*, 89(15):154104, 2006.

[163] D. Lundin and K. Sarakinos. An introduction to thin film processing using high-power impulse magnetron sputtering. *Journal of Materials Research*, 27(5):780–792, 2012.

[164] P. B. Barna and M. Adamik. Fundamental structure forming phenomena of polycrystalline films and the structure zone models. *Thin solid films*, 317(1-2):27–33, 1998.

[165] J. A. Thornton. The microstructure of sputter-deposited coatings. *Journal of Vacuum Science & Technology A: Vacuum, Surfaces, and Films*, 4(6):3059–3065, 1986.

[166] A. Anders. A structure zone diagram including plasma-based deposition and ion etching. *Thin Solid Films*, 518(15):4087–4090, 2010.

[167] Y. Pauleau. Generation and evolution of residual stresses in physical vapour-deposited thin films. *Vacuum*, 61(2-4):175–181, 2001.

[168] J. Alami, P. Eklund, J. M. Andersson, M. Lattemann, E. Wallin, J. Bohlmark, P. Persson, and U. Helmersson. Phase tailoring of ta thin films by highly ionized pulsed magnetron sputtering. *Thin Solid Films*, 515(7-8):3434–3438, 2007.

[169] S. Konstantinidis, J. P. Dauchot, and M. Hecq. Titanium oxide thin films deposited by high-power impulse magnetron sputtering. *Thin Solid Films*, 515(3):1182–1186, 2006.

[170] A. Anders. Tutorial: Reactive high power impulse magnetron sputtering (r-hipims). *Journal of applied physics*, 121(17):171101, 2017.

[171] M. J. Donachie. *Titanium: a technical guide*. ASM international, 2000.

[172] C. Gandini, V. Lacquaniti, E. Monticone, C. Portesi, M. Rajteri, M. L. Rastello, E. Pasca, and G. Ventura. Correlation of critical temperatures and electrical properties in titanium films. *International Journal of Modern Physics B*, 17(04n06):948–952, 2003.

[173] A. Tiwari, H. Satoh, M. Aoki, M. Takeda, N. Hiromoto, and H. Inokawa. Fabrication and analytical modeling of integrated heater and thermistor for antenna-coupled bolometers. *Sensors and Actuators A: Physical*, 222:160–166, 2015.

[174] M. Ukibe, M. Koyanagi, M. Ohkubo, H. Pressler, and N. Kobayashi. Characteristics of ti films for transition-edge sensor microcalorimeters. *Nuclear Instruments and Methods in Physics Research Section A: Accelerators, Spectrometers, Detectors and Associated Equipment*, 436(1-2):256–261, 1999.

[175] C. O'Mahony, M. Hill, P. J. Hughes, and W. A. Lane. Titanium as a micromechanical material. *Journal of Micromechanics and Microengineering*, 12(4):438, 2002.

[176] A. T. Tran, O. Wunnicke, G. Pandraud, M. D. Nguyen, H. Schellevis, and P. M. Sarro. Slender piezoelectric cantilevers of high quality aln layers sputtered on ti thin film for mems actuators. *Sensors and Actuators A: Physical*, 202:118–123, 2013.

[177] D. Ratnayake, M. D. Martin, U. R. Gowrishetty, D. A. Porter, T. A. Berfield, S. P. McNamara, and K. M. Walsh. Engineering stress in thin films for the field of bistable mems. *Journal of Micromechanics and Microengineering*, 25(12):125025, 2015.

[178] K. Hofmann, B. Spangenberg, M. Luysberg, and H. Kurz. Properties of evaporated titanium thin films and their possible application in single electron devices. *Thin Solid Films*, 436(2):168–174, 2003.

[179] K. Zeil, S. D. Kraft, S. Bock, M. Bussmann, T. E. Cowan, T. Kluge, J. Metzkes, T. Richter, R. Sauerbrey, and U. Schramm. The scaling of proton energies in ultrashort pulse laser plasma acceleration. *New Journal of Physics*, 12(4):045015, 2010.

[180] S. Banerjee and P. Mukhopadhyay. *Phase transformations: examples from titanium and zirconium alloys*. Elsevier, 2010.

[181] N. Adachi, Y. Todaka, K. Irie, and M. Umemoto. Phase transformation kinetics of ω-phase in pure ti formed by high-pressure torsion. *Journal of materials science*, 51(5):2608–2615, 2016.

[182] A. R. Kilmametov, Y. Ivanisenko, A. A. Mazilkin, B. B. Straumal, A. S. Gornakova, O. B. Fabrichnaya, M. J. Kriegel, D. Rafaja, and H. Hahn. The $\alpha\rightarrow\omega$ and $\beta\rightarrow\omega$ phase transformations in ti–fe alloys under high-pressure torsion. *Acta Materialia*, 144:337–351, 2018.

[183] H. Dammak, A. Barbu, A. Dunlop, D. Lesueur, and N. Lorenzelli. $\alpha\rightarrow\omega$ phase transformation induced in titanium during ion irradiations in the electronic slowing-down regime. *Philosophical magazine letters*, 67(4):253–259, 1993.

[184] H. Dammak, A. Dunlop, and D. Lesueur. Phase transformation induced by swift heavy ion irradiation of pure metals. *Nuclear Instruments and Methods in Physics Research Section B: Beam Interactions with Materials and Atoms*, 107(1-4):204–211, 1996.

[185] V. Lavrentiev, C. Hammerl, B. Rauschenbach, A. Pisanenko, and O. Kukharenko. $\alpha\rightarrow\omega$-phase transformation in titanium induced by power ion-beam irradiation. *Philosophical Magazine A*, 81(2):511–527, 2001.

[186] M. Angiolini, H. Dammak, and A. Dunlop. ω phase in individual latent tracks induced by irradiation of α-titanium with megaelectronvolt fullerenes. *Philosophical Magazine Letters*, 82(2):81–89, 2002.

[187] V. Lavrentiev, C. Hammerl, B. Rauschenbach, and O. Kukharenko. Formation of hardened surface layers in titanium under irradiation with intense ion beams. *Scripta materialia*, 44(4):625–630, 2001.

[188] Y.-T. Cheng and W.-J. Meng. Epitaxial growth of omega-titanium on the (111) surface of alpha-iron. *Physical review letters*, 76(21):3999, 1996.

[189] F. E. Wawner Jr and K. R. Lawless. Epitaxial growth of titanium thin films. *Journal of Vacuum Science and Technology*, 6(4):588–590, 1969.

[190] Y. Sugawara, N. Shibata, S. Hara, and Y. Ikuhara. Interface structure of face-centered-cubic-ti thin film grown on 6h–sic substrate. *Journal of Materials Research*, 15(10):2121–2124, 2000.

[191] S. K. Kim, F. Jona, and P. M. Marcus. Growth of face-centred-cubic titanium on aluminium. *Journal of Physics: Condensed Matter*, 8(1):25, 1996.

[192] M. Fazio, D. Vega, A. Kleiman, D. Colombo, L. M. F. Arias, and A. Márquez. Study of the structure of titanium thin films deposited with a vacuum arc as a function of the thickness. *Thin Solid Films*, 593:110–115, 2015.

[193] I. Petrov, P. B. Barna, L. Hultman, and J. E. Greene. Microstructural evolution during film growth. *Journal of Vacuum Science & Technology A: Vacuum, Surfaces, and Films*, 21(5):S117–S128, 2003.

[194] D. Magnfält, G. Abadias, and K. Sarakinos. Atom insertion into grain boundaries and stress generation in physically vapor deposited films. *Applied Physics Letters*, 103(5):051910, 2013.

[195] X. Gao, J. Sun, Y. Fu, D. Jiang, D. Wang, L. Weng, and M. Hu. Improved wear resistance of ws2 film by lt-deposited ti interlayer with ω phase structure. *Vacuum*, 155:423–427, 2018.

[196] J. Chakraborty, K. Kumar, R. Ranjan, S. G. Chowdhury, and S. R. Singh. Thickness-dependent fcc–hcp phase transformation in polycrystalline titanium thin films. *Acta Materialia*, 59(7):2615–2623, 2011.

[197] L. Fedeli. *High field plasmonics*. Springer, 2016.

[198] J. U. Brackbill. On energy and momentum conservation in particle-in-cell plasma simulation. *Journal of Computational Physics*, 317:405–427, 2016.

[199] K. Yee. Numerical solution of initial boundary value problems involving maxwell's equations in isotropic media. *IEEE Transactions on antennas and propagation*, 14(3):302–307, 1966.

[200] J. VonNeumann and R. D. Richtmyer. A method for the numerical calculation of hydrodynamic shocks. *Journal of applied physics*, 21(3):232–237, 1950.

[201] J.-L. Vay, A. Almgren, J. Bell, L. Ge, D. P. Grote, M. Hogan, O. Kononenko, R. Lehe, A. Myers, C. Ng, et al. Warp-x: A new exascale computing platform for beam–plasma simulations. *Nuclear Instruments and Methods in Physics Research Section A: Accelerators, Spectrometers, Detectors and Associated Equipment*, 909:476–479, 2018.

[202] C. J. Werner, J. S. Bull, C. J. Solomon, F. B . Brown, G. W. McKinney, M. E. Rising, D. A. Dixon, R. L. Martz, H. G. Hughes, L. J. Cox, et al. Mcnp version 6.2 release notes. Technical report, Los Alamos National Lab.(LANL), Los Alamos, NM (United States), 2018.

[203] A. Ferrari, P. R. Sala, A. Fasso, J. Ranft, U. Siegen, et al. Fluka: a multi-particle transport code. Technical report, Stanford Linear Accelerator Center (SLAC), 2005.

[204] S. Agostinelli, J. Allison, K. Amako, J. Apostolakis, H. Araujo, P. Arce, M. Asai, D. Axen, S. Banerjee, G. Barrand, et al. Geant4—a simulation toolkit. *Nuclear instruments and methods in physics research section A: Accelerators, Spectrometers, Detectors and Associated Equipment*, 506(3):250–303, 2003.

[205] F. Salvat, J. M. Fernández-Varea, and J. Sempau. Penelope-2006: A code system for monte carlo simulation of electron and photon transport. In *Workshop proceedings*, volume 4, page 7. Universitat de Barcelona, 2006.

[206] J. Allison, K. Amako, J. E. A. Apostolakis, H. A. A. H. Araujo, P. A. Dubois, M. A. A. M. Asai, G. A. B. G. Barrand, R. A. C. R. Capra, S. A. C. S. Chauvie, R. A. C. R. Chytracek, et al. Geant4 developments and applications. *IEEE Transactions on nuclear science*, 53(1):270–278, 2006.

[207] J. Allison, K. Amako, J. Apostolakis, P. Arce, M. Asai, T. Aso, E. Bagli, A. Bagulya, S. Banerjee, G. J. N. I. Barrand, et al. Recent developments in geant4. *Nuclear Instruments and Methods in Physics Research Section A: Accelerators, Spectrometers, Detectors and Associated Equipment*, 835:186–225, 2016.

[208] A. Mantero, H. Ben Abdelouahed, C. Champion, Z. El Bitar, Z. Francis, P. Guèye, S. Incerti, V. Ivanchenko, and M. Maire. Pixe simulation in geant4. *X-Ray Spectrometry*, 40(3):135–140, 2011.

[209] Z. Francis, M. El Bast, R. El Haddad, A. Mantero, S. Incerti, V. Ivanchenko, Z. El Bitar, C. Champion, M. A. Bernal, and M. Roumie. A comparison between geant4 pixe simulations and experimental data for standard reference samples. *Nuclear Instruments and Methods in Physics Research Section B: Beam Interactions with Materials and Atoms*, 316:1–5, 2013.

[210] S. B. Ahmad, J. E. Thompson, F. E. McNeill, S. H. Byun, and W. V. Prestwich. Particle induced x-ray emission and ion dose distribution in a biological micro-beam: Geant4 monte carlo simulations. *Nuclear Instruments and Methods in Physics Research Section B: Beam Interactions with Materials and Atoms*, 295:30–37, 2013.

[211] S. Incerti, P. Barberet, G. Deves, C. Michelet, Z. Francis, V. Ivantchenko, A. Mantero, Z. El Bitar, M. A. Bernal, H. N. Tran, et al. Comparison of experimental proton-induced fluorescence spectra for a selection of thin high-z samples with geant4 monte carlo simulations. *Nuclear Instruments and Methods in Physics Research Section B: Beam Interactions with Materials and Atoms*, 358:210–222, 2015.

[212] L. Pandola, C. Andenna, and B. Caccia. Validation of the geant4 simulation of bremsstrahlung from thick targets below 3 mev. *Nuclear Instruments and Methods in Physics Research Section B: Beam Interactions with Materials and Atoms*, 350:41–48, 2015.

[213] J. P. Wellisch, M. Kossov, and P. Degtyarenko. Electro and gamma nuclear physics in geant4. *arXiv preprint nucl-th/0306012*, 2003.

[214] L. Quintieri, M. G. Pia, M. Augelli, P. Saracco, M. Capogni, and G. Guarnieri. Quantification of the validity of simulations based on geant4 and fluka for photo-nuclear interactions in the high energy range. In *EPJ Web of Conferences*, volume 153, page 06023. EDP Sciences, 2017.

[215] A. Fassò, A. Ferrari, and P. R. Sala. Photonuclear reactions in fluka: cross sections and interaction models. In *AIP conference Proceedings*, volume 769, pages 1303–1306. American Institute of Physics, 2005.

[216] S. C. Fultz, R. L. Bramblett, J. T. Caldwell, N. E. Hansen, and C. P. Jupiter. Photoneutron cross sections for v 51 and co 59. *Physical Review*, 128(5):2345, 1962.

[217] V. V. Varlamov, N. G. Efimkin, B. S. Ishkhanov, V. V. Sapunenko, and M. E. Stepanov. Evaluation of cu-63, 65 (g, np) and cu-63, 65 (g, p) reaction cross sections in the energy range of giant dipole resonance and isospin splitting of the gdr of cu nuclei. *Bull Rus Acad Sci Phys*, 59:911, 1995.

[218] H. Beil, R. Bergere, P. Carlos, A. Lepretre, A. De Miniac, and A. Veyssiere. A study of the photoneutron contribution to the giant dipole resonance in doubly even mo isotopes. *Nuclear Physics A*, 227(3):427–449, 1974.

[219] A. J. Koning, D. Rochman, J.-C. Sublet, N. Dzysiuk, M. Fleming, and S. Van Der Marck. Tendl: complete nuclear data library for innovative nuclear science and technology. *Nuclear Data Sheets*, 155:1–55, 2019.

[220] H. Luo, F. Gao, and A. Billard. Tunable microstructures and morphology of zirconium films via an assist of magnetic field in hipims for improved mechanical properties. *Surface and Coatings Technology*, 374:822–832, 2019.

[221] B. Wu, Y. Yu, J. Wu, I. Shchelkanov, D. N. Ruzic, N. Huang, and Y. X. Leng. Tailoring of titanium thin film properties in high power pulsed magnetron sputtering. *Vacuum*, 150:144–154, 2018.

[222] A. P. Ehiasarian, A. Vetushka, Y. A. Gonzalvo, G. Sáfrán, L. Székely, and P. B. Barna. Influence of high power impulse magnetron sputtering plasma ionization on the microstructure of tin thin films. *Journal of applied physics*, 109(10):104314, 2011.

[223] A. Kramida, Y. Ralchenko, and J. Reader. Team 2015, nist atomic spectra database (ver. 5.3). *National Institute of Standards and Technology, Gaithersburg, MD (Available at: http://physics. nist. gov/asd)*, 2018.

[224] P. R. Bevington and D. K. Robinson. Data reduction and error analysis. *McGrawâ€“Hill, New York*, 2003.

[225] Y. L. Jeyachandran, B. Karunagaran, S. K. Narayandass, D. Mangalaraj, T. E. Jenkins, and P. J. Martin. Properties of titanium thin films deposited by dc magnetron sputtering. *Materials Science and Engineering: A*, 431(1-2):277–284, 2006.

[226] V. Chawla, R. Jayaganthan, A. K. Chawla, and R. Chandra. Microstructural characterizations of magnetron sputtered ti films on glass substrate. *journal of materials processing technology*, 209(7):3444–3451, 2009.

[227] A. Y. Chen, Y. Bu, Y. T. Tang, Y. Wang, F. Liu, X. F. Xie, and J. F. Gu. Deposition-rate dependence of orientation growth and crystallization of ti thin films prepared by magnetron sputtering. *Thin Solid Films*, 574:71–77, 2015.

[228] G. Liu, Y. Yang, N. Jin, X. Luo, B. Huang, P. Li, and Z. Kou. The structural characterizations of ti-17 alloy films prepared by magnetron sputtering. *Applied Surface Science*, 427:774–781, 2018.

[229] M. Ferrari and L. Lutterotti. Method for the simultaneous determination of anisotropic residual stresses and texture by x-ray diffraction. *Journal of Applied Physics*, 76(11):7246–7255, 1994.

[230] E. Besozzi, D. Dellasega, A. Pezzoli, A. Mantegazza, M. Passoni, and M. G. Beghi. Coefficient of thermal expansion of nanostructured tungsten based coatings assessed by substrate curvature method. *Materials & Design*, 137:192–203, 2018.

[231] E. Besozzi, D. Dellasega, V. Russo, C. Conti, M. Passoni, and M. G. Beghi. Thermomechanical properties of amorphous metallic tungsten-oxygen and tungsten-oxide coatings. *Materials & Design*, 165:107565, 2019.

[232] G. G. Stoney. The tension of metallic films deposited by electrolysis. *Proceedings of the Royal Society of London. Series A, Containing Papers of a Mathematical and Physical Character*, 82(553):172–175, 1909.

[233] F. J. Jing, T. L. Yin, K. Yukimura, H. Sun, Y. X. Leng, and N. Huang. Titanium film deposition by high-power impulse magnetron sputtering: influence of pulse duration. *Vacuum*, 86(12):2114–2119, 2012.

[234] N. Arshi, J. Lu, C. G. Lee, J. H. Yoon, B. H. Koo, and F. Ahmed. Thickness effect on properties of titanium film deposited by dc magnetron sputtering and electron beam evaporation techniques. *Bulletin of Materials Science*, 36(5):807–812, 2013.

[235] R. Checchetto. Titanium thin film deposition in a deuterium atmosphere. *Thin Solid Films*, 302(1-2):77–83, 1997.

[236] Z. Y. Hang and C. V. Thompson. Grain growth and complex stress evolution during volmer–weber growth of polycrystalline thin films. *Acta Materialia*, 67:189–198, 2014.

[237] F. Cemin, G. Abadias, T. Minea, C. Furgeaud, F. Brisset, D. Solas, and D. Lundin. Benefits of energetic ion bombardment for tailoring stress and microstructural evolution during growth of cu thin films. *Acta Materialia*, 141:120–130, 2017.

[238] F. Cemin, D. Lundin, C. Furgeaud, A. Michel, G. Amiard, T. Minea, and G. Abadias. Epitaxial growth of cu (001) thin films onto si (001) using a single-step hipims process. *Scientific reports*, 7(1):1–10, 2017.

[239] E. Vassallo, R. Caniello, M. Canetti, D. Dellasega, and M. Passoni. Microstructural characterisation of tungsten coatings deposited using plasma sputtering on si substrates. *Thin Solid Films*, 558:189–193, 2014.

[240] L.-P. Yue, W. Yao, Z. Qi, and Y. He. Microstructure of nanometre crystalline films prepared by ion-beam sputtering. *Journal of materials science letters*, 13(18):1311–1313, 1994.

[241] A. Aguayo, G. Murrieta, and R. De Coss. Elastic stability and electronic structure of fcc ti, zr, and hf: a first-principles study. *Physical Review B*, 65(9):092106, 2002.

[242] A. Saedi and M. J. Rost. Thermodynamics of deposition flux-dependent intrinsic film stress. *Nature communications*, 7(1):1–6, 2016.

[243] J. Ren, X. Liu, Q. Lei, Q. Wang, X. Zhang, X. Zhang, X. Lu, H. Xue, and Y. Ding. Deformation behavior of pure titanium with a rare hcp/fcc boundary: An atomistic study. *Materials Research*, 23(1), 2020.

[244] D. Flötotto, Z. M. Wang, L. P. H. Jeurgens, E. Bischoff, and E. J. Mittemeijer. Effect of adatom surface diffusivity on microstructure and intrinsic stress evolutions during ag film growth. *Journal of Applied Physics*, 112(4):043503, 2012.

[245] F. J. Karasek. Fabrication of target foils by rolling techniques. *Nuclear Instruments And Methods*, 102(3):457–458, 1972.

[246] A. Lübcke, A. A. Andreev, S. Höhm, R. Grunwald, L. Ehrentraut, and M. Schnürer. Prospects of target nanostructuring for laser proton acceleration. *Scientific reports*, 7(1):1–8, 2017.

[247] H. Schwoerer, S. Pfotenhauer, O. Jäckel, K.-U. Amthor, B. Liesfeld, W. Ziegler, R. Sauerbrey, K. W. D. Ledingham, and T. Esirkepov. Laser-plasma acceleration of quasi-monoenergetic protons from microstructured targets. *Nature*, 439(7075):445–448, 2006.

[248] V. L. Stout and M. D. Gibbons. Gettering of gas by titanium. *Journal of applied physics*, 26(12):1488–1492, 1955.

[249] A. Pazzaglia, A .Maffini, D. Dellasega, A. Lamperti, and M. Passoni. Reference-free evaluation of thin films mass thickness and composition through energy dispersive x-ray spectroscopy. *Materials Characterization*, 153:92–102, 2019.

[250] M. Borghesi and U. Schramm. Summary of working group 2: Ion beams from plasmas. *NIMPA*, 829:137–140, 2016.

[251] M. Nishiuchi, H. Sakaki, T. Hori, P. R. Bolton, K. Ogura, A. Sagisaka, A. Yogo, M. Mori, S. Orimo, A. S. Pirozhkov, et al. Measured and simulated transport of 1.9 mev laser-accelerated proton bunches through an integrated test beam line at 1 hz. *Physical Review Special Topics-Accelerators and Beams*, 13(7):071304, 2010.

[252] A. Henig, S. Steinke, M. Schnürer, T. Sokollik, R. Hörlein, D. Kiefer, D. Jung, J. Schreiber, B. M. Hegelich, X. Q. Yan, et al. Radiation-pressure acceleration of ion beams driven by circularly polarized laser pulses. *Physical Review Letters*, 103(24):245003, 2009.

[253] C. A. J. Palmer, N. P. Dover, I. Pogorelsky, M. Babzien, G. I. Dudnikova, M. Ispiriyan, M. N. Polyanskiy, J. Schreiber, P. Shkolnikov, V. Yakimenko, et al. Monoenergetic proton beams accelerated by a radiation pressure driven shock. *Physical review letters*, 106(1):014801, 2011.

[254] D. Haberberger, S. Tochitsky, F. Fiuza, C. Gong, R. A. Fonseca, L. O. Silva, W. B. Mori, and C. Joshi. Collisionless shocks in laser-produced plasma generate monoenergetic high-energy proton beams. *Nature Physics*, 8(1):95–99, 2012.

[255] D. E. King. Dlib-ml: A machine learning toolkit. *The Journal of Machine Learning Research*, 10:1755–1758, 2009.

[256] M. Gauthier, C. B. Curry, S. Göde, F. E. Brack, J. B. Kim, M. J. MacDonald, J. Metzkes, L. Obst, M. Rehwald, C. Rödel, et al. High repetition rate, multi-mev proton source from cryogenic hydrogen jets. *Applied Physics Letters*, 111(11):114102, 2017.

[257] Ž. Šmit, P. Pelicon, J. Simčič, and J. Istenič. Metal analysis with pixe: The case of roman military equipment. *Nuclear Instruments and Methods in Physics Research Section B: Beam Interactions with Materials and Atoms*, 239(1-2):27–34, 2005.

[258] L. De Viguerie, L. Beck, J. Salomon, L. Pichon, and P. Walter. Composition of renaissance paint layers: simultaneous particle induced x-ray emission and backscattering spectrometry. *Analytical chemistry*, 81(19):7960–7966, 2009.

[259] V. Palonen, K. Mizohata, T. Nissinen, and J. Räisänen. External beam iba set-up with large-area thin si3n4 window. *Nuclear Instruments and Methods in Physics Research Section B: Beam Interactions with Materials and Atoms*, 380:11–14, 2016.

[260] C. McGuffey, A. Raymond, T. Batson, R. Hua, G. M. Petrov, J. Kim, C. M. Krauland, A. Maksimchuk, A. G. R. Thomas, V. Yanovsky, et al. Acceleration of high charge-state target ions in high-intensity laser interactions with sub-micron targets. *New Journal of Physics*, 18(11):113032, 2016.

[261] D. Doria, K. F. Kakolee, S. Kar, S. K. Litt, F. Fiorini, H. Ahmed, S. Green, J. C. G. Jeynes, J. Kavanagh, D. Kirby, et al. Biological effectiveness on live cells of laser driven protons at dose rates exceeding 109 gy/s. *AIP Advances*, 2(1):011209, 2012.

[262] A. Yogo, K. Sato, M. Nishikino, M. Mori, T. Teshima, H. Numasaki, M. Murakami, Y. Demizu, S. Akagi, S. Nagayama, et al. Application of laser-accelerated protons to the demonstration of dna double-strand breaks in human cancer cells. *Applied Physics Letters*, 94(18):181502, 2009.

[263] C. Stoeckl, W. Theobald, T. C. Sangster, M. H. Key, P. Patel, B. B. Zhang, R. Clarke, S. Karsch, and P. Norreys. Operation of a single-photon–counting x-ray charge-coupled device camera spectrometer in a petawatt environment. *Review of scientific instruments*, 75(10):3705–3707, 2004.

[264] F. James. A review of pseudorandom number generators. *Computer physics communications*, 60(3):329–344, 1990.

[265] M. Scisciò, M. Migliorati, L. Palumbo, and P. Antici. Design and optimization of a compact laser-driven proton beamline. *Scientific reports*, 8(1):1–11, 2018.

[266] K. Zeil, J. Metzkes, T. Kluge, M. Bussmann, T. E. Cowan, S. D. Kraft, R. Sauerbrey, and U. Schramm. Direct observation of prompt pre-thermal laser ion sheath acceleration. *Nature communications*, 3(1):1–6, 2012.

[267] G. A. Becker, S. Tietze, S. Keppler, J. Reislöhner, J. H. Bin, L. Bock, F. E. Brack, J. Hein, M. Hellwing, P. Hilz, et al. Ring-like spatial distribution of laser accelerated protons in the ultra-high-contrast tnsa-regime. *Plasma Physics and Controlled Fusion*, 60(5):055010, 2018.

[268] A. Macková, D. MacGregor, F. Azaiez, J. Nyberg, and E. Piasetzky. *Nuclear physics for cultural heritage*. Nuclear Physics Division of the European Physical Society, 2016.

[269] O. Enguita, T. Calderón, M. T. Fernández-Jiménez, P. Beneitez, A. Millan, and G. Garcıéa. Damage induced by proton irradiation in carbonate based natural painting pigments. *Nuclear Instruments and Methods in Physics Research Section B: Beam Interactions with Materials and Atoms*, 219:53–56, 2004.

[270] J. Metzkes, T. E. Cowan, L. Karsch, S. D. Kraft, J. Pawelke, C. Richter, T. Richter, K. Zeil, and U. Schramm. Preparation of laser-accelerated proton beams for radiobiological applications. *Nuclear Instruments and Methods in Physics Research Section A: Accelerators, Spectrometers, Detectors and Associated Equipment*, 653(1):172–175, 2011.

[271] S. Raschke, S. Spickermann, T. Toncian, M. Swantusch, J. Boeker, U. Giesen, G. Iliakis, O. Willi, and F. Boege. Ultra-short laser-accelerated proton pulses have similar dna-damaging effectiveness but produce less immediate nitroxidative stress than conventional proton beams. *Scientific reports*, 6:32441, 2016.

[272] M. Schollmeier, S. Becker, M. Geißel, K. A. Flippo, A. Blažević, S. A. Gaillard, D. C. Gautier, F. Grüner, K. Harres, M. Kimmel, et al. Controlled transport and focusing of laser-accelerated protons with miniature magnetic devices. *Physical review letters*, 101(5):055004, 2008.

[273] X. Llovet, C. J. Powell, F. Salvat, and A. Jablonski. Cross sections for inner-shell ionization by electron impact. *Journal of Physical and Chemical Reference Data*, 43(1):013102, 2014.

[274] L. Volpe, R. Fedosejevs, G. Gatti, J. A. Pérez-Hernández, C. Méndez, J. Apiñaniz, X. Vaisseau, C. Salgado, M. Huault, S. Malko, et al. Generation of high energy laser-driven electron and proton sources with the 200 tw system vega 2 at the centro de laseres pulsados. *High Power Laser Science and Engineering*, 7, 2019.

[275] J. Baumann, R. Gnewkow, S. Staeck, V. Szwedowski-Rammert, C. Schlesiger, I. Mantouvalou, and B. Kanngießer. Photon event evaluation for conventional pixelated detectors in energy-dispersive x-ray applications. *Journal of Analytical Atomic Spectrometry*, 33(12):2043–2052, 2018.

[276] G. Abadias, E. Chason, J. Keckes, M. Sebastiani, G. B. Thompson, E. Barthel, G. L. Doll, C. E. Murray, C. H. Stoessel, and L. Martinu. Stress in thin films and coatings: Current status, challenges, and prospects. *Journal of Vacuum Science & Technology A: Vacuum, Surfaces, and Films*, 36(2):020801, 2018.

[277] G. Milluzzo, V. Scuderi, A. Alejo, A. G. Amico, N. Booth, M. Borghesi, G. A. P. Cirrone, G. Cuttone, D. Doria, J. Green, et al. A new energy spectrum reconstruction method for time-of-flight diagnostics of high-energy laser-driven protons. *Review of Scientific Instruments*, 90(8):083303, 2019.

[278] W. Hong, X.-L. Wen, L Wei, B. Zhu, Y.-C. Wu, K.-G. Dong, C.-Y. Jiao, B. Wu, Y.-L. He, F.-Q. Zhang, et al. Detailed calibration of the pi-lcx: 1300 high performance single photon counting hard x-ray ccd camera. *Chinese Physics B*, 26(2):025204, 2017.

[279] S. A. Pikuz, O. V. Chefono, S. V. Gasilov, P. S. Komarov, A. V. Ovchinnikov, I. Y. Skobelev, S. Y. Ashitkov, M. V. Agranat, A. Zigler, and A. Y. Faenov. Micro-radiography with laser plasma x-ray source operating in air atmosphere. *Laser and Particle Beams*, 28(3):393–397, 2010.

[280] R. Van Grieken and A. Markowicz. *Handbook of X-ray Spectrometry*. CRC press, 2001.

[281] A. Halbach. Sparselizard-the user friendly finite element c++ library, 2017.

[282] C. Geuzaine and J.-F. Remacle. Gmsh: A 3-d finite element mesh generator with built-in pre-and post-processing facilities. *International journal for numerical methods in engineering*, 79(11):1309–1331, 2009.

[283] D. J. S. Findlay. Analytic representation of bremsstrahlung spectra from thick radiators as a function of photon energy and angle. *Nuclear Instruments and Methods in Physics Research Section A: Accelerators, Spectrometers, Detectors and Associated Equipment*, 276(3):598–601, 1989.

[284] M. J. Berger and S. M. Seltzer. Bremsstrahlung and photoneutrons from thick tungsten and tantalum targets. *Physical Review C*, 2(2):621, 1970.

[285] V. Starovoitova and C. Segebade. High intensity photon sources for activation analysis. *Journal of Radioanalytical and Nuclear Chemistry*, 310(1):13–26, 2016.

[286] I. Krausová, J. Mizera, Z. Řanda, D. Chvátil, and P. Krist. Nondestructive assay of fluorine in geological and other materials by instrumental photon activation analysis with a microtron. *Nuclear Instruments and Methods in Physics Research Section B: Beam Interactions with Materials and Atoms*, 342:82–86, 2015.

[287] Z. Řanda, J. Kučera, and L. Soukal. Elemental characterization of the new czech meteorite 'moravka'by neutron and photon activation analysis. *Journal of Radioanalytical and Nuclear Chemistry*, 257(2):275–283, 2003.

[288] Z. Randa, J. Frána, J. Mizera, J. Kucera, J. K. Novák, J. Ulrych, A. G. Belov, and O. D. Maslov. Instrumental neutron and photon activation analysis in the geochemical study of phonolitic and trachytic rocks. *Geostandards and Geoanalytical Research*, 31(3):275–283, 2007.

[289] R. A. Aliev, E. I. Gainullina, A. N. Ermakov, B. S. Ishkhanov, and V. I. Shvedunov. Use of a split microtron for instrumental gamma activation analysis. *Journal of Analytical Chemistry*, 60(10):951–955, 2005.

[290] G. Lutz. The analysis of biological and environmental samples for lead by photon activation. *Journal of Radioanalytical and Nuclear Chemistry*, 19(2):239–244, 1974.

[291] J. S. Hislop and D. R. Williams. The determination of lead in biological materials by high-energy γ-photon activation. *Analyst*, 97(1150):78–78, 1972.

[292] S. Landsberger and W. F. Davidson. Analysis of marine sediment and lobster hepatopancreas reference materials by instrumental photon activation. *Analytical chemistry*, 57(1):196–203, 1985.

[293] I. Prencipe, J. Fuchs, S. Pascarelli, D. W. Schumacher, R. B. Stephens, N. B. Alexander, R. Briggs, M. Büscher, M. O. Cernaianu, A. Choukourov, et al. Targets for high repetition rate laser facilities: needs, challenges and perspectives. *High Power Laser Science and Engineering*, 5, 2017.

[294] T. Chagovets, S. Stanček, L. Giuffrida, A. Velyhan, M. Tryus, F. Grepl, V. Istokskaia, V. Kantarelou, T. Wiste, J. C. Hernandez Martin, et al. Automation of target delivery and diagnostic systems for high repetition rate laser-plasma acceleration. *Applied Sciences*, 11(4):1680, 2021.

[295] N. Booth, R. Clarke, R. Heathcote, D. Neely, R. Pattathil, D. Rusby, C. Spindloe, D. Symes, M. Tolley, and S. Tomlinson. High-rep rate target development for ultra-intense interaction science at the central laser facility. In *Target Diagnostics Physics and Engineering for Inertial Confinement Fusion III*, volume 9211, page 921107. International Society for Optics and Photonics, 2014.

[296] Y. Gershuni, D. Roitman, I. Cohen, E. Porat, Y. Danan, M. Elkind, A. Levanon, R. Louzon, D. Reichenberg, A. Tsabary, et al. A gatling-gun target delivery system for high-intensity laser irradiation experiments. *Nuclear Instruments and Methods in Physics Research Section A: Accelerators, Spectrometers, Detectors and Associated Equipment*, 934:58–62, 2019.

[297] C. Willis, P. L. Poole, K. U. Akli, D. W. Schumacher, and R. R. Freeman. A confocal microscope position sensor for micron-scale target alignment in ultra-intense laser-matter experiments. *Review of Scientific Instruments*, 86(5):053303, 2015.

[298] J. Schwarz, P. Rambo, M. Kimmel, M. Geissel, G. Robertson, M. Ramsey, D. Headley, and B. Atherton. Debris mitigation techniques for petawatt-class lasers in high debris environments. *Physical Review Special Topics-Accelerators and Beams*, 13(4):041001, 2010.

[299] B. Maróti, Z. Kis, L. Szentmiklósi, E. Horváth, G. Káli, and T. Belgya. Characterization of a south-levantine bronze sculpture using position-sensitive prompt gamma activation analysis and neutron imaging. *Journal of Radioanalytical and Nuclear Chemistry*, 312(2):367–375, 2017.